Energy potential of the Ecca Group from the southern Main Karoo Basin, South Africa

Stuart Alexander Campbell

Doctor of Philosophy

December 2018

Dedication

To my mother and brother for their unwavering support

Familia Ante Omnia

Abstract

Energy shortages and sporadic, controlled blackouts have been a defining feature of South Africa's aging national energy grid for more than a decade. To investigate local energy sources from shale gas, two boreholes were drilled in the southern Main Karoo Basin into the Permian-aged Ecca Group by the Karoo Research Initiative. Borehole KZF-1 (Western Cape) intersected thick shale successions of the lower Ecca Group and revealed the stratigraphic duplication of the Whitehill (shale gas target) and Prince Albert Formations. This structural deformation was most likely as a result of the organic-rich formations, acting as a decollement for thrust faults related to the north-south directed compression of the Cape Orogeny. Reservoir compartmentalisation and gas escape along porous fault zones hinder hydrocarbon exploration in the area. Borehole KWV-1 (Eastern Cape) revealed thick successions of turbiditic sandstones and a moderately elevated geothermal gradient. The clastic rocks have low permeabilities and high thermal conductivities. Analysis of the petro- and thermophysical data from the Ripon Formation sandstones, from both the core and nearby Ecca Pass outcrop location, show the potential of the formation as an Enhanced Geothermal Reservoir, with temperatures exceeding 100°C being suitable for energy production from a binary geothermal power plant. The comparison of combined gamma-ray logs, geothermal potential of samples (specific heat capacity, thermal diffusivity, and thermal conductivity) and lithological logs show a correlation between lithological composition and geothermal reservoir potential that can be identified in gamma-ray log patterns. These correlations can be extrapolated for purposes of geothermal exploration in non-cored nearby boreholes. The numerous pre-existing faults, decreasing from the basin's southern margin towards the basin interior, elevate the risk of inducing seismic events from the use of reservoir stimulation techniques associated with energy exploration, as well as wastewater management associated with future extraction activities.

Table of Contents

List of Figures

List of Tables

Acknowledgements

I would like to thank my new supervisors, Dr. Ian Stimpson and Dr. Stuart Egan, for taking me in and providing me with invaluable feedback on my work. My appreciation goes out to Keele University for providing me with funding to continue with my PhD after my initial funding was withdrawn. I would like to thank Nils Lenhardt and Mattys Dippenaar from the University of Pretoria for their work on heat in place calculations and ground water studies respectively, which contributed towards my first publication '*Geothermal energy from the Main Karoo Basin (South Africa): An outcrop analogue study of Permian sandstone reservoir formations*'. Additionally, thanks goes out to Philip Mielke of the Technische Universität Darmstadt who analysed all the geothermal samples that contributed to my second publication '*Geothermal energy from the Main Karoo Basin? New insights from borehole KWV‑1 (Eastern Cape, South Africa)*'. My deepest gratitude goes out to Dr. Adam Bumby of Marine and Petroleum Geology for assistance with my accepted manuscript '*Permian black shales of the Karoo Basin (South Africa): Structural controls and implications for shale gas resource potential'*. All three manuscripts are incorporated into my PhD thesis. I would also like to convey my gratitude to my fellow PhD candidates in the office who are always there to bounce ideas off and who are never too busy to offer their support. Lastly, I would like to give thanks to Victoria Newall for proof reading every page of my typed work for spelling and grammatical errors.

1. Introduction

The earliest account of South African geology was published in 1652 by Jodocus Hondius III, based on information supplied by survivors of the wrecked ship Haarlem from a water well dug through five sedimentary units near Table Bay Cape Town. In 1926 Du Toit published the Geology of South Africa documenting the complete Karoo Supergroup. His investigations and observations, made on horseback, provided some of the earliest evidence for continental drift (Du Toit and Reed, 1927; Du Toit, 1937).

The Main Karoo Basin is a Gondwanan foreland basin covering much of South Africa (Figure 1.1). The basin covers around 700,000 km² with siliciclastic rocks ranging in age from the Carboniferous to the Jurassic. The basin has recorded the climatic transition from ice-house to hot-house (McCarthy and Rubidge, 2005) with the fill of the basin comprising basal glacial tillite, deep-marine black shales, deltaic and fluvial sandstones and mudstones through to aeolian sandstones, with the sedimentary succession covered by flood basalts related to the breakup of Gondwana (Johnson et al., 2006).

The Main Karoo Basin contains excellent economic reserves of coal and uranium with minor conventional hydrocarbon plays (Department of Energy, 2015; EIA, 2015). South Africa has the ninth-largest recoverable coal reserves in the world and contains 95% of Africa's total coal (EIA, 2015). The country is the sixth largest coal producer in the world with commercial operations in existence since 1857 (Hancox and Götz, 2014). South Africa hosts world class uranium reserves, having an estimated reserve base of 433,364 t of uranium, or around 7% of global proven reserves in 2010 (Kotze, 2012).

Electricity production in South Africa relies heavily on coal, located within the northeast of the basin. The country is currently nearing an energy crisis with controlled rolling blackouts

the result of the state energy utility's efforts to manage generation shortages. The process of 'load shedding' (Dekker et al., 2012) results in systematic area-wide blackouts in order to reduce the strain on aging power stations and inconsistent coal supplies. Load shedding has increasingly become more common with a steady population growth and lagging energy infrastructure development, incurring negative socio-economic consequences.

The southern Main Karoo Basin was explored for oil during the 1960's and 1970's; however studies revealed poor potential due to the combination of folding, low porosity and permeability, and high thermal maturity as well as the adverse effects of numerous dolerite intrusions (Rowsell and de Swart, 1976).

In the northeast of the Main Karoo Basin the Ecca Group contains South Africa's' vast economic coal reserves (Hancox and Götz, 2014). Recent global interest in shale gas has brought the Ecca Group, located within the south of the basin, into focus. Total reserves of gas for sub-Saharan Africa are estimated to be 4 trillion cubic meters (141 trillion cubic feet) with 52% of this from the marine black shales of the Ecca Group within the southern Main Karoo Basin of South Africa (Castellano et al., 2015).

Laterally extensive organic rich shales overlain by thick sandstone successions may provide unconventional sources of energy, in the form of shale gas and geothermal, in order to combat South Africa's growing energy shortage. The shale gas potential of the southern Ecca Group has yet to be thoroughly investigated outside of theoretical gas in place calculations (Castellano et al., 2015), based on total organic carbon (TOC) measurements from old oil exploration boreholes, and no geothermal assessments have been made (outside of this study) on the deep sandstones within the southern Main Karoo Basin.

In 2015, two boreholes (KZF-1, KWV-1) were drilled in the Western and Eastern Cape Provinces (Figure 1.1), as part of the Karoo Research Initiative, to further investigate the

shale gas potential of the organic rich Whitehill Formation within the Ecca Group. The drill cores from the boreholes as well as an outcrop exposure (Ecca Pass), along a road cutting in the Eastern Cape, were studied and revealed somewhat unexpected features. The borehole drilled within the Western Cape Province (borehole KZF-1), proximal to the Cape Fold Belt, intersects the shale gas target formation at shallow depths, however the normally uniform formation was structurally chaotic. The second borehole drilled within the Eastern Cape Province (KWV-1) intersected very thick successions of turbiditic sandstones (> 1000 m) at depth before reaching the shale gas target formation.

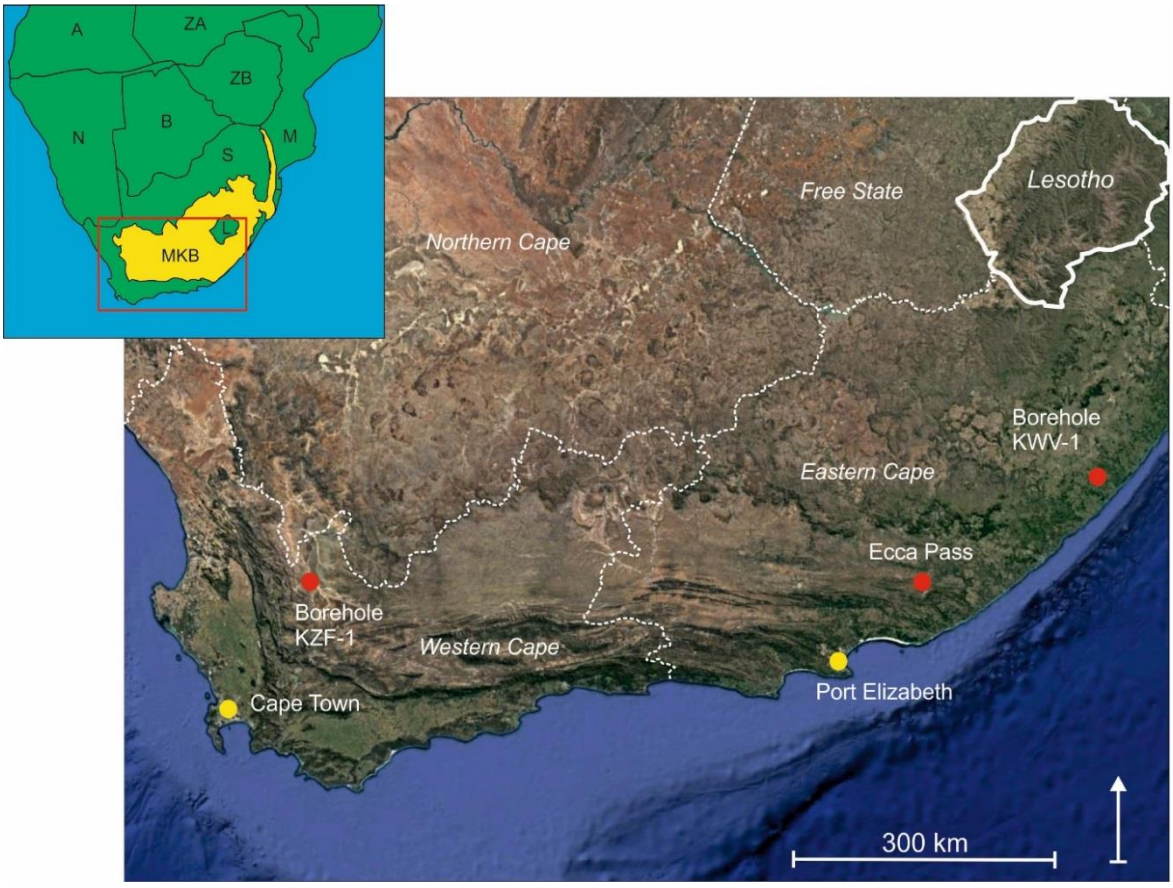

Figure 1.1: Study locations Borehole KZF-1 (Western Cape), Borehole KWV-1 and the Ecca Pass (both Eastern Cape) and location of map within Southern Africa (red box insert) and the Main Karoo Basin. S: South Africa, MKB: Main Karoo Basin, L: Lesotho, M: Mozambique, N: Namibia, B: Botswana, ZB: Zimbabwe, ZA: Zambia, A: Angola. Modified from Google Earth Pro 7.3.1. (12/14/15) Western Cape, South Africa. 32°35'45.21"S, 23°16'53.87"E, Eye Alt. 959.93 km. 2018 AfriGIS (Pty) Ltd. [09/10/17].

1.1. Aims and Objectives

The main aim of this thesis is to investigate the heat and power potential of the Ecca Group (Karoo Supergroup) within the southern Main Karoo Basin of South Africa.

The first objective of this thesis is to place borehole KZF-1 (Figure 1.1) within the established geotectonic framework of the region, as well as investigating the effects of regional scale tectonic events (e.g. Hälbich, 1983; Lindeque et al., 2011; Hansma et al., 2016) on the shale gas potential of the organic-rich Whitehill Formation. The potential effects of extracting shale gas from within a tectonically complicated setting will also be explored in light of recent environmental and social concerns around 'fracking' (c.f. NRC, 2013; Clarke et al., 2014).

Deep sedimentary basins around the globe are currently being assessed with regards to geothermal utilisation (direct heat use) due to ongoing technological advances (Zhu 2015; Hirst et al., 2015; Aretz et al., 2016). South Africa does not currently include any geothermal resources within the national energy mix (Department of Energy, 2015). Therefore, the second objective of this study is to provide a detailed description of the petro- and thermophysical rock properties of the thick sandstone successions intersected in borehole KWV-1 (Figure 1.1) in comparison with the same formation exposed along a road cutting (Ecca Pass; Figure 1.1), and identify potential exploration areas by providing an estimation of heat in place. The comparison of thermophysical properties between formations at depth and at the surface may provide the start of a valuable data set for future geothermal exploration, where drilling is initially to costly or not feasible, but where similar outcrops can be easily accessed.

It is hoped that the interpretations made in this thesis will facilitate careful planning before any shale gas exploration and extraction activities commence. Additionally it is hoped that

this thesis will provide information that will encourage the discussion around using alternative sources of energy, even on a small scale, in order to facilitate the transition towards newer and cleaner sources of energy in South Africa.

1.2. Methodology Overview

Boreholes KZF-1 and KWV-1 represent the first deep Karoo boreholes since hydrocarbon exploration ceased in the 1960s and 70s. The cores are stored at the Counsel for Geosciences in Pretoria. Both boreholes were logged by Weatherford Slimline Services after coring was completed using a Dual Spaced Neutron tool, Dual Spaced Density tool, Caliper tool and Formation Dipmeter.

Lithological and geophysical logs of both boreholes and lithological logs of the Ecca Pass outcrop, as well as rock samples from all three-study areas, form the subject matter of this thesis. Samples were analysed using standard light microscopy and using a scanning electron microscope with electron dispersive spectrometry where applicable. Appropriate samples were analysed for porosity and permeability as well as density, thermal conductivity, thermal diffusivity and specific heat capacity. One sample was analysed for palynology in order to assess the provenance of the organic matter (i.e. terrestrial vs marine). A model for the tectonic features observed in borehole KZF-1 was made using illustrative software based on observations and previous research conducted in the area. Mathematical calculations of specific heat capacity and heat in place, based on laboratory analyses, followed the published methodology used in similar previous studies. In-depth methodologies are detailed in the individual research chapters (Chapter 3, 4 and 5).

1.3. Summary of remaining chapters

Chapter 2 is a compilation of the previous research conducted on the Main Karoo Basin. Formation of the Main Karoo Basin, and the regional tectonic framework, including the Cape Fold Belt, is discussed before delving into the stratigraphy of the Main Karoo Basin. Lithostratigraphy and biostratigraphy are detailed, followed by an in-depth review of the Ecca Group, including its formations, genesis and energy potential.

Chapters 3 and 4 contain studies on the stratigraphic duplication of black shales and, the geothermal potential of Permian sandstone formations, respectively. Each study contains an introduction, placing the study in context, followed by a literature synthesis relevant to the study along with the methodologies employed during research.

Chapter 5 investigates the potential of using wireline gamma-ray logs as a tool for identifying geothermal reservoirs from existing boreholes.

Chapter 6 builds on the individual discussions in Chapters 3, 4 and 5, and draws parallels between the studies including the potential for induced seismicity from energy extraction activities. Topics of interest for further research are also summarised.

2. Geological Setting

This chapter will discuss the formation of the Main Karoo Basin and Cape Fold Belt as well as the stratigraphy of the basin including biostratigraphy and chronostratigraphy before focusing more closely on the Ecca Group of the Karoo Supergroup.

2.1. Overview

The Main Karoo Basin is part of a series of Gondwanan foreland basins including the Paraná Basin in South America, the Beacon Basin in Antarctica and the Bowen Basin in Australia (Figure 2.1) (De Wit and Ransome, 1992; Veevers et al., 1994; Catuneanu et al., 1998; Catuneanu and Elango, 2001; Catuneanu and Bowker, 2001). The basin covers around 700,000 km² and sedimentation from ca. 300 Ma (Upper Carboniferous) to ca. 180 Ma (Toarcian) (Johnson et al., 2006; Tankard et al., 2009). It is underlain by basement

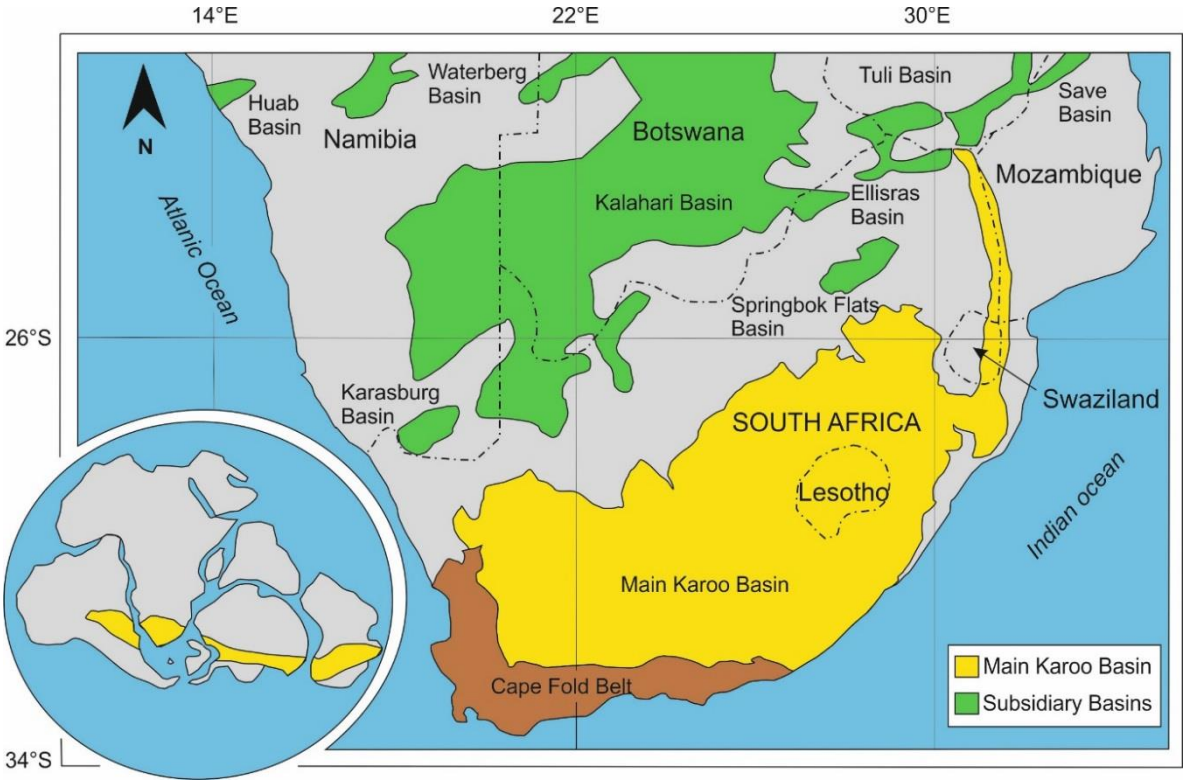

Figure 2.1: Locations of the Main Karoo Basin, subsidiary basins and Cape Fold belt in Southern Africa and corresponding basins in South America, Antarctica and Australia (see insert). Diagram modified from Black et al., (2016).

comprising the Kaapvaal Craton in the north (granitoids), the Namaqua-Natal Metamorphic Belt (gneiss) in the south and Cape Fold Belt (meta-sedimentary) along its southern margin (Johnson et al., 2006). The sedimentary succession wedges out against the basement in the north and cumulatively reaches a thickness of 12 km above the basement in the south (ibid.).

2.2. Regional Tectonic Framework

The longstanding model is that the Main Karoo Basin constitutes a retro-arc foreland basin developed by northward oblique subduction of oceanic lithosphere (palaeo-Pacific plate) under western Gondwana (Figure 2.2), from the Upper Carboniferous onwards and subsequent development of a wide fold thrust belt, the Cape Fold Belt (CFB) (Johnson, 1991; Cole, 1992; Catuneanu et al., 1998; Catuneanu et al., 2002; Johnson et al., 2006). According to Catuneanu (2004), accommodation space in the Main Karoo Basin was created by flexural subsidence due to orogenic loading and dynamic subsidence. The foreland system was segregated into foredeep, forebulge and back-bulge provinces by initial flexural isostatic subsidence. Later in the development of the Karoo Basin, flexural subsidence was supplemented by dynamic subsidence due to mantle flow, which created additional accommodation space across the entire foreland system (Catuneanu, 2004).

More recent interpretations of formation of the Karoo Basin suggests strike-slip tectonics led to the development of the CFB and the adjacent Karoo Basin comparable to a flexural foreland basin (Tankard et al., 2012). However, Flint et al. (2011) contest that regionally pronounced large-scale subsidence occurred due to dynamic topography (mantle flow) related to the subducting slab. This resulted in a series of interconnected marine basins that are older than the generally accepted foreland basin stage of the Karoo Basin.

By contrast the CFB has been compared to a Jura-type fold belt that formed due to arc-continent collision with subduction to the south (Lindeque et al., 2011; Pañgaro and Ramos,

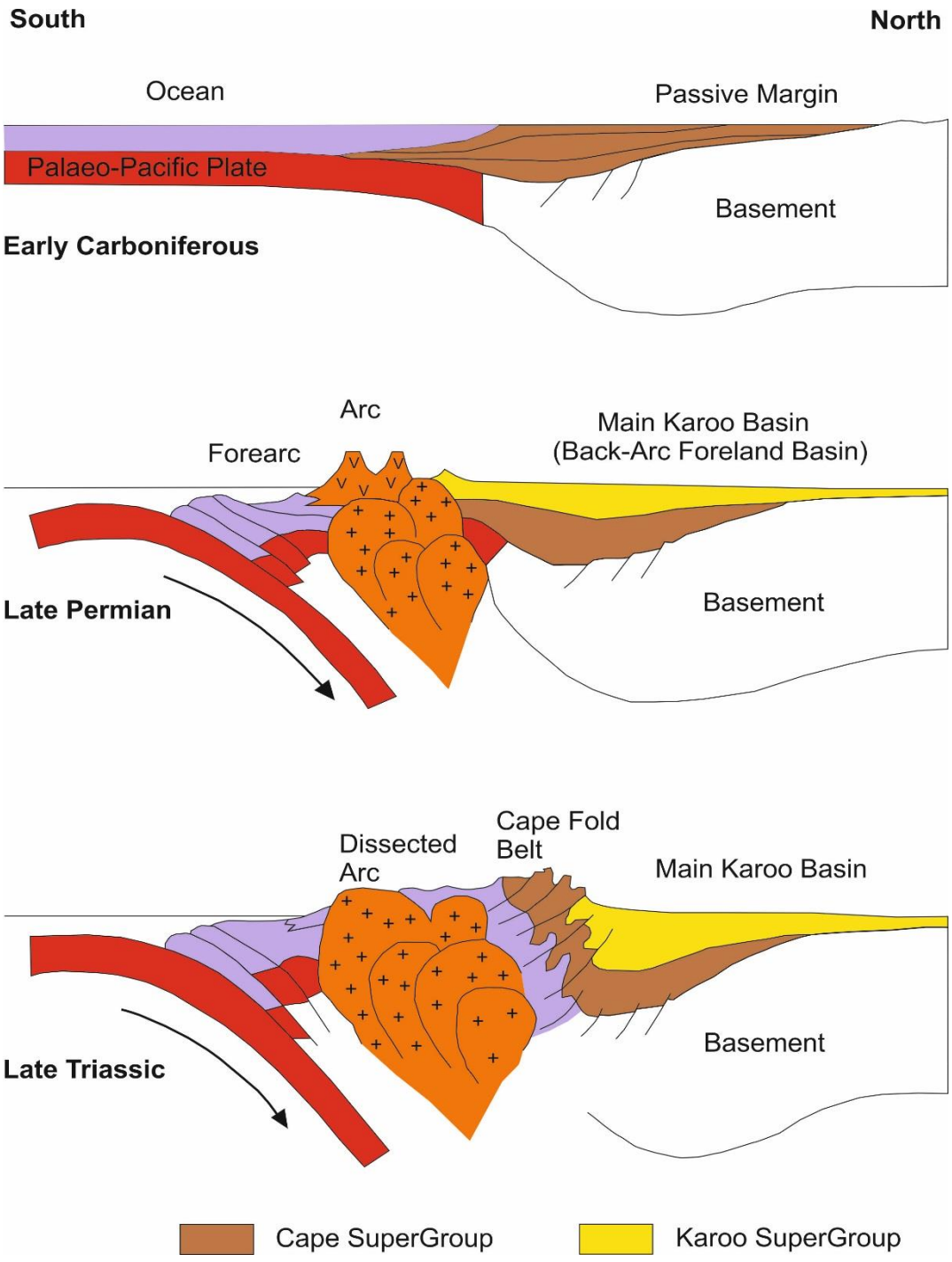

Figure 2.2: The longstanding interpretation is that the Main Karoo Basin constitutes a retro-arc foreland basin developed by northward oblique subduction of oceanic lithosphere (Palaeo-Pacific plate) under western Gondwana from the Late Carboniferous onwards and subsequent development of a wide fold thrust belt, the Cape Fold Belt (modified from Johnson et al., 2006).

2012). Miller et al. (2016) argued that collision occurred between the Patagonia landmass and the Rio de la Plata-Kalahari Shields and subsequently led to subduction to the south (Figure 2.3) based on recent seismic profiling and U-Pb geochronology. The authors cite the lack of recognizable magmatism and metamorphism in the Cape Fold Belt as detrimental to the northward subduction model; evidence of a magmatic arc only exists south of the Cape Fold Belt palaeo-position (de Wit, 1977; Pankhurst et al., 2006). The Colorado magnetic discontinuity (Ramos, 2008) is inferred to be evidence of a suture zone between the Patagonia landmass and the Rio de la Plata-Kalahari Shield by Miller et al. (2016).

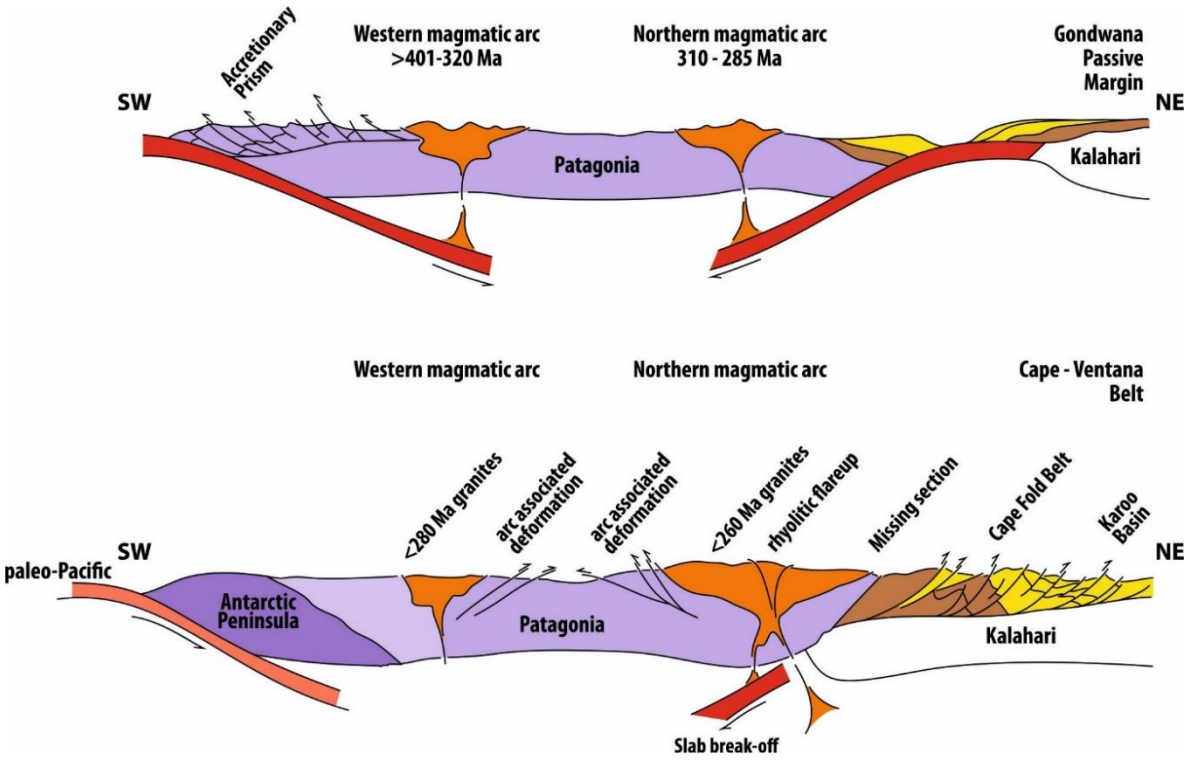

Figure 2.3: Schematic cross section through south-west Gondwana prior to ca. 300Ma (top) and Late Paleozoic deformation ca. 200 Ma. Modified after Miller et al., (2016).

2.3. Cape Fold Belt

In the Early Palaeozoic, sediments of the Cape Supergroup were deposited along a continental margin during a period of extensional tectonism. Sedimentation continued into the Late Palaeozoic and was followed by deposition of Karoo sediments (Hälbich, 1983, 1992; Shone and Booth, 2005). Towards the end of the Palaeozoic, tectonic inversion led to subduction-related compression along the convergent southwestern margin of Gondwana (Figure 2.4) and the development of the Cape Fold Belt (Trouw and de Wit, 1999) resulting in deformation of the Cape Supergroup, the underlying basement, as well as lower units of the Karoo Supergroup (Figure 2.5; Lindeque et al., 2011) by northwards-directed shortening (de Wit and Ransome, 1992).

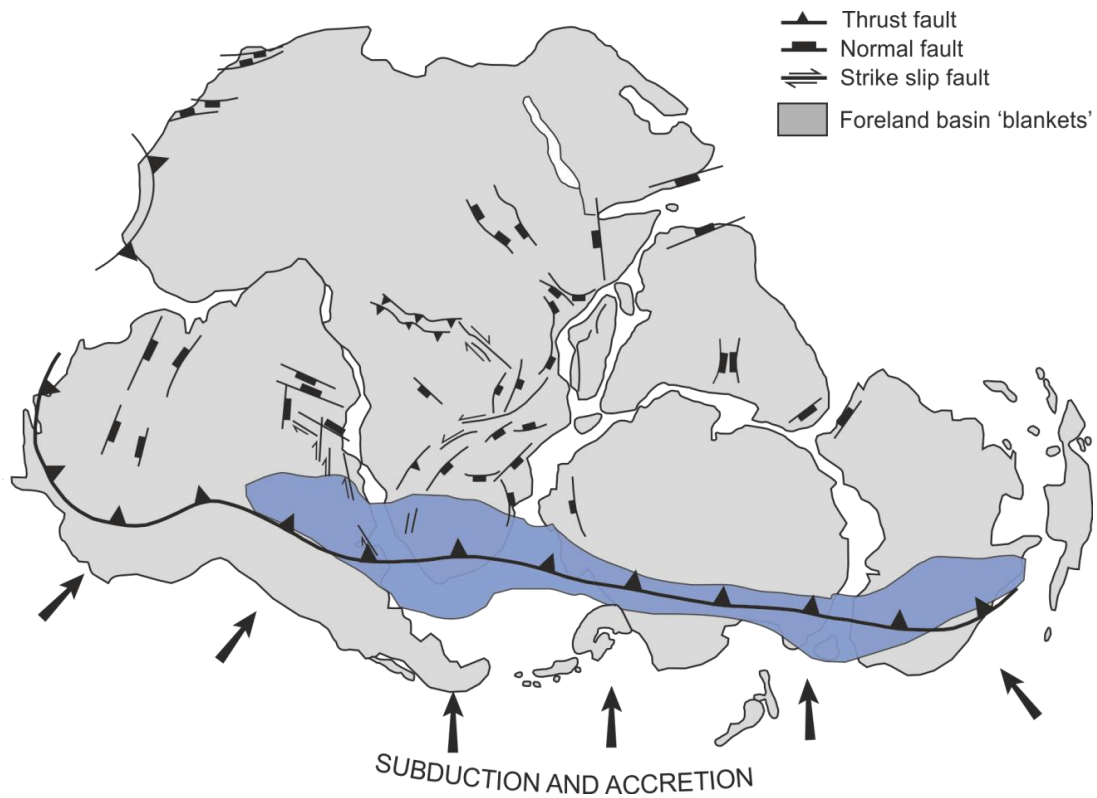

Figure 2.4: Foreland basins created by northwards subduction along the southern margin of Gondwana. Modified from de Wit and Ransome (1992).

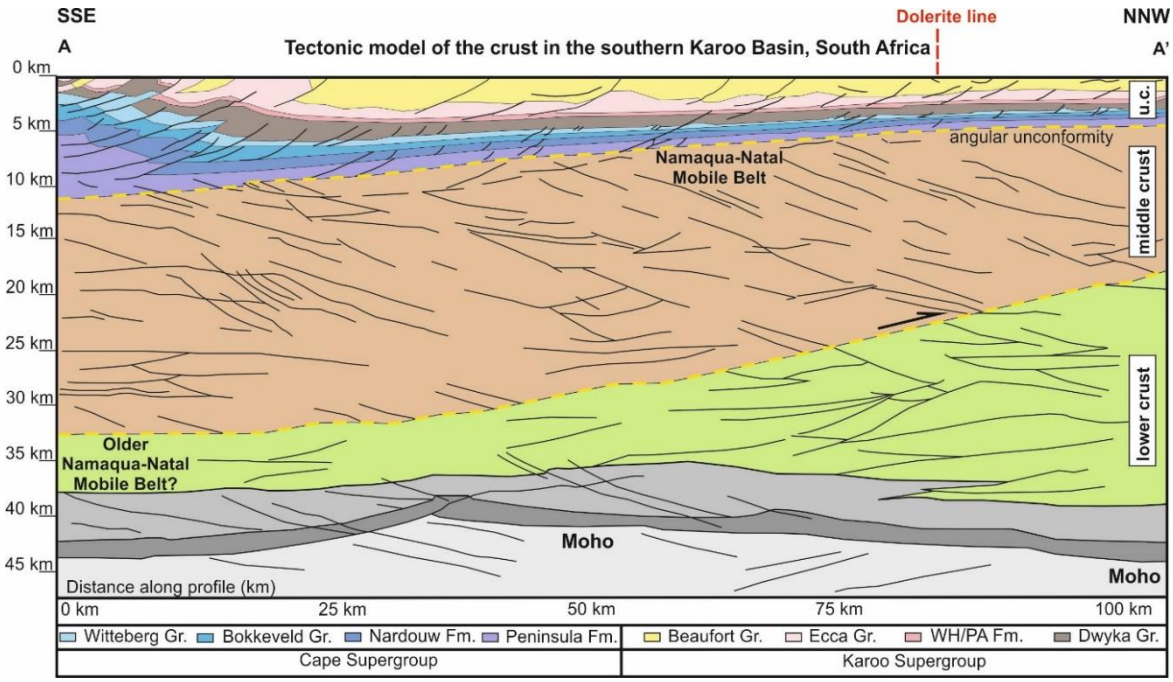

Figure 2.5**:** Tectonic model of the crust in the southern Karoo Basin based on a seismic reflection profile from A (Prince Albert) to A' (Slingersfontien), modified from Lindeque et al. (2011). For transect line see Figure 2.7.

The Cape Fold Belt is mostly thick skinned and formed along pre-existing crustal fabrics (de Beer, 1992; Newton et al., 2006; Paton et al., 2006). The majority of the Cape Fold Belt consists of the east-striking Swartberg and Langeberg anticlines and the associated Cango and Worcester faults. The Cape Orogeny was also influenced by large NE-striking basement fault zones. In profile, the anticlines form large scale north-verging transpressional flower structures (Tankard et al., 2009). Deformation divided into strike-slip and contractional components with interpretation based mainly on en echelon faults and folds (e.g. Warmwaterberg, Rooiberg, and Kammanassieberg), flower structures, and restraining fault bends (Tankard et al., 2009).

Based upon structural grain, fold style and the amount of shortening, the Cape Fold Belt is subdivided into three main zones (Hälbich, 1983):

- The north-trending western branch (western limb, Figure 2.7), displaying relatively open, upright, first-order folds and monoclines (de Villiers, 1944; Söhnge, 1983).

- The east-trending southern branch (southern limb, Figure 2.7), exhibiting a much higher degree of deformation, as indicated by the north-verging, recumbent first-order folds, a high incidence of second order folds and local out-of-the-forelimb thrusting (Hälbich, 1983). Both branches are cut by numerous post-orogenic normal faults, while some northerly-directed thrusts in the southern branch cut through basement and cover (Hälbich, 1983; Lindeque et al., 2011).
- A third structural domain is the area of intersection of the two belts at the core of the regional curve defined by the western and southern branches (de Villiers, 1944; de Beer, 1992). This area is characterized by numerous NE-trending folds and was termed a "syntaxis" by de Villiers (1944).

2.3.1. Age Constraints

Attempts at constraining the timing of orogeny and formation of the Cape Fold Belt have been made using $^{40}Ar/^{39}Ar$ dates from muscovites and biotites from rocks of the Cape Supergroup. The closure temperature of muscovite is ca. 425°C (Harrison et al., 2009) and ca. 300°C for biotite (McDougall and Harrison, 1999). Results have been speculative due to the incorporation of pre-existing metamorphic and detrital micas, combined with the low grade of metamorphism generated during the Cape Orogeny (<350°C; Hälbich and Cornell, 1983). The following are values produced to constrain deformation over the last half century (summarised in Figure 2.6):

(1) Gentle et al. (1978) calculated a value of 248.3 ± 1.5 Ma for Cape Fold Belt deformation from a biotite concentrate.

(2) Hälbich et al. (1983) used muscovites to calculate a range of 450 – 200 Ma with distinct tectonic events at 278 and 258 Ma.

(3) Gresse et al. (1992) produced a range of values between 600 – 200 Ma with tectonic events at 294, 276, 259, 239, and 223 Ma from whole rock analyses.

(4) Hansma et al. (2016) constrained deformation between 281 – 246 Ma and detrital samples between 559 – 447 Ma. The authors proposed a bimodal deformation sequence with the start of orogenesis at 276 – 262 Ma and cooling history or the start of a second phase between 255 – 248 Ma.

(5) Blewett and Phillips (2016) calculated the final stage of orogenesis at 253 Ma with mixed age muscovite populations between 440 – 255 Ma and a large population over 440 Ma.

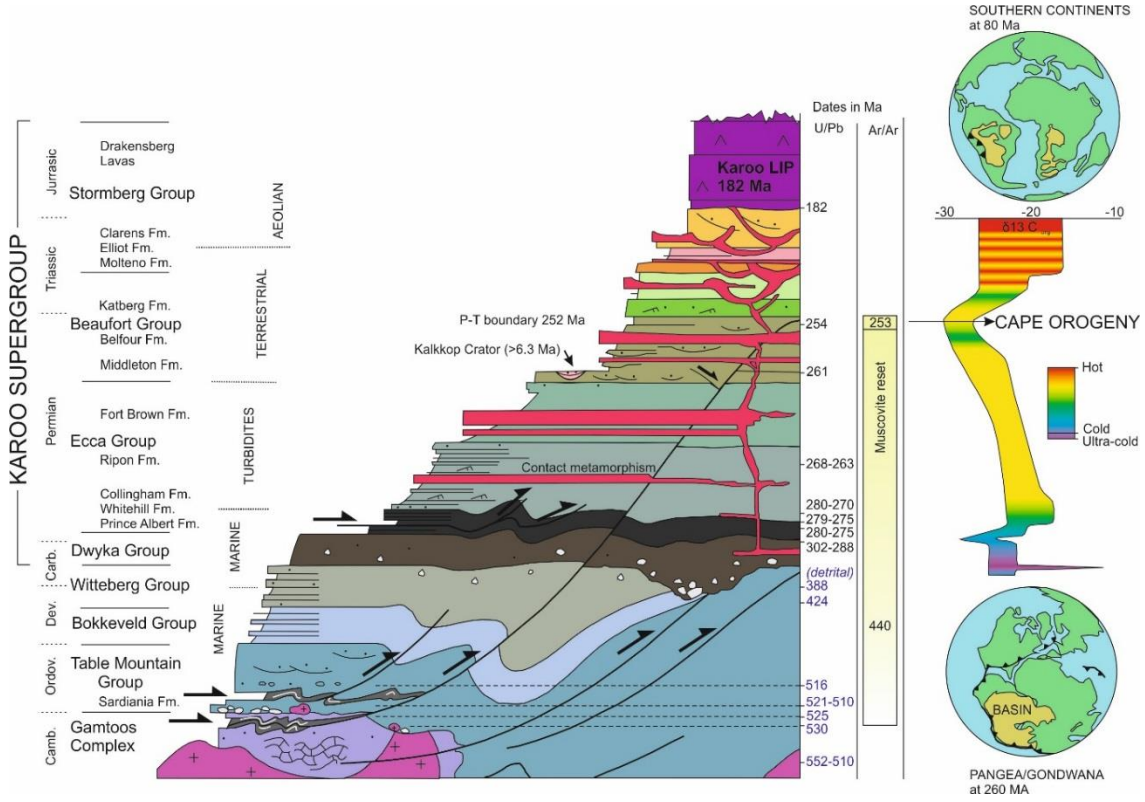

Figure 2.6: Summary of the generalised Cape-Karoo stratigraphy with U/Pb and Ar/Ar dates, δ13 C $_{org}$ values, and palaeogeography. Diagram modified from Linol and de Wit (2016). Periods from Johnson et al. (2006). Camb: Cambrian, Ordov: Ordovician, Carb: Carboniferous.

Dating of detrital zircons has provided information on the source of the Cape Supergroup sediments. Blewett and Phillips (2016) recognise three time intervals:

(1) 1200 – 1000 Ma attributed to sediments from the Namaqua-Natal Metamorphic Belt and the Pan-African Orogenic belts.

(2) 650 – 500 Ma ascribed to sediments from the Mozambique Belt and,

(3) 500 – 400 Ma which has had no specific terrane attributed to providing sediment.

2.4. Stratigraphy of the Karoo Supergroup

The onset of Karoo sedimentation occurred during the Late Carboniferous and continued until the break-up of Gondwana during the Middle Jurassic at ca. 183 Ma (Figure 2.6) (Johnson et al., 2006). A total sediment infill thickness of 12 km is attained within the southeastern part of the Main Karoo Basin, with sediment sourced from the north (Cargonian Highlands) as well as from the south (Cape Fold Belt mountain range) (McCarthy and Rubidge, 2005). Flint et al. (2011) contests that during the Ecca Group time there was no source area nearby and studies by Johnson (1991), Andersson et al. (2004), Van Lente (2004) and King (2005) suggest the Cape Fold Belt was not emergent at the time of deep water deposition of the lower Karoo Supergroup.

The Karoo Supergroup is divided into the Dwyka Group (Late Carboniferous to Early Permian), the Ecca Group (Mid Permian), followed by the Beaufort Group (Permian-Triassic) and the Stormberg Group (Late Triassic to Early Jurassic) (Figure 2.6) (Visser, 1996; Johnson et al., 2006; Catuneanu et al., 1998). The entire succession is capped by up to 1.4 km of basaltic lavas of the Drakensberg Group. The numerous formations of the Karoo Supergroup document changing environmental conditions from the glacio-marine deposits of the Dwyka Group to the marine-deltaic deposits of the Ecca Group through to the fluvial-deltaic sediments of the Beaufort Group and the fluvial-lacustrine and aeolian sandstones of the Stormberg Group (Johnson et al., 2006).

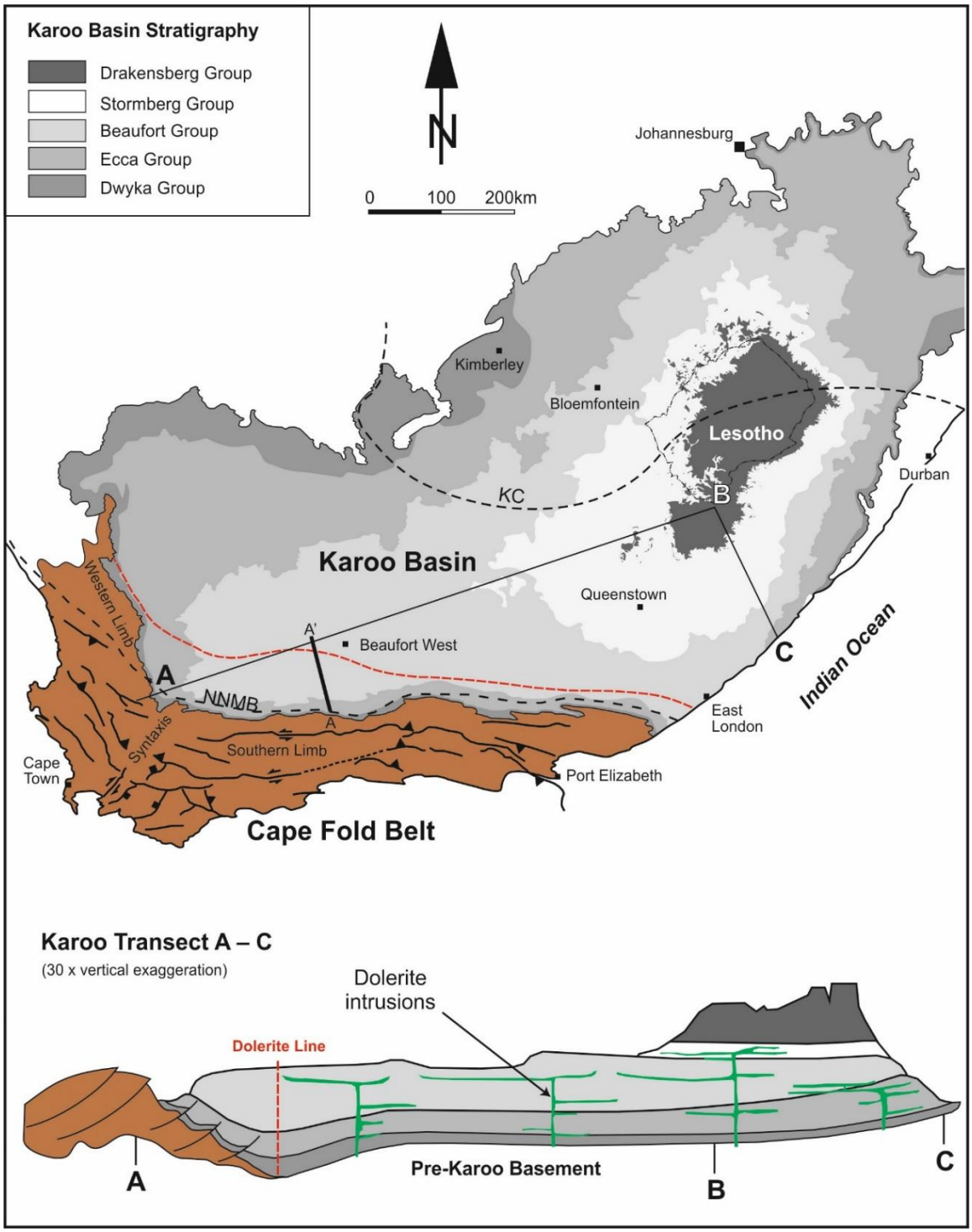

Figure 2.7: Stratigraphy and distribution of the Karoo Supergroup based on Catuneanu et al. (1998), and Cape Fold Belt (Tankard et al., 2009), modified from Bordy et al. (2004). KC: Kaapvaal Craton. NNMB: Namaqua-Natal Metamorphic Belt. Transect ABC: see insert, transect A – A': see Figure 2.5.

2.4.1. Lithostratigraphy

I. Dwyka Group

The Late Carboniferous to Early Permian Dwyka Group is a succession of diamictites (Figure 2.8), varved glacial deposits and fluvial deposits up to 800 m thick. The Dwyka Group rests on glaciated Precambrian bedrock surfaces along the northern margin of the basin and in the south it overlies the Cape Supergroup unconformably or paraconformably (Johnson et al., 2006; Flint et al., 2011). The formation of the Dwyka Group coincided with the migration of Gondwana over the South Pole and marked the onset of Karoo Basin sedimentation at approximately 310-300 Ma (Flint et al., 2011). Rhyolitic/dacitic and basaltic/andesitic tuff beds within the glaciomarine sediments of the Dwyka Group in Namibia reveal new evidence for an early onset of proximal bimodal volcanic activity in southern Africa (Stollhofen et al., 2000).

II. *Ecca Group*

The Permian Ecca Group is composed of 16 formations reflecting the lateral facies changes that are characteristic of this group. This group comprises predominantly siliciclastic sediments capped by the fluvial Beaufort Group (Johnson et al., 2006). The basal Prince Albert and Whitehill formations are fairly extensive throughout the Karoo Basin but overlying formations are geographically dependant. The Lower Ecca Group represents deep-water basinal environments. The basal Prince Albert Formation has a maximum thickness of 100 m of predominantly dark grey mudrock. The overlying Whitehill Formation constitutes up to 80 m of black, carbonaceous pyrite-bearing shale. These units are highly condensed (low sedimentation rates) and contain almost no clastic input.

The Collingham Formation is made up of 70 m of a rhythmic alteration of dark grey siliceous mudrock and very thin beds of yellow tuff (K-bentonite). A regional marker, the Matjiesfontein chert bed (uniformly thick over 5000 km²) is found within the Collingham Formation.

Figure 2.8: Dywka Group diamictite with variable sized clasts in a dark matrix, exposed in a roadside quarry near the Ecca Pass (Eastern Cape, South Africa).

The Upper Ecca Group consists of submarine slope channel/levee systems (Hodgson et al., 2011). The Ripon Formation is up to 1000 m thick of fine-grained lithofeldspathic sandstone alternating with clastic rhythmite and mudrock. The Fort Brown Formation consists of up to 1000 m of rhythmite and mudrock with intercalated sandstone (Bouma and Wickens 1994, Catuneanu et al., 2002; Johnson et al., 2006; Flint et al., 2011).

Palaeoclimatic modelling indicates a shift from tundra-like vegetation to more warm and humid conditions, with swamp-like vegetation and hence a change in depositional systems in the Permian (Götz and Ruckwied, 2014). The Prince Albert Formation contains shallow-

water carbonates and clastics whilst the Whitehill Formation is indicative of marine anoxic conditions with pelagic Mesosaurid reptiles and palaeoniscoid fishes preserved (Scheffler et al., 2006). See section 2.5 for more detailed descriptions of the Ecca Group formations pertinent to this study.

III. Beaufort Group

The Beaufort Group records the transition to terrestrial depositional systems with well-preserved continental vertebrates and macroflora (Groenewald and Kitching, 1995; Smith, 1995; Gastaldo et al., 2005). The group is subdivided into the Adelaide Subgroup (5000 m - 800 m thick) and the Tarkastad Subgroup (2000 m - 150 m thick). The dominant lithologies include fluvial-deltaic mudstones and sandstones with occasional granulestones and pebbles (Johnson et al., 2006). The numerous rhyodacitic volcanic air-fall tuffs interbedded throughout the Ecca and Beaufort Groups are thought to have been produced by a Late Palaeozoic Gondwanan magmatic arc (Figure 2.2). Permian aged silicic-andesitic volcanic and plutonic rocks (Choiyoi and Puesto Viejo magmatic suites) are exposed in what is now northern Patagonia. Choiyoi and Puesto Viejo magmatism dates from 276 Ma to 234 Ma and is responsible for air-fall ash deposits in the Paraná and Cuyo basins (Spalletti et al., 2008; Rocha-Campos et al., 2011) in South America, in addition to the Karoo Basin in South Africa based on palaeogeography and geochemistry (López-Gamundi, 2006).

IV. Stormberg Group

The Stormberg Group is subdivided into the Molteno, Elliot and Clarens Formations. The basal Molteno Formation (Late Triassic) is made up of alternating medium to coarse grained sandstones and grey mudrocks with secondary quartz overgrowths and has a maximum thickness of 600 m in the south. It formed as a result of bedload-dominated rivers flowing across extensive braid-plains. The Elliot Formation (Late Triassic) comprises an alternating

sequence of red and green-grey mudrock and fine to medium grained sandstone, attaining a maximum thickness of 500 m in the south. The Elliot Formation is a typical "red bed" fluvial deposit. Progressive warming and aridity resulted in the once meandering channels becoming shallower and more ephemeral, with aeolian conditions prevalent in the uppermost part of the formation (Johnson et al., 2006). The Clarens Formation (Late Triassic/ Early Jurassic) is comprised primarily of sandstone (up to 300 m thick) representing desert conditions and associated dune, playa lake, sheet flood and stream deposits (Johnson et al., 2006).

2.4.2. Biostratigraphy

The stratigraphy of the Karoo Basin has primarily been constructed using vertebrate macrofossil assemblages (Broom, 1903; Von Huene, 1925, Von Huene and Pompeckj, 1931; Kitching 1978). Vertebrate biozones have also played a role in models for the Karoo Basin development and its palaeoenvironmental reconstruction (Catuneanu et al., 1998; Rubidge, 2005; Smith, 1995). Temporal constraints for Karoo vertebrate biozones have been obtained by faunal correlation with better dated continental sedimentary deposits worldwide (Rubidge, 2005). The first major stratigraphic correlation using microfossil assemblages was performed by Hart (1964) who investigated the marine black shales of the Ecca Group followed by Falcon (1973) who subdivided the coalfields of South Africa. Recent correlations between coal seams and black shales were performed by Ruckwied et al. (2014).

2.4.3. Age Constraints

The sedimentary and volcanic record of the Karoo Supergroup extended from the Late Carboniferous to the Early Jurassic. Up until recently the age of the strata underlying the lavas of the Drakensberg and Lebombo Groups and their equivalents to the north had been based entirely on palaeontological evidence. However, success is being achieved in dating

thin volcanic ash (K-bentonite) layers that occur in the Dwyka, Ecca and Beaufort Groups (Johnson et al., 1996). Zircon U-Pb sensitive high-resolution ion microprobe (SHRIMP) dates have been calculated for several intervals:

Basal Main Karoo Basin

(1) Dates of 302 ± 3 Ma to 288 ± 3 Ma bracketing the Dwyka Group (Bangert et al., 1999),

(2) 274.8 ± 1.5 Ma to 270 ± 1 Ma for the basal Collingham Formation of the Ecca Group (Fildani et al., 2007; Turner, 1999),

(3) 262.8 ± 2 Ma to 252.7 ± 2 Ma for the Laingsburg and 256.0 ± 2.0 Ma to 254.4 ± 1.8 Ma for the Schoorsteenberg formations of the Ecca Group (Fildani et al., 2007, 2009),

Mid Main Karoo Basin

(4) 252.5 ± 0.7 Ma for the Balfour Formation (Palingkloof Member) of the Beaufort Group (Coney et al., 2007),

Top Main Karoo Basin

(5) 185–180 Ma for the basaltic lavas that overlie the Karoo succession based on $^{40}Ar/^{39}Ar$ geochronology (Duncan et al., 1997; Jourdan et al., 2005).

McKay et al. (2015) calculated dates that corroborate and replicate several previously published dates, however there is a large variance between dates at the base of the Ecca Group, with McKay et al. (2015) calculating an age of 275 Ma and Bangert et al. (1999) calculating an age of 288 Ma. This large variance affects the chronostratigraphy of the base the Ecca Group (Figures 2.9 and 2.10).

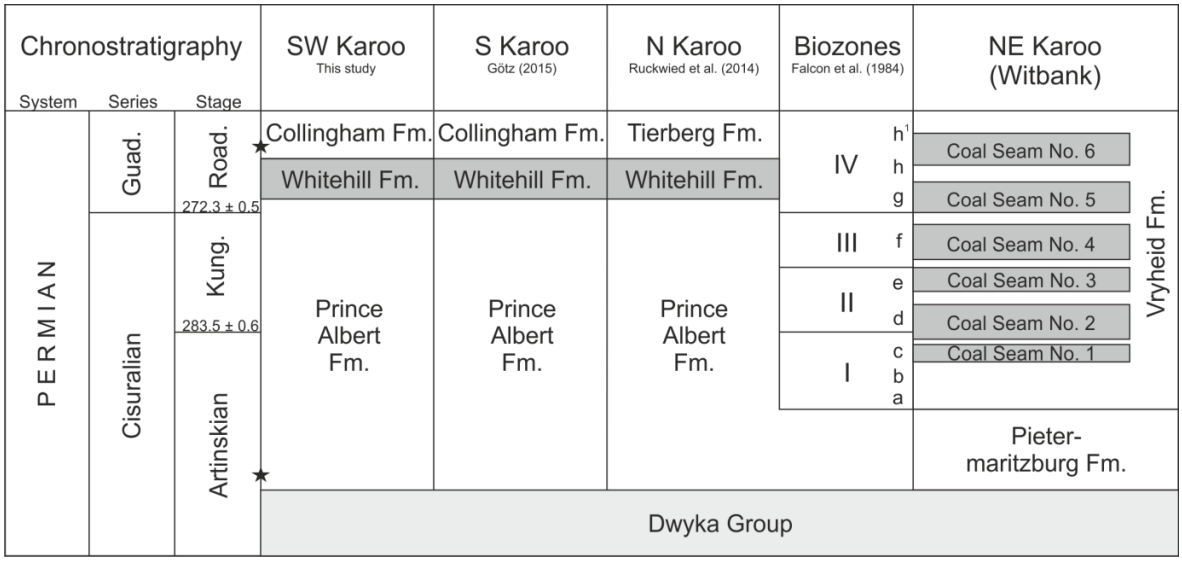

Figure 2.9: Basin wide correlation of black shales and coal seams modified from Ruckwied et al. (2014). Radiometric ages for the base of the Collingham Formation: 270 ± 1 Ma (Turner, 1999) and 268 ± 3.2 Ma. (McKay et al., 2015). Radiometric ages for the base of the Prince Albert Formation: 288 ± 3.0 Ma (Bangert et al., 1999). Ages of the chronostratigraphic chart from Cohen et al. (2013).

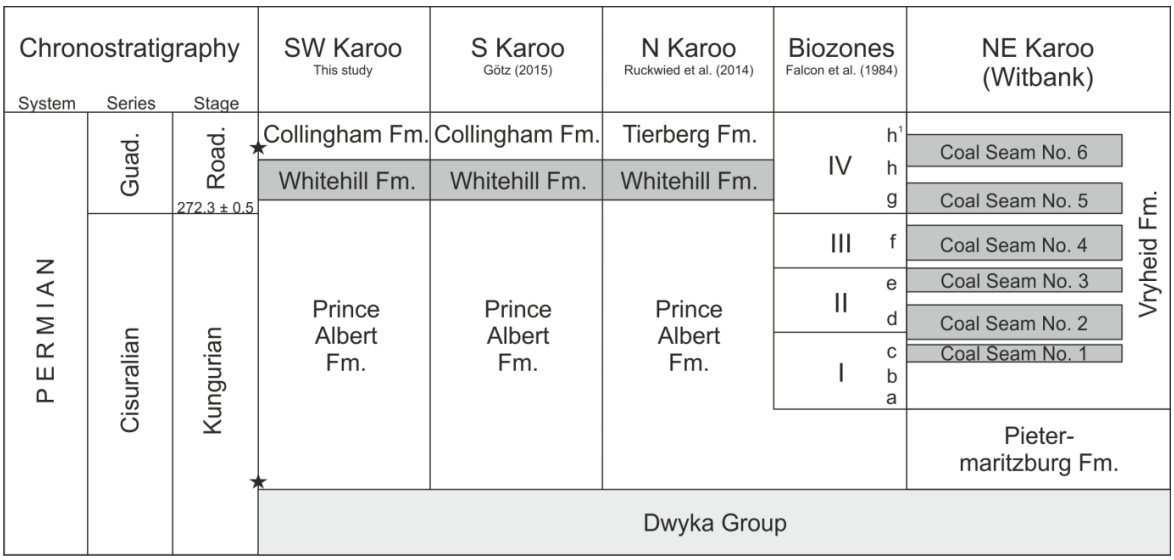

Figure 2.10: Basin wide correlation of black shales and coal seams modified from Ruckwied et al. (2014). Radiometric ages for the base of the Collingham Formation: 270 ± 1 Ma (Turner, 1999) and 268 ± 3.2 Ma. (McKay et al., 2015). Radiometric ages for the base of the Prince Albert Formation: 275 Ma (McKay et al., 2015). Ages of the chronostratigraphic chart from Cohen et al. (2013).

2.5. The Ecca Group

The following section will document the previous research performed on the Ecca Group in general before discussing the formations pertinent to this study in more detail. The Ecca Group is estimated to contain world-class reserves of unconventional shale gas, as well as the possibility for geothermal energy, and has therefore been the focal point of new research from both industry and academia in South Africa and abroad.

2.5.1. Overview

In the early 20th century Haughton (1925, 1928) was the first person to study trace fossils from the Ecca Shales of the Cape Province. He also described the geology between Grahamstown and Port Elizabeth. Du Toit (1926) published The Geology of South Africa documenting the complete Karoo Supergroup. Hart (1964) provided palynological evidence from Ecca Group sediments for the existence of the 'Karoo Sea' and tried to ascertain its boundaries. Next, Johnson (1966, 1976) logged and described the formations of the Ecca Group (Figure 2.11) at the type locality, the Ecca Pass. Then, Kingsley (1979, 1981) proposed a composite turbidite-delta-fluvial model for the sedimentation for the Permian Ecca and Lower Beaufort Groups in the Eastern Cape of South Africa. Oelofsen (1987) compared the biostratigraphy of the Whitehill and Irati Shale Formations of the Karoo and Paraná basins. He concluded that the two formations may represent a transcontinental isochronous unit based on the striking similarity in the biota of the two formations, and the presence of specimens of the same species of vertebrates in both basins. Visser (1992) suggested that the Whitehill Formation was deposited during a highstand sea-level in a juvenile foreland basin. He proposed a terrestrial source of the organic material stating that fresh-water plumes carried organic-rich mud from the basin margin into an anoxic deep marine setting. Faure and Cole (1999) presented geochemical evidence (C, O, S isotopes and

hydrogen and oxygen indices) from the Whitehill, Irati and Huab Formations and Black Rock Member, in the south-western Gondwana basins. The data suggest the manifestation of a lacustrine microbial bloom event covering approximately 5 million km² that peaked in the upper half of the black shale units.

Recently, Santos et al. (2006) presented the first SHRIMP zircon age data from bentonitic ash fall layers intercalated with the Irati sedimentary rocks of the Paraná Basin. SHRIMP analysis performed on the euhedral and prismatic grains revealed an age of ca. 278.4 ± 2.2 Ma; interpreted as the crystallization age of the volcanic eruption. Based on this new dating, the Irati Formation should be placed in the Lower Permian (Cisuralian), Artinskian in age, substantially modifying the traditional ages previously attributed to this unit. Branch et al. (2007) acquired magnetotelluric (MT) data along three profiles across the Karoo Basin in South Africa and reported on electrical conductivity, vitrinite reflectance, and impedance spectroscopy studies that were undertaken. Flint et al. (2011) reported on the depositional architecture and sequence stratigraphy of the lower Karoo Supergroup and Geel (2013) undertook a comprehensive and detailed lithological, sedimentological, structural and geochemical description on a core (SFT2) of the lower Ecca Group with emphasis on the shale gas characteristics of the Whitehill Formation. McKay et al. (2015) performed U-PB zircon SHRIMP geochronology from tuff layers along the southern margin of the basin and concluded that strata of the Ecca Group appear coeval across the southern margin of the basin with the base of the Ecca Group dated at ca. 270 Ma. Numerous studies have been conducted on the Whitehill Formation and its stratigraphic equivalents namely, the Whitehill Formation in southern Namibia, the Huab Formation in northwestern Namibia, the Irati Formation in the Paraná Basin Brazil and the Black Rock Member of the Port Sussex Formation of the Falkland/Malvinas Islands as well as the Collingham and Ripon Formations (Thomas, 2001; Trewin et al., 2002; Smithard et al., 2015, Linol and de Wit, 2016 and

authors there within). Campbell (2016a; 2016b- this study) performed the first assessment of the geothermal potential of the deep sandstones from outcrop and borehole samples.

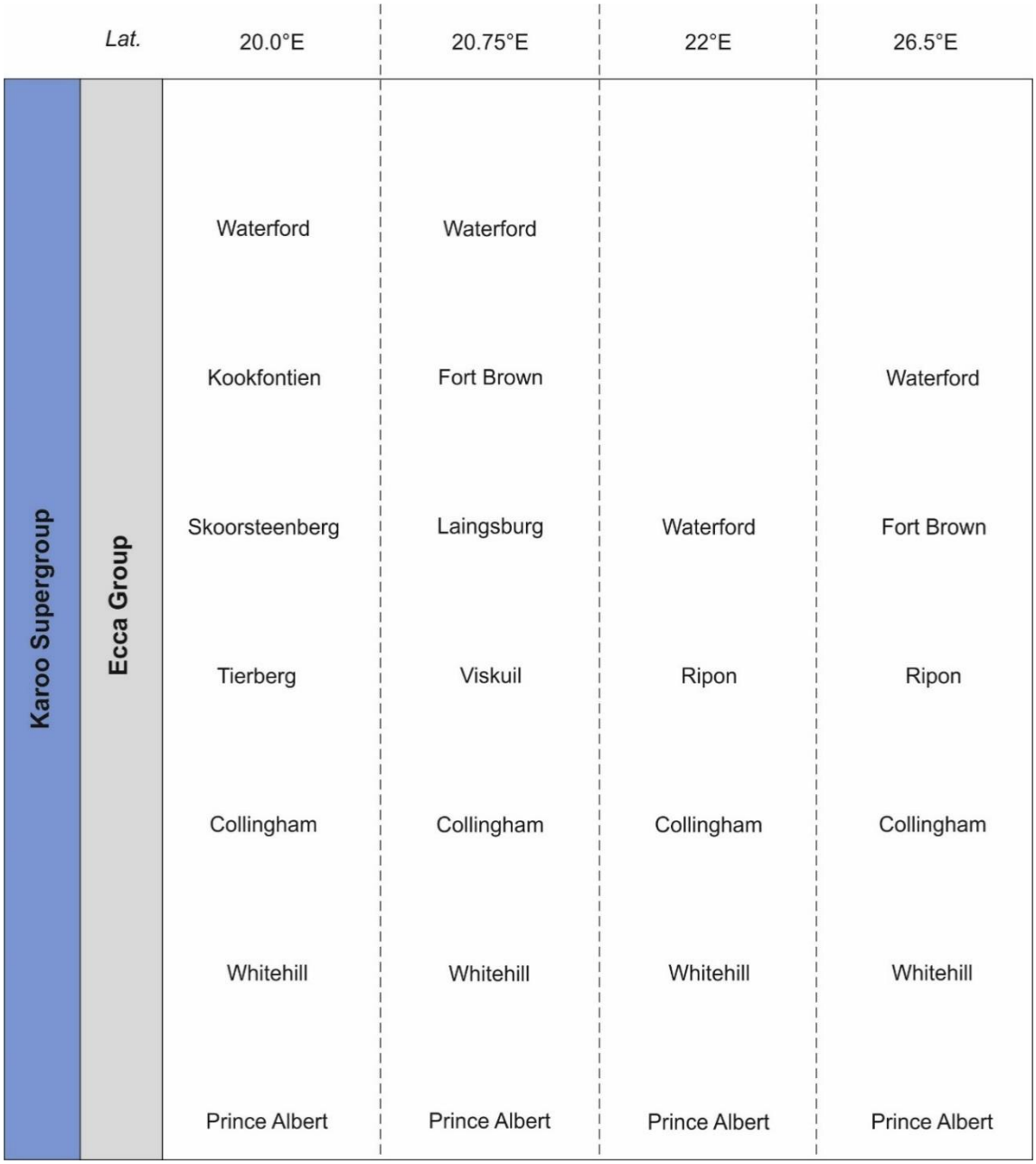

Figure 2.11: Formations of the Permian aged Ecca Group of the Karoo Supergroup. Lateral facies variations are reflected in formation changes. Vertical changes reflect shallowing from a deep marine to deltaic palaeoenvironment. Modified after McKay et al. (2015).

2.5.2. Prince Albert Formation

The basal Prince Albert (PA) Formation forms a sharp, conformable contact with the underlying Dwyka Group and the overlying Whitehill Formation. The PA Formation is confined to the south-western half of the basin and pinches out northwards or merges with the Vryheid or Pietermaritzburg Formations. It has a maximum thickness of 300 m and consists of predominantly dark grey mudrock (Johnson et al., 2006), and as observed at the Ecca Pass type locality (Figure 2.12) (Campbell, 2014). Johnson et al. (2006) recognises two distinct geographically dependant facies:

(1) A northern facies comprising a transition from underlying glacial deposits to micaceous and silty shale with minor black carbonaceous shale, fine to medium-grained feldspathic arenite and wacke. Numerous concretions are also present. Marine fossils have been recorded by McLachlan and Anderson (1973).
(2) A southern facies characterised by pyritic shale as well as chert and phosphatic and carbonate concretions. Visser (1994) recorded shark remains along with various marine fossils.

Herbert and Compton (2007) argue that the PA Formation was deposited as a result of suspension settling both during and after glaciation that predominated during Dwyka Group times (Late Carboniferous to Early Permian) based on concretion geochemistry. The authors also proposed that some sediment input was associated with periodic turbidites and mudflows. Smith et al. (1993) attribute the PA Formation to turbidites. Johnson et al. (2006) attribute the mudrocks of the PA Formation to suspension settling of mud in a marine environment with sand deposited by traction fall-out from turbidity currents. Herbert and Compton (2007) postulate that the phosphatic and carbonate concretions formed under reducing conditions in areas of cold-water upwelling. The organic content in the muds may

have derived from the cold-water upwelling (ibid.). Juvenile magmatic zircons from tuff beds near the base of the formation in Namibia yielded U-Pb ages between 289.6 ± 3.8 Ma and 288.0 ± 3 Ma (Bangert et al., 1999), indicating an Early Permian (Artinskian) age.

Figure 2.12: Olive-green fresh and reddish weathered shales of the Prince Albert Formation (see Figure 2.11) exposed along the Ecca Pass (Eastern Cape, South Africa).

2.5.3. Whitehill Formation

The overlying Whitehill Formation comprises on average 15 m (up to 80 m) of condensed black, laminated carbonaceous pyrite-bearing shale (Johnson et al., 2006; Geel et al., 2013, Campbell, 2014). The shale is very thinly laminated and contains total organic carbon of up to 17% (Cole and McLachlan, 1991). The Whitehill shale is contemporaneous with the Irati Formation of the Parana Basin in Brazil (Cole and McLachlan, 1991). In outcrop at the Ecca Pass type location, the Whitehill Formation is distinctly white (Figure 2.13), due to the presence of gypsum from the breakdown of pyrite, and is a valuable marker horizon (Johnson

et al., 2006). The formation exhibits both lateral and vertical variations in silt content (Cole and Basson, 1991) and sporadic tuff beds have been reported from this formation (Johnson et al., 2006). Five distinct facies have been proposed for the Whitehill Formation by Chukwuma and Bordy (2016), ranging from:

(1) High bioproductivity with suspension settling of pelagic material at the anoxic and sulfidic water-sediment interface,
(2) sporadic anoxic and sulfidic iron-poor sediment-water conditions,
(3) reworked sediment by currents in bed-load transport with developing oxic bottom waters,
(4) increasing sediment gravity flows with temporary oxic bottom waters,
(5) hyperpycnal flows and massive deposition of sand and silt in a fully oxygenated water body.

Sedimentological and palaeontological evidence suggest that the Whitehill Formation accumulated over a few million years within a stratified deep water body, with high primary productivity in oxygenated surface waters, and reducing bottom waters preserving organic matter (Smithard et al., 2015 and authors there within). Scheffler et al. (2006) interpreted the Whitehill Formation as a marine anoxic deposit with Mesosaurid reptiles and palaeoniscoid fishes preserved. Recent palynological studies (Ruckwied et al., 2014) demonstrated that the depositional environment of the Whitehill shales is laterally more complex, ranging from marginal marine to stratified deep marine. Palynostratigraphy points towards a late Early Permian to early Middle Permian (Kungurian-Roadian) age (Ruckwied et al., 2014).

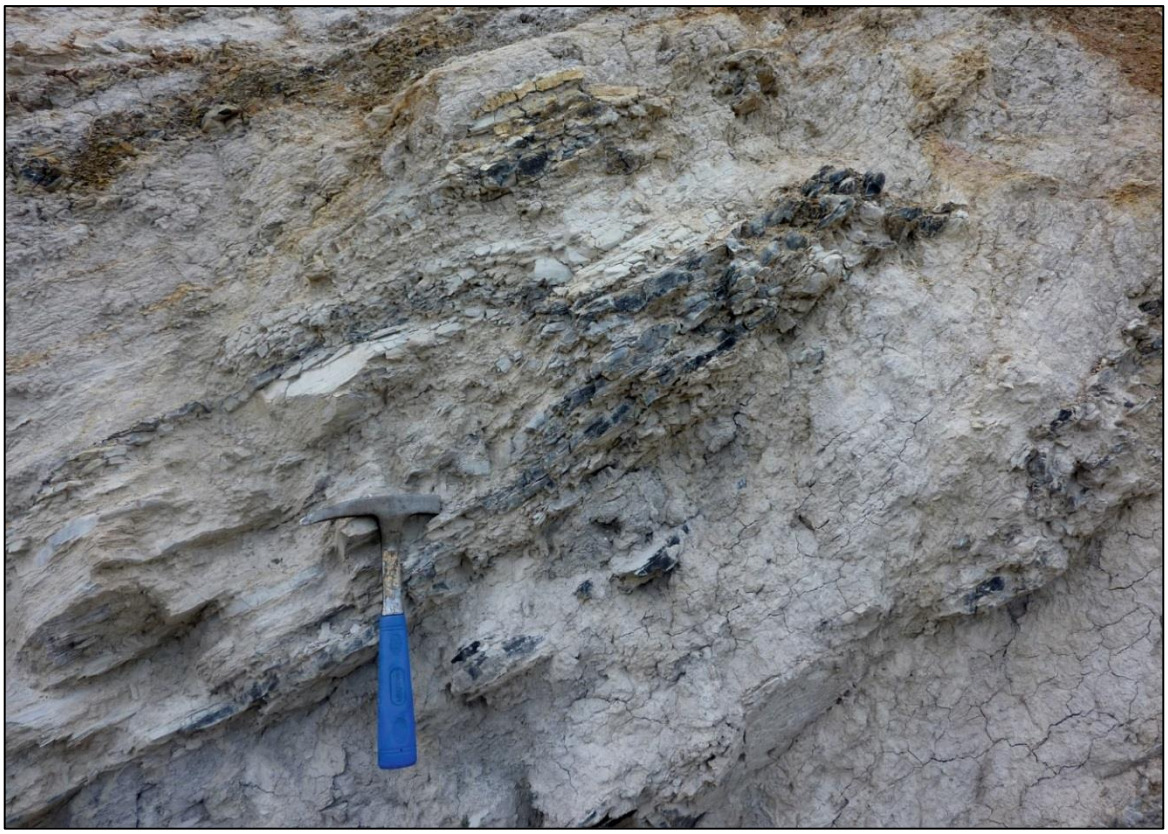

Figure 2.13: Weathered Whitehill Formation (see Figure 2.11) with characteristic white gypsum, from the breakdown of sulphides, exposed along the Ecca Pass (Eastern Cape, South Africa).

The southern portion of the basin has been interpreted to be a deep water basinal environment (Figure 2.14) with low levels of sedimentation and anoxic bottom conditions shallowing over time to submarine channel levee/slope systems. The formation of black shales was likely stopped due to the occurrence of turbidity currents that commenced during deposition of the Collingham Formation (Schulz et al., 2016). The central part of the basin has been interpreted to be a shallower sandier facies (shelf) with higher sedimentation rates and fluctuations in bottom water anoxia.

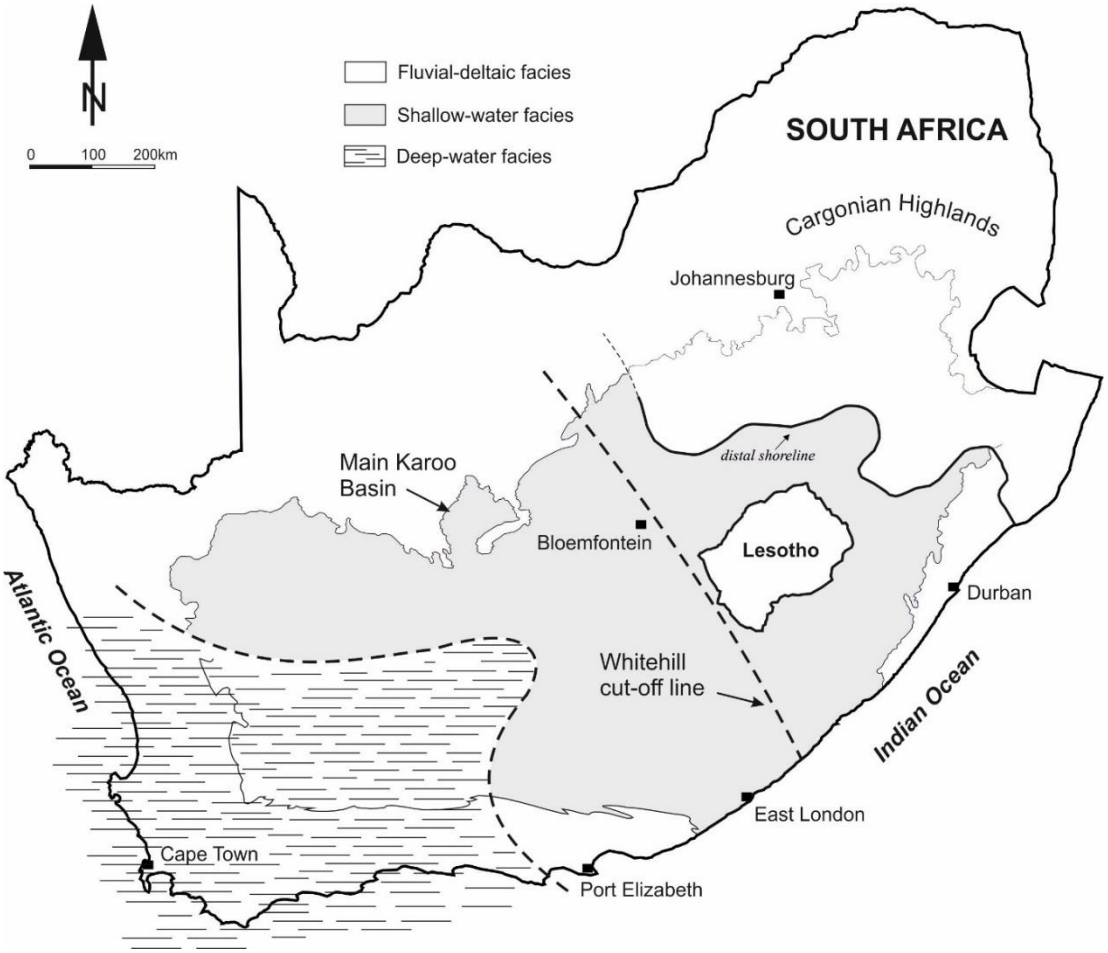

Figure 2.14: Palaeogeographic reconstruction of the Main Karoo Basin at the end of the Early Permian showing the depositional environments of the lower Ecca Group shales. Modified after Visser (1992). Note: Coals deposited in the fluvial-deltaic facies (NE portion of the basin) correlate with the lower Ecca shales (Ruckwied et al., 2014).

The north eastern part of the basin contains terrestrial coals with indications of possible trangresssions/regressions (Hart, 1964; Visser, 1992; Johnson et al., 2006).

2.5.4. Collingham Formation

The Collingham Formation is between 30 m and 70 m thick and is laterally extensive within the Main Karoo Basin (Johnson et al., 2006) and it is underlain by the Whitehill Formation and overlain by the Ripon Formation (Southern subbasin), Vischkuil Formation (Laingsburg subbasin), and the Tierberg Formation (Tanqua subbasin) (Viljoen, 2004). Rhythmically intercalated dark grey fissile mudstone and olive-coloured K-bentonite layers characterise this formation (Figure 2.15) as observed in outcrop at the Ecca Pass type location (Campbell, 2014). Tuff layers near the base and top of the formation produced dates of 268.2 to 261.1 Ma respectively, constraining deposition to a 7 million year period (McKay et al., 2015). In the western portion of the basin the Collingham Formation contains minor siltstone to fine-grained sandstone (Johnson et al., 2006; Black et al., 2016). A basin-wide chert layer known as the Matjiesfontien Chert Bed (uniformly thick over 5000 km^2) occurs within the lower half of the formation and is used as a marker horizon (Johnson et al., 2006).

In the southern and southwestern part of the basin the Collingham Formation can be subdivided into three members according to Viljoen (2004): the lower Zoute Kloof Member, the Buffels River Member and the upper Wilgehout River Member. The lower two members are separated by the Matjiesfontien Chert Bed (ibid.).

Figure 2.15: Intercalated yellow-weathering K-bentonite tuff layers and darker fissile mudstones of the Collingham Formation (see Figure 2.11) exposed along road cuttings of the Ecca Pass (Eastern Cape, South Africa).

The numerous K-bentonite tuffs are deemed to be rhyodacitic volcanic ash aerially transported from the south and southwest, and derived from volcanoes located in what is now northern Patagonia where Permian aged silicic-andesitic volcanic and plutonic rocks are exposed (Viljoen, 2004). Tuffaceous horizons have an average thickness of 1.64 cm and show a greater degree of weathering compared to the mudstones (Campbell 2014; Black et al., 2016).

The lower part of the formation is deemed to have formed by settling of pelagic and hemiplegic material in a basin floor setting, while the upper portion consists of basin floor and turbidity current deposits. Deposition was periodically interrupted by volcanic ash falls (Viljoen, 2004; Schulz et al., 2016).

2.5.5. Ripon Formation

The Ripon Formation is on average 600 m – 700 m thick with a maximum of over 1000 m in the eastern portion of the Main Karoo Basin (Johnson et al., 2006). As documented in outcrop, the formation is composed of interbedded, poorly sorted very fine- to medium-grained sandstones, and dark-grey mudrock (Figure 2.16; Campbell, 2014). Two age dates from ash layers within the formation are Late Guadalupian (263.1 and 262.5 Ma) (McKay et al., 2015).

Figure 2.16: The Ripon Formation (see Figure 2.11) turbidites with erosive contact between Bouma division 'e' and overlying 'a' exposed along the Ecca Pass road cut (Eastern Cape, South Africa).

Kingsley (1977, 1981) distinguished 3 members for this formation in the eastern portion of the basin (Figure 2.17):

(1) The basal Pluto's Vale Member comprising rhythmic turbiditic units of very fine- to fine-grained greywacke upwards fining to siltstone and shale,

(2) the Wonderfontein Member consisting of greenish-grey, laminated to massive mudstone with a single thick greywacke unit in the middle of the member and,

(3) the overlying Trumpeters Member made of turbiditic upwards fining greywackes and mudstones.

The Ripon Formation correlates with the Laingsburg and Vischkuil Formations in the Laingsburg subbasin, and the Skoorsteenberg and Tierberg Formations in the Tanqua subbasin (Figure 2.17) (Catuneanu et al., 2002). The Ripon Formation pinches out westwards and northwards in the subsurface (Johnson et al., 2006).

Campbell (2014) studied the Ripon Formation along Ecca Pass road cuttings and observed a regular and sequential pattern of deposition with upwards fining of grains and thinning of layers within a sequence. Sequences are repeated with variations only in layer thickness. Campbell (2014) recognised Bouma divisions '*a*, *b*, *d*, and *e*' within sequences:

a) An erosive base followed by massive medium grained sandstone containing rounded rip-up clasts of the underlying lithology, usually mudstone. Erosive bases display tool marks including bounce and skip marks as well as occasional fossilised plant remains,

b) planar laminated fine to very fine grained sand,

d) planar laminated silt and,

e) planar laminated clay with occasional preserved plant remains along with bioturbation.

Division ‘c’ is absent possibly due to the rapid deposition of sand preventing the formation of ripples (ibid.).

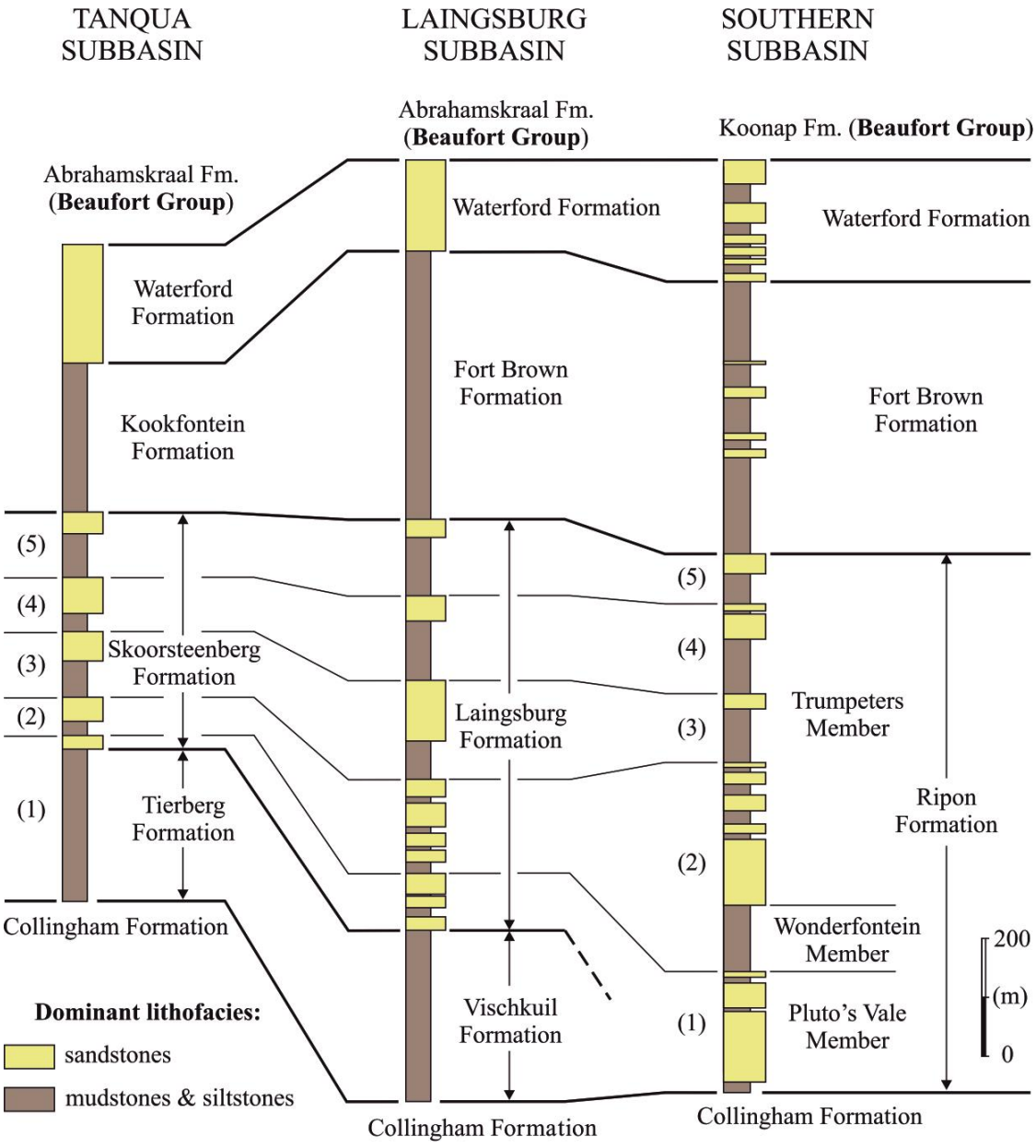

Figure 2.17: Stratigraphic correlation of the Ripon Formation with contemporaneous formations laterally across the Main Karoo Basin. Five distinct gravity flow events across the entire foredeep have been recognised, resulting in the submarine fan systems in each of the subbasins. Modified after Catuneanu et al. (2002).

The Ripon Formation was interpreted as being deposited by turbidity currents in a submarine fan complex due to the structures preserved as well as an absence of shallow water indicators (Kingsley 1977; 1981). Catuneanu et al. (2002) compiled a palaeogeographic reconstruction of environments prevalent during the Early Permian Main Karoo Basin (Figure 2.18) which indicates a general shallowing from SW to NE with a northerly transport direction indicated by the Pluto's Vale and Trumpeters Members.

The prevailing palaeoenvironment during the deposition of the Ripon Formation is shallower than the palaeoenvironment during the deposition of the PA and Whitehill Formations which is in accordance with a deep sedimentary basin gradually filling over time as proposed by Johnson et al. (2006).

2.5.6. Tierberg Formation

The Tierberg Formation, located in the Tanqua subbasin (Figure 2.17), attains a maximum thickness of 700 m in the western portion of the basin, thinning to approximately 350 m towards the northeast and overlies the Collingham Formation (Johnson et al., 2006). The formation is composed of laminated dark grey mudstones and siltstones with some yellowish tuffaceous beds as well as calcareous concretions (Johnson et al., 2006; Oliveira et al., 2011). The Tierberg Formation was deposited from suspension in a deep basinal environment with sediment sourced from deep-water fan complexes (Figure 2.18) (Johnson et al., 2001; Van Dijk et al., 2002) and has been called a turbidite (Linol et al., 2016). The upper portion of the formation contains a number of upwards coarsening cycles, from mudstone to very fine-grained sandstone, up to 10 m thick, with common soft sediment deformation and bioturbation with trace fossils preserved (Johnson et al., 2006). Palaeocurrrent indicators suggest transport to the NE/ENE (ibid.). Radiometric data available from ash layers place

this formation in the Middle to Late Permian (Fildani et al., 2007, 2009; Rawcliffe et al., 2012).

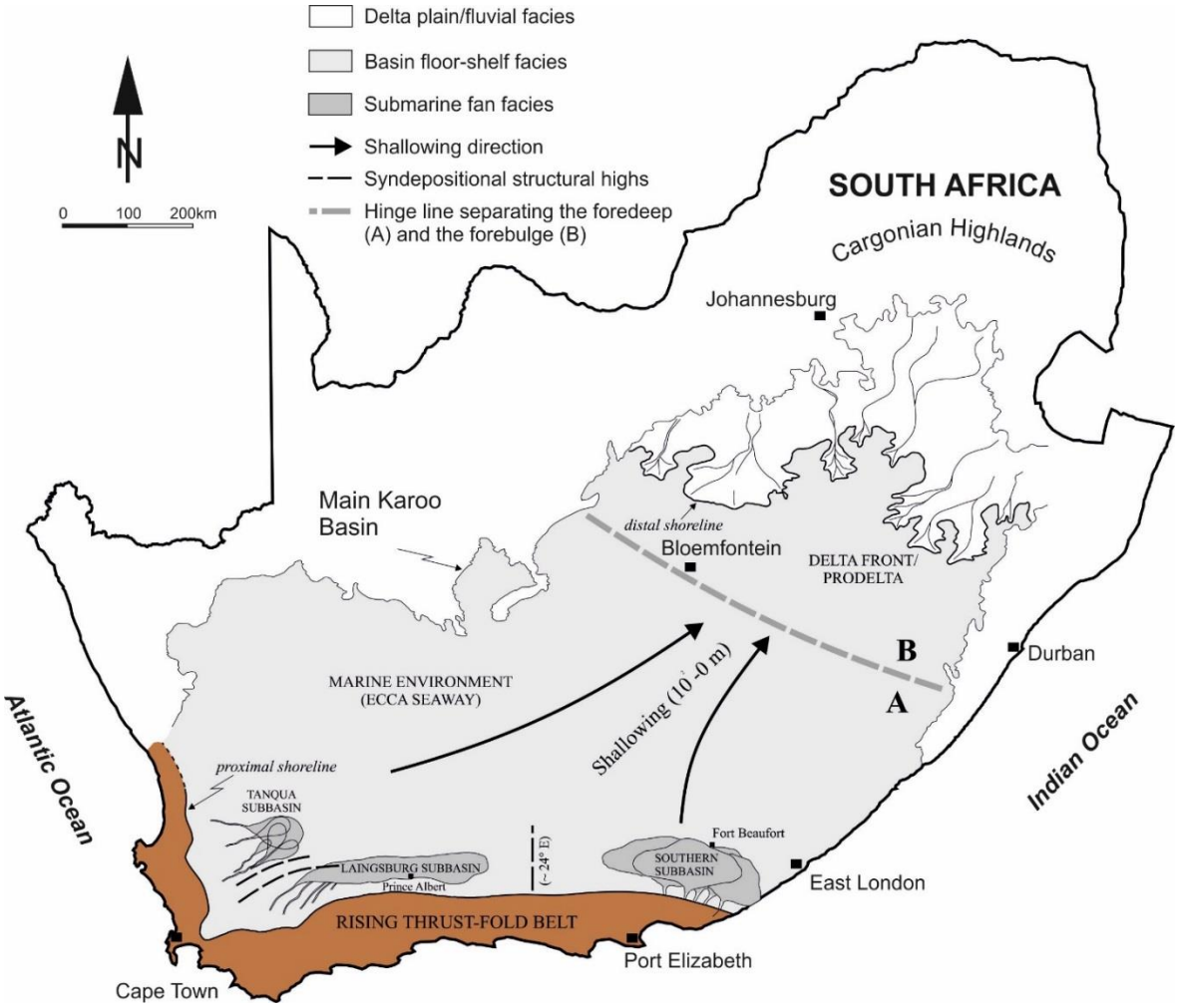

Figure 2.18: Palaeogeographic reconstruction of the Main Karoo Basin during the Early Permian showing the depositional environments of the submarine fans across the sub-basins. Modified after Catuneanu et al. (2002).

2.5.7. Marine versus non-marine

An academic debate has existed regarding the overall depositional environment of the Main Karoo Basin during Dywka to Ecca Group times (Late Carboniferous to Mid-Permian) with researchers divided into two camps; marine and non-marine, often with conflicting information being presented.

Evidence against the marine nature of the Ecca Group sediments was provided by Cole and McLachlan (1991) who gave evidence for evaporitic conditions in a shallow brackish-water intra-cratonic sea (halite crystal imprints) and stated that 'there is no palaeontological evidence of a marine depositional environment'.

Faure and Cole (1999) provide geochemical analyses, as shown by stable isotope (C, O, and S) evidence from organic matter, carbonates and pyrite, for the occurrence of lacustrine microbial blooms in brackish to fresh water. The authors suggest that black shales in the Whitehill Formation were created by anoxia occurring beneath algal mats, however no stromatolites have been reported from this formation.

Visser (1978) undertook palaeobathymetry studies on the Ecca Group and suggested that the Whitehill Formation was deposited in a shallow water (<200 m) land locked basin with the periodic influx of saline water. The authors suggest that black shales of the Whitehill Formation were formed by the deposition of black humic muds under reducing conditions within the sediment. The authors propose that the Main Karoo Basin attained its maximum water depth, up to 500 m, during the deposition of the Tierberg Formation, however a study by van Dijk et al. (2002) presented possible tetrapod trace fossils from the Tierberg Formation that were created by a diving animal in shallow water.

Herbert and Compton (2007) analysed carbonate and phosphatic concretions from the lower Ecca Group and underlying Dwyka Group. The authors concluded that calcite and phosphatic concretions precipitated from a mixture of meteoric and glacial melt waters, rather than Permian seawater based on $\delta^{18}O$ values (7.8 to 8.9‰ SMOW) and, Sr concentrations and $^{87}Sr/^{86}Sr$ ratios (0.716–0.737) that are significantly greater than Permian seawater (0.708).

The shales and sandstones observed in the southern and central part of the basin are generally accepted to be of marine origin by most researchers. Marine indicators include the presence of conodonts, acritarchs, nautiloid cephalopods (Hart, 1964), several marine trace fossil assemblages (Turner et al., 1981), sedimentological evidence and the presence of glauconite in turbidites (Johnson 1966; 1976; 2006; Visser, 1994; Veevers et al., 1994; Flint et al., 2011; Geel et al., 2013; Ruckwied et al., 2014).

The fact that glauconite was documented in turbiditic sandstones of the Ecca Pass (Figure 4.10C) and that contemporaneous basins existed on a scale that spans the southern hemisphere (Figure 2.1) is nearly irrefutable evidence of a marine origin. The papers that argue against a marine signature warrant closer analysis in order to establish if the same conclusion would be reached with alternate interpretations of the results.

2.5.8. Dolerite Intrusions

Dolerite sills and dykes occur throughout the Karoo Basin (Figure 2.19) with the southern extent of intrusions marked by the so-called dolerite line (Veevers et al., 1994). The thickest sills are up to 200 m thick, representing extensive (>200 km diameter) sheets emplaced in the organic-rich shales of the lower Ecca Group. Higher in the Karoo stratigraphy, sills are emplaced in the sandstone-dominated upper Ecca and Beaufort Groups and form nested saucer-shaped intrusions with individual thicknesses of about 100 m and characteristic diameters of 20 km – 60 km. Dolerite intrusions occur at a high frequency at intervals of 10s of metres (Smith, 1990). Sills are less common in the uppermost part of the basin, the Stormberg Group (Smith, 1990; Johnson et al., 1996; Catuneanu et al., 2005), whereas dykes are common and form 120–180 km long lineaments such as the 100 m– 200 m wide Gap Dykes. Sills are absent in the Drakensberg Group lavas, suggesting that they were emplaced prior to the main phase of flood volcanism or that emplacement within the lavas was

prevented. The Karoo sills are dominantly tholeiitic basalts to basaltic andesites, although more evolved sills are also present locally (Marsh and Eales, 1984; Neumann et al., 2011). Recently published U-Pb zircon data (Svensen et al., 2012) indicate that basin-scale emplacement took place within an interval of less than 0.5 Ma and could represent a single magma emplacement event. The peak of volcanic activity in South Africa and Lesotho is recorded at 183 ± 1 Ma by $^{40}Ar/^{39}Ar$ dating of the Drakensberg basalts and some Karoo Basin dykes and sills (Duncan et al., 1997; Jourdan et al., 2005; 2007).

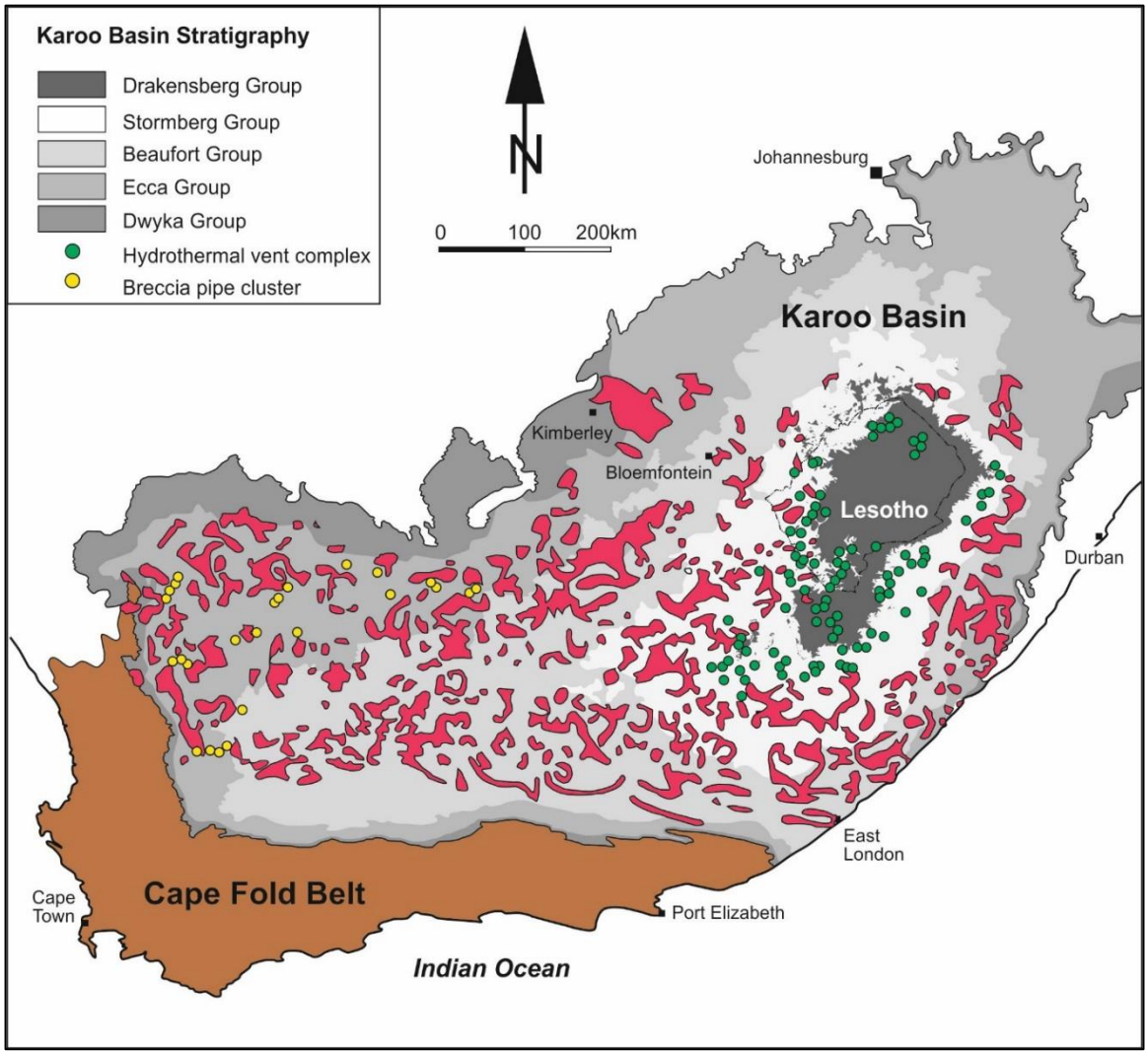

Figure 2.19: Distribution of dolerite sill intrusions, hydrothermal vent complexes and breccia pipe clusters in the Main Karoo Basin. Approximately 390,000 km^2 of the basin contains dolerite intrusions (Svenson et al., 2007). Modified after Catuneanu et al. (1998) and Svenson et al. (2007).

2.5.9. Energy Potential

Recently, a large focus has been placed on the possibility of unconventional gas resources in the Main Karoo Basin of South Africa. Total reserves for unconventional gas across sub-Saharan Africa are estimated to be 4,000 billion m^3, with 52% of this amount coming from South Africa (Castellano et al., 2015). The southern Karoo Basin was first explored by SOEKOR during the late 60's and early 70's. Karoo argillites were targeted for oil with the hope of finding reservoirs produced by the effects of the adjacent Cape Fold Belt. Geochemical and carbon reflectance analysis revealed poor oil potential of the southern Karoo basin due to the combination of folding, low porosity and permeability and high thermal maturity of reservoir rocks (Rowsell, 1976). The hydrocarbon potential of the Karoo Basin was downgraded due to the lack of reservoirs in contact with source rocks, as well as the adverse effects of dolerite intrusions in the northern portion of the basin. The southern portion of the basin was deemed over-mature due to depth of burial as well as the effects of the Cape Fold Belt (ibid.). However, during exploration several minor high pressure, low volume gas shows were discovered. One particular well (CR1/68) drilled near Graaf Reinet (Figure 2.20, 2.21) produced a strong flow of methane gas in fractured carbonaceous Ecca Group shales (Fort Brown Formation) on the flank of a dolerite sill (Rowsell, 1976). The well has a tested flow rate of 1.84 million scf/day at 2072 psi, (2563 m to 2612 m) but showed depletion in approximately two days (ibid.). With advances in technology, several international companies have shown interest in exploring for and extracting gas from the organic rich shales of the Ecca Group, particularly the Prince Albert and Whitehill Formations, via hydraulic fracturing (Petroleum Agency SA, 2015).

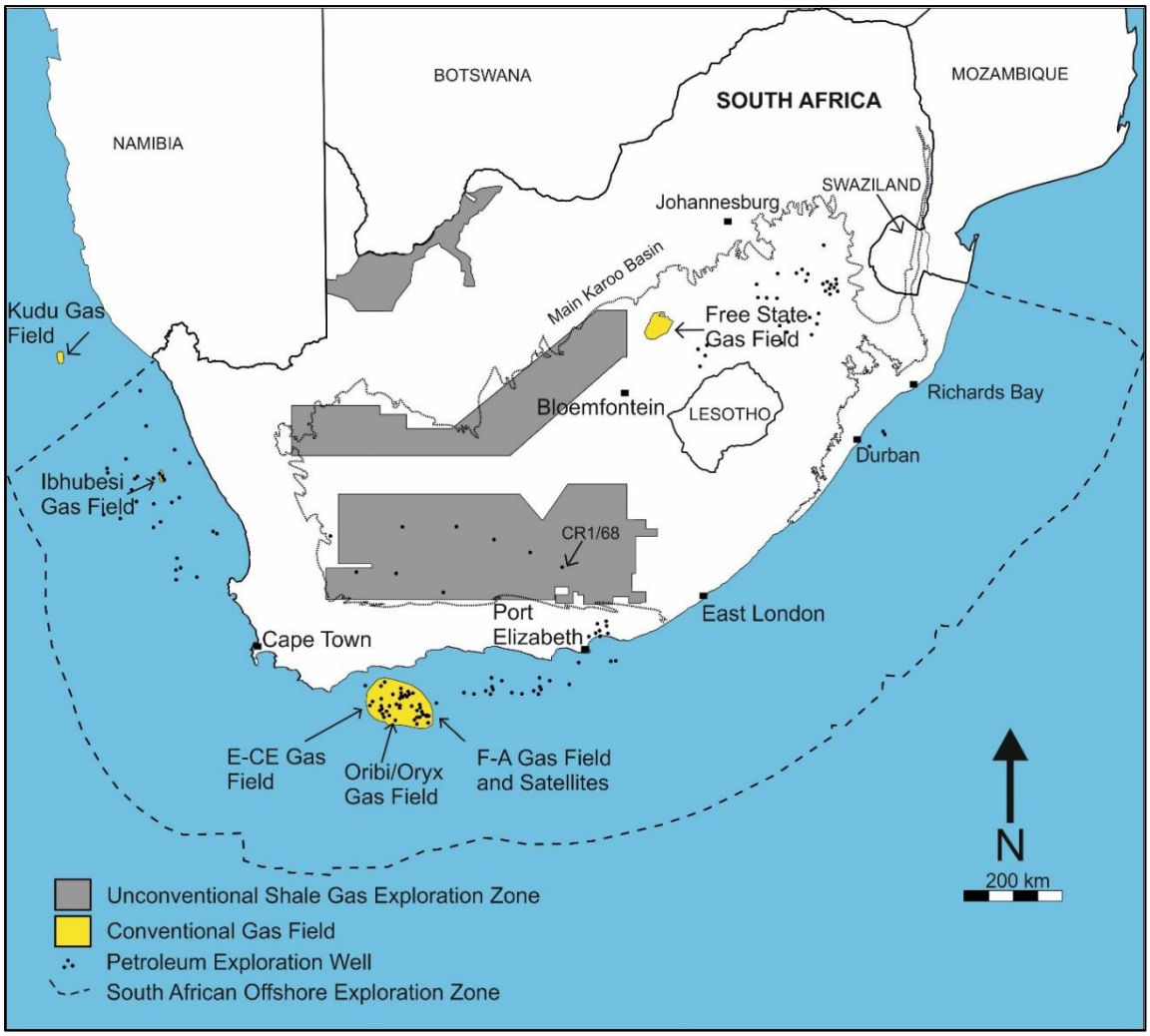

Figure 2.20: Summarised conventional and unconventional hydrocarbon fields and exploration zones in South Africa. Diagram modified from Petroleum Agency SA (2015).

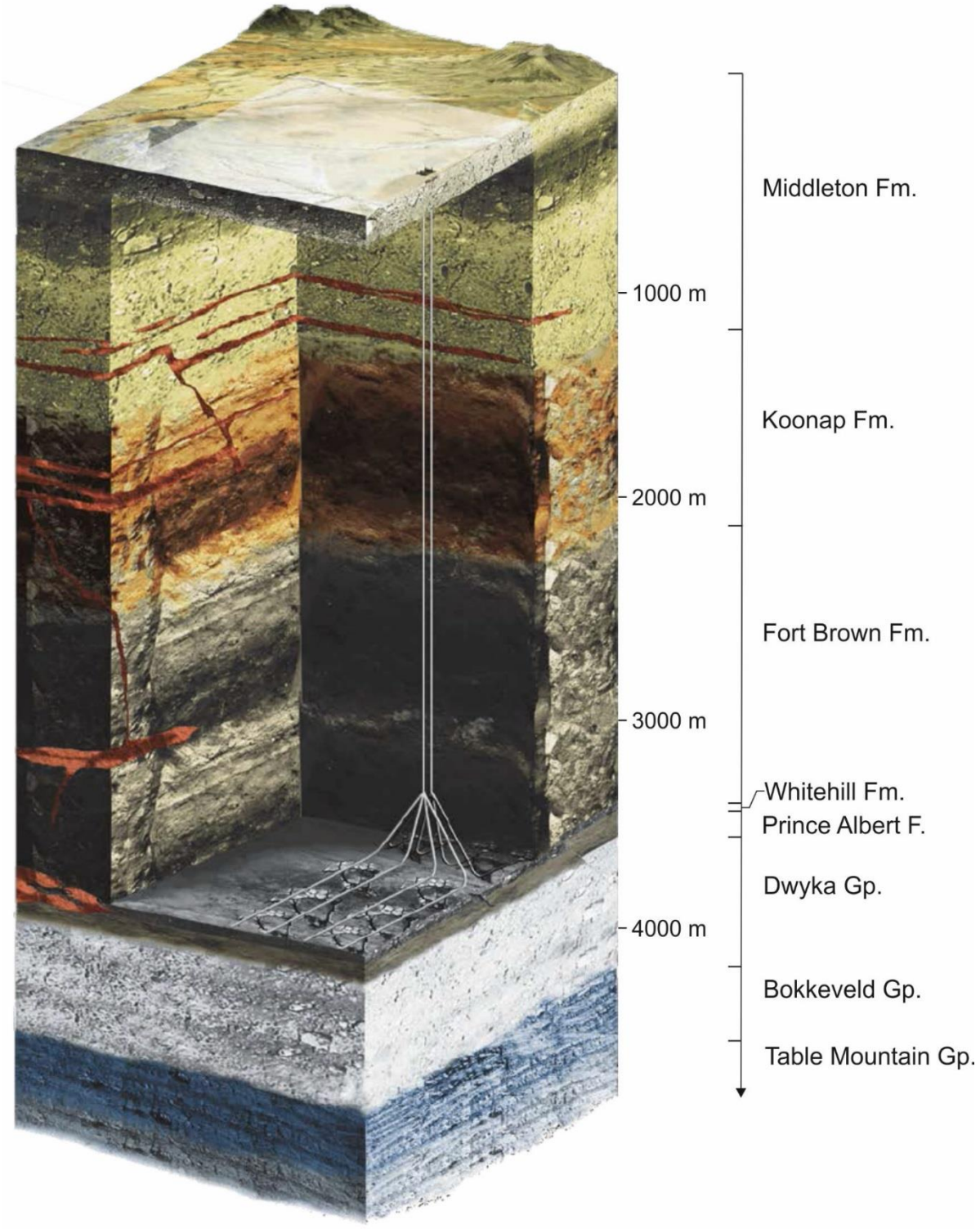

Figure 2.21: Stratigraphy of borehole CR1/68 with potential for hydraulic stimulation of the lower Ecca Shales. Modified from Decker (2013).

According to Decker (2013) the prerequisites for a successful gas-bearing shale include:

(1) TOC > 2%

(2) R_o > 1%

(3) rich in quartz (brittle)

(4) rich in carbonates (porous)

(5) low in clays (ductile)

I. Upper Ecca Shales

The TOC and thermal maturity of the upper Ecca Shales (Fort Brown and Waterford Formations) is substantially lower than that of the lower Ecca Shales (Collingham, Whitehill and Prince Albert Formations) (Kuuskraa et al., 2013). The upper Ecca shales have an average TOC of 1 – 2% and thermal maturity ranging from 0.9 – 1.1 % R_o, falling in the oil to wet gas window (ibid.).

II. Lower Ecca Shales

The lower Ecca shales include the basal Prince Albert Formation (pg. 26) and the overlying Whitehill (pg. 27) and Collingham (pg. 31) Formations. Table 2.1 summarises the reservoir properties of the lower Ecca shales.

The Prince Albert Formation contains TOC ranging from 1.5 – 5.5% with an average of 2.5% and has a high thermal maturity of 2 – 4% R_o, well within the dry gas interval (Kuuskraa et al., 2013).

The Whitehill Formation is the main target for shale gas exploration. The Formation has a TOC range from 0.5 to 17% with an average of 6% (Oelofsen, 1987; Cole and McLachlan, 1991, Kuuskraa et al., 2013). Vitrinite reflectance values range from 1 – 4% (Decker, 2013). The deepest portion of the southern basin is deemed over-mature; however, maturity may

decrease northwards (Geel, 2013). The Whitehill Formation is composed of up to 50% quartz in some areas (Decker, 2013) but also contains a high percentage of clays (Geel, 2013). Hydrogen and oxygen indices indicate a mixture of Type 1 (algal) and Type II (planktonic) kerogen (Faure and Cole, 1999; Geel, 2013).

The Collingham Formation has a lower TOC than the Whitehill Formation, ranging from 2 – 8%, having a high thermal maturity of 3% R_o (Kuuskraa et al., 2013). Abundant volcanic ash layers (TOC 0.1%; Black et al., 2016) may have diluted the overall organic content of the formation. Black et al. (2016) proposed that the Collingham Formation would be a suitable cap-rock for the Whitehill Formation.

Evaluations of potential shale gas reserves in the Main Karoo Basin are estimated at between 32-485 trillion cubic feet (tcf); a reduction in the original estimate due to the potential loss of gas associated with the intrusion of dolerites in the basin (Decker and Marot, 2012).

Table 2.1: Shale gas reservoir properties. Modified after (Kuuskraa et al., 2013).

Basic Data	Basin/Gross Area		Karoo (612,273 km^2)		
	Shale Formation		Prince Albert	Whitehill	Collingham
	Geologic Age		L. Permian	L. Permian	L. Permian
	Depositional Environment		Marine	Marine	Marine
Physical Extent	Prospective Area (km^2)		155,865	155,865	155,865
	Thickness (m)	Organically Rich	122	61	61
		Net	37	30	24
	Depth (m)	Interval	1,800 - 3,200	1,600 - 3,000	1,600 - 3,000
		Average	2,600	2,400	2,400
Reservoir Properties	Reservoir Pressure		Mod. Overpress.	Mod. Overpress.	Mod. Overpress.
	Average TOC (wt. %)		2.5%	6.0%	4.0%
	Thermal Maturity (% Ro)		3.00%	3.00%	3.00%
	Clay Content		Low	Low	Low
Resource	Gas Phase		Dry Gas	Dry Gas	Dry Gas
	GIP Concentration (Bcf/mi^2)		42.7	58.5	36.3
	Risked GIP (Tcf)		385.3	845.4	327.9
	Risked Recoverable (Tcf)		96.3	211.3	82.0

III. Dolerite Intrusions

According to Kuuskraa et al. (2013) the high thermal maturity of the Prince Albert, Whitehill and Collingham Formations is in part due to the presence of igneous intrusions. The Whitehill Formation in the southern Main Karoo Basin, that is proximal to dolerite intrusions, has experienced low grade metamorphism (250 - 300°C), while the same formation in the Northern Cape and southern Namibia has undergone slight burial metamorphism (~180°C) (Smithard et al., 2015).

According to Svensen et al. (2007), TOC contents and vitrinite reflectance data from contact aureoles indicate an organic carbon depletion from the lower Ecca Shales. The same authors reported thousands of breccia pipes (cylindrical structures approximately 150 m in diameter) containing brecciated and metamorphosed black shale formed by gas pressure accumulation due to metamorphism. The western Main Karoo Basin may have lost up to 27,400 Gt of CO_2 due to dolerite intrusions (ibid.). Exploration for, and evaluation of, shale gas within the Main Karoo Basin will be highly dependent on the geometry of subsurface dolerite intrusions (Smithard et al., 2015).

2.6. Conclusions

The Main Karoo Basin is a retro-arc foreland basin underlain by a stable metamorphic basement and bounded to the south by a fold-thrust belt (Johnson et al., 2006). The basin ranges in age from Late Carboniferous to Middle Jurassic with a total sediment thickness of approximately 12 km covering an area of 700 000 km² (ibid.).

The Karoo Supergroup contains 5 Groups (4 sedimentary, 1 igneous) that record the environmental transition from ice-house to hot-house. Depositional environments include glacial (Dwyka Group), deep marine (Ecca Group), deltaic/fluvial (Beaufort Group) and, fluvial/aeolian (Stormberg Group). Sedimentation within the basin was interrupted by

extensive flood basalts (Drakensburg Group) relating to the breakup of Gondwana, with the entire sedimentary succession intruded by dolerite feeder dykes and sills (Johnson et al., 2006).

The deep marine Ecca Group has recently aroused interest within industry and academia due to the thick successions of organic-rich shale located within the southern Main Karoo basin (Decker and Marot, 2012). The high TOC black shales of the Whitehill Formation, located beneath thick successions of turbiditic sandstones, are seen as the most prospective, however, exploration for unconventional hydrocarbons is still in its infancy.

3. Permian black shales of the Karoo Basin: Structural controls and implications for shale gas resource potential

This chapter investigates the causes of the stratigraphic duplication of the Whitehill Formation as documented in borehole KZF-1, and associated implications for resource potential.

3.1. Introduction

Structural elements of the Cape Fold Belt and its Karoo foreland basin have been studied within the broader geotectonic context (e.g., Veevers, 2004; Tankard et al., 2009; Booth, 2011; Lindeque et al., 2011) and were recently also addressed in detailed outcrop studies (Fagereng, 2012; Fagereng and Byrnes, 2015). However, there is a lack of high-resolution data from boreholes which inhibits a reliable overall interpretation of the geotectonic setting. Recently, the possibility of large-scale extraction of unconventional shale gas from within the Main Karoo Basin of South Africa has been suggested (Geel, 2013). Total reserves for unconventional gas across sub-Saharan Africa are estimated to be 4 trillion cubic metres, with 52 percent of this amount from South Africa (Castellano et al., 2015).

The southern Main Karoo Basin was first explored by SOEKOR during the late 60's and early 70's (e.g.,Winter et al., 1970; Rowsell and de Swardt, 1976). Karoo shales were targeted as oil source rocks, with the aim of finding reservoirs produced during the Cape Orogeny. Geochemical and carbon reflectance analysis revealed poor oil potential of the southern Karoo Basin due to the combination of folding, low porosity and permeability, and high thermal maturity of reservoir rocks. The hydrocarbon potential of the Main Karoo Basin was downgraded due to the lack of reservoirs in contact with source rocks, as well as the adverse effect of dolerite intrusions (Duncan and Marsh, 2006). The southern portion of the

basin was deemed over-mature due to depth of burial as well as the effects of the Cape Fold Belt (Rowsell and de Swardt, 1976).

In this study attention is drawn to the duplication of lithological units involving the potential shale gas reservoir (Whitehill Formation) and the underlying Prince Albert Formation, in a borehole (KZF-1) drilled through the lower Karoo Supergroup rocks in the Ceres area (Western Cape) of South Africa (Figure 3.4).

This study aims to place borehole KZF-1 within the established regional geotectonic framework of the Cape Fold Belt along the southern margin of the Main Karoo Basin, as well as investigating the shale gas potential. Deciphering the local effects of regional scale tectonic events, such as reservoir compartmentalisation and fault sealing (Cerveny et al., 2004; Ligtenberg, 2005; Gale et al., 2007), is necessary in evaluating the shale gas potential of the reservoir.

The formation of thrusts and the characterisation of décollement zones are contrasted with syndepositional structures identified in outcrops further afield, to better constrain the formation of the structures observed in the borehole. Ultimately, understanding the effects of deformation on the shale gas potential of the Permian Whitehill Formation, intersected in borehole KZF-1, will add valuable information to the resource potential in the foreland region of the Cape Fold Belt.

3.2. Black Shales

In geological literature the term ‘black shale’ generally refers to a variety of fine-grained organic matter-rich mudrocks found in a wide range of sedimentary environments from lacustrine to deep marine abyssal plains (Trabucho-Alexandre et al., 2012). Black shales are usually fine grained, compacted sediments that display distinct lamination, usually

deposited under oxygen-poor bottom waters, which accumulate in deep-water basinal locations. Many black shales are hemipelagites, pelagites or fine grained turbidites (Einsele, 1992; Wignall and Newton, 2001; Ketris and Yudovich, 2009). However, with regards to petroleum geology, black shale is a mudrock with organic matter in concentrations greater than 1%, deposited in an oxygen poor environment, leading to the formation of hydrocarbon source rocks (Allaby and Park, 2013).

3.2.1. Composition

Black shale forming muds are commonly composed of 40-60% clay minerals, 30% quartz, 10% feldspars, and 10% carbonate-iron oxide cements (Sethi and Schieber, 1998; Cox and Lowe, 1995). The dark colour is caused by two components: dispersed iron sulphides and organic compounds (Schieber, 2003). According to Boggs (2009) the transition of colours in shales from light grey to dark grey to black is associated with increasing carbon content of the shales in comparison to the variations from red to purple to greenish-grey caused by decreasing ratios of Fe^{3+}/Fe^{2+}. The abundance of organic matter in sediments controls the oxidation state of iron by yielding electrons to force iron into a reduced state (ibid.).

3.2.2. Depositional Environments

Marine environments with reduced circulation between oxygen-rich surface waters and the sea floor are the most favourable sites for the deposition of black shales and may be thousands of square kilometres in extent in modern-day oceans (Arthur and Sageman, 1994). Other favourable areas include reduced or anoxic swamps and tidal flat zones, estuaries, lakes and lagoons with high nutrient supply, shelves and upper continental slopes under zones of coastal upwelling and widely extended deep-sea regions during periods of sluggish ocean circulation (Figure 3.1) (Einsele, 1992; Reading, 1996; Nichols, 2009).

Arthur and Sageman (1994) suggested that sea floor anoxia is created by either the presence of a stratified water column (Preservation model) leading to the disassociation of the photic-zone from bottom waters, or, increased productivity rates (Productivity model) resulting in unfulfilled demand for dissolved O_2. When the tissues of an organism decay, in an oxygen-deficient environment, resistant fractions of organic substances such as cellulose, fats, resins and waxes become incorporated into the accumulating sediment as kerogen (Boggs, 2009; Cornford, 2005).

Factors leading to the formation of black shales are therefore determined by organic input, consumption by microbial activity and dilution by terrigenous clastic, biogenic carbonate or silica.

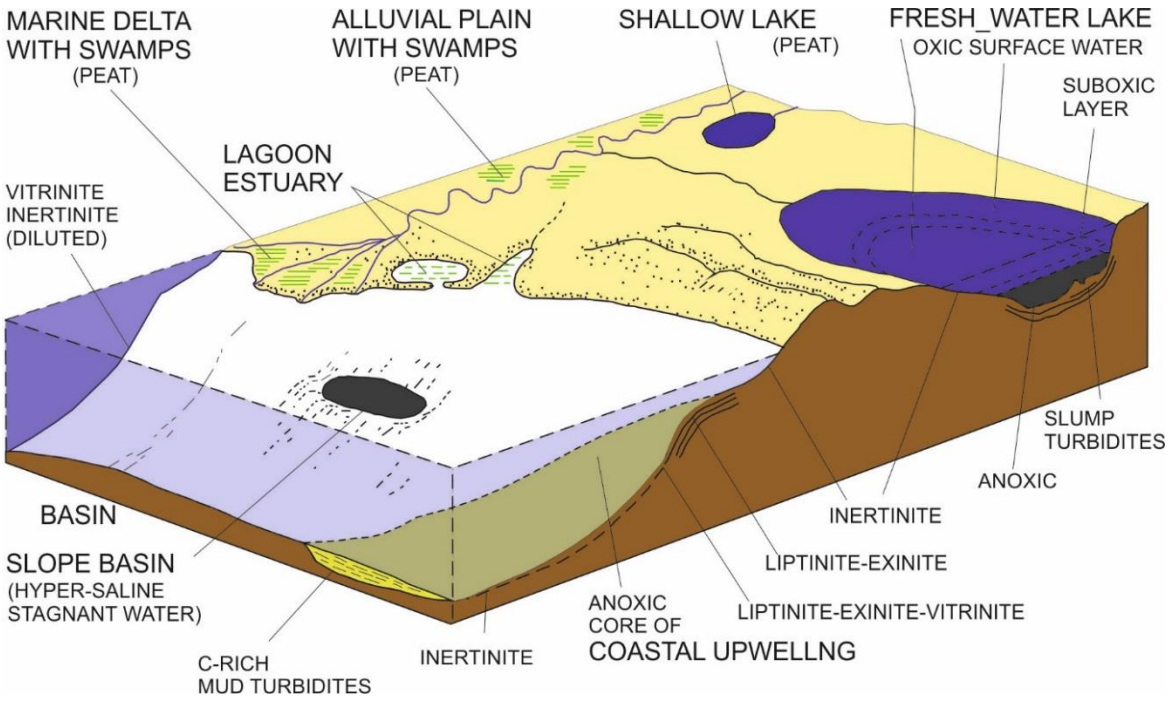

Figure 3.1: Schematic diagram showing major depositional environments for the accumulation of organic-rich sediments. Diagram modified from Einsele (1992).

3.2.3. Hydrocarbon Potential

Black shales are major source rocks for petroleum reserves (Wignall, 1994). Most aquatic or littoral sedimentary environments have an abundant supply of organic matter in order to produce black shales, provided the depositional environment is conducive to organic matter preservation. Black shales typically contain 3% - 10 % organic matter compared to an oil-shale or kerogen-shale that contains over 20%. Oil can be extracted from shale by pyrolysis and the hydrocarbons produced will depend on the types of organic matter present (Tourtelot, 1979; Tyson, 1995).

Black shales are crucial source rocks for oil reserves (Wignall, 1994; Werne et al., 2002; Piper and Calvert, 2009). In the evaluation of petroleum source rocks the *Total Organic Content* (TOC) concentration is a critical factor. TOC in black shales range from 1% - 15%. When compared to carbonates, shale source rocks require a higher TOC value to reach favourable source potential, possibly due to a lower efficiency of expulsion of any generated hydrocarbon (Cornford, 2005). Degens (1965) deduced the average organic matter content to be approximately 2.1 wt% in mudstones, 0.29 wt% in limestones and 0.05 wt% in sandstones. A few shales can reach in excess of 20% TOC as seen in the Lower Silurian 'hot' shales of Northern Africa (Einsele, 1992; Lüning et al., 2000, 2003a, 2003b).

3.2.4. Age Constraints

Black shales are present throughout geological history (Figure 3.2) and are developed when specific geological settings and environmental controls are suitable for the deposition of organic-rich sediments. Organic rich sediments form when and where organic matter accumulates at a faster rate than it can be destroyed (Tourtelot, 1979). The widespread distribution of black shales in the Phanerozoic is predominantly limited to six stratigraphic intervals, which together represent approximately one-third of Phanerozoic time (Trabucho-

Alexandre et al., 2012). The petroleum source rocks from the six intervals have provided more than 90% of the world's known hydrocarbon reserves (Klemme and Ulmishek, 1991).

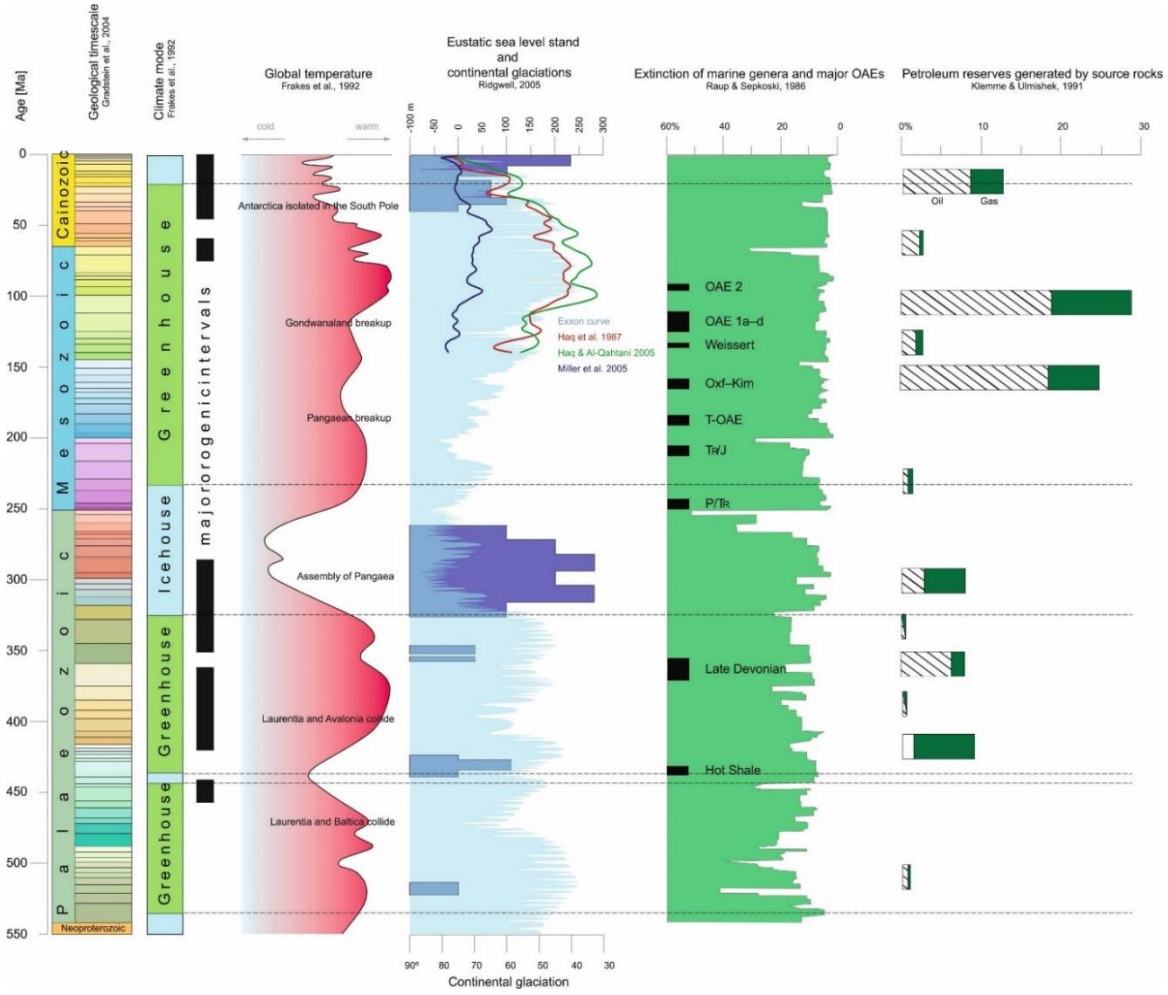

Figure 3.2: Patterns of various indicators of global change during the Phanerozoic (modified after Trabucho-Alexandre *et al*., 2012). From left to right: Phanerozoic geological timescale (Gradstein and Ogg, 2004), climate mode (Frakes et al., 1992), major orogenic intervals, global temperature (Frakes et al., 1992), eustatic sea level stand (Exxon curve; Haq et al., 1987; Haq and Al-Qahtani, 2005; Miller et al., 2005), continental glaciations (Ridgwell, 2005), extinction of marine genera and major oceanic anoxic events (OAEs) (Raup and Sepkoski, 1986), petroleum reserves generated by source rocks (Klemme and Ulmishek, 1991).

3.3. Preservation and Depositional Mechanisms

Most of the widespread ancient black shales deposits have no direct modern equivalents. A modern depositional equivalent such as the Black Sea is of limited use when studying deposits of the ancient past. Ancient deposits have therefore been studied intensively using modern techniques in attempts to better constrain models of formation in order to update or to replace modern analogues (Potter et al., 2005). The "deep anoxic basin" model for black shales has been the prevalent model for many years however, increased examination has led to the discovery of a wide range of depositional settings for black shale formation (Figure 3.1) (Schieber, 1998, 1999; Stow et al., 2001; Wignall and Newton, 2001; Schieber, 2003; Harris, 2005; Trabucho-Alexandre et al., 2012).

Three primary models have previously been proposed as the controlling factors of source rock development (Katz, 2005; Harris, 2005):

(1) The elevated primary production model – elevated rates of organic productivity in the photic zone, stimulated by high nutrient flux cause the rate of supply of organic matter to the sediment surface to be sufficiently high. If input outstrips degradation, then some are preserved (Pedersen and Calvert, 1990; Stow et al., 2001).

(2) The enhanced organic preservation model - oxygen-poor deep waters limit oxidation reactions that degrade organic-matter (Demaison and Moore, 1980). The lack of oxygen inhibits macro and meso benthic activity in favour of microbial activity. Consequently, the lack of (macro) burrowing lowers the amount of time organic-matter resides near the sediment surface in any of the oxidant zones, and prevents deep-penetration pore-water circulation and inhibits gut microbial activity (Stow et al., 2001).

(3) The burial-rate model - the slow accumulation of clastics or carbonates that would otherwise dilute organic matter. During periods of low burial rates, increased sedimentation serves to isolate organic matter from an oxidising water body and enhance organic-matter content; at high burial rates, increased sedimentation dilutes the organic-matter (Tyson, 2001; 2005).

Tyson (1987) claimed that the Productivity and Preservation models are incompatible. High productivity rates suggest sustained nutrients and hence vigorous circulation (upwelling) of the water column, whereas the Preservation model is typically generated by stratification of the water column, preventing nutrient circulation and leading to generally low productivity (Wignall, 1994).

Historically, researchers have generally viewed the controlling factors for source rock development as independent leading to distinct source-rock depositional models, however upon reviewing these 'independent' models it was concluded that no single factor provides a fully comprehensive representation of source-rock development (Katz, 2005; Tyson, 2005). The processes of anoxia in the water column and high productivity may not be completely independent of one another, instead favouring a combination of both processes according to recent studies by Calvert and Fontugne (2001), Werne et al. (2002), Rimmer (2004) and Wei et al. (2012). Despite the major differences in the two models, they are notoriously difficult to infer within ancient organic rich sediments, due to poor palaeoproductivity proxies and the inability to constrain sedimentation rates (Wignall, 1994; Werne et al., 2002).

Alternate factors have been identified that may also influence organic-matter content. Firstly, the sulfurisation of organic molecules may make them significantly more resistant to oxidation, enhancing their preservation in oxidising environments. Such a mechanism has

been demonstrated in the laboratory by van Dongen et al. (2003). Secondly, the relative proportion of resistant biopolymers may differ depending on the genetic type of organic-matter. This may lead to an enhancement through selective preservation (Stow et al., 2001). Lastly, the adsorption of organic molecules on or within clay minerals may serve to physically shield them from chemical attack, a process which has been shown to preserve organic matter on modern continental shelves (Hedges and Keil, 1999).

3.4. Structural Controls on Hydrocarbon Permeability

Foreland fold-and-thrust belts are one of the remaining frontiers for hydrocarbon exploration where large discoveries can still be expected (Roure and Sassi, 1995). The detailed effects of tectonic and structural deformation within potential and existing hydrocarbon reservoirs (i.e. reservoir compartmentalisation) is crucial for resource determination, reservoir appraisal and reserve booking as well as the amount of economic oil or gas that might be attributed to any given well drilled in a field (Jolley et al., 2010).

3.4.1. Reservoir Compartmentalisation

Reservoir compartmentalisation – the separation of a hydrocarbon accumulation into a number of individual fluid/pressure compartments – occurs when flow is prevented across ‘sealed’ boundaries in the reservoir (Jolley et al., 2010). Jolley et al. (2010) continues to state that these boundaries are caused by numerous geological and fluid dynamic factors, but there are two basic types: (1) ‘static seals’ that are totally sealed and therefore withhold hydrocarbons over geological time; (2) ‘dynamic seals’ that are low to very low permeability flow barriers that reduce hydrocarbon migration. Dynamic seals allow for equilibration across a boundary over geological time-scales, but act as seals over production time-scales, because they prohibit crossflow at normal production rates – causing fluid contacts,

saturations and pressures to progressively segregate into ‘dynamic’ compartments (Jolley et al., 2010).

Reservoir compartmentalisation is a complex subsurface uncertainty that is the product of the combination of stratigraphic architecture, structural architecture, fault permeability and diagenesis, all of which must be considered in the analysis of reservoir compartmentalisation.

3.4.2. Stratigraphic Compartmentalisation

The stratigraphic architecture of the reservoir forms the fundamental building block upon which the other compartmentalisation uncertainties (structural, fault seal and diagenesis) must be applied. The primary depositional fabric and stratigraphic architecture of a depositional system defines the sand body connectivity network and hence determines the stratigraphic compartmentalisation potential of the reservoir (Ainsworth, 2010). Compartmentalisation within conventional hydrocarbon systems (fluvial and marine) is the focus of on-going research (Jolley et al., 2010); however stratigraphic compartmentalisation of unconventional reservoirs is not well constrained. The distribution of target lithologies (organic-rich shales) within a potential reservoir may be influenced by depositional conditions, diagenesis as well as tectonics.

3.4.3. Structural Compartmentalisation

According to Mildren et al. (2002), Davies and Handschy, (2003) and Cerveny et al. (2004), faulting is a focal feature in fold and thrust zones and faults are the primary pathways for fluids in many basins worldwide, especially in the deeper subsurface. Faults can be a transmitter of, or a barrier to, fluid flow and pressure communication, and are crucial in hydrocarbon migration/accumulation within semi-consolidated to lithified rocks. The integrity of structurally-bound hydrocarbon traps is dictated by the sealing potential of

bounding faults. The rock properties that develop within the fault zones affect the fault's ability to seal. These properties are affected by the local facies, reservoir-fluid types and saturations, pressure differences across faults, fault zone architecture, burial and fault histories and associations of the lithologies across the faults. Faults that do not form a seal may prevent oil and gas from accumulating, permitting migration through structures in the subsurface, while open and permeable faults within an established reservoir may result in lost-circulation problems during drilling operations.

Sealing faults may transform a relatively large and continuous hydrocarbon reservoir into compartments that then behave as a collection of smaller reservoirs (Cerveny et al., 2004; Ligtenberg, 2005).

Faults are generally mapped from seismic data and incorporated into geological models as discrete dislocation planes. However faults are not simple smooth surfaces – they are 3D zones of strain that develop during the evolution of a fault through its propagation, linkage, and slip consolidation phases (McKie et al, 2010). These fault zones are composed of smeared, disarranged and re-aggregated fragments of the host lithostratigraphy (Kristensen et al., 2008) and a related assemblage of meso- to small-scale faults and fractures that host a variety of fault-rock types and mineral fills (Shipton et al., 2005).

The total flow retarding/sealing effect of a fault is caused by the collective distribution of the re-arranged juxtapositions caused by lithological smearing and fragmentation, the increase of capillary entry pressures caused by permanent porosity and permeability collapse within fault rocks, and the extreme tortuosities imposed on potential fluid flow pathways by the complexity of the fault zone architecture (Mckie et al., 2010).

3.5. Borehole KZF-1

3.5.1. Location

Borehole Karoo Zandfontien 1 (KZF-1) was drilled in the Western Cape of South Africa (32°50'30.43"S 19°44'33.02"E) to the northeast of Cape Town (Figure 3.3). The borehole was drilled to a depth of 671 m by Geoserve Exploration Drilling PTY LTD.

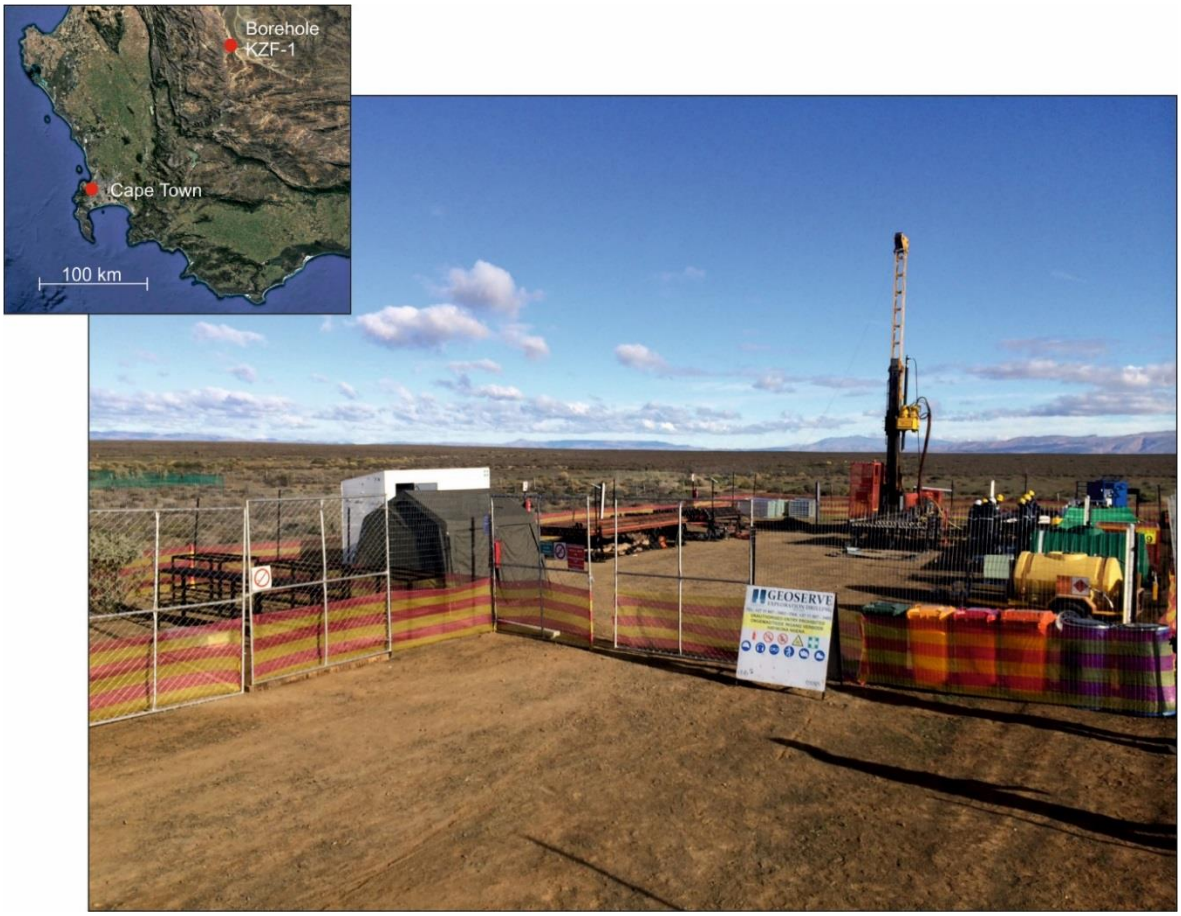

Figure 3.3: Borehole KZF-1 drill site in the Western Cape of South Africa (see insert) at an elevation of 510 m above sea level. Photo source: KARIN.

Borehole KZF-1 represents the first deep Karoo borehole since the SOEKOR exploration drilling undertaken in the 1960s and 1970s. The core is housed at the Council for Geoscience (CGS), Pretoria, South Africa.

3.5.2. Lithological and petrophysical data

I. Methodology for Lithological Analysis

Borehole KZF-1 was drilled through four formations of the Ecca Group (Tierberg, Collingham, Whitehill, Prince Albert) as well as the upper portion of the Dwyka Group (Figure 3.4 & Appendix A). Formations were differentiated by shale colour (Munsell Colour System) and streak. A detailed log was produced by Dr. Doug Cole of the Counsil for Geosciences (Appendix A).

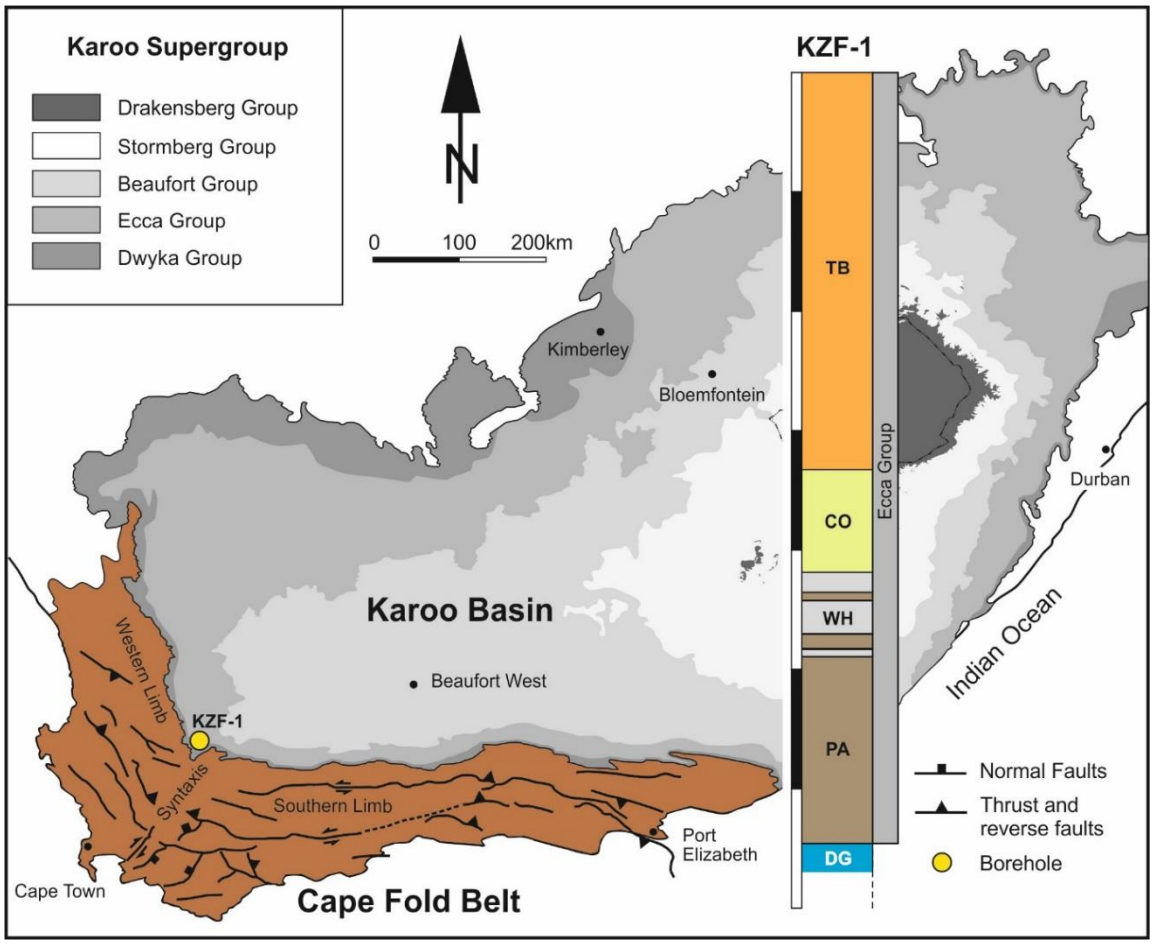

Figure 3.4: Stratigraphic log of borehole KZF-1 within the context of the Main Karoo Basin and Cape Fold Belt. Abbreviations: *TB* Tierberg Formation, *CO* Collingham Formation, *WH* Whitehill Formation, *PA* Prince Albert Formation, *DG* Dwyka Group. Scale bar = 100 m. Modified after Catuneanu et al. (1998).

Standard polished thin sections were prepared at Keele University, and analysed using a light microscope and scanning electron microscope with Energy Dispersive Spectroscopy (EDS) following standard practices (Knight et al., 2002). EDS was performed on portions of the thin section that contained a representative range of minerals in order to gauge relative elemental abundance. EDS was also performed on unusual structures or grains to aid identification. See section 3.5.4: methodology for analysis of geophysical data.

II. Results

Tierberg Formation Core

The Tierberg Formation (Figure 3.5a) contains fractured and weathered massive black shale within the first 25 metres of the borehole. Between the depths of 25 m and 60 m, the Tierberg Formation is composed of near massive black shale with a weakly defined bedding texture and disseminated pyrite along bedding and in fractures. Yellow tuffaceous layers, ranging from 1 cm - 2 cm in thickness, were observed intermittently. Major core loss was experienced between the depths of 38 m – 41 m. Between the depths of 60 m – 110 m the formation is composed of banded black shale, with bedding defined by dark grey bands 1 - 3 cm thick as well as brownish yellow mudstone layers up to several centimetres thick (Figure 3.5a). Calcite bands, rip-up clasts of shale and disseminated pyrite are present between 70 m – 75 m in depth. Major core loss was experienced between the depths of 82 m – 83 m. From 110 m to 190 m the Tierberg Formation is composed of alternating mudstone/shale and fine-grained sandstone layers. Sandstone layers range in thickness from a few millimetres up to 3 cm and exhibit upwards fining and soft sediment deformation in places. The formation continues to a depth of 342.55 m with alternating fine-grained sandstones and laminated banded shale with a near horizontal dip.

Tierberg Formation Microscopy

The fissile shales of the Tierberg Formation are composed of matrix-supported, angular to subrounded degraded feldspars and quartz, with moderate sphericity, within a fine grained matrix of clay and dark organic matter (Figure 3.6a). Minor lithic fragments, carbonates, muscovite, apatite, pyrite and zircon were documented (Figure 3.7a). Bioturbation of the immature shales was observed within distinct horizons, with no clear bedding discernible in thin sections.

Collingham Formation Core

The Collingham Formation (Figure 3.5b) starts at a depth of 342.55 m and comprises horizontally bedded dark grey to black near massive shale, with very weak bedding that is defined by lighter coloured beds. The shale is intercalated with yellow-brown tuff layers up to 12 cm in thickness (Figure 3.5b). Tuff layers are separated by up to 30 cm of shale. A 5.4 cm dark grey chert layer occurs at a depth of 364.74 m bounded by very fine-grained sandstone layers, 3 mm at base and 11 mm at top. A 19 cm thick brecciated fault zone was observed at a depth of 401.53 m with calcite veining around fragments, and slickenside development throughout. Very fine-grained sandstone layers were observed intermittently throughout the Collingham Formation.

Collingham Formation Microscopy

Matrix-supported, clumped elongate lath-shaped fragments of organic matter, and angular to subrounded quartz grains, along with sericitised feldspars with minor biogenic clasts within an aluminosilicate matrix characterise the immature shales of the formation (Figure 3.6b; 3.7b).

Whitehill Formation Core

The Whitehill Formation, composed of black carbonaceous shale with faint bedding (Figure 3.5c), was intersected at a depth of 420.45 m. The black shale contains occasional 1 mm to 3 mm brown shale beds. Disseminated pyrite bands less than 1 mm thick are common throughout the Whitehill Formation. Calcite veins up to 3 mm thick are common in high angle joints. Numerous brecciated horizons as well as faults were observed within the formation (Figure 3.5d and Figure 3.10).

Whitehill Formation Microscopy

The immature organic shale contains angular quartz and dolomite crystals, with low sphericity, within a black clay, pyrite and organic matter matrix (Figure 3.6c; Figure 3.7c). Zoned dolomite crystals (Figure 3.8, a–j) were documented with magnesium rich cores, and iron and manganese rich rims.

Prince Albert Formation Core

From a depth of 499.78 m the Prince Albert Formation is composed of dark grey to black shale intercalated with greenish tuff layers up to 17 cm thick (Figure 3.5e). Some green tuff layers contain black, match-stick like fragments of shale resulting in a black speckled appearance on the core surface. Bedding dip is near horizontal ranging from 3° to 8°. Between the depths of 558 – 559.50 m artesian water was encountered in a vertical fracture and at 626 m warm (24°C) sulphurous artesian water was intersected.

Prince Albert Formation Microscopy

The immature shales of the Prince Albert Formation contain needle and blade shaped organic matter fragments, with degraded feldspars and minor pyrite and quartz within a light brown fine grained matrix (Figure 3.6d). Bioturbated horizons were documented with no visible

bedding present in thin sections. A putative feeding tunnel was observed, (Figure 3.7d), with a depletion of organic matter, aluminium and sodium within the burrow (Figure 3.8, k–t). The burrow is enriched in silica, iron, calcium, sulphur and copper.

Dwyka Group

The Dwyka Group tillite was intersected at a depth of 648 m and consists of elongate and rounded light grey particles in a grey shaley groundmass. Bedding is well defined in places by dark grey interbeds 5 mm to 3 cm thick. Grey green tuff beds are occasionally present. Strong flowing (400 litres per second) warm (43°C) artesian water was intersected in fractures at a depth of 671 m.

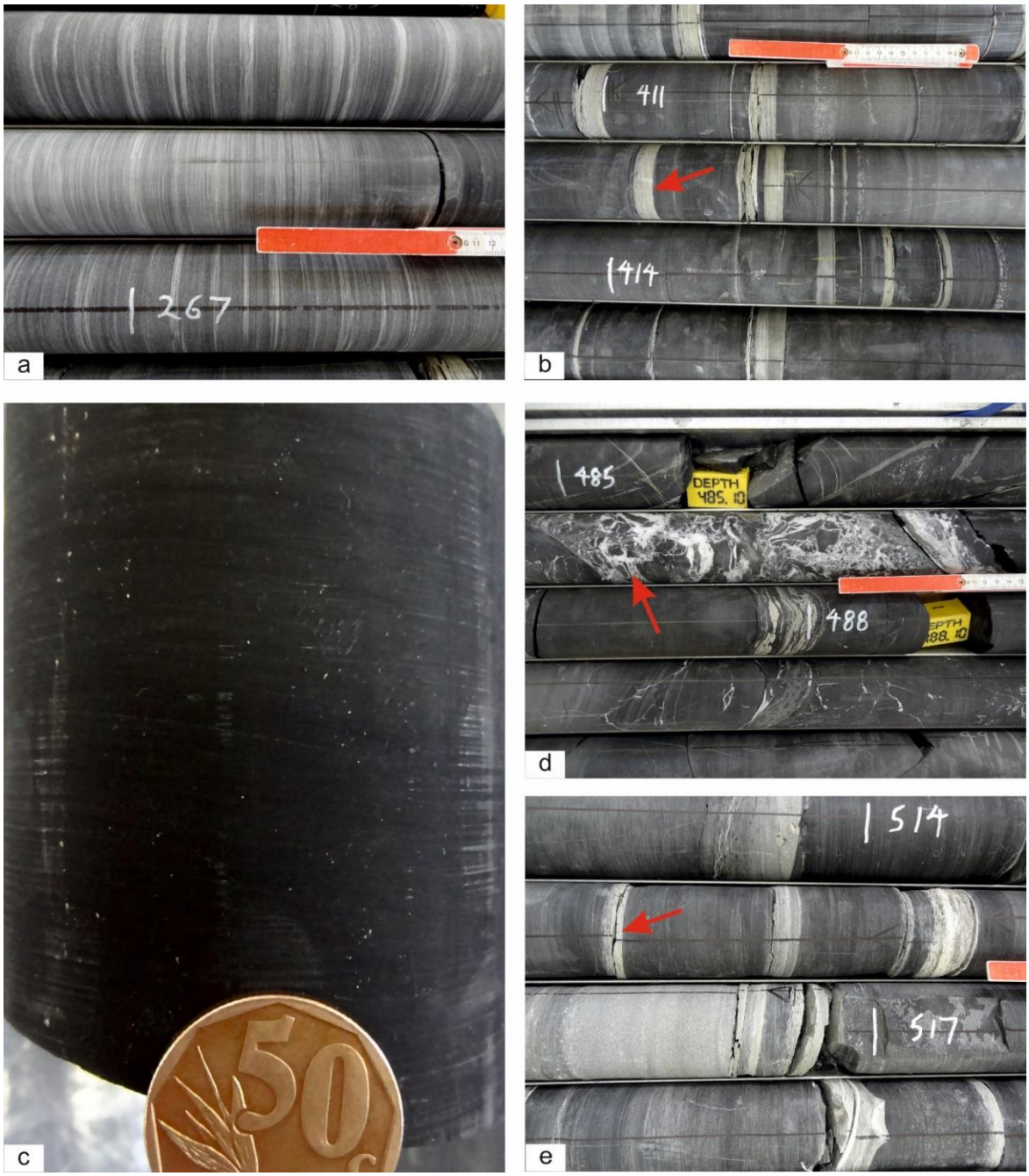

Figure 3.5: Lithology and deformation of Permian formations intersected in borehole KZF-1. **a:** Alternating light and dark bands within Tierberg Formation shales. **b:** Shales of the Collingham Formation with numerous greenish-grey tuff layers (arrowed). **c:** Black shales of the Whitehill Formation. **d:** Structural deformation (quartz veins and shale breccia) at the Whitehill/Prince Albert contact. **e:** Prince Albert Formation shale and sandstone with numerous greenish-grey tuff layers (arrowed).

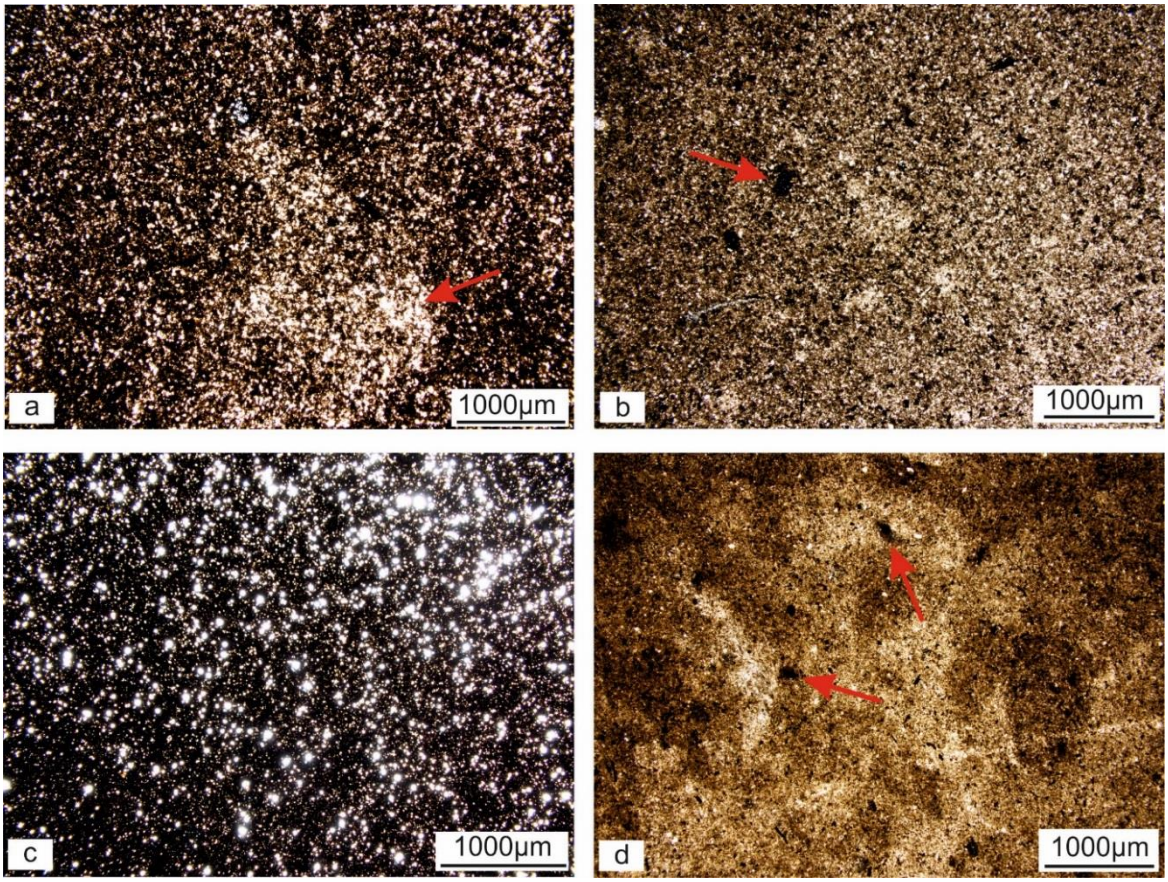

Figure 3.6: Thin section micrographs from borehole KZF-1 samples. **a:** Angular to sub-rounded quartz, feldspar and lithic fragments (arrowed) within a clay and organic matter matrix, Tierberg Formation (204.57 m). **b:** Organic matter fragments (arrowed), angular to sub-rounded quartz and degraded feldspars within a light brown clay matrix, Collingham Formation (386.28 m). **c:** Angular, low sphericity dolomite and quartz grains within an organic-rich matrix, Whitehill Formation (457.30 m)**. d:** Clustered laths of organic matter (arrowed) and altered feldspar grains within a light brown bioturbated clay matrix, Prince Albert Formation (561.96 m).

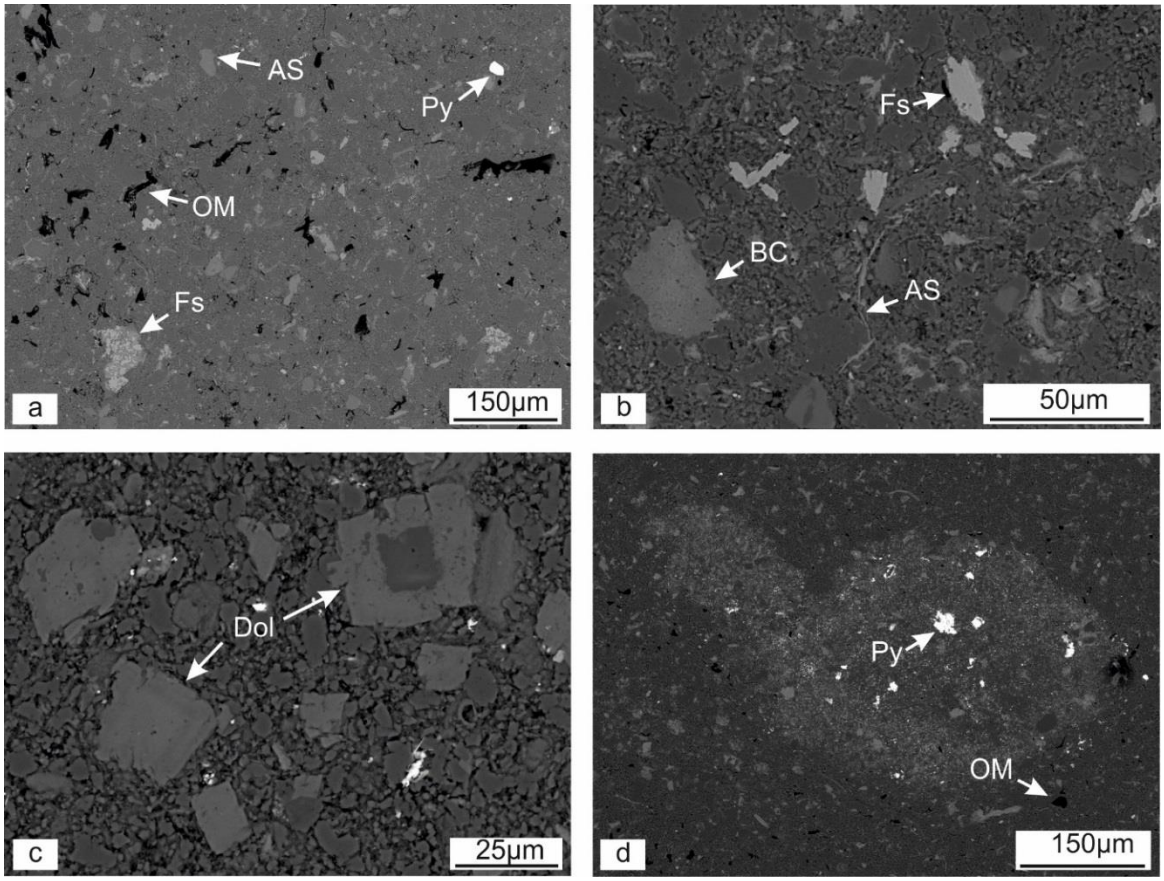

Figure 3.7: Scanning electron microscope backscatter images from borehole KZF-1 samples **a:** Degraded feldspar (Fs), organic matter (OM), pyrite (Py) and aluminosilicates (AS), Tierberg Formation (204.57 m). **b:** Feldspar (Fs), biogenic carbonate (BC), and aluminosilcates (AS), Collingham Formation (386.28 m). **c:** Dolomite (Dol) crystals, zoned and un-zoned, Whitehill Formation (457.30 m). **d:** A putative biogenic tunnel enriched in pyrite (Py) and depleted in organic matter (OM), Prince Albert Formation (561.96 m).

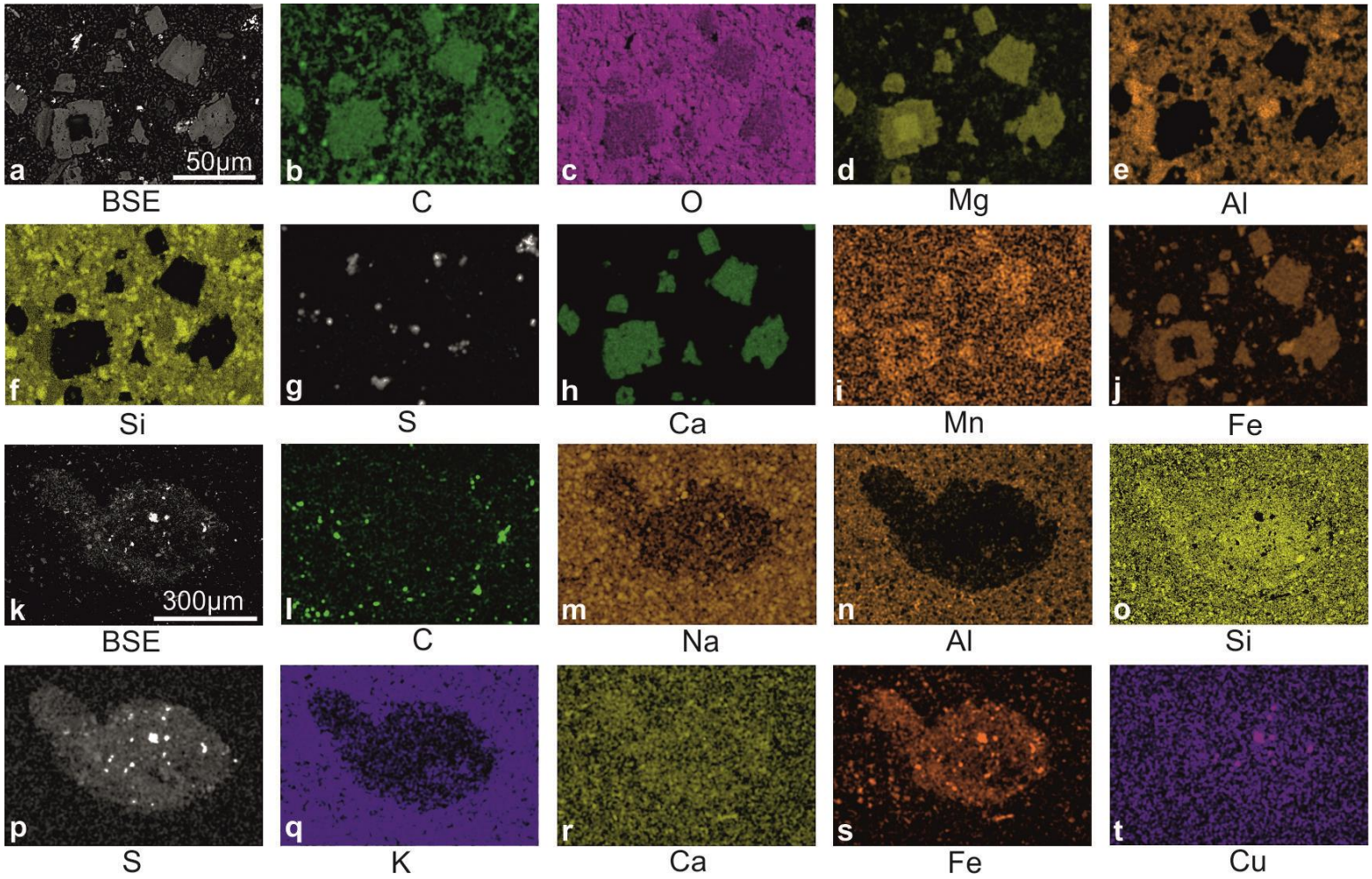

Figure 3.8: Element maps of scanning electron microscope backscatter images across zoned and unzoned dolomite crystals from the Whitehill Formation, (a–j) (457.30 m) and a biogenic tunnel from the Prince Albert Formation (k–t) (561.96 m). Note: Brighter colours indicate element enrichment. BSE (backscattered electron), Aluminium (Al), Calcium (Ca), Carbon (C), Iron, (Fe), Magnesium (Mg), Manganese (Mn), Oxygen (O), Silica (Si), and Sulphur (S), Copper (Cu), Potassium (K), Sodium (Na). Scale bar applies from a–j and k–t respectively.

3.5.3. Stratigraphic Duplication

Sharp normal contacts were observed between the Tierberg and Collingham formations as well as between the Collingham and Whitehill formations (Figure 3.10a). Stratigraphic repetition of the Whitehill and Prince Albert formations was observed within an interval of 58.92 m (439.95 m – 498.87 m), where contacts between these formations occur five times (Figure 3.9).

The first contact between the overlying Whitehill Formation and the underlying Prince Albert Formation occurs at a depth of 439.95 m (Figure 3.9) and appears to be a normal sedimentary contact exhibiting soft sediment deformation. Rounded and elongated lenses and fragments of silty grey shale within black shale were observed as well as disseminated pyrite (Figure 3.10b). The Prince Albert Formation between the depths of 439.95 m and 443.30 m comprises light grey to grey shale with a near horizontal bedding angle. Black carbonaceous breccia with dense network quartz veining, slickensides, and fold structures were observed at depths of 439.95 m and 442.83 m, and numerous grey-green tuff beds 3 mm to 5 cm thick were observed between 441.45 m and 442.83 m in depth.

The second contact between the overlying Prince Albert Formation and the underlying Whitehill Formation occurs at a depth of 443.30 m (Figure 3.9 and Figure 3.10c) and appears structurally deformed. The contact consists of highly brecciated black shale with abundant cross-cutting quartz veins. Polished shale slickenside fragments were observed in a minor fault zone. Angular fragments of white quartz, up to 1 cm in length, occur within black shale adjacent to the fault in a zone with a dip of 45° relative to the vertical core. Slickensides were identified in massive black shale below the contact at 10 cm intervals.

The Whitehill Formation between the depths of 443.30 m and 481.20 m is predominantly composed of rhythmically bedded black carbonaceous shale with bedding dips varying

between 20° and 55°. Numerous brecciated horizons are present consisting of black carbonaceous shale fragments within abundant quartz veins and slickensides (444.60 m – 447.10 m, 455.12 m – 466.00 m).

The third contact occurs between the depths of 481.20 m and 481.65 m (Figure 3.9 and Figure 3.10d). This interval contains tectonised black shale with numerous quartz veins up to 3 cm thick. The contact interval contains several slickensides that occur within lighter coloured layers. In some instances the slickensides are bounded by a layer up to 2 cm thick of fault breccia. The fault breccia is comprised of angular black fragments, less than 5 mm in diameter, within a white quartz matrix. The slickensides dip at an angle of 40° to the core. The Prince Albert Formation between the depths of 481.20 m and 486.59 m consists of dark grey to black shale with a bedding angle up to 70° with quartz veins, less than 3 mm thick, spaced tens of centimetres apart, throughout.

The fourth contact occurs at 486.59 m (Figure 3.9 and Figure 3.10e). At this depth tectonised massive black shale and slickensides dipping at 40° were observed. Between the depths of 486.24 m to 486.64 m brecciated black shale occurs within a white matrix containing isolated pyrite lenses and veins of quartz. Slickensides were identified within massive black shale. The Whitehill Formation between the depths of 486.59 m and 498.87 m is composed of dark grey to black shale intercalated with numerous quartz veins up to 3 mm thick with a steep bedding angle up to 75°.

The fifth contact occurs at a depth of 498.87 m within highly tectonised shale (Figure 3.9 and Figure 3.10). The shale has a pale grey colour and has experienced a high degree of disintegration. Slickensides were observed at a depth of 499.06 m.

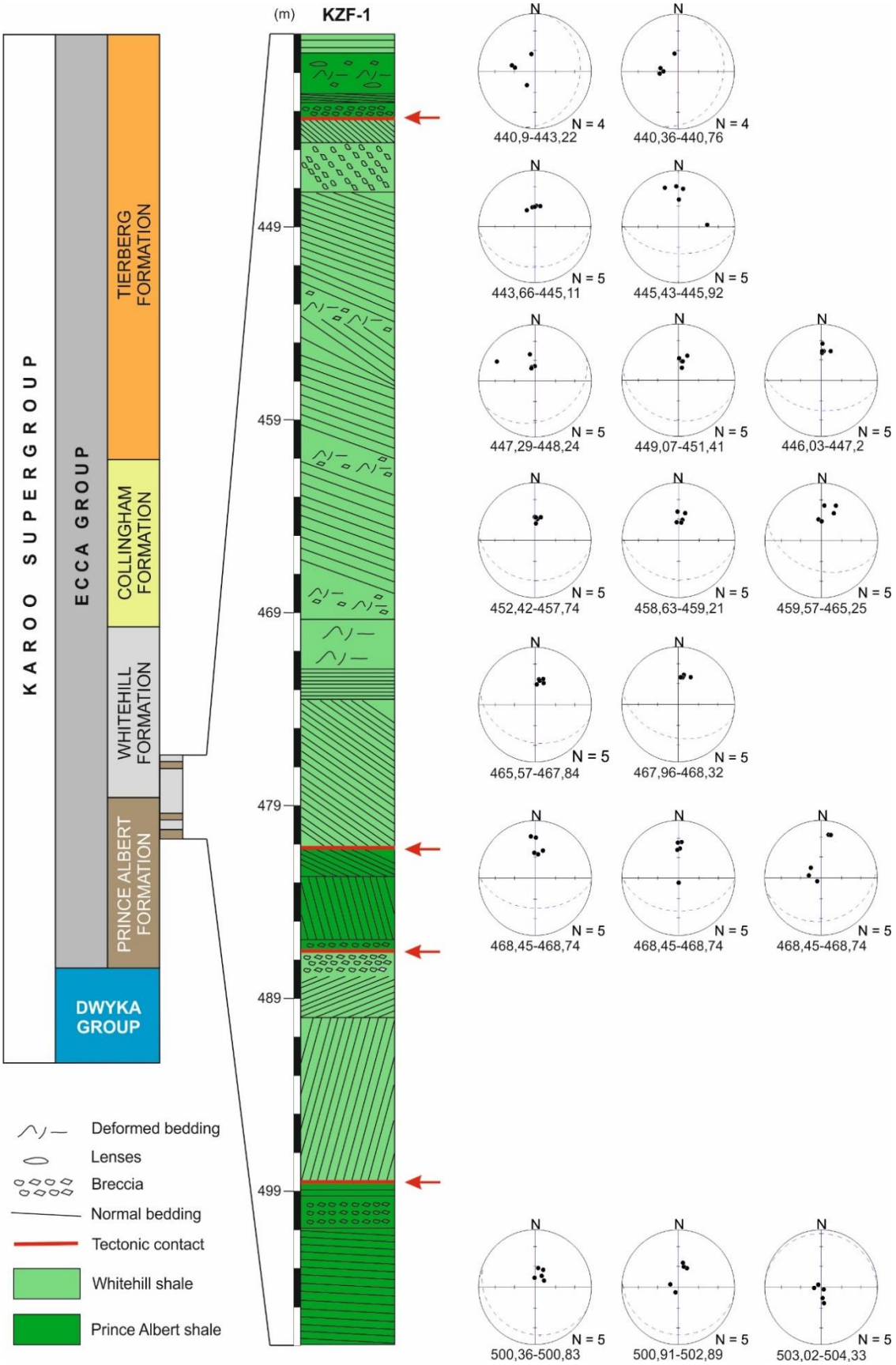

Figure 3.9: Stratigraphic and structural log of borehole KZF-1 between the depths of 439.95 m and 507 m, with corresponding bedding dip on stereonets (Equal Area Schmidt, n = 5). No dip meter data is available between the depths of 468.74 m and 500.36 m due to caving. Abbreviations: Fm. = Formation. Red arrows on this diagram indicate tectonized contacts.

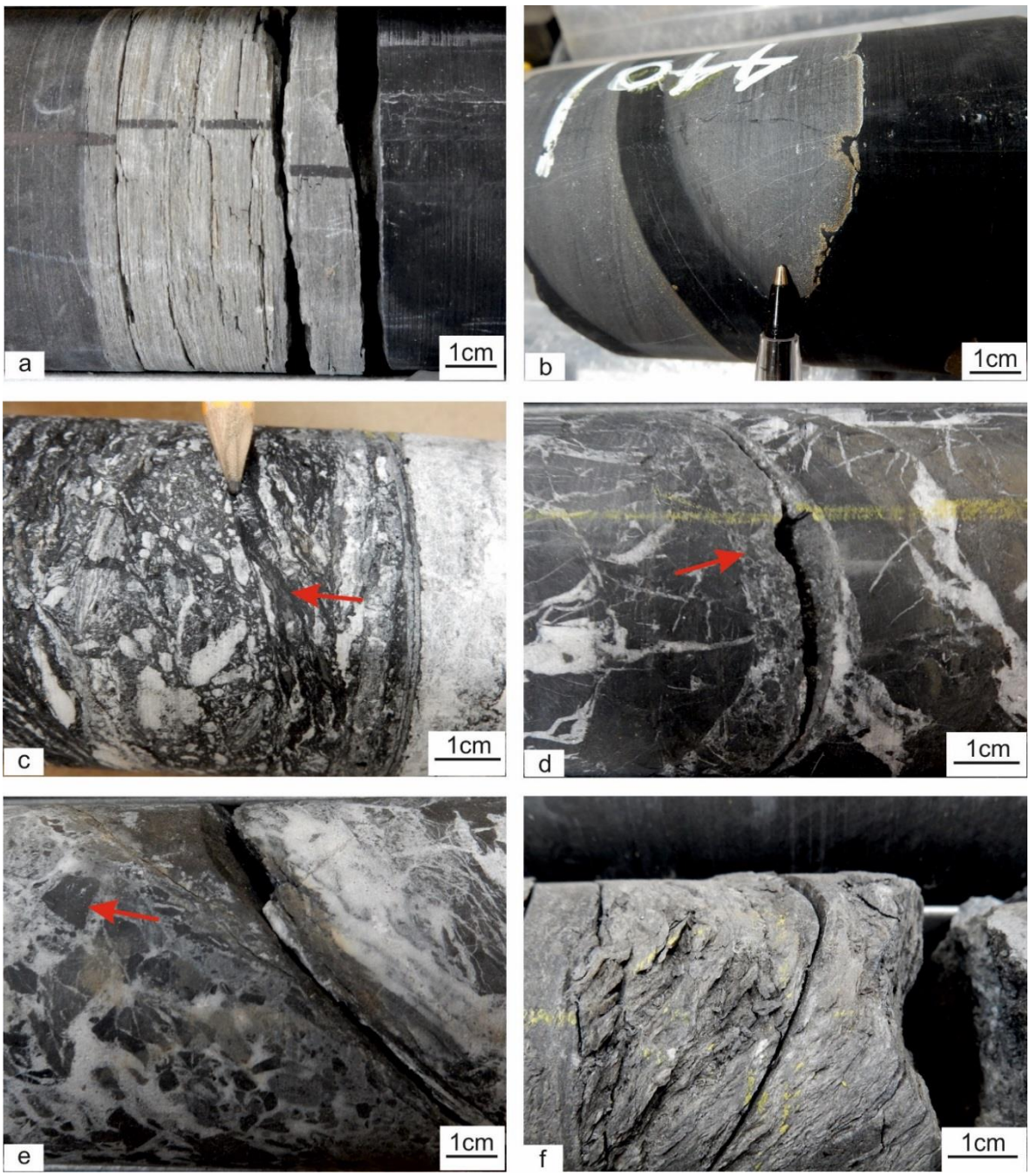

Figure 3.10: Formation contacts within the studied interval (439.95 – 507 m) from borehole KZF-1. **a:** Contact between the Collingham and Whitehill formations at a depth of 420.46 m. **b**: Contact between the Whitehill and Prince Albert formations at a depth of 439.95 m. **c**: Deformed black shale (arrowed) of the Whitehill Formation in contact with the Prince Albert Formation at a depth of 443.3 m. **d**: Fault gauge bounded slickenside (arrowed) at the Whitehill Formation – Prince Albert Formation contact at a depth of 481.50 m. **e**: Black shale breccia (arrowed) adjacent to a steeply dipping slickenside. Contact of the Prince Albert Formation and Whitehill Formation at a depth of 486.29 m. **f**: Tectonized and degraded black shale at the lowermost contact between the Whitehill and Prince Albert formations at a depth of 498.87 m.

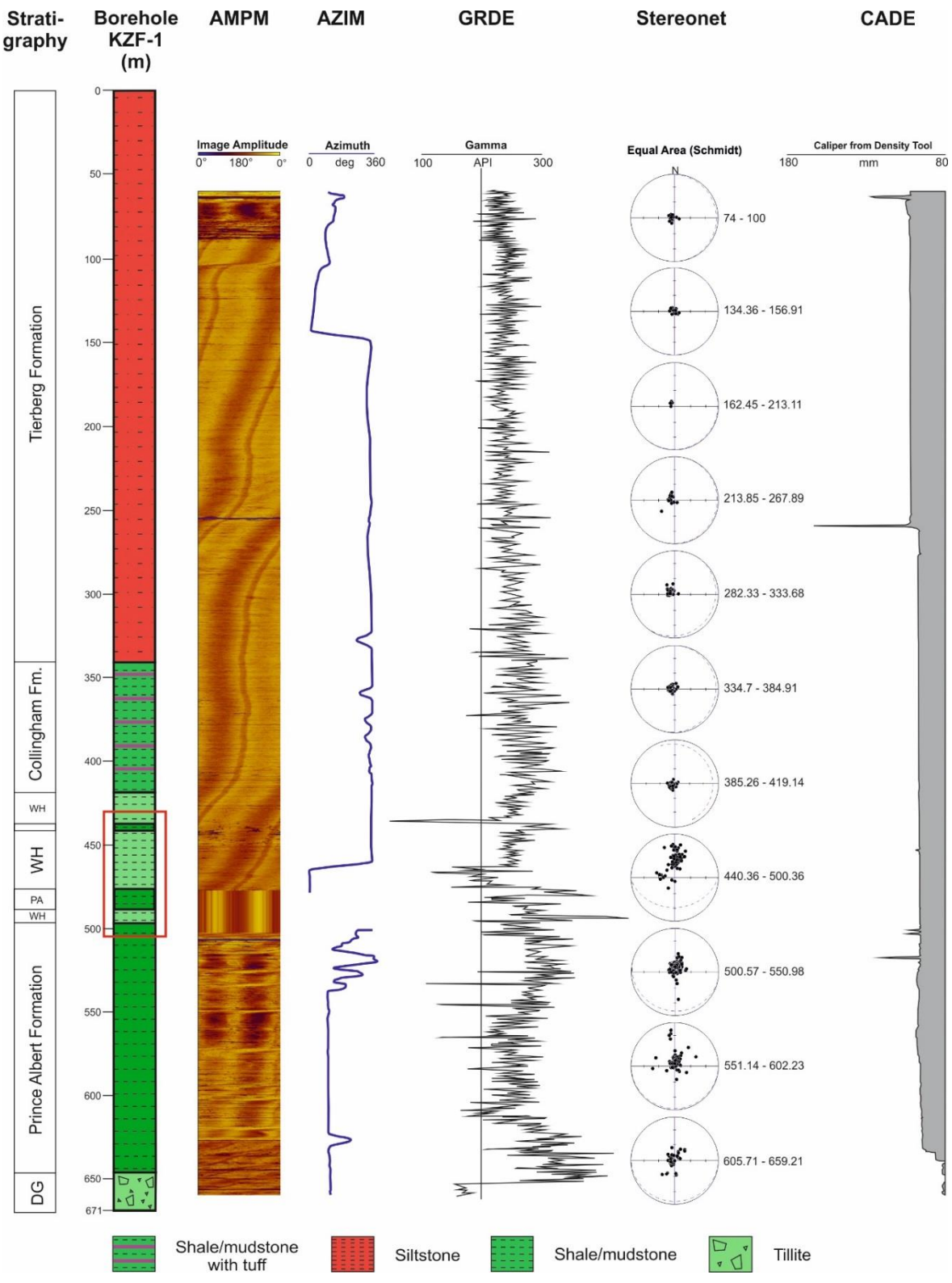

Figure 3.11: Stratigraphic and lithological overview log of borehole KZF-1 with corresponding representative bedding dip on stereonets (Equal Area Schmidt), image amplitude (AMPM), azimuth (AZIM), gamma (GRDE), and caliper from density (CADE). No dip meter, image amplitude or azimuth data was available between the depths of 468.74 m and 500.36 m due to caving. All data represent a 49-point moving average with n = 6500. Gamma ray values over 200 API indicate 'hot shales' (Lüning et al., 2000; 2003; 2005; Loydell et al., 2009). Abbreviations: WH = Whitehill, PA = Prince Albert, DG = Dwyka Group, Fm. = Formation.

3.5.4. Downhole Geophysical Data

I. Methods for the Analysis of Borehole KZF-1

Although the entire borehole was analysed, focus was directed on the most pertinent interval of 58.92 m (439.95 - 498.87 m) because it contains the target formations for shale gas exploration. Immediately after drilling was completed, the borehole was logged by Weatherford Slimline Services using the Dual Spaced Neutron tool, Dual Spaced Density tool, Caliper, and Formation Dipmeter. The sondes were recorded simultaneously in main and repeat runs. A program called WellCAD Reader (reader only), provided by Weatherford, was used to view a combination log of all the data provided by the company. Descriptions of tools used (below) was provided by Weatherford (2011).

A total of 773 measurements were made with a Formation Dipmeter tool, which provides azimuth and dip angle data from the borehole wall with resolution of up to four measurements per metre (weatherford, 2011). 73 measurements were recorded within the studied interval (439.95 m – 498.87 m); however, no data were recorded from borehole sections that experienced caving (stratigraphic interval between 419.14 m – 440.36 m and 470.11 m – 500.36 m; Figure 3.9). Dipmeter data were analysed using SpheriStat™ structural software. Bedding dip recorded, on stereonets, was compared to the lithological log as well as the other geophysical logs, in order to identify trends and to see if bedding remained tilted away from identified zones of structural deformation.

The Dual Spaced Neutron tool (NN2) measures the natural-gamma radioactivity of the formation surrounding the borehole (Weatherford, 2011). The most significant naturally-occurring sources of gamma radiation are potassium-40 and daughter products of uranium and thorium decay series (Serra, 1984). Gamma emissions can commonly be correlated with rock type or with fracture infilling. Potassium^{40} is abundant in some feldspar and mica, and

uranium and thorium can be concentrated by geochemical processes (Cochran et al., 1986). The count rate of the neutron detector is inversely related to the hydrogen content of the rocks surrounding the borehole, and is primarily a measure of the amount of water and hydrocarbons in the rocks (Weatherford, 2011). Gamma trends are recorded in American Petroleum Institute (API) units. PAST statistical software (Hammer et al., 2001) was used to smooth the gamma ray data to a 49 point moving average as well as to graphically display the data versus depth. The resolution of the unfiltered gamma ray data was very high (one measurement every centimetre) and resulted in a chaotic graphical log of the data so progressive smoothing factors (up to a 49 point moving average) were used until an acceptable amount of 'noise' had been removed. Gamma ray data is compared to bedding dip as well as lithological data in order to ascertain if lithology (shale versus tuff) or structural deformation had any control.

The Dual Spaced Density tool (NN6) consists of a gamma ray source and two detectors (Weatherford, 2011). Gamma rays emitted by the source are scattered by the enclosing rock wall and absorbed as a direct function of the electron density of the rock unit (ibid.). The Compton-scattered gamma radiation that is measured at the gamma ray detector on the sonde is inversely related to the electron density of the rock (ibid.). 6500 measurements were recorded across the studied interval (439.95 m – 498.87 m) and PAST statistical software was used to smooth (49 point moving average) and to graphically display the data. Resistivity logs measure the bulk resistivity of a rock which is a function of porosity and pore-fluid (Emery and Myers, 1996).

Porosity data was compared to density and gamma ray data, as well as the lithological log, in order to identify zones of anomalous data readings such as areas of structural deformation (Figure 3.12). Observations were made graphically by plotting the data as curves (gamma ray, porosity, density) alongside lithological and structural logs, and visually deducing the

relationships between all the components based on the reaction of the curves. These relationships were then tested statistically in X-Y plots (Figure 3.13) with an R^2 value of 1 indicating a linear relationship.

II. Results

Data recorded in the first 55 m of the borehole were excluded because rocks across this section are extremely weathered and difficult to identify (Figure 3.9). Throughout the borehole gamma ray values tend to increase with depth with an average above 200 API (Figure 3.11). Above the study interval (55 m – 439.95 m) gamma ray data is relatively consistent, with no large positive or negative deviations, whilst image amplitude and stereonet data show a relatively horizontal and undeformed rock succession. Two zones (60 m; 250 m) experienced washout as illustrated by the caliper from density tool data.

Below the study interval (498.87 m – 671 m) scattered dip and dip direction data as well as irregular image amplitude data were recorded with large erratic positive and negative deviations observed within the gamma ray values.

Dip and dip direction data recorded across the study interval (439.95 m – 498.87 m) (Figure 3.9) show a general south dipping trend with density and porosity being consistent throughout (Figure 3.12) with only minor deviations observed. Combined gamma ray signals were recorded within the study interval (Figure 3.12) and have an average API of 234.27. Large negative deviations were observed within the gamma ray data that correspond to horizons of structural deformation within the studied section of the borehole. Positive gamma ray deviations largely correspond to negative density deviations and positive porosity deviations. Two discrete tuff horizons were observed in the Prince Albert Formation at depths of 442.83 m and 499.08 m that match positive deviations of the gamma ray, density and porosity data.

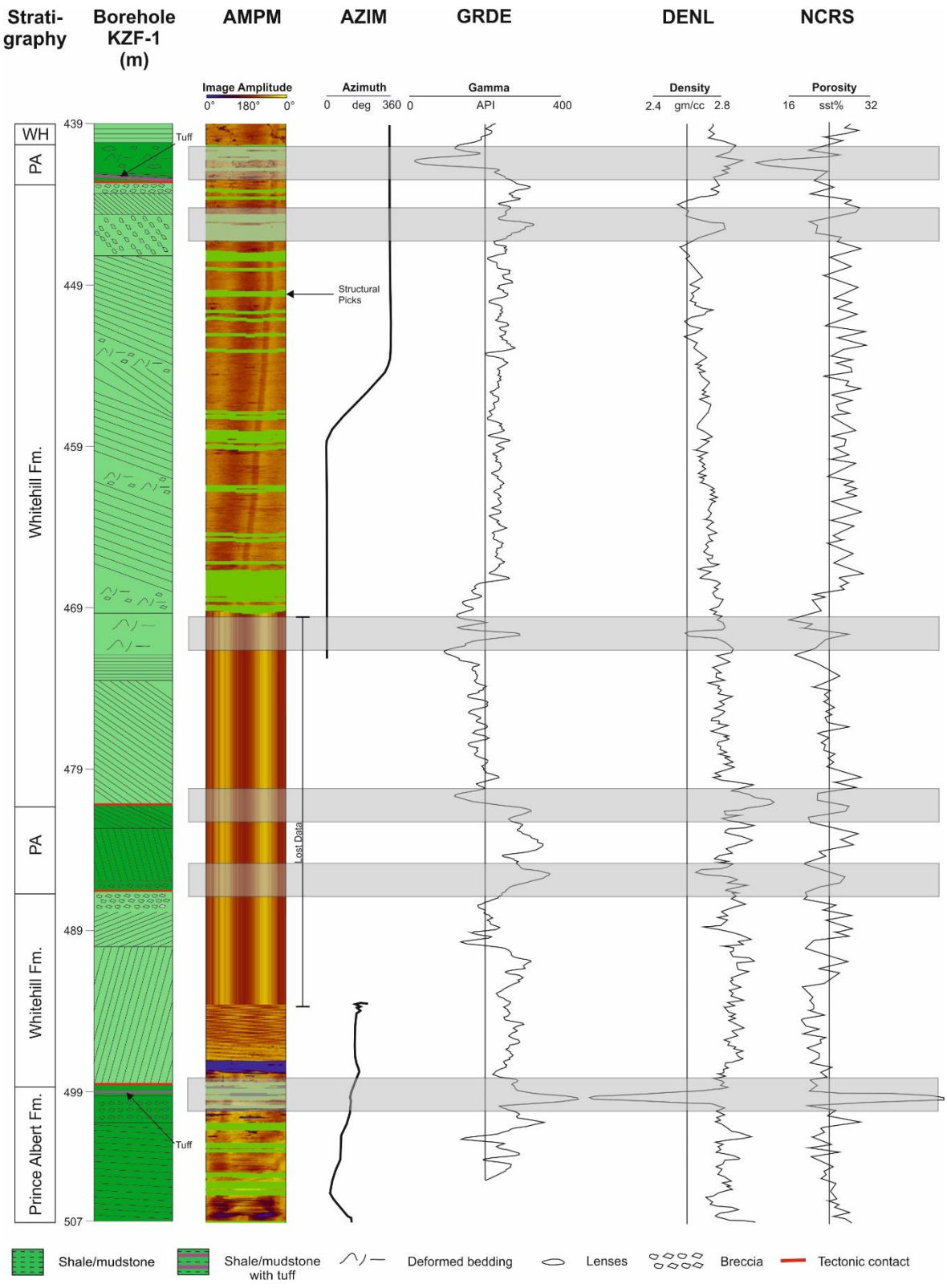

Figure 3.12: Stratigraphic, lithological and structural logs of borehole KZF-1 between the depths of 439 and 507 m with corresponding image amplitude (AMPM), azimuth (AZIM), gamma (GRDE), density (DENL) and porosity (NCRS) data. All data represent a 49-point moving average with n = 6500. Gamma ray values over 200 API indicate 'hot shales' (Lüning et al., 2000; 2003; 2005; Loydell et al., 2009). Grey bars highlight data correlations. Abbreviations: PA = Prince Albert, WH = Whitehill, Fm. = Formation.

III. Data Correlation

A strong correlation between gamma ray, density, porosity and structure is evident throughout the borehole (Figure 3.12 and Figure 3.13). In general, positive deviations in gamma and porosity data match negative deviations in density data. Large deviations in all three data types correlate with structurally deformed horizons in image amplitude and observed structural deformation in the lithological log. Where no image amplitude data was recorded, structural deformation can be inferred due to correlation of deviations across gamma, porosity and density data (Figure 3.12). Two discrete tuff layers within the study interval correlate with large data deviations (Figure 3.12), however the numerous tuff layers within the Collingham and Prince Albert formations (Figure 3.19 and Figure 3.5b, e) exhibit no discernible correlations with geophysical data at current resolution.

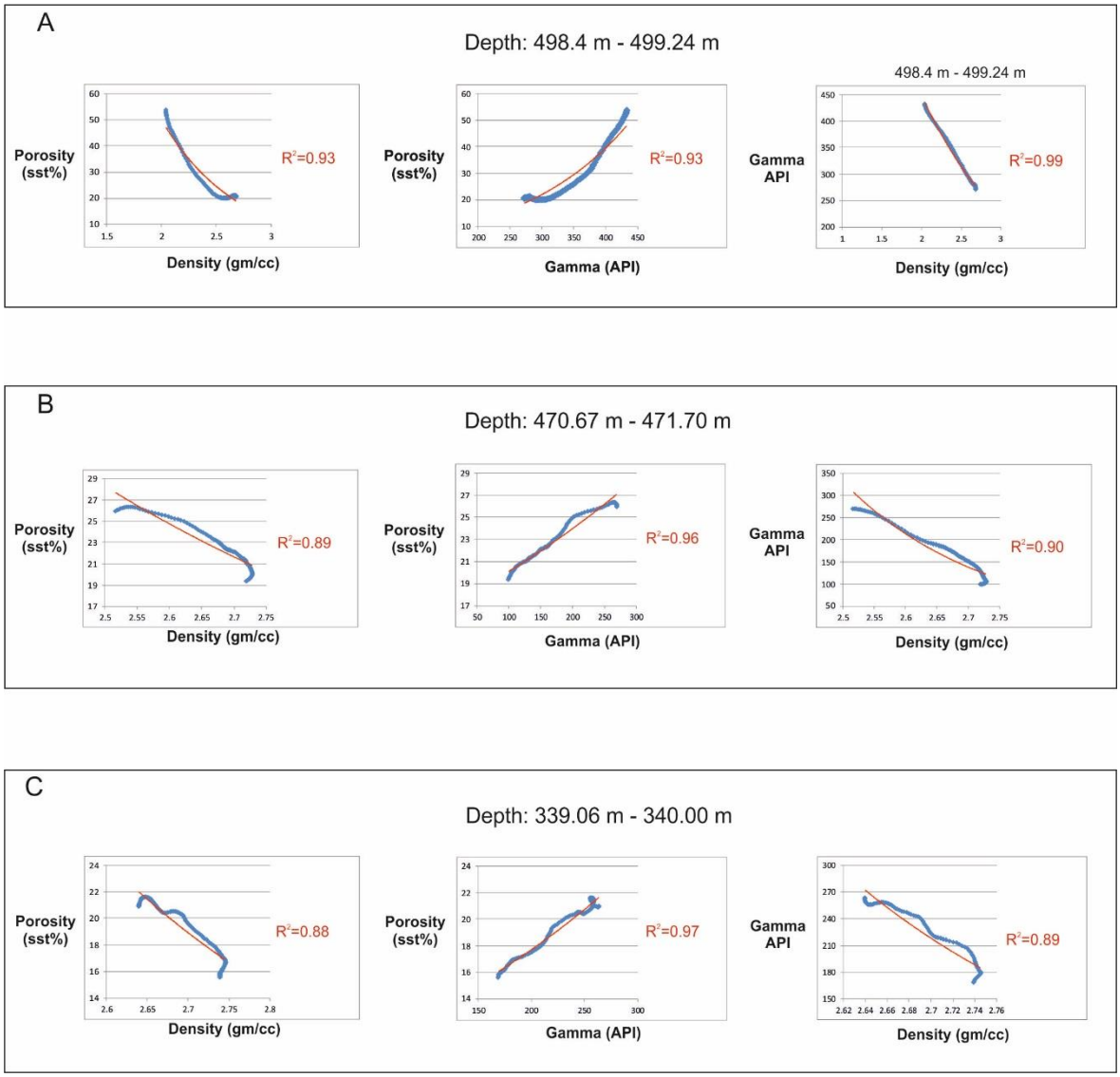

Figure 3.13**:** Porosity *versus* density, porosity *versus* gamma, and gamma *versus* density for selected depths within the study interval (A: 498.4 m – 499.24 m; B: 470.67 m – 471.70 m; C: 339.06 m – 340.00 m). All data represent a 49-point moving average with data recordings every 1 centimetre. R^2 (coefficient of determination) values and regression line (red) close to 1 indicate a linear relationship.

3.6. Discussion

3.6.1. Syn-sedimentary vs. tectonic deformation

The sediments of the Karoo Supergroup were deposited in a 'layer cake' stratigraphy (Catuneanu et al., 1998; Johnson et al., 2006). The principal features that characterise the lower Ecca Group shales (Prince Albert and Whitehill Formations) are: (1) the finely laminated sheet like bed geometries; (2) clay to minor silt grain size of the sediment; (3) the organic-richness of the shale. These characteristics, in conjunction with palynological studies (Ruckwied et al., 2014), support an interpretation of a distal mud- and silt-prone stratified deep marine environment in a low-gradient basin floor setting. In borehole KZF-1, two sections of the older Prince Albert Formation are interleaved with the younger Whitehill Formation, and are bounded by unconformable structurally deformed contacts. The two most likely mechanisms for the development of this abnormal stratigraphy will be discussed, namely, syn-sedimentary deformation and tectonic deformation.

Bedding parallel intervals of chaotic facies are commonly identified and referred to as mass transport deposits (MTDs). These are interpreted to be the products of mass-wasting processes on water-saturated muddy submarine slopes that are prone to failure (Van Der Merwe et al., 2009). Some basin margin successions comprise significant proportions of MTDs. For example, 50% - 60% of the ponded succession of mini-basin's in the Brazos Trinity system in the north-western Gulf of Mexico (Beaubouef et al., 2003), 50% of the deep-water offshore Brunei (McGilvery and Cook, 2003) and 90% of parts of the offshore Nile section (Newton et al., 2004) comprise MTDs.

Two main controlling mechanisms are commonly invoked for the emplacement of mass transport deposits, namely: (1) tectonic activity including earthquakes, basin floor structures, diapiric intrusions (e.g. Coleman and Garrison, 1977; Hampton and Bouma, 1977; Coleman

et al., 1980, 1998), and (2) ‘gravity tectonics’ (shelf and upper slope extensional growth faults and toe of slope compressional thrusts), driven by sediment loading (e.g. Sultan et al., 2004, 2007).

The structural features observed in borehole KZF-1, could be linked to mass wasting of sediment in a low angle basin floor setting triggering slides of more consolidated sediment, along decollement horizons. Critical rheology of the substrate would be needed for this style of deformation to be possible in a low-gradient distal basin floor setting. A similar process has been proposed in other large- and small-scale mass-transport deposits (Schnellmann et al., 2005; Minisini et al., 2007; Dasgupta, 2008).

The observed steep bedding angles in the core could have been caused by block rotation, or slump folding, with semi-consolidated detached fragments causing the breccia along the unconformable contacts. Several generations of mass transport deposits would account for the observed stratigraphy in borehole KZF-1.

Borehole KZF-1 lies proximal to the Cape Fold Belt and it is plausible that orogeny-driven earthquakes or uplift, resulting in increased sediment supply, could trigger mass wasting in the nearby basin margin. However, petrographic and geochemical studies of the SW Karoo turbidites (Johnson, 1991; Andersson et al., 2004; Van Lente, 2004) and tectonic models/structural reconstructions of the Cape Fold Belt (King, 2005), suggest that the fold belt was not emergent at the time of deep-water deposition. Estimated sedimentation rates for the condensed Whitehill and Prince Albert shales of 7 million years oppose a drastic increase in sediment supply (Van Der Merwe et al., 2009).

The majority of documented offshore studies indicate that major mass failure events are important in the initiation of deep water sedimentation (Norem et al., 1990; Masson et al., 1998; Gee et al., 1999, 2001, 2006; Frey-Martinez et al., 2005; Moscardelli et al., 2006;

Moscardelli & Wood, 2008). Conversely, an abrupt change in sedimentation rate is documented only at the upper boundary of the Collingham Formation (Van Der Merwe et al., 2009), suggesting that Whitehill and Prince Albert shale deposition was not coeval with Cape Orogeny and a corresponding increase in sedimentation.

Van Der Merwe et al. (2009) documented 10 m – 70 metre thick intervals of deformed strata within undeformed sediments of the Vischkuil Formation (Tierberg Fm. equivalent), interpreted as synsedimentary mass movement deposits. The deformed intervals within undeformed sediments comprised: (1) a lower division of tight down-flow verging folds dissected by thrust planes that sole out onto a highly sheared décollement surface that are interpreted as slides; (2) the lower divisions are overlain by an upper division of chaotic lithofacies with large contorted clasts of sandstone supported by a fine-grained matrix interpreted as a debrite. Apart from the difference in depositional setting, a contrast can be made with the features observed in borehole KZF-1 for the purpose of constraining deformation.

In contrast, brecciated intervals up to 10 cm thick, were documented bounding fault planes within borehole KZF-1. The angular mudstone-clast supported breccia does not compare closely to the debrites observed by that of Van Der Merwe et al., (2009) higher up in the stratigraphy. Adjacent to the brecciated zones, bedding remains intact, although commonly tilted, and no chaotic bedding, folding or dewatering structures were documented.

The undeformed, faint to well-defined, laminated bedding and lack of mass wasting related structures between the majority of fault planes, suggest that the sediment was lithified prior to deformation. The less than one metre thick fold structures, observed at depths of 439.95 and 442.83 metres (Figure 3.9), may represent evidence for small scale syn-depositional deformation, such as slumping, prior to lithification. However, the breccia bound fault planes

and undeformed thrust packages suggest an overall tectonic origin for the observed stratigraphic repetition in the core, as documented by Lindeque et al., (2011) with regional seismic showing that that the lower Ecca Group of the Karoo Supergroup is disrupted by low-angle thrust faults rooted in a zone of local décollements (Figure 2.5).

The features observed in borehole KZF-1 are likely to be effects from the north-verging southern limb of the Cape Fold Belt, caused by subduction along the southern margin of Gondwana (de Wit and Ransome, 1992). The kinematics of the faults in the core are directly comparable to that of the Cape Fold Belt. Movement on the thrusts in the Cape Fold Belt is predominantly towards the north (Booth and Shone, 2002), and primarily south-dipping fault planes are documented within the study interval of the core (Figure 3.9).

Figure 3.14 depicts a simplified model for the proposed development of the features observed. Low angle, south-dipping, north-verging stacked thrusts, caused the duplication of stratigraphic formations by emplacing the older Prince Albert Formation over the younger Whitehill Formation. Steeper angle thrusts propagating along weak rheological contacts, between the organic-rich Whitehill Formation and the relatively organic-poor Prince Albert Formation (organic-rich décollement zones), result in tectonic contacts between the younger overlying Whitehill Formation and the underlying older Prince Albert Formation as observed in the core.

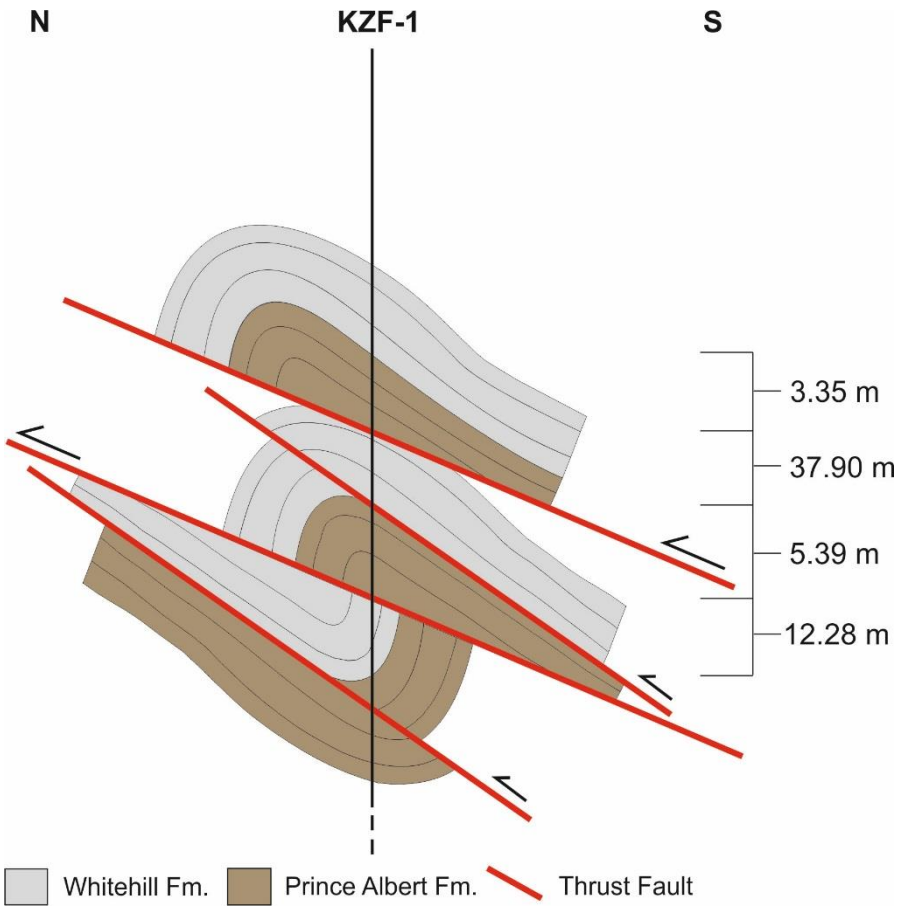

Figure 3.14**:** A model of stacked thrusts and reverse faults that accounts for the tectonic features observed in borehole KZF-1. Thicknesses of individual thrusts is indicated in metres. Horizontal scale is unknown.

Individual bedding planes may have acted as décollement surfaces resulting in higher angle thrusts (Figure 3.14). Fagereng and Byrnes (2015) observed bedding parallel faulting along weak planes, with a range of slip (reverse) increments in chevron folds of the Prince Albert Formation in outcrops. In borehole KZF-1, changes in bedding angles, of up to 75° on a metre scale, within the footwall syncline could be the result of block rotation between the thrusts.

The numerous slickensides, observed throughout the core at closely spaced regular intervals support the interpretation that bedding planes were acting as décollement surfaces in folded

strata. However, no slickensteps were observed to constrain the direction of movement, possibly due to the softness of the lithology.

Alternatively, a moderately south dipping hanging wall anticline with a steeper north dipping or subvertical limb, would result in north verging folds. However, a steep or subvertical hanging wall anticline would not account for the moderate to horizontal dip of the lower Prince Albert Formation (Figure 3.14).

Cross-cutting quartz veins, 1 mm – 5 mm thick, orientated 45° - 90° to the fault plane were documented (Figure 3.10d). These veins may represent quartz filled tension gashes that have propagated perpendicular to the fault plane. Larger, 5 mm – 10 mm thick, irregularly-shaped fractures within the fault breccia have also been filled by quartz (Figure 3.10d). Silica-rich fluid could have migrated along fault planes and brecciated horizons in order to cement the fault breccia as observed in the core.

Figure 3.10c depicts angular quartz clasts within a black shale matrix, which is in contrast to the angular shale clasts within a white quartz matrix from adjacent to other fault planes (Figure 3.10d, e). Reactivation of the fault plane may have led to deformation of the original quartz-cemented shale breccia. The quartz being more competent than the shale, formed angular clasts while the less competent shale clasts and shale wall rock were smeared and formed the matrix. Reactivation of fault planes would be possible with multi-phase orogeny, as proposed by Hansma et al. (2016) and Hälbich (1983).

Fluid migration along fault planes may also have led to the removal of organic matter from the shale adjacent to the contact at a depth of 498.87 m (Figure 3.10f). Based on the presence of tensile veins, in mutually cross-cutting relationship with bedding-parallel slickenfibre-coated veins, Fagereng and Byrnes (2015) deduced that local fluid pressure was in excess of the least compressive stress in the Prince Albert Formation.

Evidence from the core shows that deformation propagated within the black shales only. High levels of organic content in the rock, up to 6 % TOC in the Whitehill Formation in borehole KZF-1 (Campbell et al., 2016c), caused decreased yield strength in comparison to the siltstones and organic-poor shales. Kerogen is a softer material than most other rock constituents; therefore an increase in TOC in the rock corresponds to a decrease in yield strength/Youngs modulus (Aoudia et al., 2010; Kumar et al., 2012; Bocangel et al., 2013). The build-up of strain by orogenic events along the southern margin of Gondwana (post-deposition and lithification) led to brittle failure within the layers of least competence (high organic content). Borehole KZF-1 is located approximately 200 km West of the seismic profile published by Lindeque et al., (2011) and confirms the proposed interpretation of the geotectonic framework in much higher resolution. Thrusting rooted in organic-rich décollements is visible on a metre scale in the borehole, with relatively undisturbed formations documented below.

Similar décollement zones based on rheological contrasts in shale horizons have been observed by Bosworth (1984) in duplex structures in the Appalachian Plateau, and by Stevens and Stone (2005) in the Last Chance thrust of the Death Valley region. Evans (1994) observed that the Middle Devonian shale section was a regional décollement zone in the central Appalachian Plateau province during the Alleghanian Orogeny. It is defined by abundant joints, veins, and slickensided fractures localized within multiple zones of organic-rich brown and black shale. These zones are distributed over tens to hundreds of metres of the Appalachian Middle Devonian shale section.

3.6.2. Effects on Shale Gas Potential

The Whitehill Formation is currently the target for shale gas exploration in the southern portion of the Main Karoo Basin and is estimated to hold 32 trillion to 485 trillion cubic feet

(Tcf) of gas (Decker and Marot, 2012). The Energy Information Administration (2013) report highlights that the northern extent of the gas-bearing shale is limited by the effect of dolerite intrusions. In the present study, it is demonstrated that the southern extent is limited by the structural architecture of the proximal Cape Fold Belt and its tectonic effects on the southern margin of the Karoo foreland basin.

Production from self-sourced reservoirs relies on natural and induced fracturing for permeability and transfer of hydrocarbons. Natural or induced fracturing is often a key to success in unconventional reservoir plays. On the other hand, fractures may compromise seals and large or well-connected fractures or faults may cause undesirable complications for unconventional reservoirs (Ferrill et al., 2014).

The effects of tectonic deformation on the shale gas potential are numerous: (1) the first major effect is that this type of faulting has resulted in compartmentalisation of the reservoir. In unconventional reservoirs stratigraphic and mixed-mode (combined stratigraphic and structural), compartmentalisation can segregate the reservoir by introducing low TOC lithologies (e.g. Prince Albert Formation) into the prospective shale gas reservoir (e.g. Whitehill Formation). Shales with high thermal exposure to the low-Greenschist metamorphism of the Cape Fold Belt (Frimmel et al., 2001) from further south in the basin could also have been thrust into the reservoir, thus 'diluting' the shale gas potential by compartmentalising the organic-rich shale. The Prince Albert Formation between the depths of 439.95 m and 443.30 m exhibits lower gamma ray values compared to the same formation between the depth of 481.20 m and 486.59 m (Figure 1.10). Compartmentalisation on such a small scale (<30 m thick Whitehill Formation) is challenging from a drilling point of view with formation thicknesses below seismic resolution. Each compartment may have its own pressure and fluid characteristics hampering field development (Cerveny et al., 2005).

(2) The second major effect on shale gas potential is the development of fracture systems associated with the fault planes. Open or mineral-filled faults and fractures have contrasting porosity and permeability, with respect to the host rock layers, and will potentially dilate, slip, and propagate, and may compartmentalize fluid pressure increase during induced hydraulic fracturing. Pre-existing structure can influence localization of damage in response to fluid injection (Smart et al., 2014; Ferrill et al., 2014).

Gas in place may escape along large fracture systems, and organic matter within the target formations may be remobilised by migrating fluids utilising fault planes. In this case, low gas contents of the shales proximal to the fault planes are expected. Indeed, desorbed and residual gas measurements from Whitehill shales from borehole KZF-1 show very low values (de Kock et al., 2016): Desorbed gas ranged from 0 to 0.047 $ml/g^{-1}/day^{-1}$, residual gas content ranged from 0.17 to 0.56 m^3/t^{-1} at standard temperature and pressure (STP).

However, the effect of the fracture system on the hydrocarbon potential of the reservoir depends to a large extent on the degree of fracture infill. Unfilled natural fractures can provide enhanced permeability or storage capacity for the reservoir as well as improving efficiency of stimulation (Gale et al., 2007). Figure 3.10d illustrates that the fractures, proximal to the fault planes, have been filled-in reducing the effectiveness of the fracture systems with regards to porosity increases. Precipitation of minerals along fault planes might also limit the potential of the fault to act as a fluid pathway and the cementation of the fault breccia is evidence for this. Fluid flow events, however, have not been constrained. It could be possible that several fluid flow events could have taken place, leading to the loss of gas before mineral precipitation took place. The multiphase Cape Orogeny (Hälbich, 1983), as well as the break-up of Gondwana (Watkeys, 2006), could have reactivated faults or initiated fluid flow within the fault network, allowing for the escape of gas. Some deformation zones appear porous and others not (Figure 3.12). The degree of fracture and breccia cementation

by quartz (Figure 3.10e versus 3.10f) may impact the level of fracture porosity, with well cemented horizons remaining less permeable.

3.6.3. Structural Controls

An average combined gamma ray signal of 234.27 API indicates the high organic matter content of the Whitehill Formation. Shales with an API above 200 are conventionally classified as 'hot shales' due to elevated uranium content (Lüning et al., 2000; 2003; 2005; Loydell et al., 2009). Hot shales are of highest economic importance as they form the source rock for most of the Palaeozoic sourced hydrocarbons (e.g., Lüning et al., 2000; 2005) and Mesozoic hydrocarbons (e.g., Ineson et al., 2001).

The correlation between gamma ray, density and porosity curves relate to the presence of low-density, low-velocity organic matter or kerogen (Fertl and Chillingar, 1988; Passey et al., 1990). A high abundance of organic matter in the rock will result in positive gamma ray and porosity excursions along with a negative density excursion.

The gamma ray excursions appear structurally controlled with all large positive and negative excursions corresponding with sections of the core containing tectonic breccias, faults, or slickensides. Gamma ray data records the combined emissions of ^{40}K, ^{232}Th and ^{238}U with thorium being the most immobile of the three (Adams and Weaver, 1958; Tribovillard et al., 2006; Rider and Kennedy, 2011; Pi et al., 2013). Uranium preserved in sedimentary basins derives from two fundamentally different sources; (1) detrital uranium bearing minerals (e.g. zircon) that have been extracted from rocks exposed to weathering and erosion in the hinterland and; (2) authigenic uranium, resulting from redox driven precipitation of uranium out of solution from the water column. Within oxygen deficient environments, uranium will be incorporated into the sediment via the reduction-induced precipitation of authigenic uranium containing phases (Parkinson, 1996). Therefore, uranium can appear in relative high

concentrations (Lüning et al., 2000) of up to approximately 200 ppm (Fisher and Wignall, 2001) within marine organic-rich black shales. In contrast, black shales deposited in lacustrine systems, more often than not exhibit no relation between uranium and TOC (Bohacs and Miskell-Gerhardt, 1998; Bohacs, 1998; Passey et al., 2010). Potassium is considered to represent the detrital fraction in shales (Wei et al., 2003), originating from the weathering and breakdown of feldspars.

Therefore, the positive and negative excursions in the gamma ray signal recorded in borehole KZF-1, within structurally deformed black shales, may point towards the remobilisation of uranium/potassium or both, along with organic matter by migrating fluids, such as the warm sulphurous artesian water encountered. Low-density values and high porosity values correspond with the high gamma ray values (Figure 3.12). These trends corroborate the hypothesis that structural-deformation-induced increases in porosity, before breccia cementation, allowed for the precipitation of remobilised uranium/potassium and organic matter. The low values of residual and desorbed gas also indicate escape of gas or remobilisation along structurally controlled fracture systems.

3.7. Conclusions

Due to the proximity of the study location to the syntaxis of the Cape Fold Belt, it can be concluded that the repetition of stratigraphic formations observed in borehole KZF-1 is most likely due to low angle thrusting and flexural slip-related reverse faults propagating through organic-rich shale décollement zones of the Whitehill Formation. Brittle deformation along fault planes, as well as limited soft sediment deformation, suggests tectonic rather than syn-sedimentary deformation. The kinematics of the north-verging, south-dipping thrusts, from borehole KZF-1, are fitting with the regional tectonic model proposed in Figure 2.5. Southerly dipping thrust faults fit with the regional tectonic regime caused by the north-

verging, southern limb of the Cape Fold Belt, related to the larger scale deformation along the southern margin of Gondwana during the Triassic, and reiterates the overall geotectonic model of the Karoo foreland basin formation (Johnson, 1991; Cole et al, 1992; Catuneanu et al., 1998; Catuneanu et al., 2002; Johnson et al., 2006; Lindeque et al., 2011; Tankard et al., 2009, 2012).

Stratigraphic and structural compartmentalisation may dilute the target formation and allow the escape of gas along fault planes, as well as the influx of fluids detrimental to the preservation of organic matter, as proven by negligible gas desorption results and low gamma ray emissions within structurally deformed horizons. Pervasive fracture infill may inhibit the ability of fractures to propagate through the gas-bearing shale during man-made hydraulic stimulation. Potential reactivation of faults due to large scale stress events may have contributed to gas escape.

The Whitehill Formation along the entire southern margin of the Karoo Basin, proximal to the Cape Fold Belt, may have acted as a décollement zone for Cape Fold Belt tectonics, regionally based on seismic data (Lindeque et al., 2011), and supported by smaller scale observations from borehole KZF-1. Future exploration and resource estimates should take into consideration the likely effects of tectonics on shale gas potential in portions of the southern basin and future studies should address high-resolution structural analyses, including core and outcrop studies.

4. Geothermal Energy from the Main Karoo Basin: A Study of Permian Sandstone Reservoir Formations

This chapter explores the geothermal potential of the Ripon Formation sandstones from the Ecca Pass as well as from Borehole KWV-1, and provides a volumetric calculation for heat in place across the southern Main Karoo Basin.

4.1. Introduction

In the coming decades global environmental issues will significantly affect patterns of energy use around the world (Li et al., 2015). Geothermal energy has undergone an enormous increase in recent years within the global mix of renewable energy exploitation. According to Montague (2016), installed global geothermal generating capacity grew from < 2,000 MWe in 1950 to over 13,000 MWe in 2015. In 2015 the USA was the largest user of geothermal power (3.5 GW) with China the largest user of direct heat (20 Twh) (ibid.). Besides high-enthalpy volcanic settings (e.g., Chambefort and Bignall 2016), deep sedimentary basins are being assessed for their geothermal energy resources with direct heat being the primary output (e.g., Eggeling et al. 2011; Zafar and Cutright, 2014; Horváth et al., 2015; Lenhardt and Götz, 2015; Zhu et al., 2015). Today, South Africa's energy demands still heavily rely on coal (Hancox and Götz, 2014), particularly in the electricity sector**.** In 2012 72% of South Africa's total primary energy consumption came from coal, followed by oil (22%), natural gas (3%), nuclear (3%), and renewables (<1%; primarily from hydropower) (IEA, 2014). For electricity generation, currently ca. 90% comes from coal-fired power stations, 5% from one nuclear power plant, and 5% from hydroelectric plants and one wind station (IEA, 2014). According to BP's (2015) Statistical Review of World Energy, the country has the highest energy consumption in Africa, accounting for 30% of total primary energy consumption on the continent in 2013. With 9.62 tons of CO_2 (last

updated in 2011), South Africa's per capita greenhouse gas emissions are the highest in Africa. South Africa ranks as the 14th largest carbon dioxide emitter on a global scale, with 473.165 million tons of CO_2 (last updated in 2012) from consumption of energy (EIA, 2015). The implementation of renewable energy in South Africa has been stagnant since 2003 and has stayed behind countries such as India, Brazil and Egypt (BP, 2015). Nevertheless, the country plans to expand renewable electricity capacity to 17.8 GW (currently 64 MW from hydroelectric plants and wind energy) by 2030 (IEA, 2014).

To date, geothermal energy has not been addressed or included in any renewable energy scheme in South Africa. The continent's geothermal resources are concentrated in the Red Sea Valley and the East African Rift System. Kenya is the principal exploiter of geothermal energy in Africa producing 45 MWe and some direct heat use. Ethiopia is the only other African country currently producing electricity from geothermal heat. Furthermore, Algeria and Tunisia obtain some direct heat from geothermal sources (GENI, 2015).

A deep sedimentary basin such as the Karoo Basin of South Africa may prove successful in supplying additional energy in the form of heat to the planned renewable energy mix of solar, wind and hydroelectric power (c.f. North China and Yuncheng Basins, Pannonian Basin; See Table 4.1). Of particular interest is the development of the cascade system of utilization (Rubio-Maya et al., 2015) where geothermal heat is utilized in a step-wise system of decreasing temperature (i.e. electricity generation, direct heat, drying and dehydration, balneology etc). Heat is less transportable than electricity so the cascade system for thermal uses only may prove to be the most applicable to Main Karoo Basin where temperature may be marginal for power generation. The Karoo Basin may provide a solution to the problem of renewable energy storage during times of high output of, for instance, solar and wind energy for times of need and low energy output.

The aim of this study is to provide a detailed description of the petro- and thermophysical rock properties of the Permian Ripon Formation from the Ecca Pass road cutting as well as borehole KWV-1 which may provide valuable information for geothermal energy applications. A first estimation of the geothermal reservoir potential will be provided for the central and southern part of the Karoo Basin by quantifying the heat in place. The results of this study may be added as important attributes into 3D reservoir models, identifying further target formations for geothermal reservoir utilization.

4.2. The Hydrological Properties of the Main Karoo Basin

So far, heat flow measurements in South Africa exist for the central part of the Kaapvaal Craton, across the Witwatersrand Basin of the Gauteng region and the surrounding mobile belts (Jones, 1993; 2001; Dhansay et al., 2014). Maximum values from the Karoo Basin range from 70–75 mW/m^2.

Groundwater occurrence and movement in the Karoo Supergroup are governed by a variety of factors, most notably the near-horizontal deposition of alternating sandstones and shales, the historical stress conditions and the abundant dolerite intrusions. The complex geometry of Karoo aquifers is due to distinct bedding-parallel fracturing, microporosity of the rock mass, and the limited storage of small-aperture fractures requiring water storage within the primary porosity (Botha et al., 1998; Botha and Cloot, 2004a, b).

Sandstones of the Ecca Group typically have very low porosities and permeabilities due to poor sorting and overburden pressure from diagenesis. This contributes to aquifers being highly anisotropic due to alignment of the sand grains in the direction of palaeoflow (Rowsell and De Swardt, 1976 in Botha et al., 1998). This was exacerbated by the extrusion of the Drakensberg lavas, resulting in slight metamorphism as overburden pressures and temperatures increased. Following extrusion of the Drakensberg Group, the groundwater

possibly became mineralised resulting in further reduction of porosity and permeability as secondary minerals were deposited in the already limited pore space (Botha et al., 1998).

Weathering and erosion coupled with isostatic uplift and severe fracturing followed deposition of the Karoo Supergroup. Two vertical and one horizontal joint sets are common with more brittle deformation noted in the non-elastic sandstones than that of the more elastic argillaceous sedimentary rocks. Sandstones are therefore intrinsically more fractured, although horizontal fractures are very likely closed at depth due to excessive overburden pressures (Botha et al., 1998).

Horizontal fracturing is localised and small scale resulting in recharge being associated with localised vertical fractures (Botha et al., 2002). Recharge estimates were found on average to be 2% - 5% of mean annual rainfall, decreasing to below 3% where thick soil cover is present and reaching 5% in hilly areas with thin soil cover (Van Tonder and Kirchner, 1990). The prevalence of these bedding-parallel, sub horizontal fractures is partly ascribed to the intrusion of the Karoo dolerites, which likely increased this fracturing. In the instance of ring dyke complexes, fracturing is believed to develop away from the intrusion, resulting in higher-yielding boreholes away from the intrusion and not distinctly associated with it (Botha et al., 1998).

Heterogeneity and anisotropy in Karoo aquifers are typically with highly variable hydraulic properties, both spatially and with depth. Intrusions are believed to have mechanically deformed the Karoo rocks through processes of bending and dilation with commonly occurring chilled edges. The thickness of these dykes determine the extent of mechanical deformation and melting. They vary in thickness between 2 m – 10 m with thicknesses up to 300 m recorded in the Eastern Karoo. Transgressive fracturing extending some distance away from dykes and dyke-sill intersections are often water-bearing (Botha et al., 1998;

Chevallier et al 2001, Botha et al., 2002). Flow is subsequently not solely horizontal and radial, but relies on linear vertical water movement through the rock matrix into horizontal fractures (Botha et al., 1998).

Information is not readily available regarding the deep Karoo aquifer systems. Some reasons for knowledge gaps are noted by Murray et al. (2006), incorporating; (1) the lack of recording of borehole information such as water strikes, depths and lithologies following drilling; (2) borehole siting for the sake of convenience rather than based on large-scale water supply; and (3) a number of socio-economic constraints such as protection of groundwater, the environment and the like.

A number of hot springs are found in South Africa with varying surface water temperatures ranging from 28°C – 64°C (Western Cape Province), <29°C – 67°C (Limpopo Province), 28°C – 52°C (Kwazulu-Natal Province), and 26°C – 37°C in the Eastern Cape Province (Steyl et al., 2012).

4.3. Geothermal Energy

Geothermal energy (from the Greek geo, meaning earth, and thermos, meaning heat) is energy made by heat inside the Earth's crust (Holt et al., 2001). According to Huenges (2010) geothermal reservoirs are heated and pressurised water and/or vapour accumulations from which heat can be extracted from the underground to the surface. The efficiency of a potential geothermal reservoir depends on temperature, depth, size, fluid flow and the process of heat extraction (ibid.).

According to Huenges (2010), heat is transferred within the crust through two mechanisms:

1. Conduction. Heat moves through a material from a hotter to a cooler zone. The efficiency of the heat transmission is as a direct result of the thermal properties of

the minerals constituting the rock. Highly conductive rocks include fractured granites, while mafic rocks are considered potential thermal insulators.

2. Convection. Convection results in anisotropic diffusion of heat; the permeability of a rock (i.e. fractures) govern the movement of hot material.

Analysing the past and current geological environment will assist in the determination of favourable and unfavourable sites with high geothermal gradients and potential geothermal reservoirs (Huenges, 2010). The general tectonic settings favourable for geothermal activity are well documented, however the detailed lithologic and structural controls on individual systems are generally not well constrained (ibid.).

4.3.1. Porosity and Permeability

According to Huenges (2010), the identification of geological units and structures that host hydrothermal fluids is fundamental in geothermal exploration. These potential reservoirs can be governed by either pore space (high porosity) or fractures (high fracture density) (ibid.).

The permeability of the continental crust is defined as the capacity of the rock to transmit fluid. Permeability is a critical geological parameter for the characterisation of the potential geothermal reservoir as it plays a primary role in heat and mass transfer (Manning and Ingebritsen, 1999).

Permeability is related to two basic properties of the rock:

1. The porosity is the ratio of pore volume to the total volume. Permeability is the measure of the fluid flow through the pore network of the rock and is directly associated with the porosity. Porosity, and therefore, permeability are linked to the arrangement of the minerals within the rocks, which is a function of the nature, size, and sorting of the minerals, and of the compaction and diagenetic history. Examples

of rocks that are generally porous and can store large amounts of fluids within their pore networks include limestones, sandstones and conglomerates. These sedimentary rocks are natural reservoirs in the crust for a variety of fluids. Permeability is the primary parameter controlling fluid flow and it can vary from 10^{-23} m^2 in intact crystalline rocks to 10^{-7} m^2 in detrital porous sediments; meaning 16 orders of magnitude variations (Manning and Ingebritsen, 1999).

2. The permeability created by fractures is linked to the discontinuities that are present within the rock along which fluid circulation is possible. Fracture permeability is generally well developed in crystalline massifs, leading to the rock being considered permeable even though granite is a non-permeable rock. Such permeability should be well developed near large fracture systems, whether active or dormant. Due of the discontinuous character of fractures and their geometrical complexity, the intrinsic permeability of such systems is more difficult to evaluate compared to stratified permeable layers (Huenges, 2010).

4.3.2. Thermophysical Rock Properties

Heat capacity, thermal diffusivity and thermal conductivity are connected through the Debye-Equation (1):

$$\rho_{r=\frac{\lambda}{c_r * \alpha}} \qquad (1)$$

Where ρ_r is the density of the reservoir rock (kg/m^3), c_r is specific heat capacity of the reservoir rock [$W \cdot s\ (kg \cdot K)^{-1}$]; λ, thermal conductivity [$W\ (m \cdot K)^{-1}$]; α, thermal diffusivity (temperature conductivity) ($m^2\ s^{-1}$).

This approach indicates that thermophysical rock properties are density controlled. Density itself is strongly dependent on the facies of sedimentary rocks (carbonates, siliciclastics, as well as volcaniclastics) (Sass and Götz, 2012).

4.3.3. Thermofacies Concept

A strong correlation between facies, representing depositional conditions, and thermophysical rock properties was proposed by Sass and Götz (2012). Provided the dependency of facies and thermophysical properties are correct, geothermal reservoir types can be correlated with facies types as shown below (Figure 4.1). Fine-grained pelagic claystones show the lowest values of permeability and thermal conductivity in comparison with sedimentary rocks of other depositional settings. Coastal and terrestrial sandstones and conglomerates represent deposits with the highest permeability and thermal conductivity because they show the highest effective porosity (high permeability) and high quartz contents (high thermal conductivity).

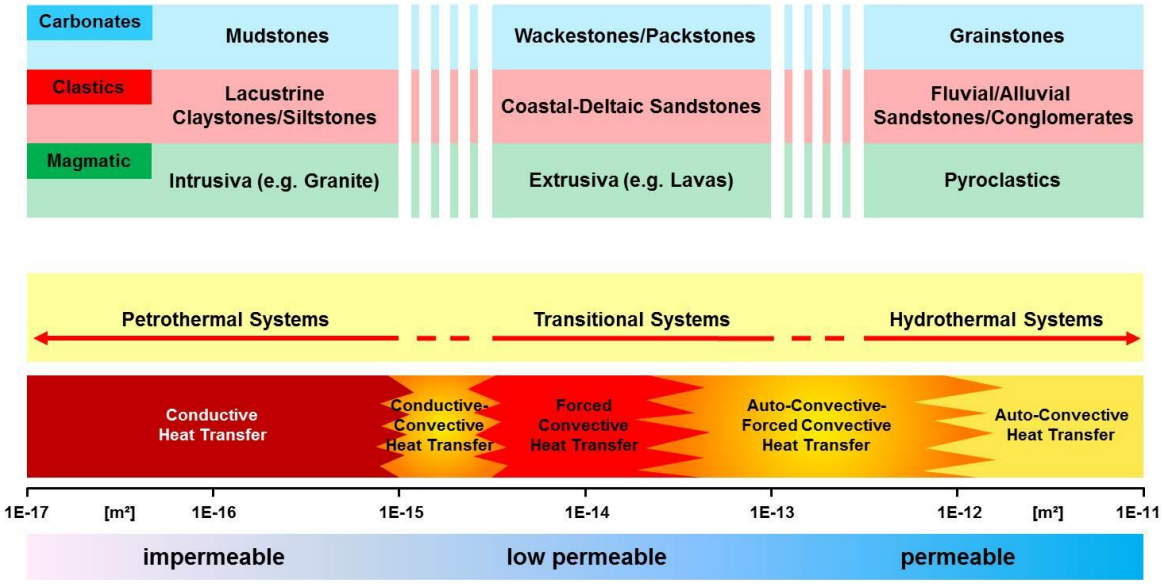

Figure 4.1: Thermophysical properties of sedimentary reservoir rocks based on examples from Palaeozoic, Mesozoic and Cenozoic series of Central Europe with correlation to a general geothermal system characterisation depending on the major heat transfer mechanism (convective vs. conductive); from Sass and Götz (2012).

In addition, silica cements lead to the highest thermal conductivity values within this group (Sass and Götz, 2012).

The application of a thermofacies approach takes place in early exploration stages when detailed reservoir information on porosity, fluid properties, secondary porosity, stress field and tectonisation etc. is not available.

4.3.4. High and Low Enthalpy Systems

The geological settings for geothermal reservoirs can vary widely. According to Huenges (2010) high enthalpy systems typically occur in magmatic, extensional or trans-tensional settings. Magmatic settings include arcs (Central America and parts of the Mediterranean), both continental and oceanic rifts (Basin and Range Province USA and Iceland), hot spots (Hawaii), and trans-tensional pull-a-part's in strike-slip fault systems (Salton Trough, California). However, high enthalpy geothermal systems are also relatively common in a-magmatic extensional and trans-tensional settings where normal fault systems are the primary control on geothermal activity, evident in the Basin and Range Province (USA) and western Turkey (Akkus et al., 2005).

Lower enthalpy systems are also found in the above settings as well as in relatively inactive tectonic environments, deep sedimentary basins (Paris and North German Basins), and convergent plate margins (Alpine orogenic belt) (Hurter et al., 2002).

4.3.5. Enhanced Geothermal Systems

Fluid pathways created by fractures and faults are crucial for the productivity of a reservoir (Huenges, 2010). A low permeability but highly porosity reservoir can be enhanced into a productive geothermal system (petrothermal system) by artificially inducing fractures not naturally found in the rock (ibid.). Geothermal exploration strives to detect hot water or

steam reservoirs in a hot and permeable environment. An enhanced geothermal system (EGS) slightly modifies this concept, as fluid pathways can be enhanced or even generated by suitable stimulation methods (Figure 4.2) (Huenges, 2010).

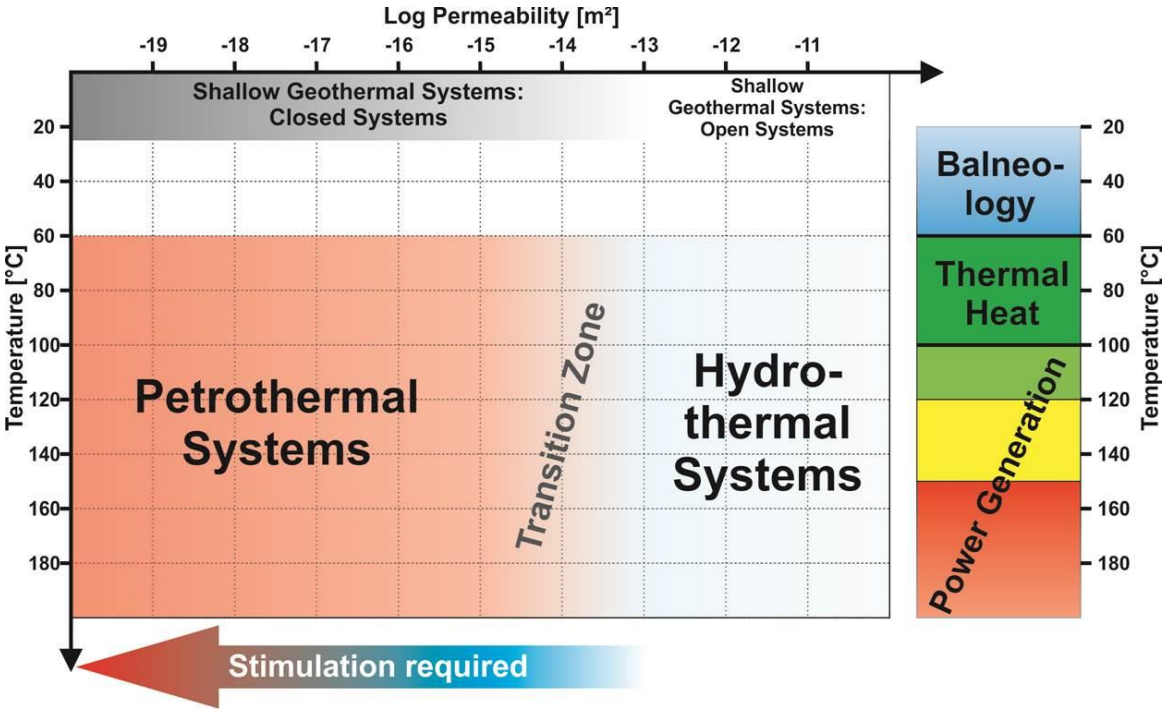

Figure 4.2: Temperature and permeability constraints of hydrothermal and petrothermal systems. From Bär (2012).

4.3.6. Deep Sedimentary Basins

Low enthalpy geothermal systems are reservoirs with a temperature less than 150°C (Chandrasekharam and Bundschuh, 2008). Recently a focus has been placed on exploring deep sedimentary basins, where the geothermal gradient of the crust (heat from radioactive decay of minerals) (Eghbal, 2015) may result in geothermal reservoirs at depth. Table 4.1 is a summary of deep geothermal basins around the world being explored or utilised for geothermal energy.

Table 4.1: Summary of deep geothermal basins from around the world.

Country	Region	Depth (m)	Ground Water Temp (°C)	Heat Flow (mW/m^2)	Output
China	North China & Weihe River-Yuncheng Basins	1500 – 4100	40 – 120	55 – 80	
Romania & Hungary	Pannonian Basin	3000 – 4000	150 – 20 0	90 – 100	720.11 MW heat
Germany	Molasse Basin	800 – 4500	70 – 140	80	3.36 MW electric + 38 MW heat
Germany	Upper Rhine Graben	2500 – 3300	135 – 160	>100	3 MW electric
Germany	North German Basin	1300 – 3800	55 – 170		0.23 MW electric + 17 MW heat
Canada	Alberta Basin	400 – 5000	120 – 150	80 – 100	Not developed
Mexico	Valley of Mexico	1800 – 2500	87 – 163	80 – 84	Not developed

Information compiled from Chen et al., 1977; Vedova, 1991; Bachu and Burwash, 1994; Cohut and Bendea, 1997; Veliciu and Šafanda, 1998; Dövényi et al., 2003; Blackwell and Richards, 2004; Kang, 2010; Schellschmidt et al., 2010; Szanyi, 2010; Wang, 2010; BINE, 2011; Majorowicz and Moore, 2013; Wang et al., 2013; Agemar, 2014; Götz et al., 2014; Hofmann et al., 2014; Homuth et al., 2014; Nádor, 2014; Homuth et al., 2015; Horváth, 2015; Liu et al., 2015; Zhu, 2015; Aretz et al., 2016.

4.3.7. Geothermal Power Generation

The Earth's geothermal resources are theoretically able to supply the planet's energy needs (Eghbal, 2015). Italy was the first country to commercially utilise geothermal power in 1913 by utilising two wells (200 - 250°C) that fed a 250 kW turbine followed in 1923 by a direct cycle (dry steam) geothermal plant. New Zealand followed in 1958 by developing a geothermal plant that utilised 200°C hot water. A dry steam geothermal plant was built shortly afterwards in the USA in 1960 (Hammons, 2004; Eghbal, 2015).

According to Rafferty (2000) the Rankine Cycle is the process of generating electricity from a heat source. Steam is generated and passed to the turbine where it expands against the

turbine blades. Heat energy is converted to mechanical energy causing the turbine to rotate. The mechanical energy is transferred through a shaft to a generator where it is converted to electrical energy. The steam is then converted back to liquid in a condenser and excess heat is delivered to a cooling tower where it is released to the atmosphere. The Kalina Cycle was developed in the 1980's to replace the Rankine Cycle, and uses an ammonium-water working fluid and an additional condenser to improve upon efficiency (Zhang et al,. 2012).

Dry steam plants account for 26% of all installed capacity (Eghbal, 2015). Single-flash steam is the most common type of geothermal power plant accounting for more than 42%, and the most efficient (ibid.). Double-flash steam power plants utilise the liquid left over after the first flash process, by piping it to a second vessel as a lower pressure where a second liquid-to-vapour flash occurs (ibid.). Binary cycle geothermal plants account for 32% of geothermal plants; they operate in a similar manner to a fossil fuel or nuclear power plant where a second fluid in a closed system is used to operate the turbine rather than the geothermal fluid (ibid.).

4.4. Methods and Materials for Geothermal Assessment

This study is based on an integrated analysis of petrographical and thermophysical data from the Permian Ripon Formation exposed along the Ecca Pass road cuttings north of Grahamstown, as well as the KWV-1 borehole. Both locations are within the Eastern Cape Province. The Ripon Formation is generally 600 m – 700 m thick, but increases in thickness to over 1000 m in the eastern part of its outcrop area, and rapidly wedges out northwards in the subsurface (Johnson et al., 2006). It is composed of poorly-sorted medium to fine-grained sandstones, alternating with siltstones and shales, and occurs at depths between 1000 m and 3500 m in the southern part of the Karoo Basin. The average thickness of sandstone units in the formation is ca. 12 m with an average minimum and maximum of 0.3 m and 44 m, respectively. Two predominant joint orientations were observed in the Ecca Pass section

(Campbell, 2014): 242/53 and 143/73 with a nearly right angle intersection (99°). Similar orientations of fractures were measured in the Triassic Beaufort Group (Senger et al., 2015).

Campbell (2014) studied the four formations exposed along the road cutting (Prince Albert, Whitehill, Collingham and Ripon) in order to assess the hydrocarbon generation potential of the shales and hydrocarbon reservoir potential of the thick sandstone successions. This study re-analysed the observations, samples and lithological logs in order to constrain the geothermal potential of the thick sandstone successions. Borehole KWV-1 was drilled in 2015 in order to assess the shale gas potential of the lower Ecca Group shales and intersected thick sandstone successions of the Ripon Formation.

In total 88 samples were selected from the Ripon Formation; 76 samples from the Ecca Pass location (Figure 4.4), and 12 samples from borehole KWV-1 (Figure 4.11). Samples were described detailing lithology as well as the occurrence of pore space and fractures. Thin sections were prepared using standard thin section preparation techniques at Rhodes University and Keele University. Petrographic analyses were conducted on thin sections using standard light microscopy.

Porosity and permeability analyses were carried out on all samples covering the entire exposed succession of the Ecca Pass. Measurements of skeletal density (helium pycnometer AccuPyc 1330) and envelope density (DryFlo pycnometer GeoPyc 1360) allowed the calculation of total porosity. Permeability measurements were conducted by usage of conditioned compressed air, using a gas pressure columnar-permeameter, developed at the Institute of Applied Geosciences, TU Darmstadt, Germany (Filomena et al., 2014). The device can measure permeability ranges from 1 D to 1 µD ($9.869 \cdot 10^{-13}$ m² to $9.869 \cdot 10^{-19}$ m²). Samples were measured in a 1 MPa confined cell with five pressure stages ranging from

0.108 MPa to 5 MPa, and a differential pressure of 80 kPa. All samples were dried overnight in a conventional oven at 105°C before the measurements.

For the determination of the dry bulk thermal conductivity and dry bulk thermal diffusivity the Optical Scanning Method, after Popov et al. (1999), was applied using a Thermal Conductivity Scanner developed by "Lippmann and Rauen GbR". In this method the surface temperature of the sample was measured by infrared temperature sensors before and after heating with a contactless heat source. The sensors and the heat source moved with constant speed and constant distance to each other along the sample and reference samples with known thermal conductivities.

The determination of both properties is based on a comparison of the cooling rates of a pre-heated sample with unknown thermal properties and the cooling rates of reference standards with known thermal properties. The methodology is non-destructive and contactless, but requires the sample surface to be sprayed with a thin layer of black acrylic lacquer to homogenize heating and temperature measurements. The measurement accuracy is stated by the manufacturer as ca. 3% (c.f. Lenhardt and Götz, 2015).

Measurements of thermal properties on dry porous samples under laboratory conditions reveal generally lower values than measurements on water-saturated samples of the reservoir. However, measurements on oven-dried core samples guarantee a very good reproducibility of the results in contrast to *in situ* values (Homuth et al., 2014). The inclusion of lithotype-specific correction and conversion equations (Fuchs et al., 2013) enables the calculation of the water-saturated matrix (bulk) thermal conductivity from data of dry-measured bulk thermal conductivity, and can be applied in a later stage of exploration to gain more accurate estimates of the resource potential. In contrast, samples of impermeable to low permeability rocks show different effects. In the reservoir, the thermal properties are

affected by temperature and pressure. Compaction closes micro-fractures and thus decreases porosity which leads to an increase of bulk density. As a result, thermal conductivity increases due to better grain-to-grain contacts and less "defects" (such as micro-fractures). Increases in temperature causes "thermal cracking" due to differential thermal expansion coefficients of the minerals (Clauser and Huenges, 1995; In: Ahrens, 1995). Hence, at depth, micro-fractures can be assumed, that are not present at ambient (laboratory) conditions. As a result, thermal conductivity decreases due to increasing "defects". Saturation generally enhances thermal conductivity and specific heat capacity in a porous rock, as water/brine has significantly higher thermal conductivity values than air. But in a low porosity rock there might be no pore space that can be filled with water, so the properties are not increased.

The geothermal map (Figure 4.19) highlighting the areas of increased heat flow and showing the locations of thermal springs and thermal artesian boreholes was created using the ESRI ArcGIS 10.0 GIS software package with data from Jones (1992), Bird et al. (2006), and Steyl et al. (2012). The relief base map with a resolution of 90 m was added from the ARCGIS online server (http://goto.arcgisonline.com/maps/World_Shaded_Relief). The outlines of South Africa and the Karoo Basin were digitized from Johnson et al. (2006). Finally, the areal extent of the areas of high heat flow were calculated using the algorithm within the polygon feature tool of ArcGIS 10.0 (Table 4.5).

A dynamic Calvet calorimeter SETARAM C80 (Calvet and Prat, 1963) was used to measure the specific heat capacity of samples from borehole KWV-1 for the temperature range of 25°C to 200°C. The device has two chambers, one of which was filled with weighted sample material, and the second chamber remained empty and acted as a reference. During the course of the measurements the temperature was increased stepwise by 0.5°C/min, while the heat flux in the sample chamber and reference chamber was measured. The difference between the heat flows is proportional to the specific heat capacity of the sample material

(Schellschmidt, 1999). The device has a temperature accuracy of +/- 0.1°C and a measurement precision of +/-0.1%.

The methodology for geothermal assessment with minimal data types was adopted from Lenhardt and Götz (2015) which utilizes the approach by Muffler and Cataldi (1978). This formula allows a direct calculation of the heat in place for each stratigraphic unit that is hotter than 60°C by using Eq. (2) and may enable a detailed regional quantification.

$$E_{th} = c_r \cdot \rho_r \cdot V \cdot (T_r - T_s) \quad (2)$$

where E_{th} is heat in place [J], c_r the specific heat capacity of the reservoir rock [$J \cdot kg^{-1} \cdot K^{-1}$], ρ_r the density of the reservoir rock [$kg \cdot m^{-3}$], V the reservoir volume [m^3], T_r the reservoir temperature [°C] and T_s the average ground surface temperature [°C]. Reservoir porosity and heat stored in reservoir fluids can be neglected due to errors of less than 5% for regional scale studies (Muffler and Cataldi, 1978) if porosity is lower than 20%.

By incorporating the bulk density ρ_b, the specific heat capacity is calculated by using Eq. (3):

$$c_p = \frac{k}{\alpha . \rho_b} \quad (3)$$

Where:

c_p = specific heat capacity

k = thermal conductivity

α = thermal diffusivity

ρ_b = density

Values for heat in place are recorded in Joules (J) as well as Terrawatt Hours (TWh) using Eq. (4). Recoverable heat is recorded in Joules and Terrawatt Hours as well as Million Barrels of Oil Equivalent (MBOE) using Eq. (5) from Hirst et al. (2015).

$1\ TWh = 3.6\ X\ 10^{15}\ Joules$ (4)

$1\ BOE = 5861520000\ J$ (5)

A palynological slide was prepared from a sample of organic rich siltstone from the Ripon Formation. Dr. Rae Jones, using standard palynological proceesing techniques (e.g. Doher, 1980), undertook processing.

Weatherford Slimline Services logged the entire borehole after drilling was completed. 502 measurements were made with a Formation Dipmeter tool, which provides azimuth and dip angle data from the borehole wall with a resolution of up to four measurements per meter. Both bedding planes and fracture planes were recorded. 93 fractures were recorded within the Ripon Formation and were plotted as planes on stereonets usings SpheriStat^{TM} structural software.

4.5. Ecca Pass Road Cutting

4.5.1. Location

The Ecca Pass road cutting (33°12'59.34"S 26°37'40.07"E) is located on the R67 approximately 15 km northeast of Grahamstown (Figure 4.3) towards Fort Beaufort. The road cutting exposes 270 m of stratigraphy.

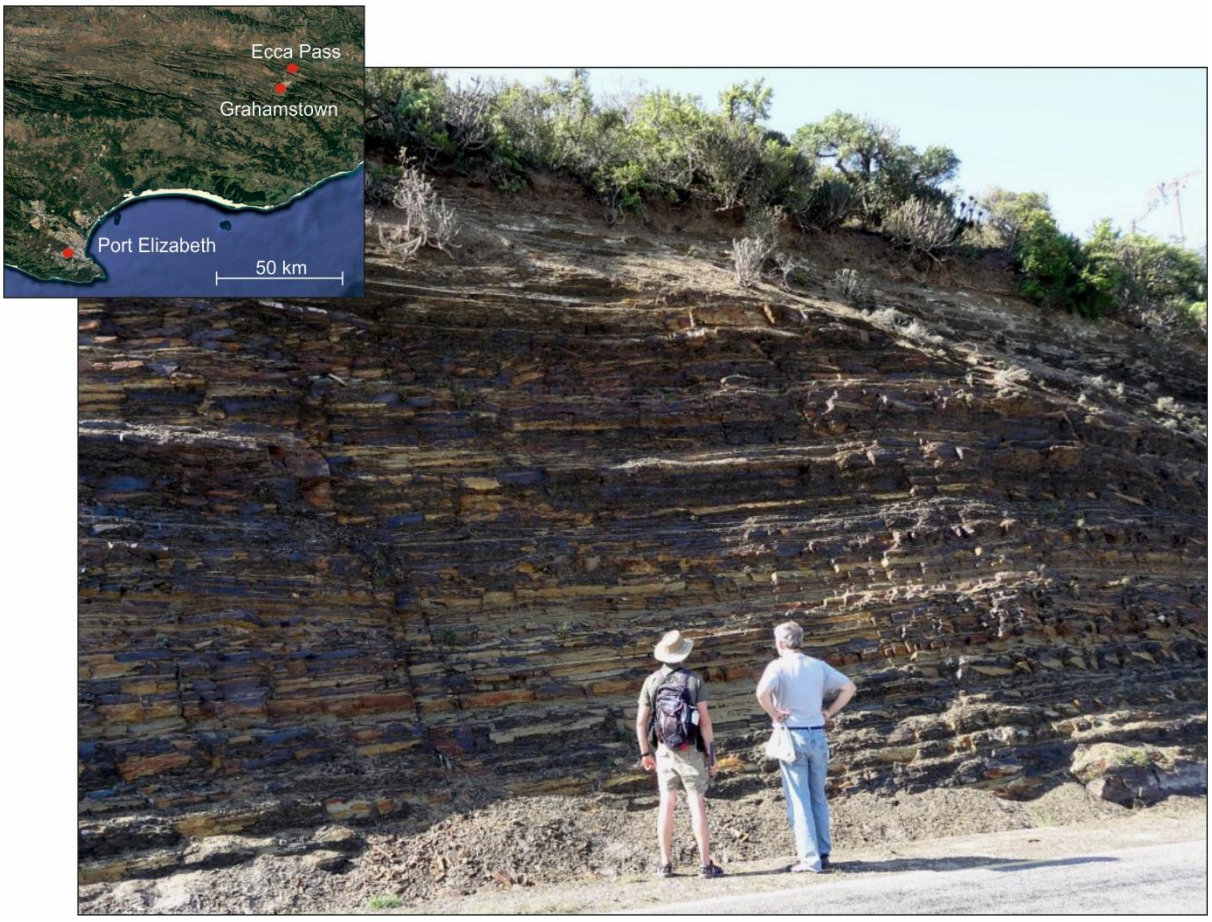

Figure 4.3: The Collingham Formation along the Ecca Pass road cut in the Eastern Cape, South Africa (see insert). Photo source: Prof. Götz (2014).

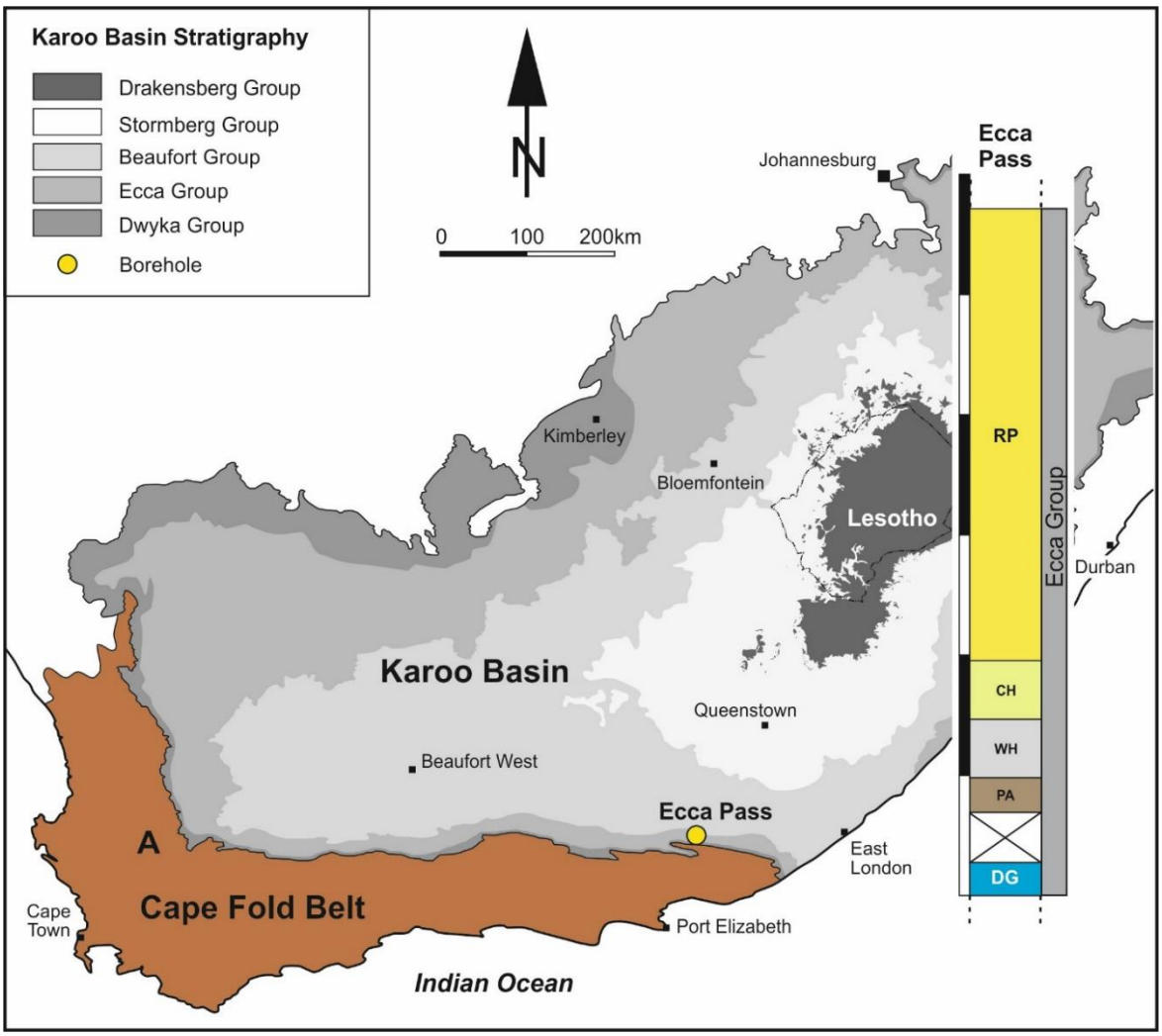

Figure 4.4: Stratigraphic log of the Ecca Pass within the context of the Main Karoo Basin. Abbreviations: *RP* Ripon Formation, *CH* Collingham Formation, *WH* Whitehill Formation, *PA* Prince Albert Formation, *DG* Dwyka Group. Scale bar = 50 m. Modified after Catuneanu et al. (1998).

4.5.2. Lithological and petrophysical data

The Ecca Pass road cutting exposes four formations of the Ecca Group (Ripon, Collingham, Whitehill and Prince Albert) as well as the upper portion of the Dwyka Group (Figure 4.4; Appendix B). Formations were differentiated based on lithology in comparison to the known stratigraphy of the area. A detailed log was produced by Campbell (2014) (Appendix B) as part of an MSc at Rhodes University.

I. Prince Albert Formation

Outcrop

The Prince Albert Formation is very poorly exposed, with a possible gradational contact with the overlying Whitehill Formation and no contact visible with the underlying Dwyka Group. The formation contains greenish-grey shale that weathers a reddish-brown. The shale is highly fragmented and partially buried in regolith. No bedding or structures were visible.

II. Whitehill Formation

Outcrop

The Whitehill Formation is 24 m thick and comprises highly weathered laminated shale (Figure 4.5a). The weathered shale ranges in colour from a pinkish-white to a pale red colour (Figure 4.5b). Laminations are visible on a millimetre scale and rhythmic variations in layer competency occur on a centimetre scale (Figure 4.5d). Several sections of folded shale were documented approximately 4 m from the base of the formation (Figure 4.5f). Folds are 20 – 30 cm in amplitude and wavelength. Aggregates of soft white nodular gypsum (Figure 4.5c) occur, cross-cutting shale bedding (Figure 4.5e). No fossil material was documented from this formation.

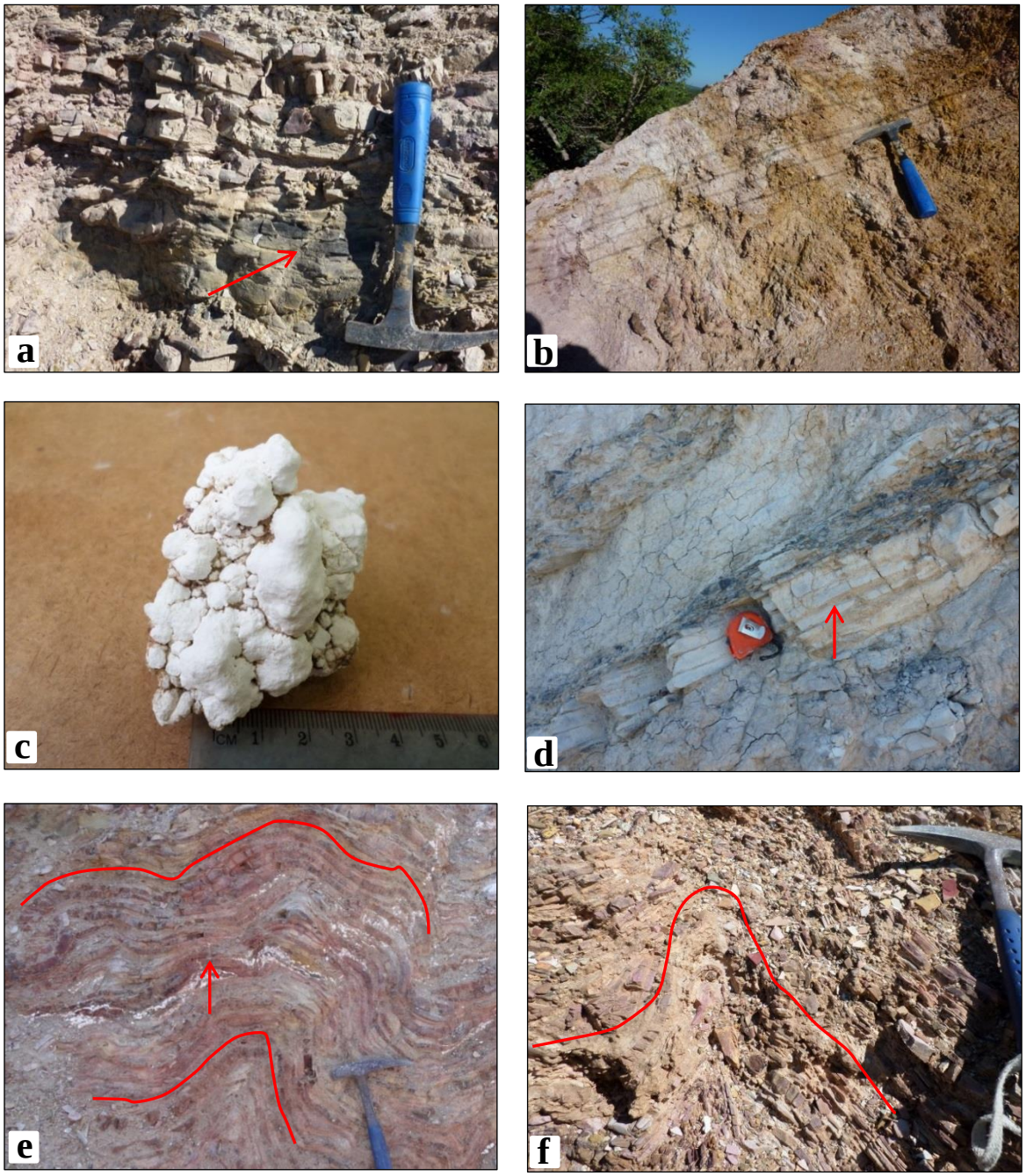

Figure 4.5: Outcropping Whitehill Formation rocks with lithologies, structures and weathering features. **(a)** Laminated dark coloured fresher shale (arrowed) within white weathered shale. **(b)** Weathered shale with characteristic white and reddish weathering colours. **(c)** An aggregate of white gypsum nodules. **(d)** Hard weathering resistant layer (arrowed) within weathered sediments. **(e)** and **(f)**: Possible water escape or deformation structures with variation in height, width and orientation with white gypsum nodules in weathered shale. NOTE: Gypsum nodules cross-cut bedding. Modified from Campbell (2014).

III. Collingham Formation

Outcrop

The Collingham Formation is 25 m thick and contains hard grey silty shales (Figure 4.6a) exposed along the road cutting. The shales weather a dark rusty red colour. The formation has a sharp contact with the overlying Ripon Formation (Figure 4.6b) and the underlying Whitehill Formation. Shale beds range in thickness from 2 cm – 10 cm and are internally laminated (Figure 4.6c). The shales of this formation are laterally extensive (Figure 4.6d). Fragmented plant remains as well as harder chert-like layers were documented within this formation. Soft greenish-yellow-weathering tuff layers are interbedded with the more competent shales. Tuff layers range in thickness from 2 cm – 5 cm and display no internal structures (Figure 4.6e). Tuff layers are spaced, on average, every 5 cm within the shales through the formation. Oval shaped concretions of less competent material were observed within more competent shale layers (Figure 4.6f).

IV. Ripon Formation

Outcrop

The Ripon Formation (Figure 4.4) contains siltstones and three sandstone lithologies: (1) very-fined grained, (2) fine grained, and (3) medium grained.

210 m of the Ripon Formation is exposed along the road cutting (Figure 4.7a). The formation is composed of greenish-grey to light grey sandstone (fresh), dark brown siltstone and minor black shale. Sandstones are generally upwards fining from medium grained to fine/very fine followed by siltstone/shale. Units range in thickness from 20 cm to several meters (Figure 4.7b).

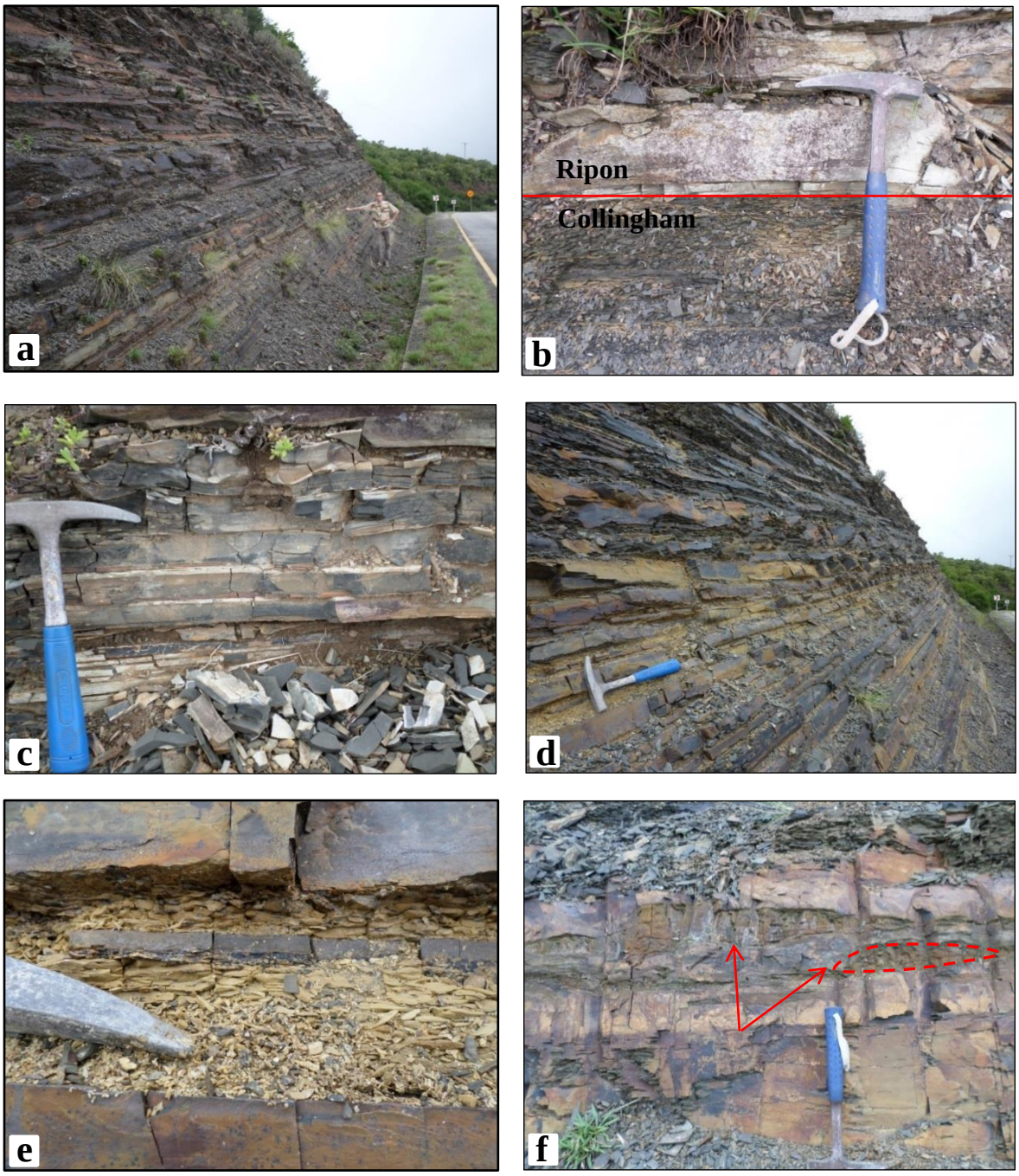

Figure 4.6: Outcropping Collingham Formation rocks with contacts, lithologies and, structures. **(a)** Well exposed interbedded shales and tuffs along the road. **(b)** Sharp planar contact between the Collingham and Ripon Formations. **(c)** White weathering in dark coloured shale. **(d)** Laterally extensive shale and tuff layers. **(e)** Fragmented tuff and competent shale. **(f)** Lenses of less competent clay-like material with average dimensions 110cm x 9cm within Collingham Fm shale. Modified from Campbell (2014).

The medium-grained sandstone beds range in colour from grey to greenish-grey and brown, and weather to light grey and dark brown. This lithology is usually massive with fining-upwards cycles. Occasional laminations are observed, ranging from 2 cm – 5 cm in thickness. The laminations show alternations between silty, darker coloured and coarser grained, lighter coloured laminae.

The fine-grained sandstones are predominantly brownish-grey to dark grey when fresh and rusty red when weathered, containing abundant plant debris.

The very fine-grained sandstones vary in colour from light-brown to grey when fresh and light brown to rusty red when weathered. The sandstones are laminated with laminae ranging in thickness from millimetres up to 5 cm. They contain abundant plant debris and organic matter.

Load casting (Figure 4.7c) and tool marks are present where sandstones overlie siltstone or shale. Rounded rip-up clasts of shale were documented proximal to the base of massive sandstone grading upwards to thinly bedded (<10 cm) then laminated.

Shales and siltstones are generally highly weathered and appeared massive, however laminations were discernible in places. The black shale is highly weathered and fragmented and occurs as pencil fragments- thin elongated shards of shale. The shale appears internally laminated.

Reddish iron oxide staining was occasionally documented on sandstones. Plant remains were observed within certain siltstone and very fine grained sandstone horizons. Large concretions (<40 cm) are present within sandstones (Figure 4.7d) and often contain a shale centre. The upper portion of the exposed Ripon Formation contains a variation of the grey sandstone containing white spots in varying proportions. The white spotted sandstone is

intermittently inter-bedded with the grey medium-grained sandstone in certain localities (Figure 4.7e).White spots are match-head sized and are usually evenly distributed throughout the sandstone (Figure 4.7f).

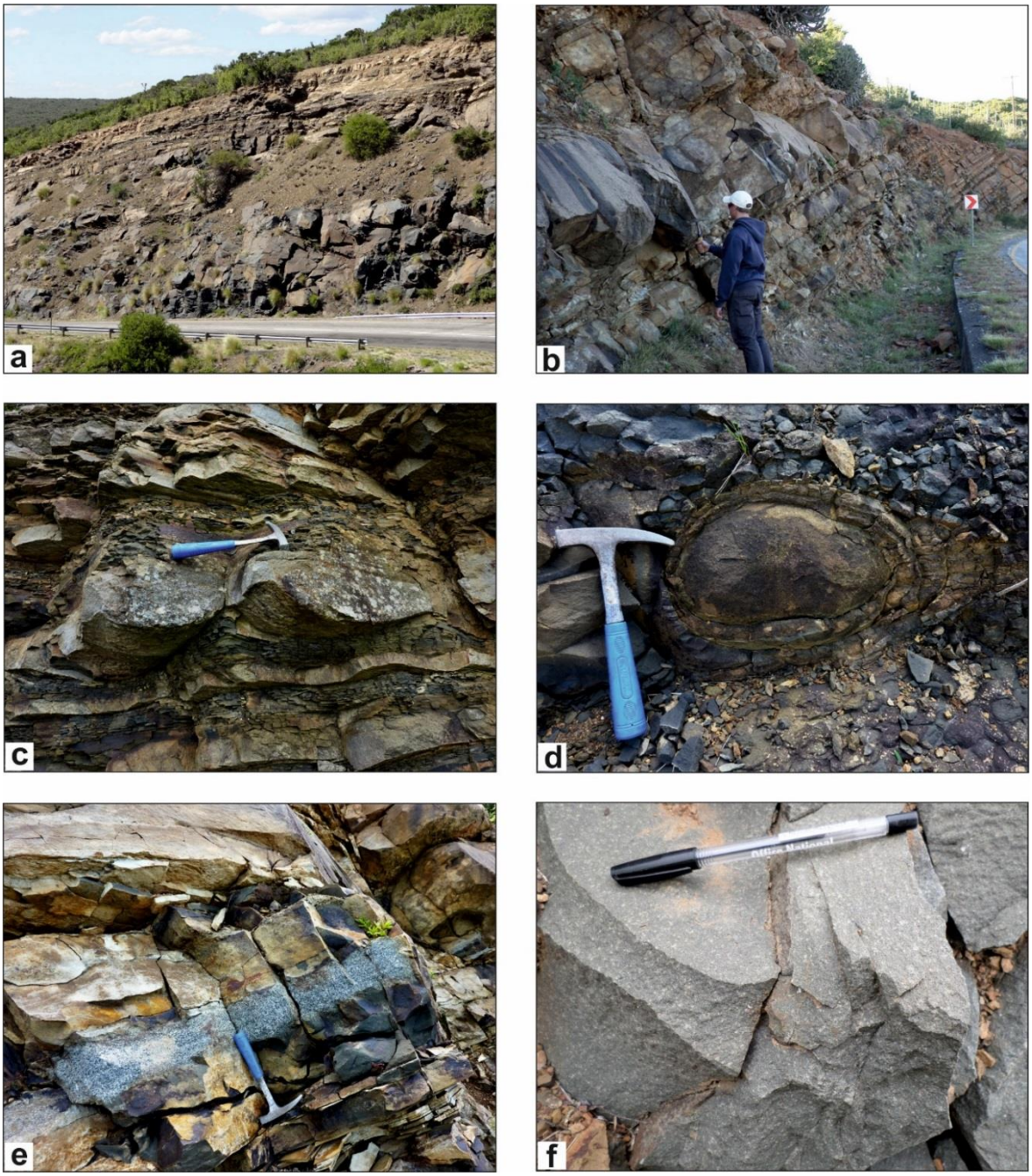

Figure 4.7: The Ripon Formation along the Ecca Pass road cutting. **(a)** Massive sandstone units. **(b)** Thick sequences of layered medium to fine grained sandstone. **(c)** Load casting of medium sandstone into siltstone. **(d)** A large concretion within medium grained sandstone. **(e)** An anomalous layer of white spotted sandstone (medium grained) within non-spotted sandstone. **(f)** Massive white spotted sandstone. Modified from Campbell (2014).

Two predominant jointing directions were observed in the Ripon Formation sandstones (Figure 4.8) and shales. The strike and dip of 40 joints were measured with an average of 242/53 and 143/73 with a nearly right-angle intersection (99°).

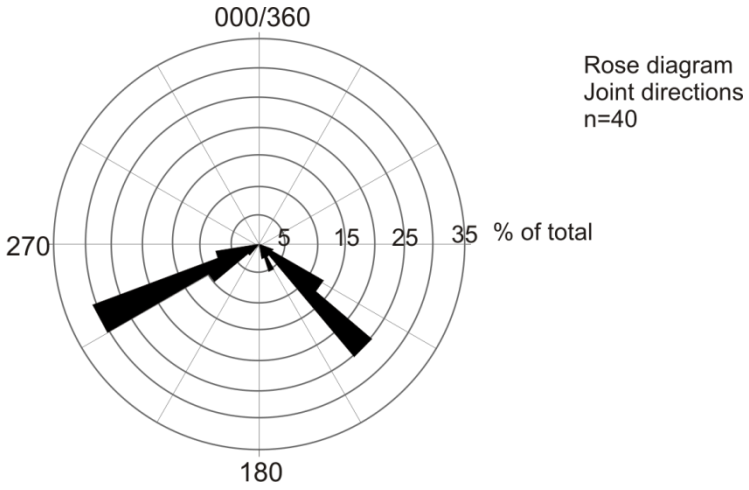

Figure 4.8: Joint directions within Ripon Formation sandstones with two dominant systems documented. From Campbell (2014).

Microscopy

Fine grained sandstones (Figure 4.10a) contain a poorly sorted amalgamation of well-rounded to sub-rounded quartz, feldspar, and lithic fragments (Figure 4.10b) set in a matrix of clay-sized particles and organic matter. Quartz and feldspar grains comprise roughly 45% of this lithology, lithic fragments 5%, while the remaining 50% is occupied by the matrix. Fine grained sandstone plots as arkose and lithic arkose/subarkose on the Pettijohn (1975) plot (Figure 4.9).

Medium grained sandstone (Figure 4.10c, d) is grain-supported with poor sorting and very well rounded to sub-rounded grains of varying size. The grains consist of: internally fractured, monocrystalline, undulatory quartz; twinned and zoned feldspar; chert particles; lithic fragments containing altered feldspar; glauconite; elongated biotite (locally replaced by limonite); and organic particles in a yellow-brown matrix. Iron oxides (hematite) are

present in organic-rich sections. Medium-grained sandstones plot as subarkose, sublitharenite and lithic arkose (Figure 4.9).

Very fine grained sandstones (Figure 4.10e) are poorly sorted, with rounded to sub-rounded quartz and feldspar grains in a matrix of dark organic matter and clay-sized particles. Pore spaces are not visible in thin sections and have most likely been filled by abundant matrix. Very fine sandstones plot as lithic arkose (Figure 4.9).

The white spotted variation (Figure 4.10f) contains moderately to well-sorted monocrystalline quartz and feldspar grains that appear equigranular in size (up to 300 µm) and are grain-supported with line contacts. Grains are angular to sub-rounded and internal fracturing of quartz grains is not as pervasive as observed in non-spotted sandstone samples but microfissures between grains are prevalent. Samples of spotted sandstone contain little or no clay, either as matrix or as alteration products. Organic matter is virtually absent. Feldspar grains display a lesser degree of alteration in comparison to non-spotted sandstone. Spotted sandstone contains biotite grains (altering to limonite) that bend around quartz and feldspar grains. Other observed minerals include chlorite and muscovite.

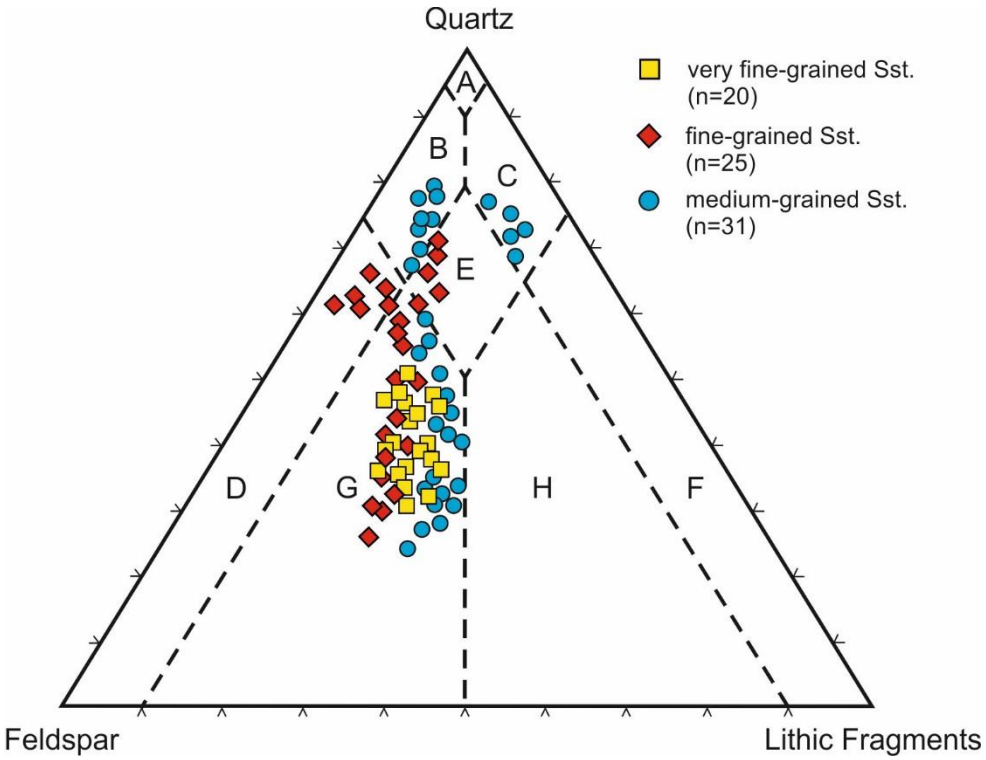

Figure 4.9. Classification of the Ecca Pass turbiditic sandstones after Pettijohn (1975). Very fine- grained sandstones plot in field G (lithic arkose), fine-grained sandstones in fields D, E and G (arkose and lithic arkose/subarkose), and medium-grained sandstones in fields B, C and G (subarkose, sublitharenite and lithic arkose). Key: A quartz arenite, B subarkose, C sublitharenite, D arkose, E lithic subarkose, F litharenite, G lithic arkose, H feldspathic litharenite.

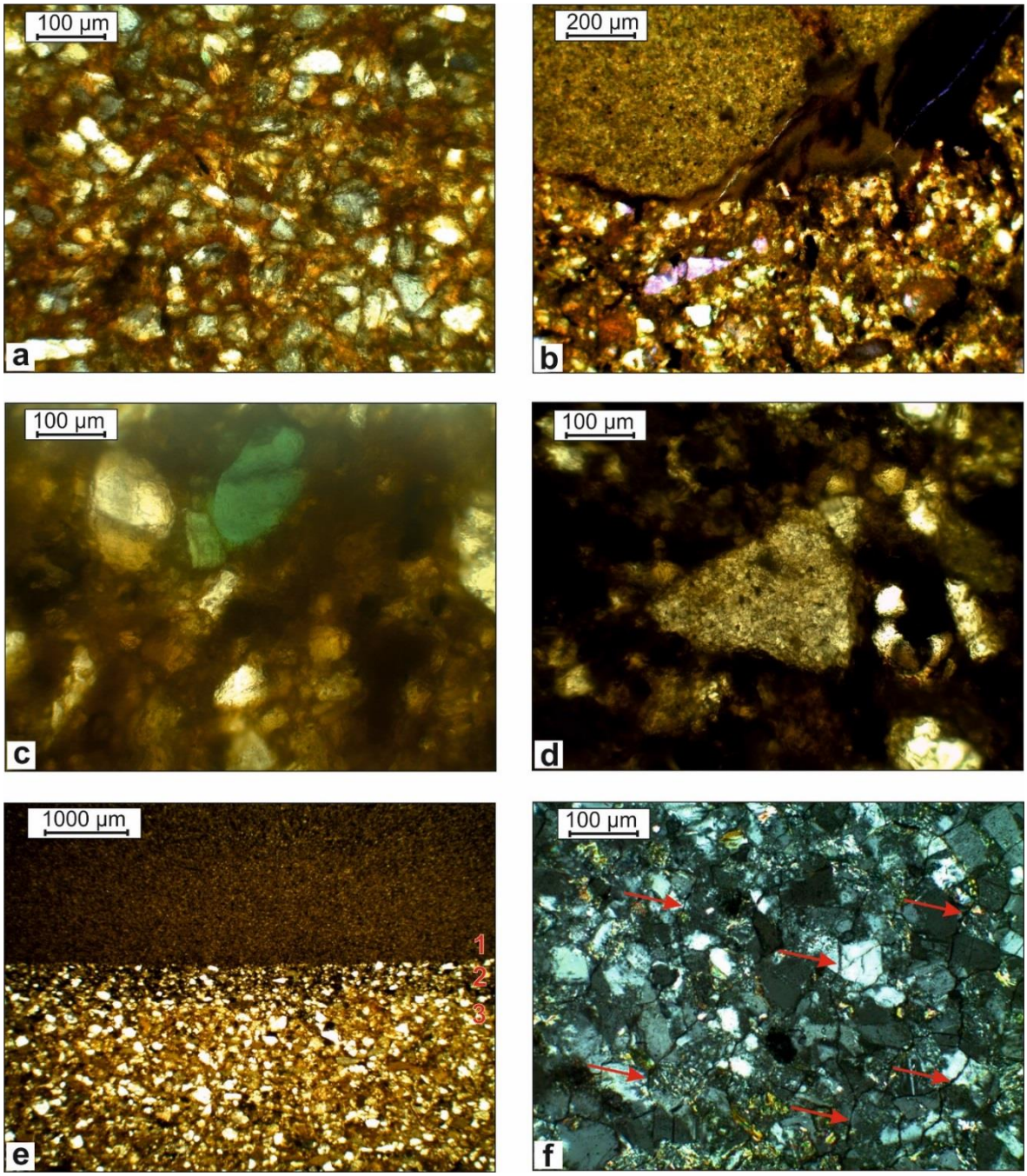

Figure 4.10: The Ripon Formation along the Ecca Pass road cutting. **(a)** Very-fine to fine grained grewacke containing rounded quartz, glauconite and feldspar grains in a clay matrix. Plane polarised light. **(b)** Quartz, feldspar, clay and organic matter adjacent to a clast of siltstone. Note: Pink colour due to incorrect thin section thickness. **(c)** Glauconite grain in clay with quartz. Plane Polarised light. **(d)** Lithic fragment in clay and organic matter with quartz. Plane polarised light. **e)** Fine-grained greywacke (3) with organic-rich layer (2) overlain by very fine sandstone/siltstone (1). **(f)** Fine grained arkose with equigranular, well-sorted, angular to sub-rounded quartz and feldspar grains with prevalent inter-granular microfissures in spotted sandstone (arrows mark microfissures). Cross polarised light. Modified from Campbell (2014).

Petro- and thermophysical rock properties

The ranges and mean values of porosity, permeability and density data of the Ripon Formation lithologies are provided in Table 4.2. The very fine-grained sandstones range in porosity from 0.02% – 1.44% with a mean of 0.73%. Their permeabilities range from $8.09 \cdot 10^{-17}$ m² – $9.22 \cdot 10^{-17}$ m² (mean $8.65 \cdot 10^{-17}$ m²), and 0.07 mD – 0.08 mD (mean value of of 0.08 mD) respectively. Mean density is 2680 kg/m^3.

Table 4.2. Petro- and thermophysical properties of the Ripon Formation sandstones, and calculated values of specific heat capacity. Red box indicated optimal lithology.

Lithology	Number of Measure-ments	Density [kg/m^3]	Porosity [%]	Permeability [m^2]	Thermal conductivity [W/(m·K)]	Thermal diffusivity [m^2/s ·10^{-6}]	Specific heat capacity [kJ/(kg·K)]
Very fine-grained sandstone	20	2680-2690 (mean 2680)	0.02-1.44 (mean 0.73)	$8.09 \cdot 10^{-17}$ – $9.22 \cdot 10^{-17}$ (mean $8.66 \cdot 10^{-17}$)	2.78-3.20 (mean 2.98)	1.15-1.64 (mean 1.39)	0.73-0.91 (mean 0.81)
Fine-grained sandstone	25	2650-2670 (mean 2660)	0.94-1.08 (mean 1.01)	$1.12 \cdot 10^{-17}$ – $1.37 \cdot 10^{-17}$ (mean $1.25 \cdot 10^{-17}$)	2.45-2.95 (mean 2.69)	0.95-1.37 (mean 1.12)	0.82-0.98 (mean 0.91)
Medium-grained sandstone	31	2630-2730 (mean 2670)	0-3.70 (mean 1.10)	$7.21 \cdot 10^{-18}$ – $9.94 \cdot 10^{-17}$ (mean $4.59 \cdot 10^{-17}$)	2.38-3.09 (mean 2.79)	0.90-1.40 (mean 1.17)	0.84-1.03 (mean 0.91)

The fine-grained sandstones range in porosity from 0.94–1.08% with a mean of 1.01%. The permeabilities of this lithology range from $1.12 \cdot 10^{-17}$ – $1.37 \cdot 10^{-17}$ m² (mean value of $1.25 \cdot 10^{-}$ m²). In millidarcy (mD) all samples of the fine-grained sandstone show uniform values of 0.01 mD. Mean density is 2660 kg/m^3.

The medium-grained sandstones range in porosity from 0.00–3.7% with a mean of 0.5%. Their permeability ranges from 0.01–0.1 mD (mean value of 0.05 mD) and $7.21 \cdot 10^{-18}$ – $9.94 \cdot 10^{-17}$ m² with a mean of $4.59 \cdot 10^{-17}$ m², respectively. Mean density is 2670 kg/m^3.

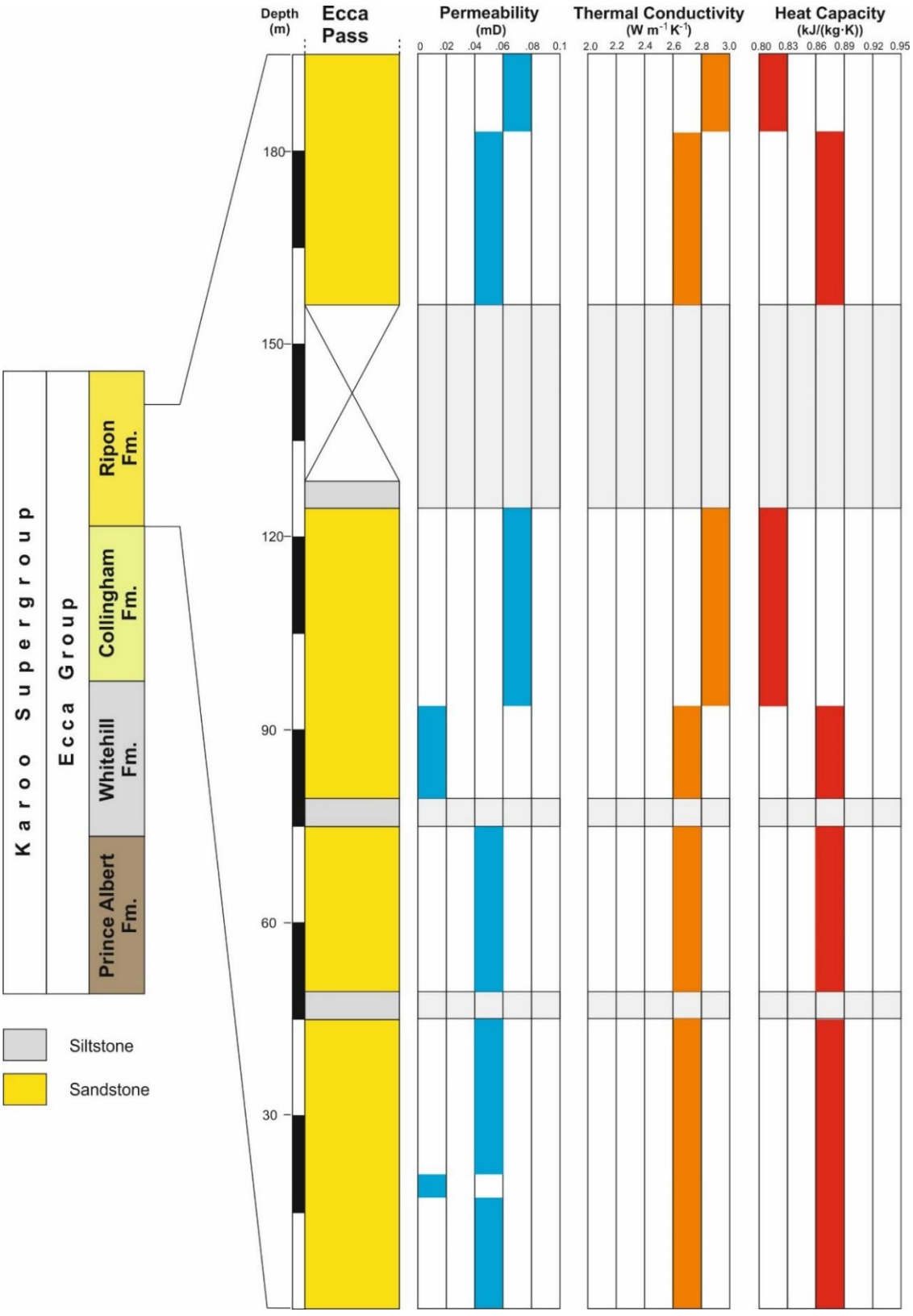

Figure 4.11: Stratigraphic log of the Ripon Formation exposed along the Ecca Pass road cutting and trends of thermophysical properties on a reservoir scale. Intervals without measurements are grey shaded. Scale bars 15 m, Fm. = Formation. All lithologies are classified as impermeable. Very fine-grained sandstones show the highest thermal conductivity. Specific heat capacity reveals the highest values in medium and fine-grained sandstones.

The thermal conductivity values of the Ripon Formation samples are shown in Table 4.2. The thermal conductivity of the very fine-grained sandstones ranges from 2.78–3.20 W/(m·K) with a mean of 2.98 W/(m·K). The fine-grained sandstones exhibit thermal conductivities ranging from 2.45–2.95 W/(m·K) with a mean of 2.69 W/(m·K), and the thermal conductivity of the medium-grained sandstones ranges from 2.38–3.09 W/(m·K) with a mean of 2.79 W/(m·K). The thermal diffusivity of the very fine-grained sandstones ranges from 1.15–1.64 (m^2 /s $\cdot 10^{-6}$) with a mean of 1.39 (m^2 /s $\cdot 10^{-6}$). The fine-grained sandstones exhibit values ranging from 0.95–1.37 ($m^2/s \cdot 10^{-6}$) with a mean of 1.12 ($m^2 /s \cdot 10^{-6}$), and the thermal diffusivity of the medium-grained sandstones ranges from 0.90–1.40 (m^2 /s $\cdot 10^{-6}$) with a mean of 1.17 ($m^2 /s \cdot 10^{-6}$).

Specific heat capacity is calculated by using Eq. (3) and shows a mean value of 0.876 kJ/(kg·K) for the clastic rocks of the Ripon Formation.

Figure 4.11 summarises the thermophysical property trends on a reservoir scale with very-fine grained sandstone exhibiting the highest thermal conductivity while specific heat capacity is highest in medium and fine-grained sandstones.

4.6. Borehole KWV-1

4.6.1. Location

Borehole Karoo Willovale 1 (KWV-1) was drilled in the Eastern Cape of South Africa (32°14'38.20"S 28°35'9.50"E) to the northeast of East London (Figure 4.12). The borehole was drilled to a depth of 2352 m by Geoserve Exploration Drilling PTY LTD.

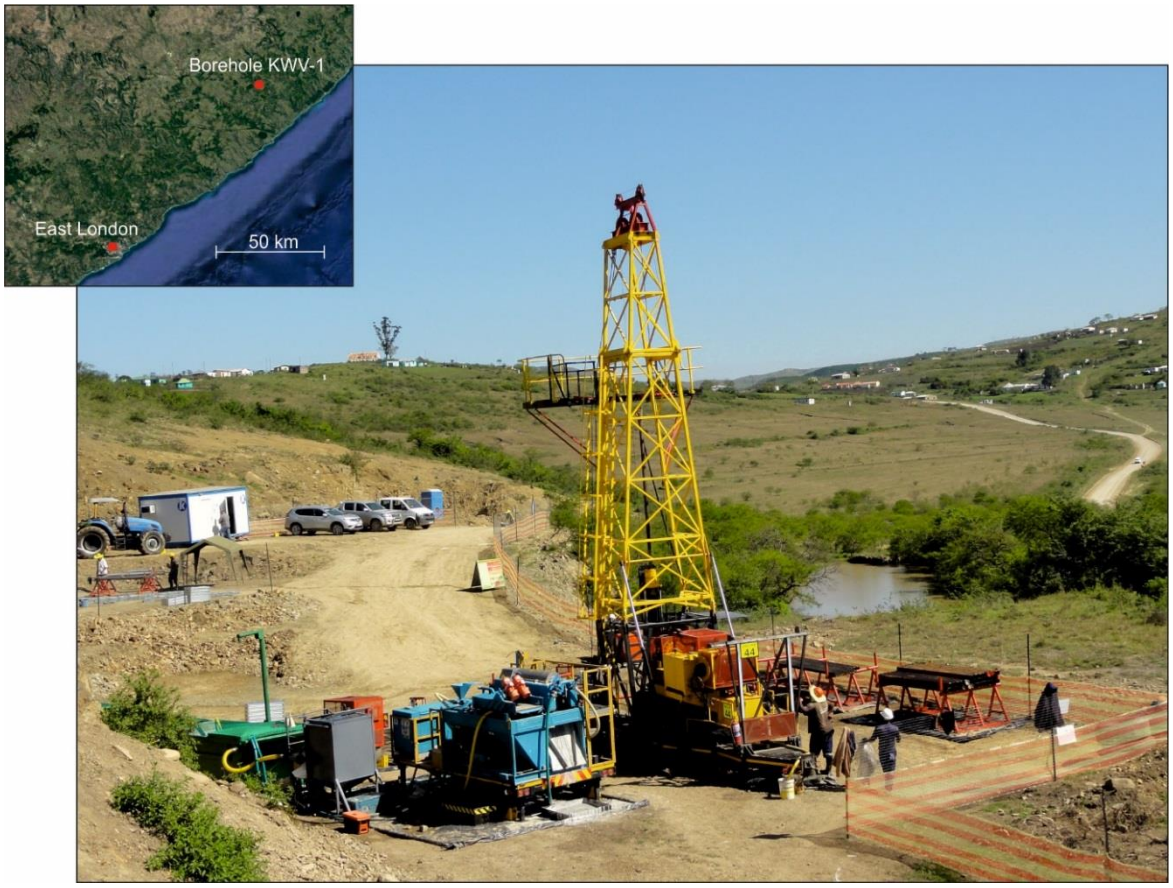

Figure 4.12: Borehole KWV-1 drill site in the Eastern Cape of South Africa (see insert) at an elevation of 263 m above sea level. Photo source: De Kock et al. (2015).

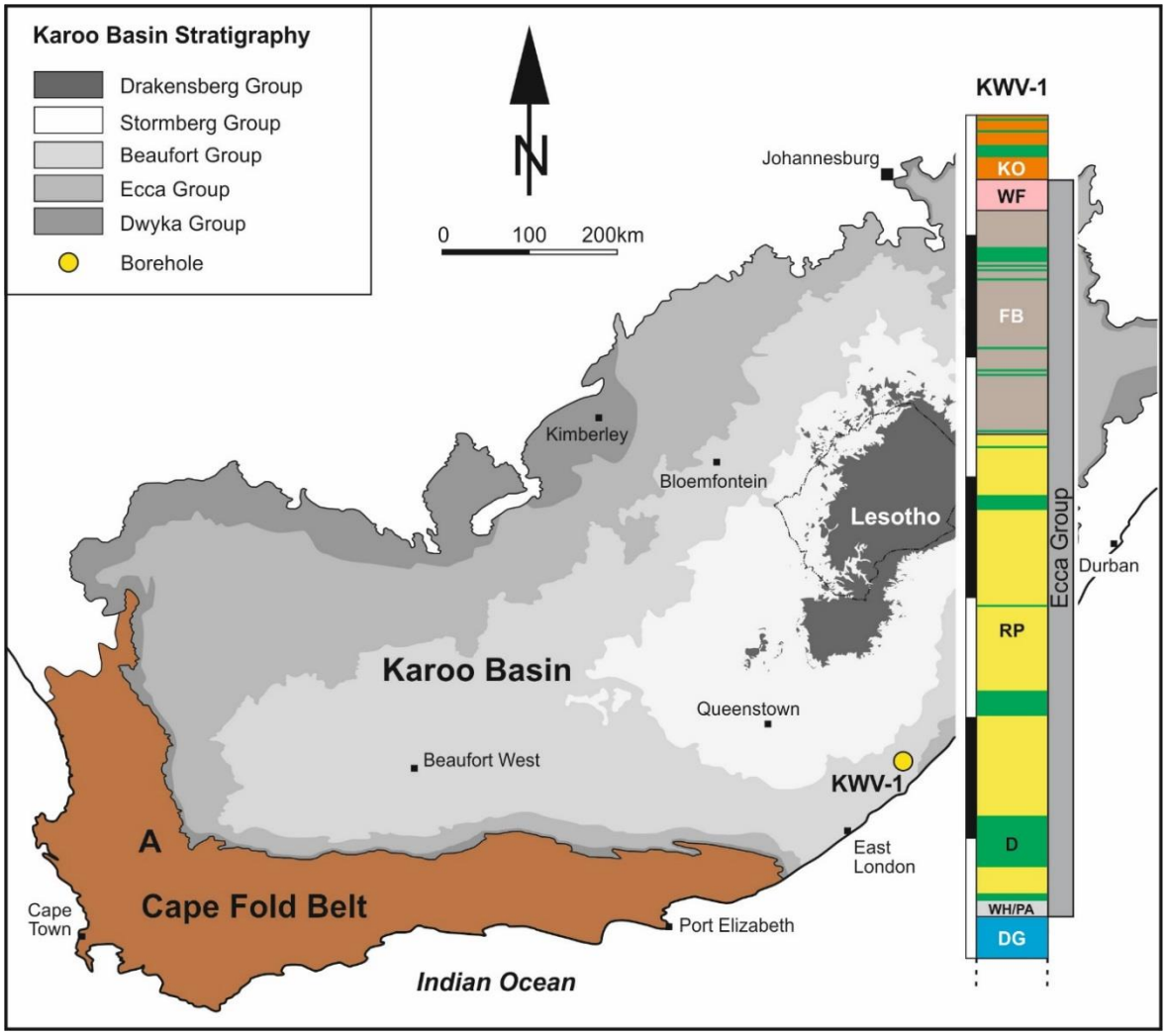

Figure 4.13: Stratigraphic log of borehole KWV-1 within the context of the Main Karoo Basin. Abbreviations: *KO* Koonap Formation, *WF* Waterford Formation, *FB* Fort Brown Formation, *RP* Ripon Formation, *WH* Whitehill Formation, *PA* Prince Albert Formation, *DG* Dwyka Group, *D* Dolerite. Scale bar = 350 m. Modified after Catuneanu et al (1998).

4.6.2. Lithological and petrophysical data

Borehole KWV-1 was drilled through the Koonap Formation (Adelaide Subgroup) of the lower Beaufort Group, and five formations of the Ecca Group (Waterford, Fort Brown, Ripon, Whitehill and Prince Albert) as well as the upper portion of the Dwyka Group (Figure 4.13; Appendix C). Formations were differentiated based on lithology compared to the

known stratigraphy of the area. A detailed log was produced by Aleck Birch of the KARIN project (Appendix C).

I. Dwyka Group

The Dwyka Group tillite consists of sub-angular sandstone and quartz fragments up to 7 cm in diameter within a grey, coarse-grained matrix. The Dwyka Group was intersected at a depth of 2339.75 m. The borehole ends at a depth of 2352.39 m within this group.

II. Prince Albert Formation

The Prince Albert Formation was intersected at 2308.4 m and is composed of shale ranging in colour from light green to black and medium to fine grained sandstone. Shales are massive to thinly bedded, with layering defined by lighter grey shale or sandstone. Pyrrhotite and pyrite occurs within both lithologies. Load casts of sandstone within shale and soft sediment deformation was documented. Concretions occur within both lithologies.

III. Whitehill Formation

The upper contact of the Whitehill Formation occurs at 2294.95 m directly below an 18 m thick dolerite intrusion. The formation is composed of black carbonaceous shale with discrete light grey, very fine-grained sandstone. Disseminated pyrite (up to 30%) and pyrrhotite were observed within the shale and on bedding planes. Soft sediment deformation was observed where sandstone overlies carbonaceous shale.

IV. Ripon Formation

Core

The Ripon Formation (Figure 4.14) contains siltstone and three distinct sandstone lithologies: (1) very fine-grained sandstones, (2) fine-grained sandstones, and (3) medium-grained sandstones. The Ripon Formation is divided into three subgroups:

The Trumpeters Member was intersected at a depth of 919.20 m and comprises dark grey, horizontally bedded, upwards fining, fine to medium grained sandstone intercalated with laminated dark grey to black shale. Sandstone beds range in thickness from 1 cm to massive and exhibit load casting where sand overlies shale. Pyrite mineralization was occasionally observed along bedding planes. A 10 m thick dolerite sill was intersected at a depth of 955.48 m within medium grained sandstones. An 8 cm wide fault was observed at 1046.40 m.

The Wonderfontein Member was intersected at a depth of 1048.40 m and consists of a greater proportion of shale in comparison to the overlying member. Shales range in colour from dark grey to black to light grey (Figure 4.14a). Bedding ranges from rhythmically bedded light and dark shale with minor sandstone to massive. Massive shales appear siltier than laminated shales. Sandstones are light grey, fine to medium grained (Figure 4.14c) with 5-8% heavy black mineral content. Rip up clasts of shale occur as a conglomerate at a depth of 1267.83 m. Wave ripple marks were also observed. A 45 m thick dolerite was intersected at a depth of 1203.72 m. A fault at 45° to the core axis was observed at a depth of 1121.95 m with a 2.5 cm thick quartz vein as well as pyritized slickenside surfaces. Sub-vertical fractures were observed intermittently (Figure 4.14d). Numerous tuffs were encountered below a depth of 1297.13 m.

The Pluto's Vale Member occurs between the depths of 1346.13 m and 2276.3 m. The member contains a larger proportion of sandstone compared with the overlying members.

Sandstones range in colour from light grey to dark grey (Figure 4.14b). Upwards fining sequences were observed with grain sizes ranging from medium to very fine. Bedding style ranges from massive to thinly bedded. Rhythmically bedded sandstone and shale, as well as darker and lighter sandstone, was documented. Load casting was occasionally found were sandstone overlies shale. Rip-up clast conglomerates occur with rounded fragments of shale within the base of large sandstone units. Shale ranges in colour from black to grey. It occurs as massive units up to 20 m thick, as well as laminated tuff-rich units. Fossilised plant remains were found, rarely, within sandstone units.

A lime-green siltstone, possibly epidotised, was intersected at a depth of 1978.95 m, along with a greenish concretion. Numerous concretions were documented intermittently usually occurring within sandstone units. Pyrrhotite, chalcopyrite and pyrite mineralisation was detected along bedding planes and quartz veins proximal to dolerite sills. Six dolerite sills were intersected (1380.78 m, 1476.85 m, 1680.67 m, 1879.10 m, 2037.30 m, 2276.13 m) ranging in thickness from 0.48 m to 148.24 m.

A fault zone was intersected at a depth of 1789.30 m consisting of fault breccia, along with a vertical fracture system with calcite/gypsum infill up to 6 mm thick. Obvious displacement of layering on either side of the fracture system was percieved. A second fault zone was intersected at a depth of 2185.85 m, at the base of a dolerite intrusion. The fault zone contains angular and rounded fragments in a very fine matrix along with quartz veins at 75° to the core axis. A third fracture zone within massive sandstone at 2233.60 m contains high angle fractures with angular fragments in a fine matrix.

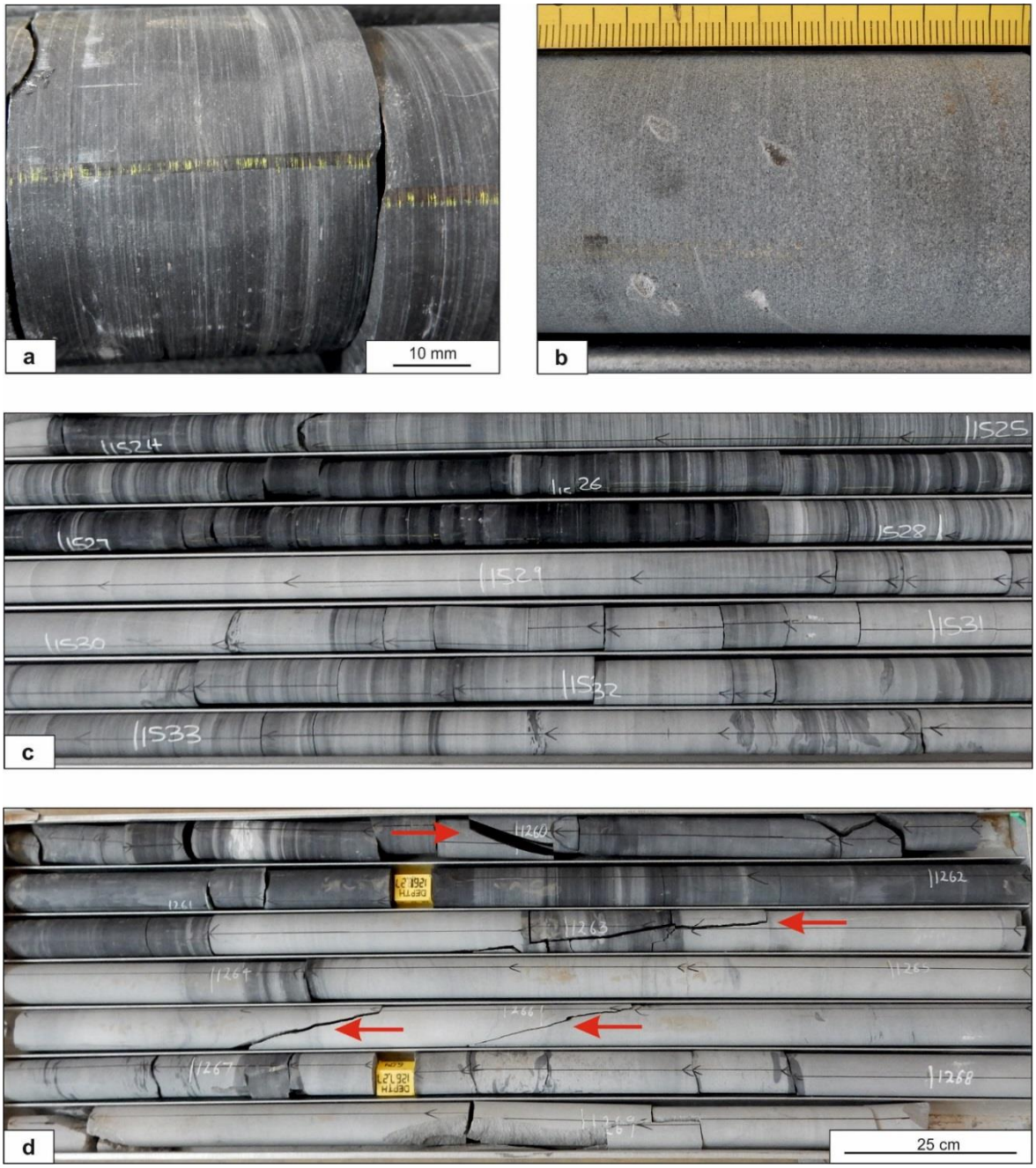

Figure 4.14: Ripon Formation sandstone and shales intersected in borehole KWV-1 **(a)** Laminated shale of the Wonderfontein Member**. (b)** Medium grained sandstone of the Pluto's Vale Member between the depths of 1530.84 – 1530.92 m. Note: scale bar in millimetres. **(c)** An overview of the thinly bedded sandstones and shales of the Wonderfontein Member. **(d)** Sandstones of the Wonderfontein Member between the depths of 1259.50 m – 1269.50 m with sub-vertical fractures (marked by red arrows).

Microscopy

Very fine-grained sandstones (Figure 4.15a) contain sub-rounded to rounded grains of quartz and feldspar as well as shale fragments in a clay-sized matrix classifying them as feldspathic greywackes (Folk 1954). Feldspars include albite as well as microcline that have been partially altered to clays. Muscovite, biotite and chlorite were also observed within the poorly sorted sandstones.

Fine-grained sandstones (lithic arkoses; Figure 4.15b) contain angular to sub-rounded quartz, albite, microcline, and lithic fragments within a clay-sized matrix. Chert fragments, zircon, chlorite and muscovite were also observed within the moderately sorted sandstone. The majority of the feldspar grains had been altered to clays, possibly sericite.

The medium-grained sandstones (lithic arkoses; Figure 4.15c) contain angular to sub-angular quartz, albite, microcline, and lithic fragments within a clay-sized matrix. Muscovite, chlorite, chert, and hornblende were also observed in the poorly to moderately sorted sandstones. The primary clay content is lower than in the very-fine and fine-grained sandstones, however the majority of feldspars have been partially altered to clays.

Siltstones (Figure 4.15d) contain angular to sub-angular quartz grains, elongate muscovite as well as chert and shale fragments in a clay-sized matrix. Abundant organic particles were also observed. Figure 4.16 displays opaque phytoclasts (a), amorphous organic material (b) a possible acritarch (c), opaque phytoclasts with remnant tracheid possibly from a vascular plant. The playnological samples are from an organic rich siltstone layer at a depth of 1316 m.

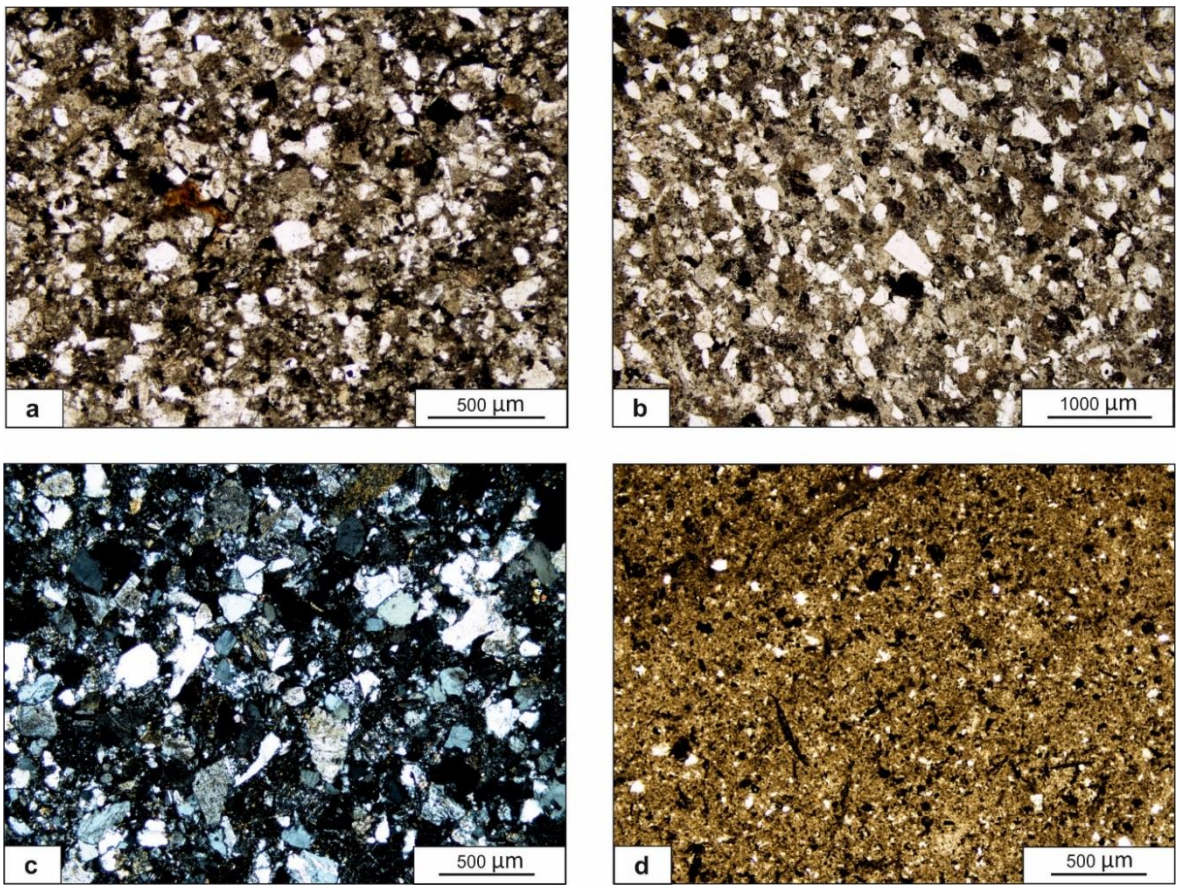

Figure 4.15: Ripon Formation intersected in borehole KWV-1 **(a)** Very fine to fine-grained feldspathic greywacke containing quartz, feldspar, lithic fragments in clay-sized matrix with organic matter. Plane polarized light. **(b)** Fine-grained lithic arkose containing predominantly quartz, lithic fragments in clay-sized matrix. Plane polarized light. **(c)** Medium-grained lithic arkose consisting of quartz, feldspar, lithic fragments in clay-sized matrix. Cross polarized light. **(d)** Siltstone containing abundant quartz and organic matter. Plane polarized light.

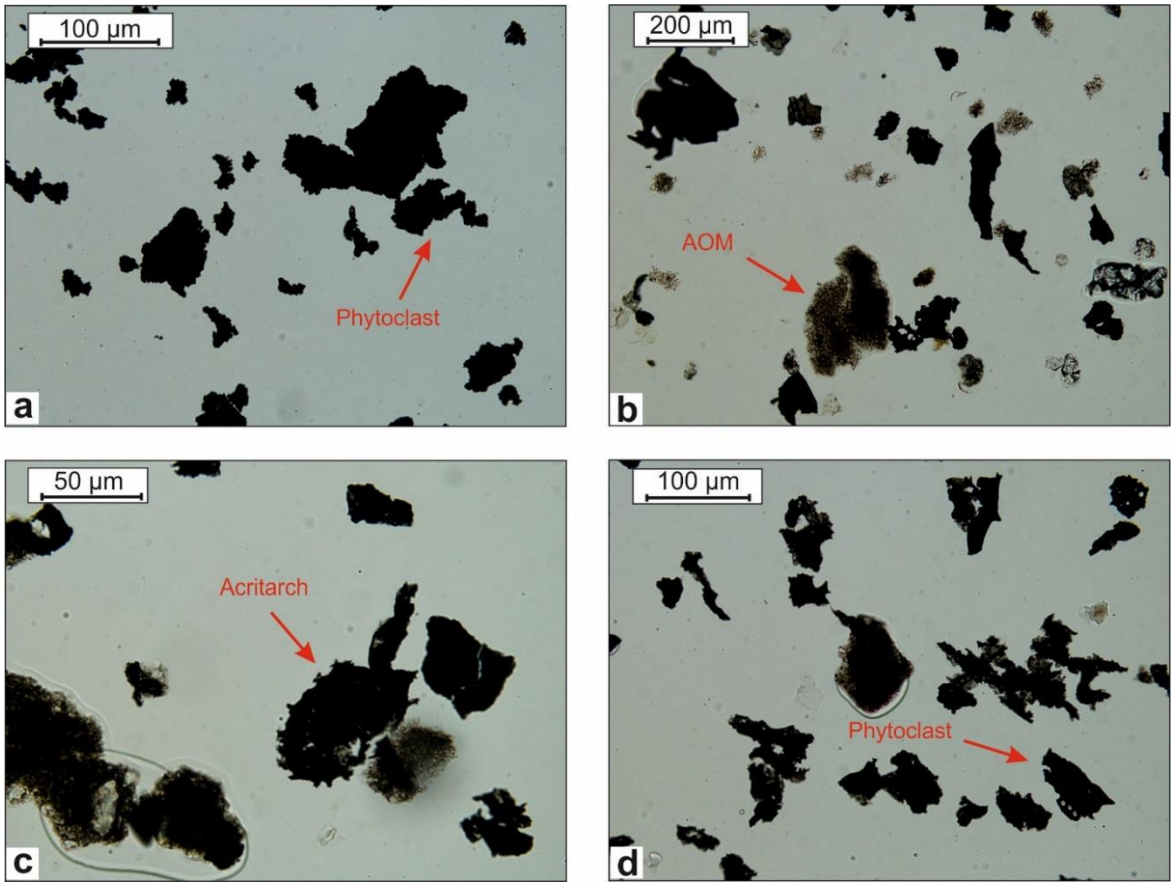

Figure 4.16: Palynological sections from a siltstone layer within the Ripon Formation (Wonderfontein Member) at a depth of 1316 m from KWV-1. **(a)** Opaque phytoclasts. **(b)** Amorphous organic material (AOM) and phytoclasts. **(c)** Possible acritarch with phytoclasts. **(d)** Remnant tracheid within a phytoclast from a vascular plant.

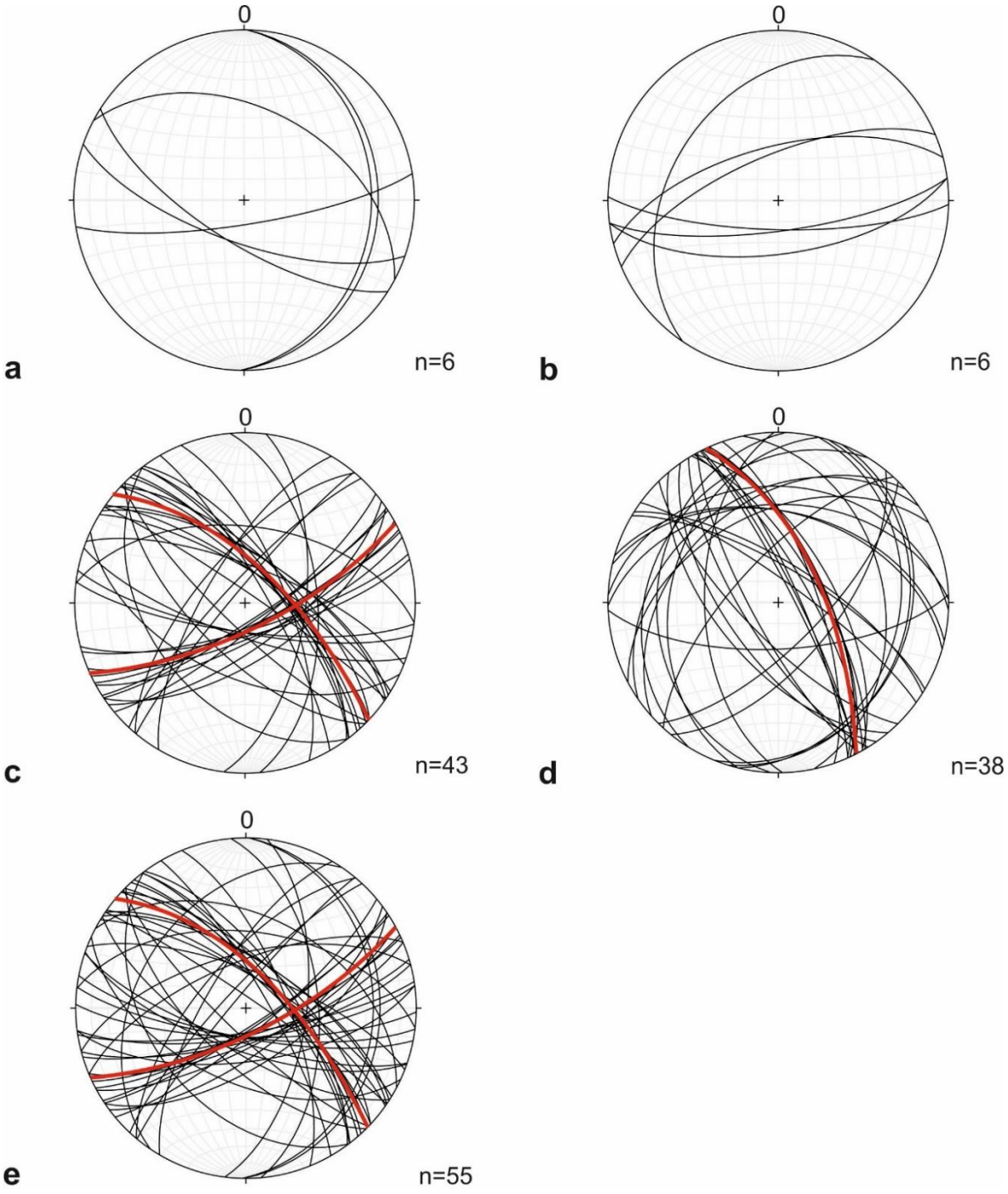

Figure 4.17: Stereonet plots (Equal Area Schmidt) of fractures recorded by the downhole Formation dipmeter tool from Ripon Formation sandstones and dolerite intrusions. **(a)** Trumpeters Member. **(b)** Wonderforntien Member. **(c)** Pluto's Vale Member. **(d)** Dolerite intrusions. **(e)** All sandstone members combined.

Fractures

Down-hole logging with the Formation Dipmeter tool recorded measurement from a possible 93 fractures within the borehole wall (Figure 4.17). The number of fractures recorded increases with depth from six measurements in the Trumpeters and Wonderfontien members, to 43 fractures in the Pluto's Vale Member. The six dolerite intrusions intersected throughout the Ripon Formation contain 38 fractures. Fracture orientations are scattered, however best fit lines suggest two predominant steeply dipping fracture orientations (NE-SW and NW-SE) intersecting at approximately 45°. The fractures associated with the dolerite intrusions are highly variable ranging from near vertical to shallow with a continuous range of orientations. A best-fit line suggests a prevalence of a steeply dipping fracture system oriented NNW to SSE. All the fractures with the Ripon Formation sandstones and dolerites are closed fractures, with no aperture recorded by the Formation Dipmeter tool.

Petro- and thermophysical rock properties

Ranges and mean values of density, porosity, permeability, thermal conductivity, and thermal diffusivity of the Ripon Formation's silt- and sandstones from borehole KWV-1 are provided in Table 4.3. Specific heat capacity at different temperatures (25°C, 80°C, 100°C, 200°C) and for extrapolated temperatures at reservoir depths are provided in Table 4.4.

Siltstones have porosities below 1%, their permeabilities are below 0.0010 mD ($9.87 \cdot 10^{-19} m^2$), the mean density is 2,740 kg/m^3. Very fine-grained sandstones range in porosity from 1.2–1.3% with a mean of 1.22%. Their permeabilities show a mean value of 0.0011 mD ($1.09 \cdot 10^{-18} m^2$), the mean density is 2,680 kg/m^3. The fine-grained sandstones range in porosity from 0.8–1.8% with a mean of 1.1%. The permeabilities of this lithology have a mean value of 0.0020 mD ($1.97 \cdot 10^{-18} m^2$), the mean density is 2,700 kg/m^3. The medium-grained sandstones range in porosity from 1.5–2.2% with a mean of 1.7%. Their permeabilities are below 0.0010 mD ($9.87 \cdot 10^{-19} m^2$), the mean density is 2,650 kg/m^3.

The thermal conductivity of the siltstones shows a mean of 3.21 W/(m·K) with a standard deviation of 0.03 W/(m·K); Very fine-grained sandstones have a mean of 3.26 W/(m·K) with a standard deviation of 0.04 W/(m·K); Fine-grained sandstones exhibit a mean of 3.67 W/(m·K) with a standard deviation of 0.05 W/(m·K); Medium-grained sandstones shows a mean thermal conductivity of 3.19 W/(m·K) with a standard deviation of 0.04 W/(m·K). Heat capacity is highest in siltstones and fine-grained sandstones (Table 4.4).

Figure 4.18 summarises the thermophysical property trends on a reservoir scale with fine grained sandstone exhibiting the highest thermal conductivity and along with siltstones have the highest specific heat capacity.

Table 4.3: Petro- and thermophysical rock properties (means) of the Ripon Formation (southern Karoo Basin, South Africa). Red box indicated optimum lithology.

Lithology	Density [kg/m^3]	Porosity [%]	Permeability [m^2]	Thermal conductivity [W/(m·K)]	Thermal diffusivity [m^2/s ·10^{-6}]	Specific heat capacity [kJ/(kg·K)]
Siltstone	2750	<1	9.87 x 10^{-19}	3.21	1.34	0.93
Very fine-grained sandstone	2680	1.22	1.09 x 10^{-18}	3.26	1.34	0.91
Fine-grained sandstone	2700	1.1	1.25 x 10^{-18}	3.67	1.52	0.89
Medium grained sandstone	2650	1.7	9.87 x 10^{-19}	3.19	1.38	0.87

Table 4.4: Specific heat capacity values (kJ/(kg·K)) at different temperatures (25°C, 80°C, 100°C, 200°C) and for extrapolated temperatures at reservoir depths 3000 m (103°C) and 3500 m (117°C), respectively. Red box indicates optimum lithology.

Location	Lithology	T = 25°C	T = 80°C	T = 100°C	T = 200°C	T = 103°C	T = 117°C
KWV-1	Siltstone	0.80	0.88	0.91	1.06	0.92	0.94
KWV-1	Very fine-grained sandstone	0.80	0.87	0.89	1.02	0.90	0.92
KWV-1	Fine-grained sandstone	0.80	0.86	0.88	1.00	0.88	0.90
KWV-1	Medium-grained sandstone	0.77	0.83	0.86	0.97	0.86	0.88

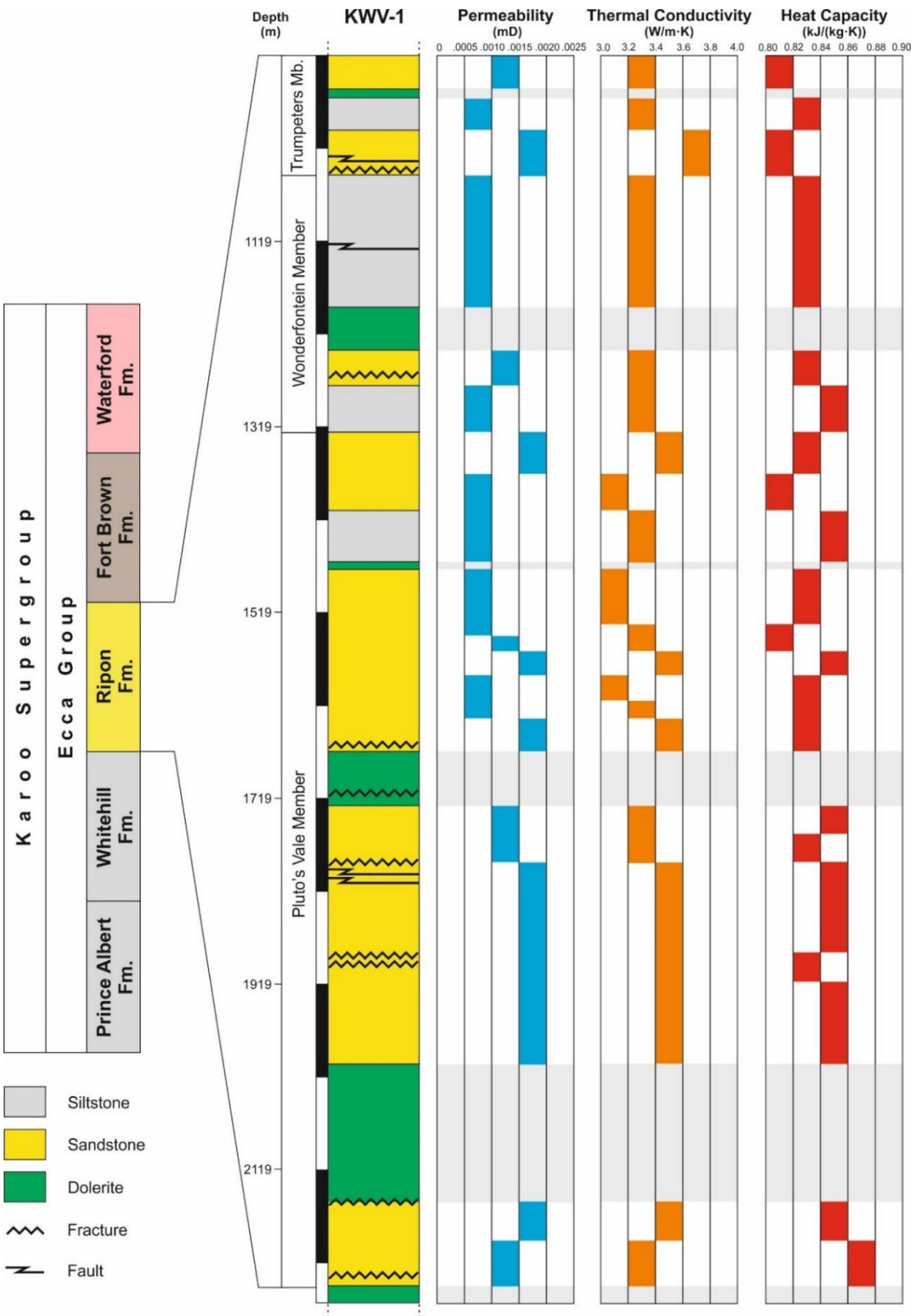

Figure 4.18: Stratigraphic log of the Ripon Formation intersected in borehole KWV-1 and trends of thermophysical properties on a reservoir scale. Intervals without measurements (dolerites) are grey shaded. Scale bars 100 m, Fm. = Formation. All lithologies are classified as impermeable. Fine-grained sandstones, (the dominant lithology), show the highest thermal conductivity. Specific heat capacity reveals the highest values in siltstones and fine-grained sandstones.

IV. Fort Brown Formation

The Fort Brown Formation was intersected at a depth of 264.5 m. The formation consists of four dominant lithologies: Sandstones are fine to medium grained and range in colour from grey to light grey. Bedding is generally massive although laminations were observed. Ripple marks and flaser bedding are common. Slumping of sandstone into finer shale was documented rarely. Concretions were noted within the sandstone units.

Shale varies in colour from dark grey to black and ranges from massive to layered with bedding defined by lighter and darker layers. Occasional discrete ripple marked sandstone layers were documented within larger shale bodies. Black coloured shale appears to be more carbonaceous than dark grey shale. Pink iron staining was observed within several shale layers. Concretions were also recorded within shale.

A clay pebble conglomerate, consisting of light grey to white, rounded clasts within a dark grey matrix, was documented. Clasts are larger (<8 mm) and more angular at the base of units and fine upwards (<2mm) and are matrix supported.

Eight dolerite intrusions were intersected (381.65 m, 424.8 m, 434.5 m, 444.9 m, 641.95 m, 774.24 m, 776.44 m, and 846.45 m) more commonly within shales than sandstones. Dolerite intrusions range in thickness from less than 1 m to 41 m. Several ‘baked contacts’ were observed comprising more crystalline lithologies containing 1 mm black specks.

Fracture zones were encountered at 291.23 m and 304.28 m containing near vertical fractures with calcite infill along with prominent brecciation and decomposition of the shale.

V. Waterford Formation

The Waterford Formation starts at a depth of 189.2 m and is composed of sandstone and mudstone. Sandstone is grey to light grey and is interbedded with grey near massive

mudstone. Some mudstone layers are more fissile and are deemed shale. Occasional ripple mark textures and flaser bedding were recorded. An upwards fining mudstone conglomerate was documented at 189.2 m. Fault zones occur at 216.9 m and 242.8 m with pyritised slickensides at 45° to the core axis along with calcite filled fractures at 70-80° to the core axis.

VI. Koonap Formation (Adelaide Subgroup)

The Koonap Formation consists of interbedded sandstones and mudstones. Sandstones are grey to light grey in colour and range from laminated to massive. Ripple mark textures as well as flaser bedding were observed. Mudstones are reddish grey to grey and range from massive to layered, with layers defined by colour differences. A matrix supported clay pebble conglomerate was intersected at a depth of 127.11 m. Red iron staining was noticed to be pervasive throughout. A 1.5 cm greenish grey tuff was observed at 184.15 m. Two dolerite sills were intersected at 14.7 m and 92.24 m and were 1.8 and 34.87 m thick respectively.

4.7. Geothermal Potential

4.7.1. Volumetric calculation

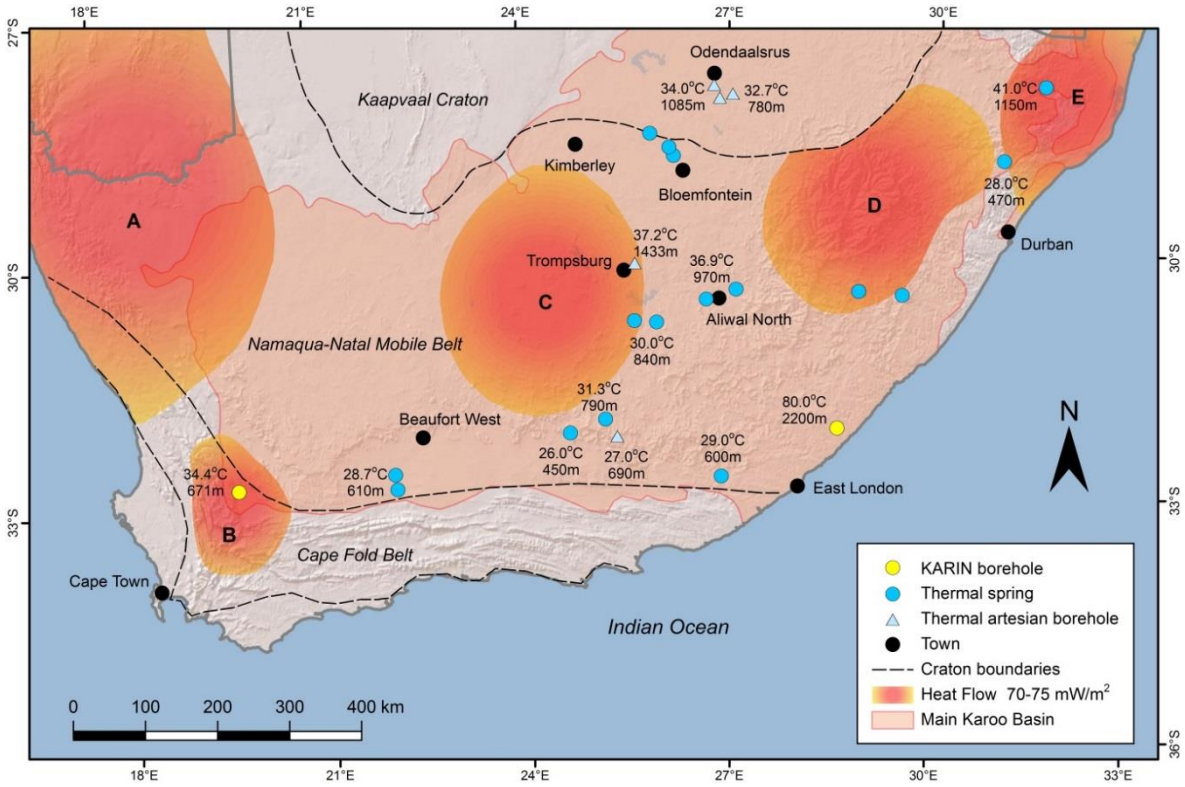

Figure 4.19: Geothermal resource base map of the Karoo Basin highlighting areas (A-E) of elevated heat flow (70-75 mW/m^2), location of thermal springs and thermal artesian boreholes with measured surface water temperatures (°C) and depth of origin (m), and location of KARIN boreholes KZF-1 (northeast of Cape Town, Western Cape, area B) and KWV-1 (northeast of East London, Eastern Cape) with measured down-hole temperatures at 671 m and 2200 m depth, respectively. Data compiled from Jones (1992), Steyl et al. (2012), De Kock et al. (2016 a,b), and Bird et al. (2006).

Data available from literature (Jones, 1992, 2001) describing areas of high heat flow within the Karoo Basin was integrated into a geographical information system for areal and volumetric calculation of potential exploration areas (Figure 4.19 A-E). The most suitable area for further investigation was the area west of Trompsburg, Free State (Area C, Table 4.5), where heat flows ranging from 70–75 mW/m^2 are observed. In this area the Ripon Formation is approximately 650 m thick. Multiplying the formation thickness (650 m) by

the area (74853.79 km^2) results in a potential geothermal exploration reservoir volume of 48654.96 km^3. The depth of the Ripon Formation in this area is assumed.

Area 123 (Figure 4.20) contains the Ripon Formation at depths exceeding 3500 m. Stratigraphic reference sections (Figure 4.20 1-3) were used from literature (Johnson et al. 2006; Steyl et al. 2012) to prove depths. A potential reservoir area of 16000 km^2 (Table 4.5) multiplied by a mean formation thickness of 650 m results in a potential reservoir volume of 10400.00 km^3.

Table 4.5. Areas of elevated hea heat flow (70-75mW/m²) within South Africa.

Area*	Location within the Main Karoo Basin	Areal extent (km²)
A	Northwestern part of the basin	162848.30
B	Southwestern part of the basin	20315.58
C	Central part of the basin	74853.79
D	Central part of the basin	62291.06
E	Northeastern part of the basin	32849.13
123	Southern part of the basin	16000.00

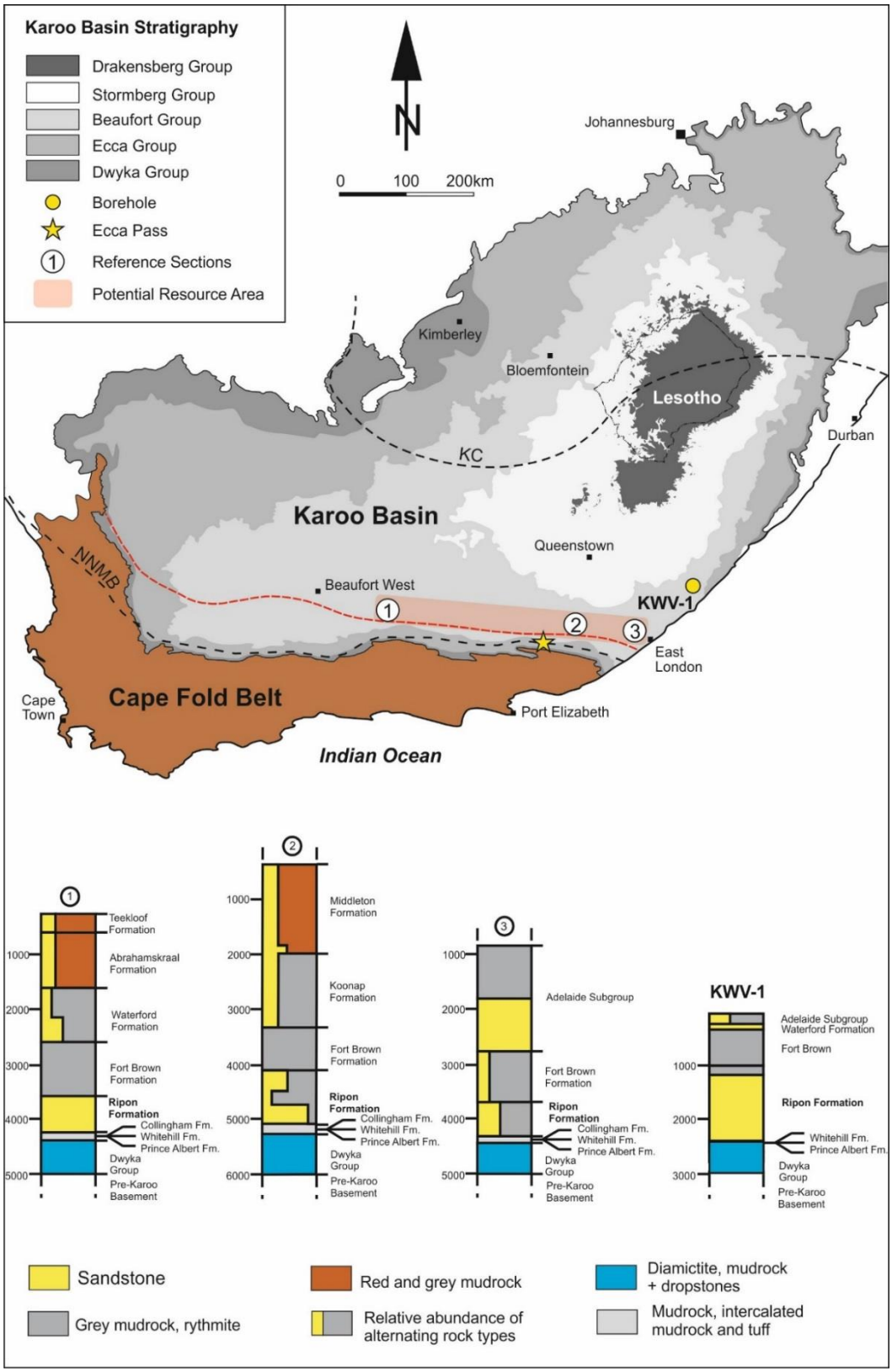

Figure 4.20: Stratigraphic reference sections (1-3) of the Permian Ecca Group (Prince Albert, Whitehill, Collingham, Ripon, Fort Brown and Waterford formations) and lower Beaufort Group (Middleton, Koonap, Abrahamskraal and Teekloof formations) in the Eastern Cape, compiled and modified from Catuneanu et al. (1998), Johnson et al. (2006) and Steyl et al. (2012), and borehole KWV-1 (this study).

4.7.2. Geothermal gradient

Down-hole temperature data from boreholes KZF-1and KWV-1 provided information on the geothermal gradient (Table 4.6). In both areas, a moderately elevated geothermal gradient was observed (mean surface temperature of 18°C). Temperatures of 80°C at 2200 m depth recorded from borehole KWV-1 indicate a geothermal gradient of 28.2°C/km in the Willowvale area northeast of East London (Eastern Cape). Temperatures of 34.4°C at 671 m recorded from borehole KZF-1 indicate a geothermal gradient of 24.5°C/km in the Ceres area (Western Cape). Reservoir temperatures (reservoir depth 3000 m) of 104°C to 117°C are thus expected in the southern Karoo Basin.

Table 4.6. Geothermal gradient calculated from borehole temperatures at depth. Note: mean surface temperature is 18°C.

Borehole	Temperature (°C)	Depth (m)	Geothermal Gradient (°C/Km)
KZF-1	34.4	671	24.5
KWV-1	80	2200	28.2

4.7.3. Heat in Place

Following the volumetric approach by Muffler and Cataldi (1978), the calculation of the heat in place provides a first estimation of the theoretically available thermal energy from a geothermal system. Heat in place (E_{th}) was calculated using lithological data from the Ripon Formation from the Ecca Pass (Tables 4.7, 4.9) exposure as well as from borehole KWV-1 (Tables 4.8, 4.10).

These data are applied to both potential exploration areas, Area C (Figure 4.19) and Area 123 (Figure 4.20). Minimum and maximum values for the geothermal gradient were used to give a range of potential heat in place at two depths 3000 m (Tables 4.7, 4.8) and 3500 m (Tables 4.9, 4.10). Heat in place is denoted in exojoules (10^{18}) and converted into terawatt hours.

Table 4.7: Heat in place using **Ecca Pass** Ripon Formation lithologies at a reservoir depth of **3000m**.

Location	Volume (m^3)	E_{th} min (EJ)	E_{th} Max (EJ)	Terawatt hours min (TWh)	Terawatt hours max (TWh)
Area C	48654963387483.1	8.42	9.67	2339.22	2686.95
Area 123	10400000000000	1.80	2.07	500.01	574.33

Table 4.8: Heat in place using borehole **KWV-1** Ripon Formation lithologies at a reservoir depth of **3000m**.

Location	Volume (m^3)	E_{th} min (EJ)	E_{th} Max (EJ)	Terawatt hours min (TWh)	Terawatt hours max (TWh)
Area C	48654963387483.1	8.66	9.94	2403.31	2760.56
Area 123	10400000000000	1.85	2.12	513.71	590.07

Table 4.9: Heat in place using **Ecca Pass** Ripon Formation lithologies at a reservoir depth of **3500m**.

Location	Volume (m^3)	E_{th} min (EJ)	E_{th} Max (EJ)	Terawatt hours min (TWh)	Terawatt hours max (TWh)
Area C	48654963387483.1	9.67	11.27	2686.95	3129.5
Area 123	10400000000000	2.09	2.40	581.09	668.93

Table 4.10: Heat in place using borehole **KWV-1** Ripon Formation lithologies at a reservoir depth of **3500m**.

Location	Volume (m^3)	E_{th} min (EJ)	E_{th} Max (EJ)	Terawatt hours min (TWh)	Terawatt hours max (TWh)
Area C	48654963387483.1	10.05	11.57	2793.04	3215.24
Area 123	10400000000000	2.15	2.47	597.01	687.26

Using lithological data from the Ecca Pass at a predicted reservoir depth of 3000 m (Table 7) a range of heat in place (HIP) for Area C is 8.42 – 9.67 EJ (2339.22 – 2686.95 TWh) and the range of HIP for Area 123 is 1.80 – 2.07 EJ (500.01 – 574.33 TWh).

Utilising the same parameters and applying the lithological data from borehole KWV-1 (Table 4.8) results in a range of HIP for Area C of 8.66 – 9.94 EJ (2403.31 – 2760.56 TWh) and a range of 1.85 – 2.12 EJ for Area 123 (513.71 – 590.07 TWh).

Using lithological data from the Ecca Pass at a predicted reservoir depth of 3500 m (Table 4.9 results in a HIP range for Area C of 9.67 – 11.27 EJ (2686.95 – 3129.50 TWh) and a range of 2.09 – 2.40 EJ (581.09 - 668.93 TWh) for Area 123.

Utilising the same parameters and applying the lithological data from borehole KWV-1 (Table 4.10) results in a range of HIP for Area C of 10.05 – 11.57 EJ (2793.04 – 3215.24 TWh) and a range of 2.15 – 2.47 EJ (597.01 – 687.26 TWh) for Area 123.

4.7.4. Economic feasibility

Techno-economic feasibility has recently been performed for a geothermal resource assessment of Permian Rotliegend formations in the Netherlands suitable for direct heat production, distinguishing between heat in place (HIP), potential recoverable heat (PRH), technical potential (PRH/30 yr), and recoverable heat (RH). Following Van Wees et al.

(2012) the recoverable heat (RH) is about 33% of the HIP and the technical lifetime of a doublet system is 30 years.

Table 4.11: Recoverable heat using **Ecca Pass** Ripon Formation lithologies at a reservoir depth of **3000m**.

Location	E_{th} min (EJ)	E_{th} Max (EJ)	Terawatt hours min (TWh)	Terawatt hours max (TWh)	Million Barrels of Oil Equivalent min (MBOE)	Million Barrels of Oil Equivalent max (MBOE)
Area C	2.79	3.19	771.94	886.69	475.9	544.2
Area 123	0.59	0.68	165.00	189.53	100.6	116.0

Table 4.12: Recoverable heat using borehole **KWV-1** Ripon Formation lithologies at a reservoir depth of **3000m**.

Location	E_{th} min (EJ)	E_{th} Max (EJ)	Terawatt hours min (TWh)	Terawatt hours max (TWh)	Million Barrels of Oil Equivalent min (MBOE)	Million Barrels of Oil Equivalent max (MBOE)
Area C	2.56	3.28	793.09	910.98	436.7	559.6
Area 123	0.610	0.70	169.52	194.72	104.0	119.4

Table 4.13: Recoverable heat using **Ecca Pass** Ripon Formation lithologies at a reservoir depth of **3500m**.

Location	E_{th} min (EJ)	E_{th} Max (EJ)	Terawatt hours min (TWh)	Terawatt hours max (TWh)	Million Barrels of Oil Equivalent min (MBOE)	Million Barrels of Oil Equivalent max (MBOE)
Area C	3.19	3.71	886.69	1032.74	554.2	632.9
Area 123	0.69	0.79	191.76	220.75	117.7	134.7

Table 4.14: Recoverable heat using borehole **KWV-1** Ripon Formation lithologies at a reservoir depth of **3500m**.

Location	E_{th} min (EJ)	E_{th} Max (EJ)	Terawatt hours min (TWh)	Terawatt hours max (TWh)	Million Barrels of Oil Equivalent min (MBOE)	Million Barrels of Oil Equivalent max (MBOE)
Area C	3.32	3.82	921.70	1061.03	566.4	651.7
Area 123	0.71	0.82	179.01	226.80	121.1	139.9

Using lithological data from the Ecca Pass at a predicted reservoir depth of 3000 m (Table 4.11) a range of recoverable heat (RH) for Area C is 2.79 – 3.19 EJ (771.94 – 886.96 TWh; 475.9 – 544.2 MBOE) and the range of RH for Area 123 is 0.59 – 0.68 EJ (165.00 – 189.53 TWh; 100.6 – 116.0 MBOE).

Utilising the same parameters and applying the lithological data from borehole KWV-1 (Table 4.12) results in a range of RH for Area C of 2.56 – 3.28 EJ (793.09 – 910.98 TWh; 436.7 – 559.6 MBOE) and a range of 0.61 – 0.70 EJ for Area 123 (169.52 – 194.72 TWh; 104.0 – 119.4 MBOE).

Using lithological data from the Ecca Pass at a predicted reservoir depth of 3500 m (Table 4.13) results in a RH range for Area C of 3.19 – 3.71 EJ (886.96 – 1032.74 TWh; 554.2 – 632.9 MBOE) and a range of 0.69 – 0.79 EJ (191.76 – 220.75 TWh; 117.7 – 134.7 MBOE) for Area 123.

Utilising the same parameters and applying the lithological data from borehole KWV-1 (Table 4.14) results in a range of RH for Area C of 3.32 – 3.82 EJ (921.70 – 1061.03 TWh; 556.4 – 651.7 MBOE) and a range of 0.71 – 0.82 EJ (179.01 – 226.80 TWh; 121.1 – 139.9 MBOE) for Area 123.

4.8. Discussion

4.8.1. Stratigraphy and depositional environment

I. Lower Ecca Group Shales

According to Johnson et al. (2006), the Permian Ecca Group contains numerous formations (16) that reflect lateral variations in depositional environment. The authors continue to state that the basal Prince Albert and Whitehill Formations occur throughout the basin, and that the remaining formations can be categorised based on geographical area as follows:

(1) Southern formations (Collingham, Visckuil, Laingsburg, Ripon, Fort Brown and Waterford).
(2) Western and northwestern formations (Tierberg, Skoorsteensberg, Kookforntien, and Waterford).
(3) Northeastern formations (Pietermatitzburg, Vryheid and Volksrust).

<u>Prince Albert Formation</u>

Johnson et al. (2006) described the southern facies of the formation as being ‘characterised by the predominance of dark-grey, pyrite-bearing, splintery shale. Geel et al. (2013) described an olive-grey mudrock from a core drilled in the Eastern Cape Province. Herbert and Compton (2007) observed phosphatic and chert concretions within a dark siltstone.

The Prince Albert Formation exposed along the Ecca Pass and intersected within borehole KWV-1 compares well with descriptions from literature. The formation is poorly exposed along the Ecca Pass and consists of fragmented shards of greenish-grey shale. Within borehole KWV-1 the formation comprises light-green to grey shale interbedded with sandstone. Sulphide mineralisation (pyrrhotite, pyrite) was observed, as well as occasional concretions.

The fine grain size of the sediment in conjunction with the laminated bedding suggest a low energy depositional environment. The presence of sulphide mineralisation may indicate the presence of reducing conditions during deposition. Discrete sandstone bodies described in borehole KWV-1 indicate periods of increased depositional energy.

The observations and inferences from this study conform to the generally accepted depositional setting of the southern Prince Albert Formation from literature. The formation represents syn- to-post glacial suspension settling of mud in a marine environment with sand deposited by turbidity currents (e.g. Johnson et al., 2006; Herbert and Compton, 2007; Geel et al., 2013).

Whitehill Formation

The Whitehill Formation in the southern portion of the basin consists of thinly laminated 'black pyrite-bearing carbonaceous shale' (Johnson et al., 2006) that weathers white under oxic conditions providing a useful marker layer (Johnson et al., 2006; Geel et al., 2013). The depositional environment of the formation is generally accepted to be of stratified-marine origin (Johnson et al., 2006). Chukwuma and Bordy (2016) identified five distinct facies for this formation.

The Whitehill Formation exposed along the Ecca Pass is highly weathered (Figure 4.5b) and consists entirely of mudstone. The distinct white colour observed is due to abundant gypsum (Figure 4.5c, e) from the breakdown of sulphides under atmospheric conditions. The characteristic white colour positively identified this formation at the study location. The finely laminated nature of the shale (Figure 4.5a) in conjunction with the large quantity of former sulphides (Figure 4.5c) indicates deposition in an environment of very low energy under anoxic conditions as described in literature (e.g. Visser, 1992; Johnson et al., 2006; Geel et al., 2013; Chukwuma and Bordy, 2016).

However, in borehole KWV-1 the laminated pyritic black carbonaceous shale is interbedded with discrete very fine-grained sandstone (Appendix C). This excursion from the usually very distinct lithology (carbonaceous shale) is described in Johnson et al. (2006) to occur only in the northeast of the basin, not in the southeast where borehole KWV-1 is located. 'The Whitehill Formation loses its distinctive lithological character towards the northeast, with its lower part containing siltstone and very fine grained sandstone' (Cole and McLachlan, 1991).

Chukwuma and Bordy (2016) describe two end-member facies: F1 consisting of pyritic carbonaceous black shale with high TOC from the settling of 'pelagic snow', and F5 comprising light grey siliceous coarse-grained shale with the deposition of sand and silt in an oxygenated water body. The occurrence of pyritic carbonaceous black shale (facies F1) interbedded with sandstone (possibly F5) within borehole KWV-1 appears anomalous. The formation exposed along the Ecca Pass would most likely fall into the more distal and anoxic end member (facies F1/F2) and it is located approximately 200 km east of borehole KWV-1 with very little latitudinal variation.

It may be possible that fine-grained sandstones were deposited into the distal anoxic portion of the basin during rare 'higher-than-usual' energy events on a basin margin submarine fan. The events would have had to have a negligible effect, any long-term overall anoxia in order for the F1 facies to be prevalent as observed in the core. Trace fossils from 'doomed pioneers' (Föllmi and Grimm, 1990), swept down in the distal basin during high energy events, could be expected within the discrete coarser layers, supporting the theory. However, no trace fossils were reported.

An alternate explanation is that the discrete sandstone bodies may have been misidentified and could possibly be as result of biogenic or volcanic sedimentation. Pelagic sediments

with a biogenic origin are the most abundant in the modern oceans (Nichols, 2009). The deposition of a calcareous ooze could produce a fine-grained limestone, or deposition of a siliceous ooze composed of Radiolaria could produce a chert with fine white spots within the rock (Nichols, 2009). The deposition of coarse silicic air-fall tuff could also produce a sedimentary layer quite different from the surrounding mudstone. The Collingham Formation contains numerous tuffs (Viljoen, 1992) and a chert layer (Johnson et al., 2006). It is plausible that a tuff or a biogenic layer could have been interpreted as a fine-grained sandstone without further investigation.

Collingham Formation

Outcrops of the Collingham Formation are limited to the southern and western portions of the Main Karoo Basin according to Johnson et al. (2006). Black et al. (2016) reported three interbedded lithologies:

(1) A dark-grey fine-grained fissile shale.

(2) A light-olive altered tuff.

(3) A rarer fine to very fine-grained sandstone.

Viljoen (1992) described a 'rhythmic alteration of thin continuous beds of hard siliceous mudrock and very thin beds of softer yellowish tuff'. The presence of the highly abundant yellowish tuff (Figure 4.6e) and the tabular and laterally extensive shale (Figure 4.6d) aided in positively identifying this formation along the Ecca Pass road cutting. The formation is generally accepted to have been deposited as a result of suspension settling in deep water with discrete low density turbidity currents responsible for the siltier and sandier layers (Kingsley, 1977; Viljoen, 1992). The authors base their palaeoenvironmental interpretation on the trace fossil assemblage in conjunction with the fine-grained nature of the sediment and the lateral extent of the beds. However, a recent study by Black et al. (2016) proposed

that the Collingham Formation was deposited in an intertidal marine or terrestrial environment.

Observations from the Ecca Pass largely concur with Johnson et al. (2006). No indicators of a tidal nature (mudcracks, herringbone cross-stratification, mud draped on cross-beds and tidal bundles; Nichols, 2009) were observed at the Ecca Pass. Additionally, tidal reworking of sediment would not be conducive to preserving thin ash layers as is characteristic of this formation (Figure 4.6d, e). Deeper lake deposits (laminated dark shale and thin turbiditic sands; Nichols, 2009) could account for the features observed, however two features counteract this theory;

(1) The wide extent of the formation,
(2) The presence of *Nereites* trace fossils observed by Kingsley (1977) and Viljoen (1992) in Johnson et al. (2006). *Nereites* trace fossils are indicative of bathyal to abyssal depths (Nichols, 2009).

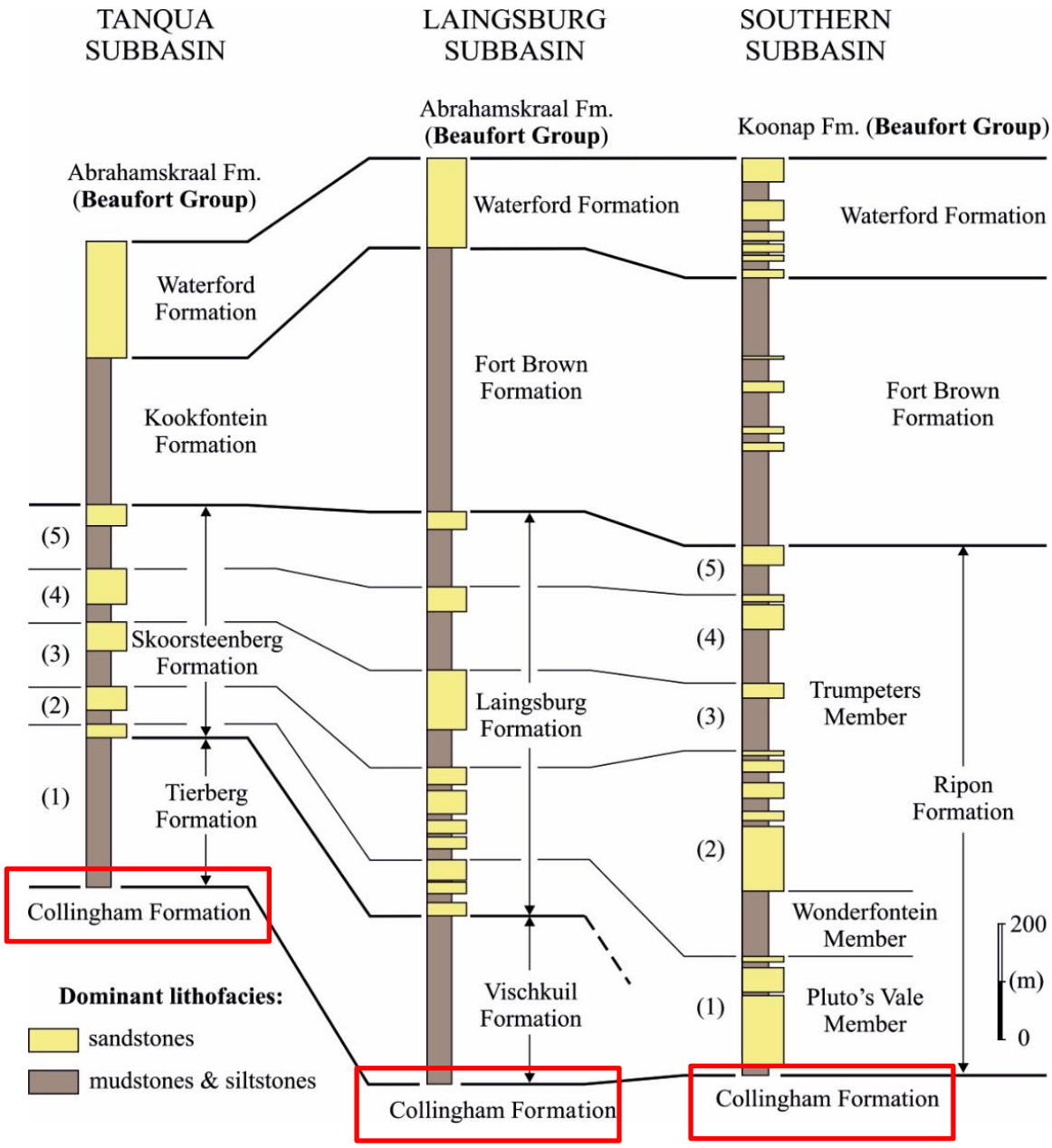

Figure 4.21: The Collingham Formation occurs below the Tierberg Formation (Tanqua Subbasin), below the Vischkuil Formation (Laingsburg Subbasin) and below the Ripon Formation (Southern Subbasin). The formation is absent in borehole KWV-1. Modified after Catuneanu et al. (2002).

The complete absence of the Collingham Formation within borehole KWV-1 (Appendix C) is anomalous. The formation occurs in the Tanqua Subbasin, the Laingsburg subbasin and the Southern subbasin (Figure 4.21). Johnson et al. (2006) includes the formation in all stratigraphic logs from the southern basin below a latitude of 32°S. However, the usually 30 m – 70 m thick characteristically ash-rich formation was not intersected by borehole KWV-1. In the borehole the Whitehill Formation is separated from the Ripon Formation by a 20 m thick dolerite intrusion (Figure 4.22).

There are several possible explanations for the absent Collingham Formation within the borehole. The first is that the usual Collingham Formation environment of deposition was locally not developed. It is plausible that a different depositional facies developed due to differing conditions (topography, currents, sediment supply) on a small scale. The major draw-back to this theory is that the voluminous volcanic ash that is characteristic of this formation is absent in the core. Air-fall ashes were deposited on a basin wide scale during the Early Permian. Volcanic tuffs have been reported from within the Tanqua, Laingsburg and Southern subbasins as well as the equivalent stratigraphy in South America (McKay et al., 2015 and authors there within). Ash deposition would be independent of any subaqueous facies except a facies where ash layers wouldn't be preserved. In the Main Karoo Basin tuff layers have been observed within tillite (Stollhofen et al., 2000), deep marine shales (Bangert et al., 1999) and turbiditic sandstones and shales (Mckay et al., 2015). If an alternative facies contemporaneous with the Collingham Formation developed then it is reasonable to expect a high volume of ash to be found within this facies, however the lower Ecca Group shales within the borehole are devoid of voluminous tuffs.

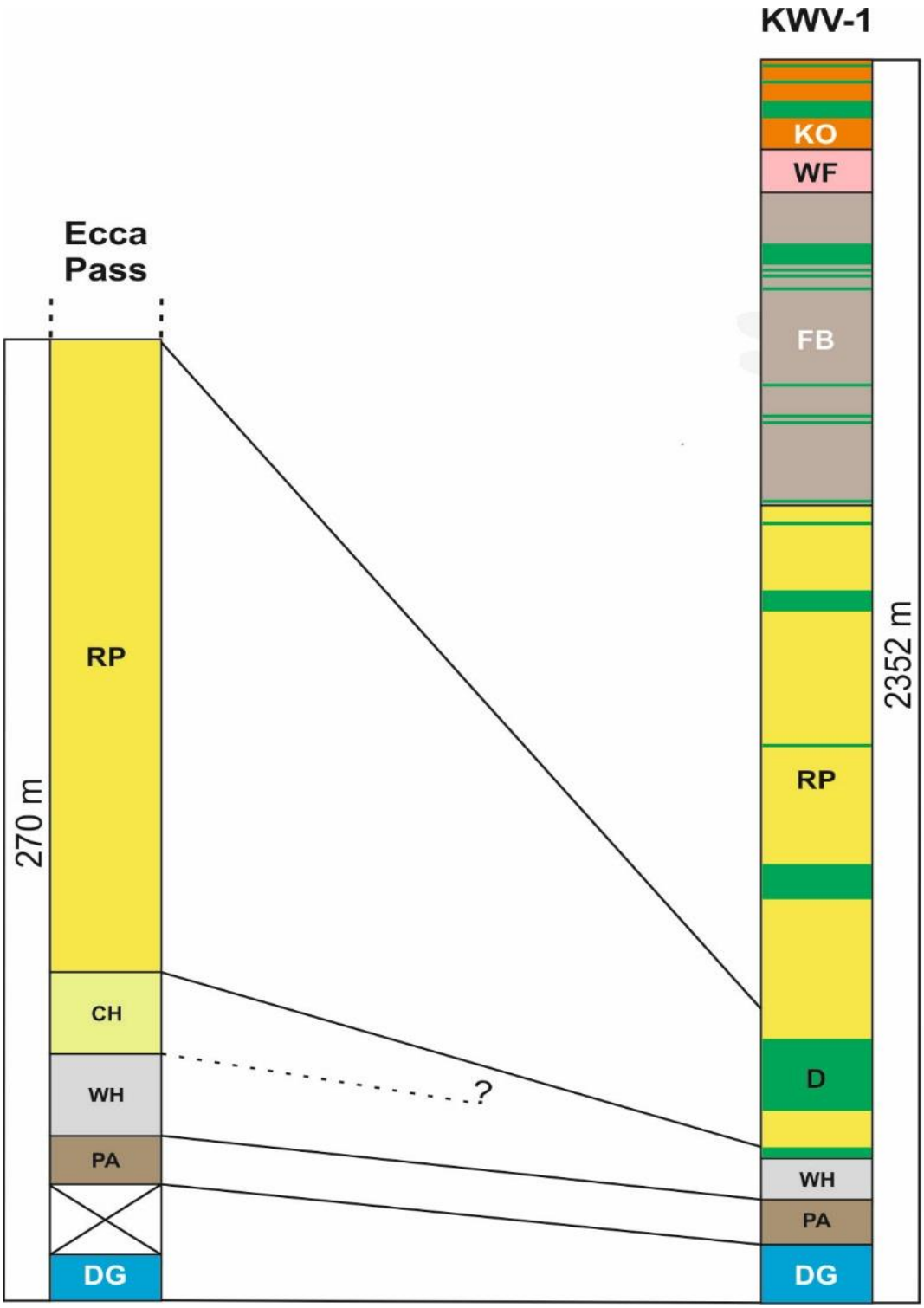

Figure 4.22: Schematic logs of the Ecca Pass and borehole KWV-1 correlating formations. The Collingham Formation is absent in borehole KWV-1. A dolerite intrusion is located between the Ripon and Whitehill formations in the borehole. Note: the two locations are 200 km apart at a similar latitude. Abbreviations: RP = Ripon Formation. CH = Collingham Formation. WH = Whitehill Formation. PA = Prince Albert Formation. DG = Dwyka Group.

A second possibility lies with the overlying turbiditic Ripon Formation. Successions of highly erosive turbidites may have scoured the underlying Collingham Formation if it was on the lower end of the thickness spectrum and not yet completely lithified. Large rip-up clasts of shale within thick sandstone packages occur at the Ecca Pass. This suggests that the shale beds the clasts originated from was completely eroded. It may be possible that a similar process occurred within the borehole region on a larger scale, locally eroding the Collingham Formation. A 42 cm thick soft sediment breccia was documented four metres from the lower boundary of the Ripon Formation. However, the lower 150 m of the Ripon Formation within borehole KWV-1 displays no large-scale rip-up shale clast conglomerate, as would be expected from such a process, and as was observed at the Ecca Pass study site. Additionally, the lower Ripon Formation in the borehole is characterised by very fine-grained sandstone with bed thickness on a millimetre scale. This suggests sediment deposition at a low energy distal location on the sea floor. Erosive bases, coarser sediment calibre and debris flow deposits (Shanmugam et al., 1985) would be expected from upper fan channelised deposits capable of intense erosion.

A third less-plausible explanation may be related to the intrusion of the 19 m thick dolerite sill at the contact of the Whitehill and Ripon formations, where the Collingham Formation should occur. If a dolerite sill intruded the Collingham Formation then it may be possible that the magma started to assimilate wall rock en-route to the surface. According to Duncan and Marsh (2006) the intrusive dolerite suite comprises the feeder system to the several-kilometres-thick flood basalt eruptions of the Drakensburg Group.

A constant stream of magma through the lithologically-weak, ash-rich formation over the eruptive period of 1-3 Ma (Duncan and Pyle, 1988; Renne et al., 1992; Baksi, 1994 in: Duncan and Marsh, 2006) may have assimilated enough wall rock to completely remove the Collingham Formation locally and in doing so expand the thickness of the sill. Any xenoliths

of wall rock would have been transported laterally with the movement of the magma, and hence would not be visible within the core. The dolerite in the core, in contact with the Whitehill and Ripon formations, would represent the last stage of intrusion at the termination of igneous activity and subsequent freezing of the magma.

It would be reasonable then to expect the dolerite to exhibit a geochemical signature reflecting the assimilation of siliceous country rock, and perhaps to show an increase in differentiation with transport distance; the eruptive lavas and higher sills having been exposed to more sedimentary rocks with upwards transport than the lower sills. However, Marsh and Mndaweni (1998) reported compositionally homogenous dykes 80 km in length. Duncan and Marsh (2006) reported that in general the basalts of the Karoo are relatively siliceous but attribute the increase to a source derived from fractionation of mantle-derived picritic precursors, and not assimilation of siliceous country rock. The authors also reported a close geochemical similarity between the dolerite suite and the eruptive lavas, nullifying the theory of wall rock assimilation during transport. The only xenoliths observed with volcanic rocks are within the upper sedimentary formations of the Karoo Supergroup where the interaction of ground water and magma have produced diatremes and breccia pipes (ibid.).

A resolute explanation for the absence of the Collingham Formation is lacking, and further investigation of the above-mentioned theories may prove fruitful.

II. Ripon Formation

The lower 224 m of the Ripon Formation is exposed along the Ecca Pass and the entire formation was intersected in borehole KWV-1. The Ripon Formation was positively identified due to the formation containing the first large quantities of sandstone in the Ecca Group. Johnson and Kingsley (1993) describe 'poorly sorted, fine to very fine-grained lithofeldspathic sandstone alternating with dark clastic rhythmite and mudrock' as characterising this formation.

The generally upwards fining sequences of medium to fine-grained sandstone followed by siltstone/mudstone (Appendix B) along with the characteristic sedimentary structures (Figure 4.7) (erosive bases, ball and pillow structures, rip up clasts) indicate a turbiditic origin of the formation. The Ripon Formation was interpreted as being deposited by turbidity currents in a submarine fan complex due to the structures preserved as well as an absence of shallow water indicators (Kingsley 1977; 1981).

Kingsley (1977; 1981) distinguished 3 members for this formation in the eastern portion of the basin:

(1) The basal Pluto's Vale Member comprising rhythmic turbiditic units of very fine- to fine-grained greywacke upwards fining to siltstone and shale.

(2) The Wonderfontein Member consisting of greenish-grey, laminated to massive mudstone with a single thick greywacke unit in the middle of the member.

(3) The overlying Trumpeters Member made of turbiditic upwards fining greywackes and mudstones.

The sandstone-dominated Ripon Formation stratigraphy of the Ecca Pass closely matches that of the Pluto's Vale Member, as illustrated by Catuneanu et al. (2002), and as described

by Johnson et al. (2006) in both lithology and thickness. The occurrence of thick shale successions within the mid to upper half of the outcrop correlate well with the generalised stratigraphy of the Pluto's Vale Member from the Southern Basin.

Along the Ecca Pass Campbell (2014) recognised Bouma divisions 'a, b, d, and e' within sequences:

a) An erosive base followed by massive medium grained sandstone containing rounded rip-up clasts of the underlying lithology, usually mudstone. Erosive bases display tool marks including bounce and skip marks as well as occasional fossilised plant remains.

b) Planar laminated fine to very fine grained sand,

d) Planar laminated silt.

e) Planar laminated clay with occasional preserved plant remains along with bioturbation.

The Bouma Sequences recorded suggest a palaeoenvironment of deposition on the proximal to mid-fan (Figure 4.23). In all cases complete Bouma Sequences were lacking. Division 'c' was not developed possibly due to the rapid deposition of sand preventing the formation of ripples. Rapid and turbulent flow velocities can be inferred where stacked sandstone layers occur containing rip-up clasts of shale. In such cases the erosive nature of the flow would have completely scoured the underlying divisions Td-e and incorporated the lithologies as semi-rounded clasts.

The thick siltstone and shale successions recorded between 23 m – 60 m on the outcrop log (Appendix B) represent Td-e or Te with suspension fall-out of the finest silt fraction along with background pelagic sedimentation. The cause of a thick shale layer with underlying and overlying medium to fine-grained sandstone suggests (1) lobe switching or (2) eustatic changes.

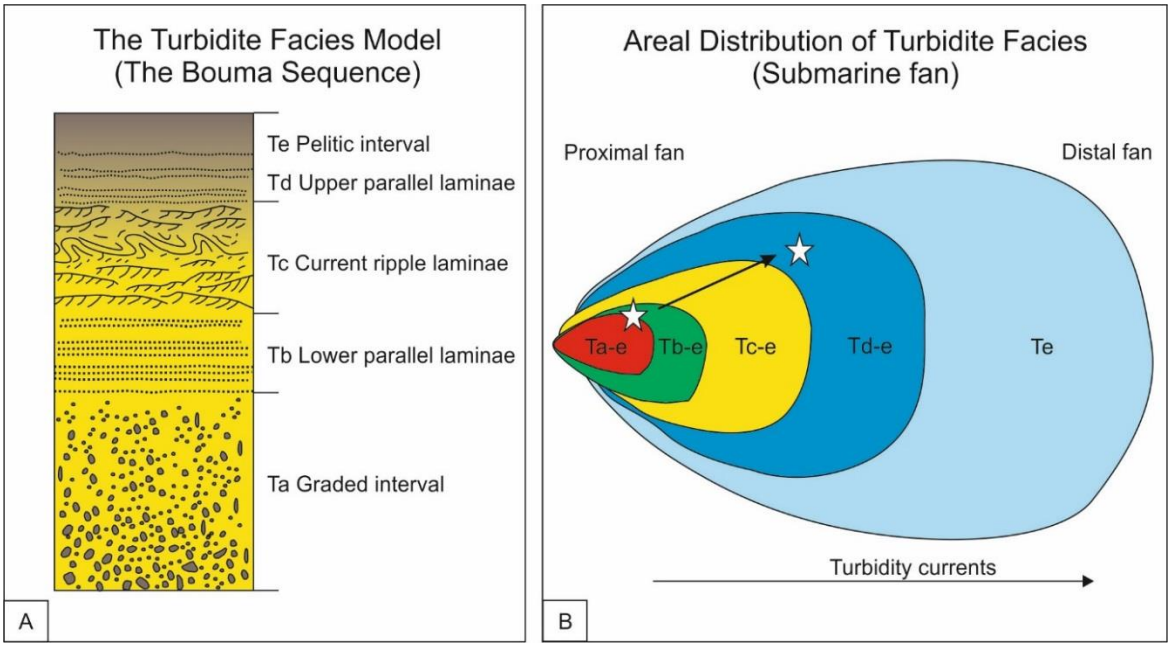

Figure 4.23: The Bouma Divisions from the Ecca Pass Ripon Formation suggest deposition on the proximal to mid-fan (stars). No complete Bouma Sequences were recorded with 'Tc' absent. After Bouma et al. (1962), modified from Shanmugum (2016).

(1) Once the individual lobe accumulates a stack of sediment above the surrounding fan, channel avulsion will occur towards a lower portion of the fan (Nichols, 2009). With sand deposition elsewhere on the fan, the original lobe may accumulate fine sediment from suspension fallout until the new lobe reaches a greater height and switching occurs again.

(2) A sudden rise in sea-level would result in an increase in accommodation space closer to the shelf (Emery and Myers, 1996). Sand deposition on the lobe would cease and an accumulation of mud and silt would be expected.

Palaeoenvironmental inferences from the small diameter core from borehole KWV-1 are difficult in comparison to outcrop exposures. However, an organic-rich siltstone layer from the Wonderforntien Member was sampled for palynological processing. Well-preserved phytoclasts and amorphous organic material were documented. Preservation of organic

matter suggests that anoxic or reducing conditions must have been prevalent during deposition. The Wonderfontien Member is predominantly composed of mudstone compared to the overlying and underlying members. The reduced energy during sediment deposition would likely have reduced water mixing (oxygen-poor bottom waters and oxygen-rich top waters) allowing for the development of a stratified water column (Preservation Model; Arthur and Sageman, 1994). Alternatively the over-supply of organic material may have led to a shortage of dissolved O_2 leading to the development of reducing conditions at the water sediment interface (Productivity Model; Arthur and Sageman, 1994).

Tracheid remnants are preserved in phytoclasts (Figure 4.16d). This feature indicates that at least some of the phytoclasts are derived from land-based vascular plants. A possible acritarch was documented in Figure 4.16c. According to Agić (2016), acritarchs are 'a major long-ranging successful group of small, capsule-like, organically preserved fossils'. They are single-celled microfossils, commonly round and either smooth or with spiny ornamentation, and are predominantly of marine origin (ibid.). The microfossil assemblage preserved in the one siltstone sample suggests that terrestrial material was transported into a marine environment. This fits well with macrofossil observations from Johnson et al. (2006) who reported carbonised plant remains and petrified logs near the base of the Ripon Formation.

4.8.2. Geothermal Potential

The assessment of a geothermal reservoir takes into consideration numerous factors. An area of favourable heat flow with a high geothermal gradient is needed. A rock formation conducive to storing and transmitting water and retaining heat at depth, within an area of high heat flow is pertinent. The rock formation ideally needs to be homogenous and voluminous. Factors such as tectonic setting and stratigraphic history also need to be considered. Table 4.15 compares favourable reservoir characteristics (reservoir geology, depths and permeabilities) across global hydrocarbon (petroleum, gas) and geothermal reservoirs. The following is a review of the geothermal potential of the Ripon Formation in the southern Main Karoo Basin.

Thermo-physical rock properties

Porosity, permeability, density, thermal conductivity and thermal diffusivity measurements were conducted on Ripon Formation sandstones in order to assess the geothermal reservoir potential of the rocks. Specific heat capacity was calculated for sandstones from the Ecca Pass, and measured, at a range of temperatures, from borehole KWV-1 samples. As a whole, the higher the values for the abovementioned parameters, the better the geothermal potential. An ideal geothermal reservoir will be porous and permeable with high thermal conductivity and diffusivity overlain by a cap rock of low thermal conductivity porosity and permeability.

The petro- and thermophysical rock properties of the Ripon Formation intersected in borehole KWV-1 at a depth between 919.20 m and 2294.95 m reveal the potential of this formation for geothermal energy utilization. Generally, impermeable fine-grained sandstones – the dominant lithology – show the highest thermal conductivity (3.71 W/(m·K)). Fine-grained sandstones and siltstones revealed the highest specific heat capacity. A comparison of outcrop and core samples shows that measurements of outcrop samples

yield slightly lower porosities and higher permeabilities, however these sandstones have permeabilities that are low to impermeable. Thermal conductivities of sandstones encountered from borehole KWV-1 are noticeably higher than those of outcrop sandstones.

The Ripon sandstones are generally tight and impermeable (Figure 4.24) in comparison with global hydrocarbon reservoirs (Ehrenberg and Nadeau, 2005). Both thermal conductivity and thermal diffusivity increase with decreasing porosity (Maqsood and Kamran, 2005). Ecca Pass outcrop sandstones exhibit a lower porosity and lower thermal conductivity compared to borehole KWV-1 samples, which is contrary to the expected relationship. According to Maqsood and Kamran (2005) 'an increase in porosity results in a greater contribution from the pore filling and a decrease in apparent density and, hence, a reduction in the thermal conductivity'. The density of the Ecca Pass outcrop samples is slightly lower than that of the borehole samples, which is also contrary to the general rule.

Table 4.15: Important characteristics of petroleum, gas and geothermal reservoirs. From Adams (2018, Pers. Comm.).

	Petroleum	Gas	Geothermal
Reservoir Geology	Clastic and carbonate	Clastic and carbonate	Clastic, carbonate and igneous
Depths (m)	500 - 4000	500 - 4000	1800 - 3000
Permeability (mD)	1000	1	50

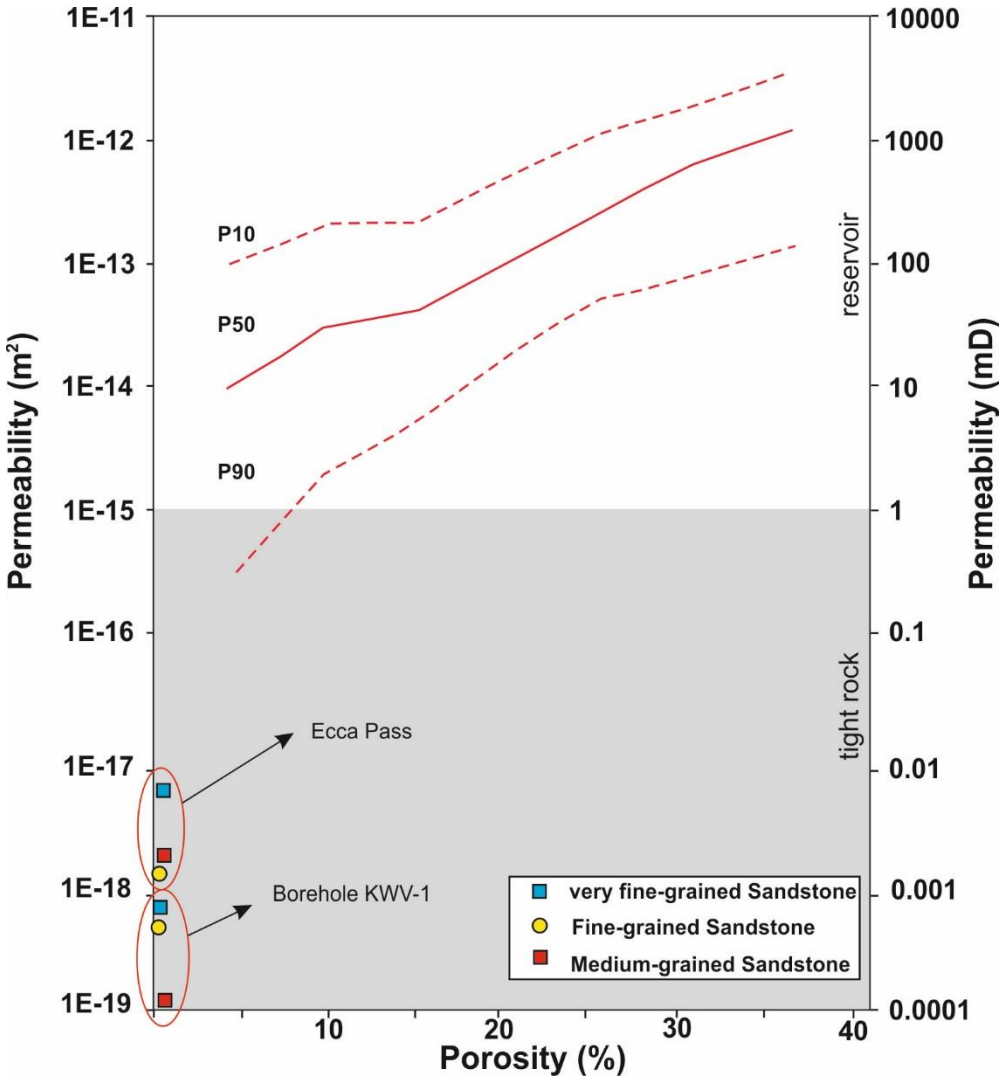

Figure 4.24: Low porosity and permeability of the three sandstone grainsizes present in Ripon Formation from the Ecca Pass and from borehole KWV-1 in comparison to global sandstone hydrocarbon reservoirs (redlines). Modified after Ehrenberg and Nadeau (2005).

Two factors need to be assessed in order to determine the reasons for the unexpected relationship. The first has to do with any mineralogical differences that exist between the sandstones at the two study locations. The second factor may have to do with the differences between an outcrop and a deep borehole.

(1) Minerals have varying thermal conductivities (W/(m·K): Quartz = 7.69, calcite = 3.59, K-feldspar = 2.31, dolomite = 3.34, muscovite = 3.89 (Clauser and Huenges, 1995; Horai, 1971 and Zimmerman, 1989 in: Maqsood and Kamran, 2005). The large difference between quartz and feldspar means that sandstone with varying proportions of these common rock-forming minerals will have large thermal conductivity differences. Thin sections from the Ecca Pass (Figure 4.10) have a high abundance of quartz, however, contacts between neighbouring quartz grains is limited because of clays enveloping the grains. Thin sections from borehole KWV-1 (Figure 4.15) also contain a similarly large percentage of quartz, however grain-to-grain contact between quartz – quartz and quartz – feldspar is improved. A higher degree of grain contact may account for the higher thermal conductivity in the borehole.

(2) Similarly, feldspars within borehole samples are more abundant and appear less weathered compared to the outcrop samples (Figure 4.15) and interstitial clay is reduced in core samples. Feldspars from sandstones located along the outcrop are subjected to a high degree of weathering, resulting in the breakdown of some feldspars into clay (Velbel, 1983). Quartz grains that were once in contact with feldspars may now be surrounded by clays. Samples from the borehole are expected to be fresher, and indeed they do exhibit a lower clay content.

Calculated specific heat capacity values for outcrops samples (Table 4.2) compare favourably with measured borehole samples within a temperature range of 25 - 80°C. Thermal diffusivity values from outcrops samples are slightly lower than borehole samples. This is due to thermal diffusivity being a product of thermal conductivity, density and specific heat capacity.

Dolerite intrusions and permeability enhancement

With favourable thermal conductivities, the lack of porosity and permeability creates an unattractive geothermal reservoir. However, the fracture systems related to the numerous dolerite intrusions may provide an improvement that can be enhanced by hydraulic stimulation. The influence of dykes and sills on permeability enhancement was studied by Senger et al. (2015) and demonstrates the high potential for fluid flow channelling along the intrusion-host rock interfaces. The study highlights the different fracture types based on the likely mode of formation, namely; (1) syn-emplacement fractures in host rocks; (2) post-emplacement fractures in dolerite; and (3) tectonic fractures in both host rock and dolerite. These three fracture types are also present in borehole KVW-1. The porosity itself does not govern the flow of water through rock, but rather its ability to store water. Water flow depends on the interconnectivity of these pore spaces, the sizes of the individual pores, the effective porosity and the water content as water saturation. For fractured systems such as these, the hydraulic conductivity (directly related to the permeability) of the fractures is more likely to govern water movement.

Outcrop data from the Ecca Pass reveal two predominant mean joint orientations of 242/53 and 143/73 in the Permian Ripon Formation and similar orientations were measured in the Permo-Triassic Beaufort sandstones studied by Senger et al. (2015). However, these authors note that open fractures decrease with increasing lithostatic pressure (depth) and are less likely to be good fluid conduits at depth.

Area C versus Area 123

Two regions with differing but favourable geothermal potential are the focus of the results in Tables 4.7 – 4.10. Both areas have differing known geothermal prerequisites, which are discussed below. Prerequisites for a prospective geothermal area are heat flow, reservoir depth and reservoir thickness.

Area C (Figure 4.19) is located in the central Main Karoo Basin. It covers an area of 74853.79 km^2 and is located within an area of known high heat flow (70 – 75 mW/m^2). Thermal artesian boreholes and thermal springs occur within and adjacent to the area. Area C is the only area of high heat flow (Figure 4.19) within range of the Ripon Formation sandstones. The unknown variables concerning this area are reservoir depth and thickness.

Area 123 (Figure 4.20) was constrained by three previously drilled boreholes. This region covers an area of 16000 km^2 with the Ripon Formation at known depths and thicknesses. A mean thickness of 650 m at depths ranging from 3000 – 3500 m was derived from the previously drilled boreholes, and used for the calculations in Tables 6 – 9. All three previously drilled boreholes document sandstones, in varying proportions, at the base of the Ripon Formation, at varying depths from the surface. Heat flow values from Area 123 are largely unknown except for the occurrence of thermal springs and thermal artesian boreholes proximal to the area.

Reservoir depth and thickness for Area C were assumed to be similar to Area 123 and therefore the same values were used. According to Johnson et al. (2006), the Ripon Formation pinches out towards the north. A schematic illustration by Catuneanu et al. (2002) shows the extent of the submarine fans during the Early Permian (Figure 4.25). However, the Ripon Formation is known from areas outside of the submarine fans in Figure E (Johnson et al., 2006), and based on that it was deemed likely that thin sandstone successions may exist at depth within Area C. However, of the two prospective regions, Area 123 contains the least unknown variables.

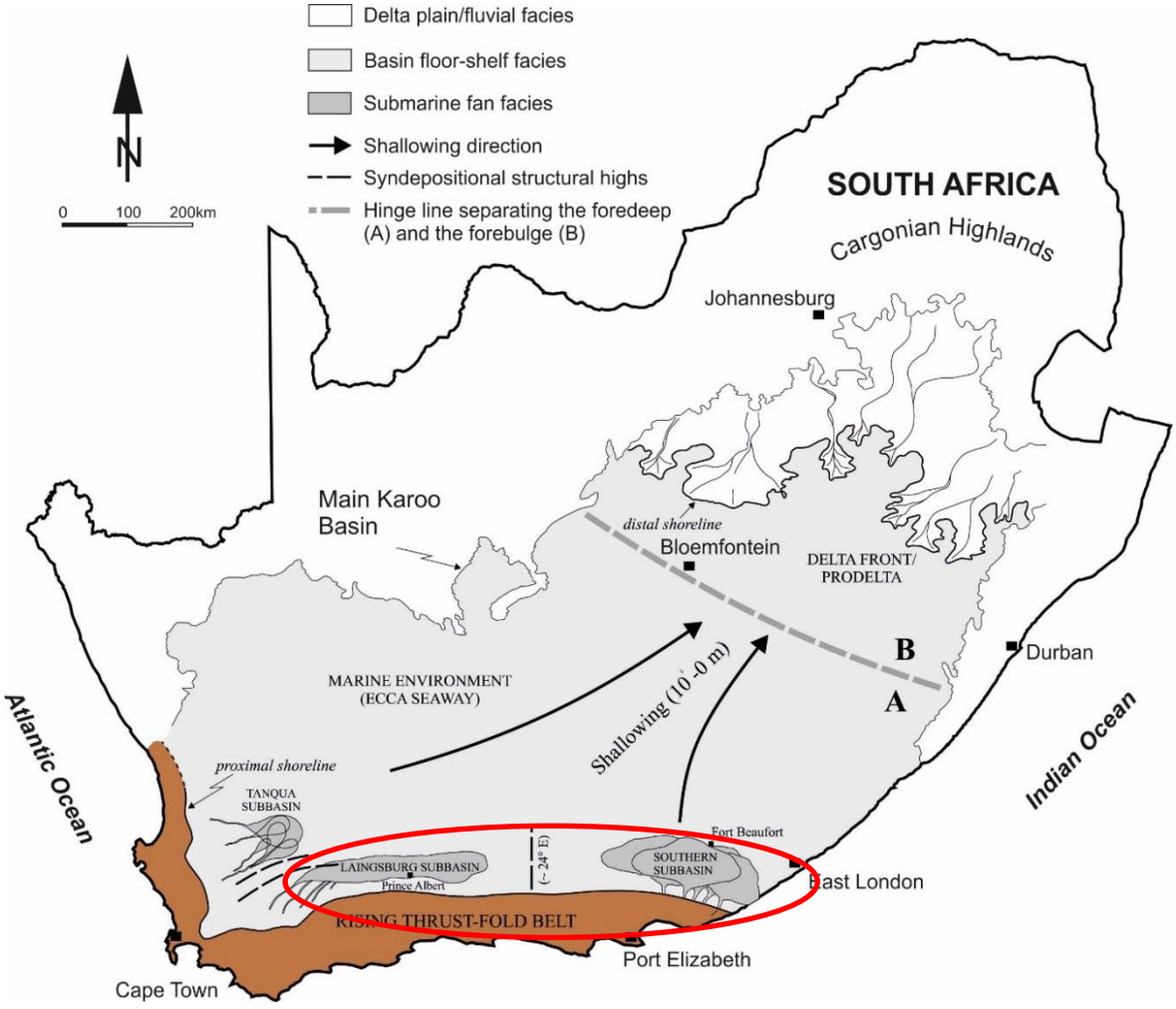

Figure 4.25: Palaeogeographic reconstruction of the Main Karoo Basin during the Early Permian showing the depositional environments and extent of the submarine fans across the sub-basins. Modified after Catuneanu et al. (2002).

Geothermal Gradient

Little information on the geothermal gradients and the heat flow across South Africa's Main Karoo Basin has been published (Jones, 1992; 2001; Bird et al., 2006; Cloete, 2010). Heat flow data from the Karoo Basin (Jones 1992; 2001) indicate areas of a moderately elevated heat flow within the basin are related to the underlying basement, the Namaqua-Natal Mobile Belt (Figure 2.5). Mean heat flow across Earth's continental crust is 65 mW/m^2 (Pollack et al., 1993). Generally, heat flow in the Namaqua-Natal Mobile Belt is much higher than in the Kaapvaal Craton. Preliminary models attribute approximately half the excess heat flow

in the Namaqua-Natal Mobile Belt to crustal radioactivity and the rest to a higher heat flux across the Moho (Jones, 1992). Geotherms based on these models agree with estimates of upper mantle pressure-temperature conditions inferred from kimberlite inclusion studies, and indicate that the lithosphere below the Kaapvaal Craton is considerably cooler and thicker than the lithosphere below the Namaqua-Natal Mobile Belt.

Variations in patterns of heat flow within the Karoo Basin are likely to be the product of different tectonic settings and kimberlite occurrence. In the northern and central parts of the basin an elevated heat flow might be related to the occurrence of young (94 Ma and younger) kimberlites (Jelsma et al., 2004). The southwestern basin part is located in the northern extension of the syntaxis of the Cape Fold Belt (Johnston, 2000), and the eastern and southeastern basin parts are located adjoining the southernmost extension of the East African rift system (Chorowicz, 2005).

Down-hole temperature data from boreholes KZF-1and KWV-1 provided information on the geothermal gradient. In both areas, a moderately elevated geothermal gradient was observed. Temperatures of 80°C at 2200 m depth recorded from borehole KWV-1 indicate a geothermal gradient of 28.2°C/km. Temperatures of 34.4°C at 671 m recorded from borehole KZF-1 indicate a geothermal gradient of 24.5°C/km in the Ceres area (Western Cape). The Earths geothermal gradient ranges from 15°C/km to 30°C/km (Earle, 2015). Reservoir temperatures (reservoir depths 3000 – 3500 m) of 104°C to 117°C are therefore expected in the southern Karoo Basin with temperatures suitable for electricity in a binary geothermal power plant. Deep groundwater, with a calculated temperature of 90°C, at a depth of ca. 1430 m (assuming a geothermal gradient of 3.69°C/100 m; Cloete, 2010) in the area west of Trompsburg (exhibiting high heat flow of 70–75 mW/m^2; Figure 4.19) would be suitable for electricity production in a binary geothermal power plant that can accept fluid temperatures as low as 57°C (Erkan et al., 2008). However, it should be noted that the

geothermal spring utilising 57°C fluids for power generation occurs in Alaska with low mean surface temperatures, as well as having a very short transport distance for heat (ibid.). The geothermal source is shallow (<300 m) with the geothermal plant located on site (ibid.).

On a local scale, direct heat use of the potential reservoir, as opposed to electricity production, is a realistic alternative to harness geothermal energy from the Karoo Basin. The transport of heat for electricity generation is inefficient; therefore, direct use of heat from low enthalpy settings is the most economical use (Chandrasekharam and Bundschuh, 2008). Employing a cascade system for direct heat use would also maximise efficiency (Rubio-Maya, 2015). Thermal springs reported by Steyl et al., (2012) show water temperatures ranging from 26°C to 41°C, with temperatures of 26°C to 31°C in the southern part, 30°C to 37°C in the central part and 28°C to 41°C in the north-eastern part of the basin. So far, thermal springs have been developed for direct use north of the Karoo Basin in the Limpopo Province north of Pretoria, where water temperatures of up to 71°C have been reported (Chevallier et al., 2014). A review of the direct utilization of geothermal energy in South Africa is given in Lund and Boyd (2015).

Heat in place and recoverable heat

Following the volumetric approach of Muffler and Cataldi (1978) leads to a first assessment of the geothermal reservoir potential of the Karoo Basin by quantifying the heat in place. This simplistic approach is especially suitable for scenarios with few data points (e.g. Korkmaz et al., 2014; Zafar and Cutright, 2014; Lenhardt and Götz, 2015) and may provide preliminary information for potential resource areas that are not well studied. Heat in place has been calculated for both prospective areas, and maximum and minimum values were calculated by using the maximum and minimum geothermal gradient as well as reservoir depth (Tables 4.7 – 4.10).

Following Van Wees et al. (2012) the recoverable heat (RH) is about 33% of the HIP and the technical lifetime of a doublet system is 30 years. The percentage of recoverable heat from the Ripon Formation may vary significantly from that of Van Wees et al. (2012) due to local techno-economic conditions. However, applying the value of 33% from that study demonstrates how much heat is unrecoverable. Nevertheless, the worst-case scenario from the Ripon Formation (using all the minimum values) results in 0.59 EJ of recoverable heat, equating to 116 million barrels of oil equivalent or 165 Terawatt hours. The best-case scenario may deliver 3.71 EJ of recoverable heat, equal to 639.2 million barrels of oil equivalent or 1061.03 Terawatt hours.

The values of heat in place (HIP) and recoverable heat (RH) from the two areas need to be considered with caution. Area C is 4.7 times larger than Area 123 by surface area therefore HIP values are much higher. Calculated HIP assumes homogenous rock properties within the reservoir and assumes that every cubic metre of the reservoir is utilised. Both of these assumptions are unrealistic in reality. However, the petro- and thermophysical rock properties of the Permian Ecca Pass succession show that the turbidites qualify as target horizons for utilization of deep geothermal reservoirs. Turbidite successions are widespread in the southern and southwestern parts of the Karoo Basin and are therefore very promising exploration targets with respect to geothermal power generation or direct heat usage.

At a later stage and with more extensive data sets, more rigorous calculations such as a Riemann-sum approach (e.g. Esposito and Augustine, 2011; Crowell and Gosnold, 2011) or the volumetric-probabilistic methods currently utilized by the U.S. Geological Survey (Williams et al., 2008; Garg and Combs, 2010) can be applied.

Geothermal Summary

The southern Karoo Basin is a promising future target for geothermal energy exploration in South Africa. The area is characterized by thrust tectonics and highly fractured clastic rocks. Sandstones of the Ripon Formation occur at depths of >3000 m and, based on data from borehole KWV-1 a high thermal conductivity and high specific heat capacity can be assumed. In the region west of East London with deep thermal springs (Steyl et al. 2012), the highly fractured sandstones south of the dolerite line might act as transitional systems (Sass and Götz, 2012). These can be further enhanced by hydraulic fracturing.

In the region northeast of East London, the fractured sandstones are intersected by dolerite sills and here fluid-flow channelling along the intrusion-host rock interfaces might serve as a natural enhancement of a petrothermal system. Such systems need reservoir stimulation for techno-economic utilization (Tester et al., 2012; Huenges, 2010), and could be operated as an enhanced geothermal system (EGS) (Hirschberg et al., 2015) or a hot-dry rock system (HDR) by man-made stimulation. However, since information on the deep Karoo aquifer systems is not readily available (Murray et al. 2006), there is a need to address this research gap to provide the necessary information on the hydraulic and hydrochemical properties of reservoir fluids to be integrated in further geothermal exploration strategies.

4.9. Conclusions

On a basin-wide scale, the heterogeneity with respect to facies and thickness of prospective sandstone reservoir formations needs be considered for future geothermal exploration activities. However, heat flow in a low permeability basin such as the Karoo is effectively very low since convective heat transfer is negligible. A predominantly conductive thermal regime can be assumed. As the potential geothermal system would rely on fractures, and these may be very variable in their transmissibility properties across a large area,

extrapolating results from a single borehole across the basin remains difficult. Furthermore, until boreholes are drilled to reservoir depth, and fluid has been extracted from a natural or artificial reservoir at an economically sustainable flow rate, no specification can be made about development of or production from the reservoir. Additionally, the permeability of potential reservoirs in unknown and therefore wells may have to be hydraulically stimulated if found to be impermeable. For future studies, the southern part of the Karoo Basin, where the Ripon Formation occurs at depths in excess of 3000 m, is seen as a key area with regard to geothermal prospectivity. The initial dataset of the KWV-1 borehole and Ecca Pass section from the southernmost part of the basin identifies this area as the most suitable for ongoing geothermal research.

For a first assessment of a potential geothermal resource and its distinct reservoir formations, data gained from outcrop analogue studies seem to lead to a conservative estimation of the reservoir capacity but prove to be useful with respect to transferability of outcrop conditions to reservoir conditions. Based on the investigations of geothermal parameters from a deep drill core, in a later stage of geothermal exploration, the integration of reservoir transfer models (e.g., Tikhomirov, 1968; Somerton, 1992; Vosteen and Schellschmidt, 2003; Abdulagatova et al., 2009) enables a more precise reservoir prognosis including numerical simulation and upscaling (Rühaak et al., 2015).

5. Wireline Facies Development for Geothermal Reservoir Exploration

This chapter explores the potential of geophysical wireline logs as a tool, for the identification of potential geothermal reservoirs, by comparing geothermal samples, from Borehole KWV-1, with combined gamma-ray logs.

5.1. Introduction

Knowledge of the location, distribution, and suitability of potential geothermal reservoirs is needed in order to thoroughly assess and develop the resource in the southern Main Karoo Basin of South Africa. An area (Figure 4.20) has been identified as containing potential geothermal energy, based on analyses conducted on core and outcrop samples from the Ripon Formation; however, very few other cores exist in the region (Johnson et al., 2006) and new cores are expensive and unfeasible to drill in the search for deep geothermal reservoirs. Borehole KWV-1 intersected the Ripon Formation at depth and the entire borehole was logged using wireline logging tools.

The aim of this study is to develop a facies framework for identifying suitable geothermal horizons, from within wireline-logged non-cored boreholes, by analysing the combined gamma-ray signature response from borehole KWV-1 in relation to analysed geothermal samples. Percussion boreholes can be drilled comparatively inexpensively and logged with wireline tools, and the resulting gamma-ray trends analysed and compared to the established geothermal facies model from borehole KWV-1 to identify horizons for future exploration.

Both the geothermal potential and the gamma-ray response of sandstones and shales are a function of grain size, clay content and mineralogy. Therefore, it should be possible to determine zones of high geothermal potential based on gamma-ray trends, which in turn are a result of depositional environment.

5.2. Submarine Fan Architecture

The variability in submarine fan characteristics is dependent on many factors that govern deep-sea sedimentation, such as sea-level variations, tectonic regime, basin structure, sediment type and gravity flow variability (Mutti and Normark, 1991). A submarine fan can be subdivided into four primary erosional and depositional architectural elements, from proximal to distal; namely, the canyon, channels, lobes, and sheet deposits (Richards et al., 1998). Components of the submarine fan are directly related to the variable depositional processes and sub-environments of deposition (Walker, 1978).

5.2.1. Channels and Levees

Submarine fan channels form on the fan surface and connect the distal part of the submarine canyon and the depositional lobes (Figure 5.1). Channels form on or in the underlying sediment, unlike canyons which cut into the bedrock (Normark, 1970). Submarine channels can be divided based on sinuosity (Shanmugam, 2016) with two types and two variations being recognised; namely, meandering or braided and convergent or divergent. Within the channel, deposits (from turbidity currents) are typically massive or poorly graded coarser sands and gravels that form lenticular turbidites (Figure 5.1) (Richards et al., 1998). Medium and high sinuosity meandering channel systems are formed when the lower part of the flow in a gravity-current erodes sediment from the outer bank, upstream of bend apexes and deposits the sediment on inner banks below the bend (Cossu et al., 2015).

Submarine channel levee deposits comprise fine grained sand, silt and mud from the more dilute portion of the turbidity current (Figure 5.1). Similar to a fluvial over-bank deposit, levee turbidites thin away from the channel with a wedge shaped geometry and can form extensive sandstone units (Richards et al., 1998; Shanmugum, 2016).

5.2.2. Depositional Lobes

The term lobe is used to denote unchannelised turbidites (Mutti, 1979) (Figure 5.1). The term ‘suprafan lobe’ was introduced for modern fans and ‘depositional lobe’ for ancient fans (Normark, 1970; Mutti and Ghibaudo, 1972), however according to Shanmugum (2016) the term ‘lobe’ has been used with varying meanings in literature. Ideally, a succession of depositional lobe progradation is upward coarsening (stacked, normally graded turbidites) capped by a channelised unit. This pattern is not always observed due to the complex deposition on the lobe (Nichols, 2009).

5.2.3. Turbidite Sheets

Turbidite sheets are turbidity current deposits not constrained to a lobe, but have expanded out over the fan (Figure 5.1). Turbidite sheets are composed of fine-grained sand, silt and mud with large lateral extent and little variability (Walker, 1978). Turbidite sheets may be interbedded with hemipelagic deposits, which are accumulations of mud fractions derived from the continents and micro fauna, that settles out of the water column onto the abyssal plain at extremely low rates of sedimentation (<1mm – 50cm/ 1000 yrs) (Shanmugum, 2016).

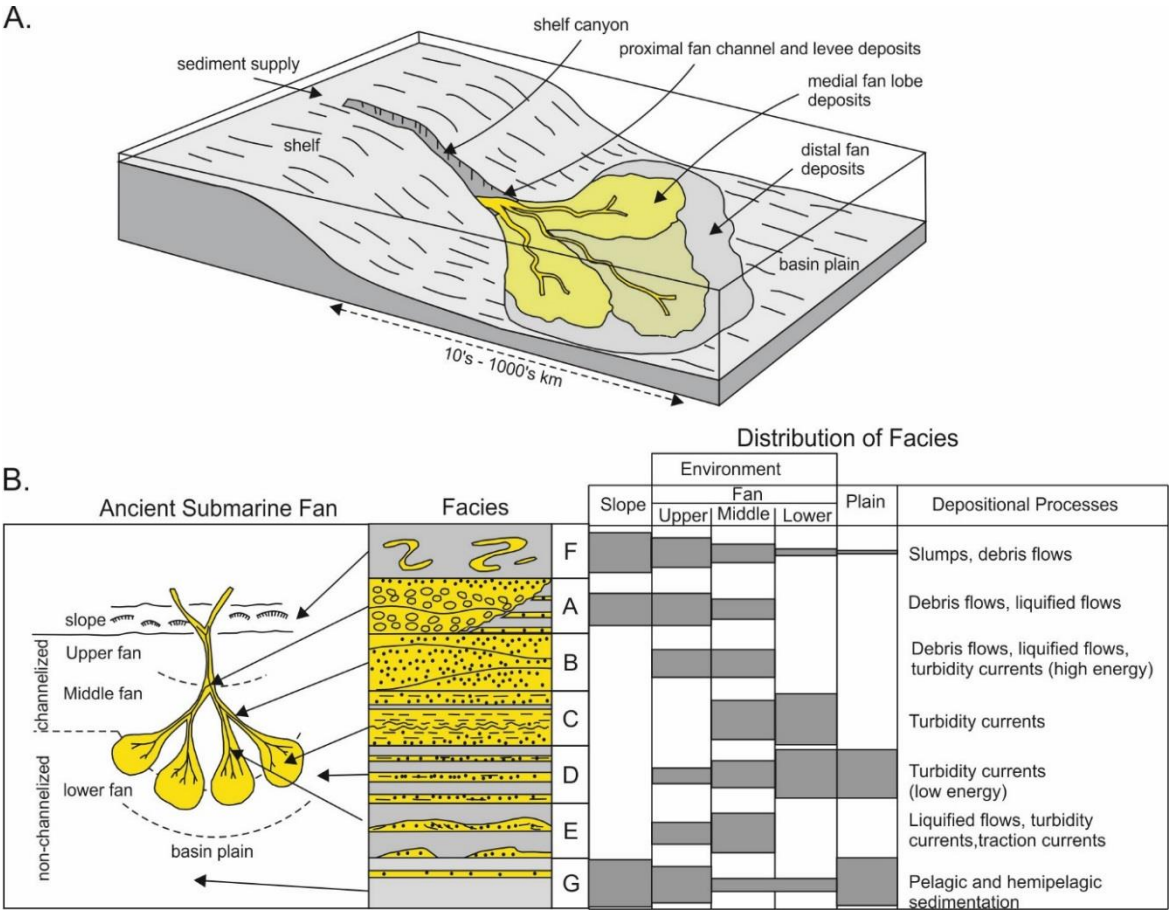

Figure 5.1A: Anatomy of a submarine fan with sediment transported from the shelf through the feeder canyon and onto the basin plain. Modified after Nichols (2009). B: Distribution of facies on an ancient submarine fan across feeder channels, depositional lobes and the basin plain (top) and depositional processes, with relative proportions (bottom). Modified from Shanmugam et al. (1985).

5.3. Gamma Log Trends in Deep Marine Settings

Radioactivity emitted by naturally occurring uranium (U), thorium (Th) and potassium (K) within sediments is recorded by the gamma-ray log (Hurst, 1990), and is used as a proxy for clay mineral content and, therefore, grainsize and depositional energy, i.e. increasing radioactivity from increasing clay content and decreasing depositional energy (Emery and Myers, 1996). According to Rider (1990), shales host substantially higher concentrations of naturally occurring radioactive elements, in comparison to quartz-rich sandstones that host neither U, Th, nor K.

Gamma-ray log profiles are commonly used to identify depositional facies, particularly of sandstones, with three main diagnostic trends (Figure 5.2): (1) The cleaning up or funnel trend (gradual upwards decrease in gamma), (2) the dirtying up or bell trend (gradual upwards increase in gamma and, (3) the boxcar or cylindrical/blocky trend (stable low values between high shoulders) (Rider, 1990; Emery and Myers, 1996).

According to Emery and Myers (1996), in deep marine settings, the *dirtying up trend* or *bell motif* may indicate a reduction in the sand proportions in thinly bedded turbidites such as may occur during the abandonment of a lobe on a submarine fan. A gradual increase in anoxity, or a shift of sedimentation from carbonate to clastic, may also result in the formation of a dirtying up succession. Conversely, the *cleaning up trend* or *funnel motif* is characteristic of a sand percentage increase in thinly bedded turbidites, as is usually attributed to part of a *bow trend* (cleaning up trend overlain by a dirtying up trend). A decrease in anoxity, or a shift of sedimentation from clastic to carbonate, may also result in the formation of a cleaning up succession.

A bow trend is a cleaning up trend overlain by a dirtying up trend of similar thickness with no sharp boundaries in between the two. Bow trends are typical of the waxing and waning of clastic sedimentation in a basinal setting, usually with turbidites developed in the middle of the 'bow'. *Boxcar log trends* are internally stable, low-gamma units with sharp shoulders, leading to a higher-gamma background unit. In a deep marine setting, boxcar trends are characteristic of turbidites (Emery and Myers, 1996).

Irregular trends usually display no variation and lack the clean character of the boxcar trend. Accumulations of shale or silt in deep-water settings will not result in the development of a clear trend (irregular) (Emery and Myers, 1996).

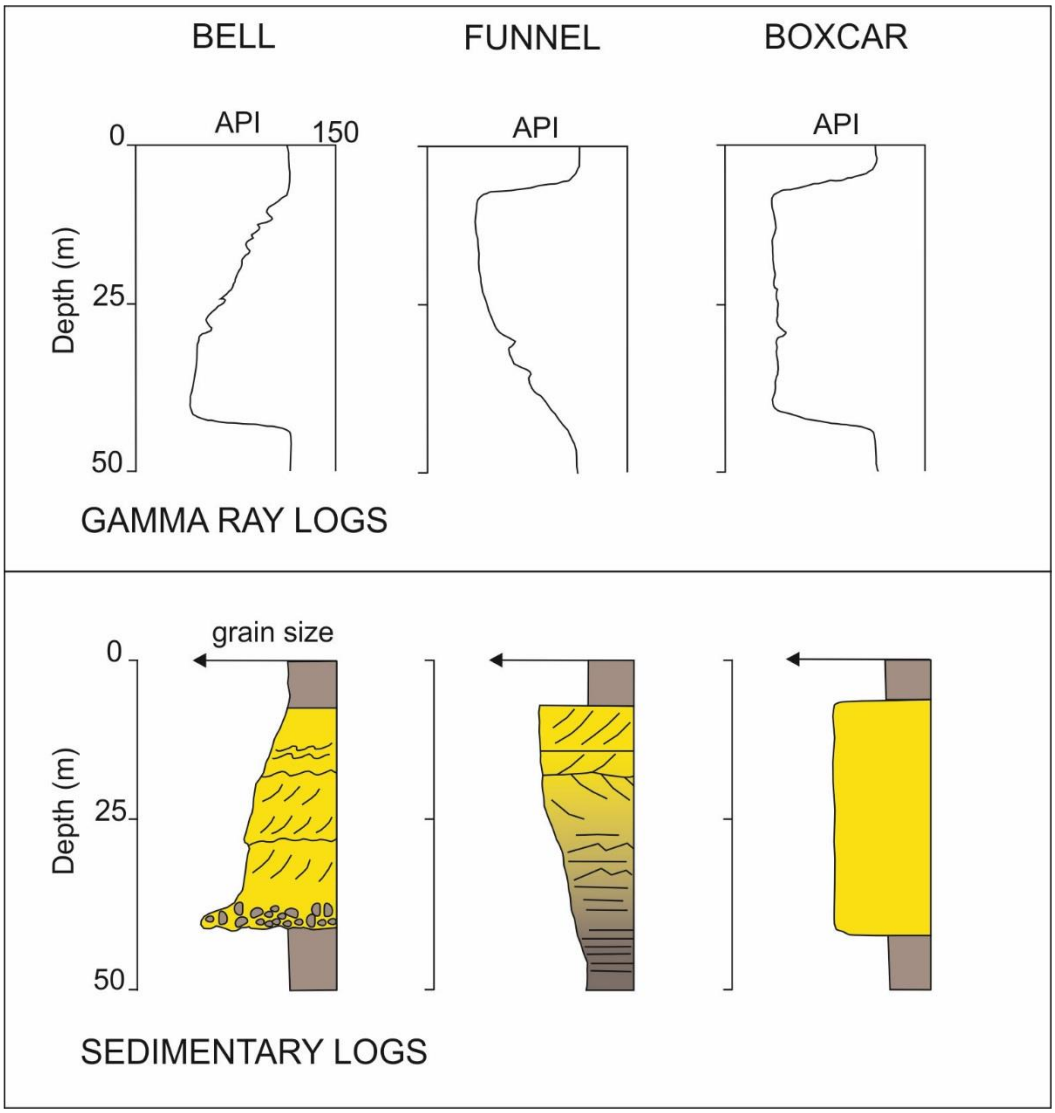

Figure 5.2: The three main gamma-ray log shapes and their equivalent sedimentary logs. Modified after Rider (1990).

5.3.1. Problems with Log Shape Trend Analysis

The premise that a high gamma signal is directly related to a fine grain size assumes that all clay is radioactive and all sand is not (Rider, 1990). Numerous factors may result in a high gamma value in sandstone or a lower gamma value in clay. Uranium enriched sandstone due to post-depositional processes, or arkosic sandstones with a high feldspar content, would present a high gamma reading (Emery and Myers, 1996). Table 5.1 displays the relative

abundance of radioactive elements from common sandstone minerals and illustrates that an arkosic or mica-bearing-lithic-rich sandstone may have a high gamma reading.

Table 5.1: Th, U, and K concentrations from common sandstone minerals. After Hurst (1990).

Mineral	Th (ppm)	U (ppm)	K (%)
Illite	10-25	1-5	3.5-8.3
kaolinite	6-47	1-12	0-0.6
chlorite	3-5	-	0-0.3
smectite	6-44	1-21	0-1.5
muscovite	0-25	2-8	7.8-9.8
biotite	0.5-50	1-40	6.2-10
K-feldspar	3-12	0.2-3	10.5-16

Dypvik and Eriksen (1983) have determined K and Th to be the dominant contributors of radioactivity in sedimentary rocks, with U having a lesser effect. The authors continue by presenting examples of numerous variations that may occur that would affect the generally accepted gamma-ray log interpretation: (1) Placer deposits of thorium and heavy mineral enriched sediments with high gamma log readings; (2) Clayey and bentonitic sediments with a lower gamma signal than an overlying coarser sandstone.

In summary, numerous factors need to be taken into account when interpreting gamma-ray log shapes including; mineralogy, palaeoenvironment, post-deposition processes, and the sedimentological relationship between ‘clay’ and ‘sand’.

5.4. Borehole KWV-1

5.4.1. Location and lithological descriptions

See Chapter 4, sections 4.6.1 and 4.6.2 for detailed lithological descriptions of the Ripon Formation including an overview borehole log and location map.

5.4.2. Methodology for Wireline Facies Development

Immediately after drilling was completed, the borehole was logged by Weatherford Slimline Services (Appendix C) using the Dual Spaced Neutron tool, Dual Spaced Density tool, Caliper, and Formation Dipmeter. The sondes were recorded simultaneously in the main, and repeat, runs. A program called WellCAD Reader (reader only), provided by Weatherford, was used to view a combination log of all the data provided by the company. Descriptions of tools used (below) was provided by Weatherford (2011).

The Dual Spaced Neutron tool (NN2) measures the natural-gamma radioactivity of the formation surrounding the borehole. The most significant naturally occurring sources of gamma radiation are potassium-40 and daughter products of uranium and thorium decay series. Gamma emissions can commonly be correlated with rock type or with fracture infilling. Potassium^{40} is abundant in some feldspar and mica, and uranium and thorium can be concentrated by geochemical processes. The count rate of the neutron detector is inversely related to the hydrogen content of the rocks surrounding the borehole, and is primarily a measure of the amount of water and hydrocarbons in the rocks. Gamma trends are recorded in American Petroleum Institute (API) units.

In this study combined gamma data is compared to lithological data, as well as samples analysed for geothermal potential, in order to identify trends in gamma (after Emery and Myers, 1996) which, in turn, are indicative are differing depositional environments/processes. 135,449 wireline measurements were recorded across the Ripon Formation.

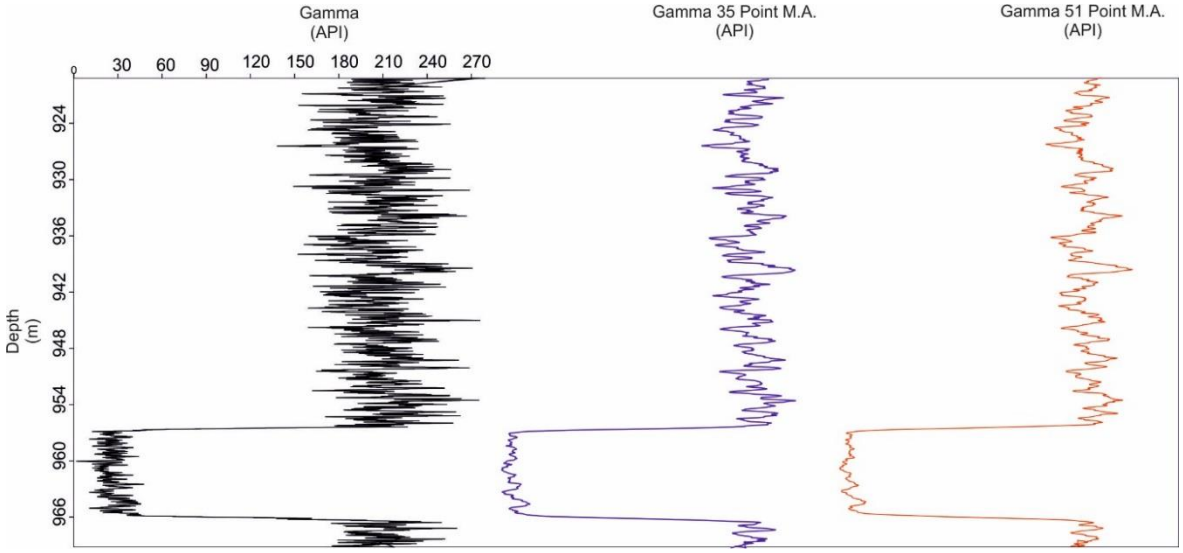

Figure 5.3: A series of gamma versus depth logs with progressive smoothing factors. Smaller scale peaks and troughs are clearly visible with a higher degree of smoothing compared to unfiltered data. Black log: Unfiltered data. Blue log: 35-point moving average. Red log: 51 point moving average.

PAST statistical software (Hammer et al., 2001) was used to smooth the gamma ray data. Past is free software for scientific data analysis, with functions for data manipulation, plotting, univariate and multivariate statistics, ecological analysis, time series and spatial analysis, morphometrics and stratigraphy (ibid.). Smoothing was performed by the 'Simple Smoothers' functions in PAST and uses an n-point moving average.

Unfiltered gamma versus depth data contains an unacceptably high amount of noise (Figure 5.3) due to the high resolution (100 measurements per metre), and no trends can be deduced from the logs. Logs displaying large stratigraphic intervals (100 m - >1000 m) require a higher smoothing factor compared to logs with smaller stratigraphic intervals. Lower

smoothing factors are used where a higher degree of detail is required over very small intervals (<10 m).

Twelve samples were selected across the Ripon Formation from within borehole KWV-1, and analysed for porosity, permeability, specific heat capacity, thermal conductivity and thermal diffusivity at the Institute of Applied Geosciences, TU Darmstadt, Germany. The dry bulk thermal conductivity and dry bulk thermal diffusivity analyses were conducted using the Optical Scanning Method after Popov et al. (1999), using a Thermal Conductivity Scanner developed by "Lippmann and Rauen GbR". In this method, the surface temperature of the sample was measured by infrared temperature sensors before and after heating with a contactless heat source. The sensors and the heat source moved with constant speed and constant distance to each other along the sample and glass reference samples with known thermal conductivities.

A dynamic Calvet calorimeter SETARAM C80 (Calvet and Prat, 1963) was used to measure the specific heat capacity of samples from borehole KWV-1 for the temperature range of 25°C to 200°C. The device has two chambers, one of which was filled with weighted sample material, whilst the second chamber remained empty and acted as a reference. During the course of the measurements the temperature was increased, stepwise, by 0.5°C each minute, while the heat flux in the sample chamber and reference chamber was measured. The difference between the heat flows is proportional to the specific heat capacity of the sample material (Schellschmidt, 1999). The device has a temperature accuracy of +/- 0.1°C and a measurement precision of +/-0.1%.

5.4.3. Gamma versus Depth Logs

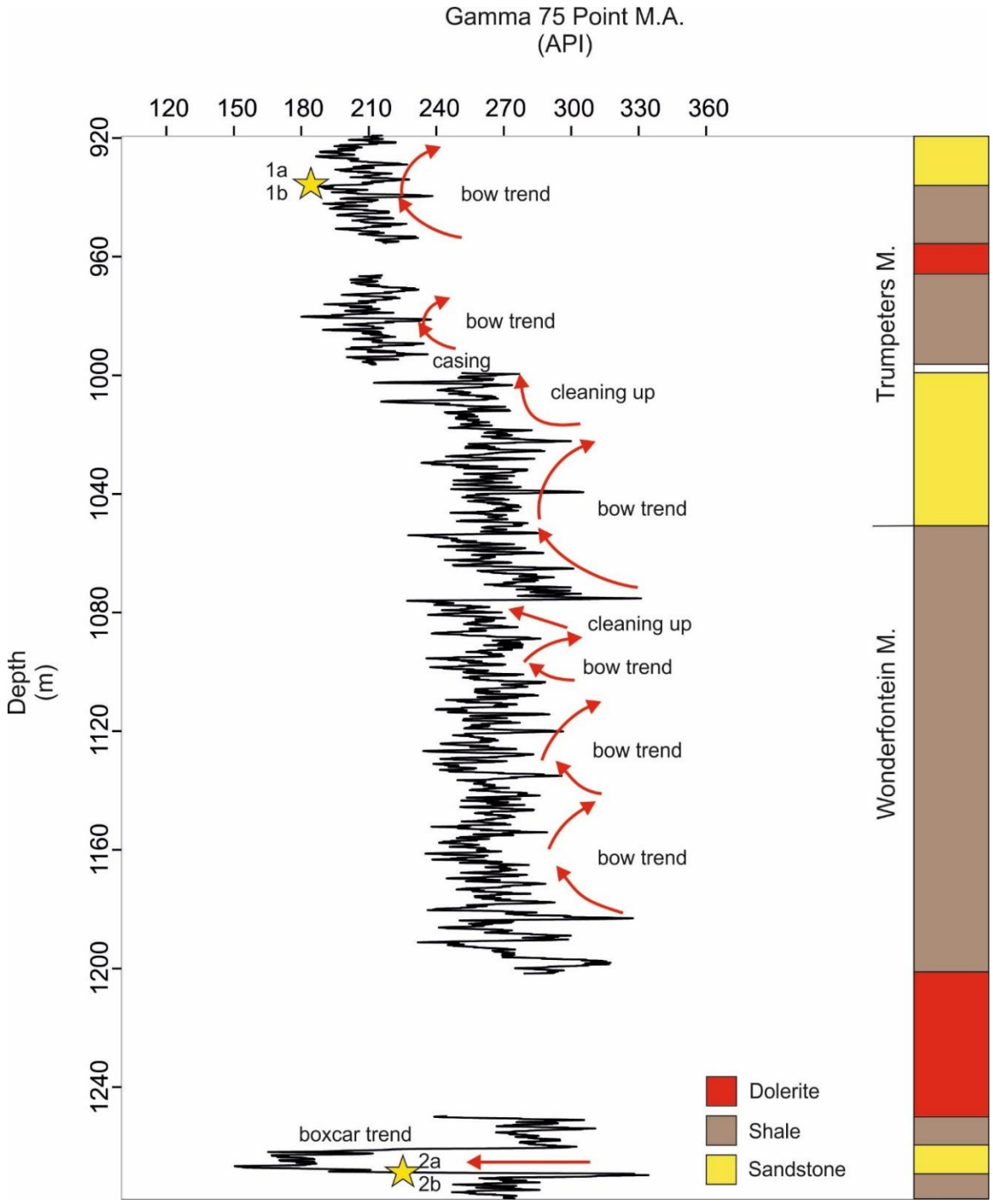

Figure 5.4: Ripon Fm. overview gamma log 1 showing cyclical cleaning up and dirtying up trends (red) on a large scale (10 m – 20 m) with smaller cycles on a metre scale. The Trumpeters Member contains a larger proportion of sandstone compared to the underlying shale-rich Wonderfontein Member. Stars indicate geothermal samples with corresponding sample number. Data from intervals containing dolerite has been removed. 75 point moving average applied.

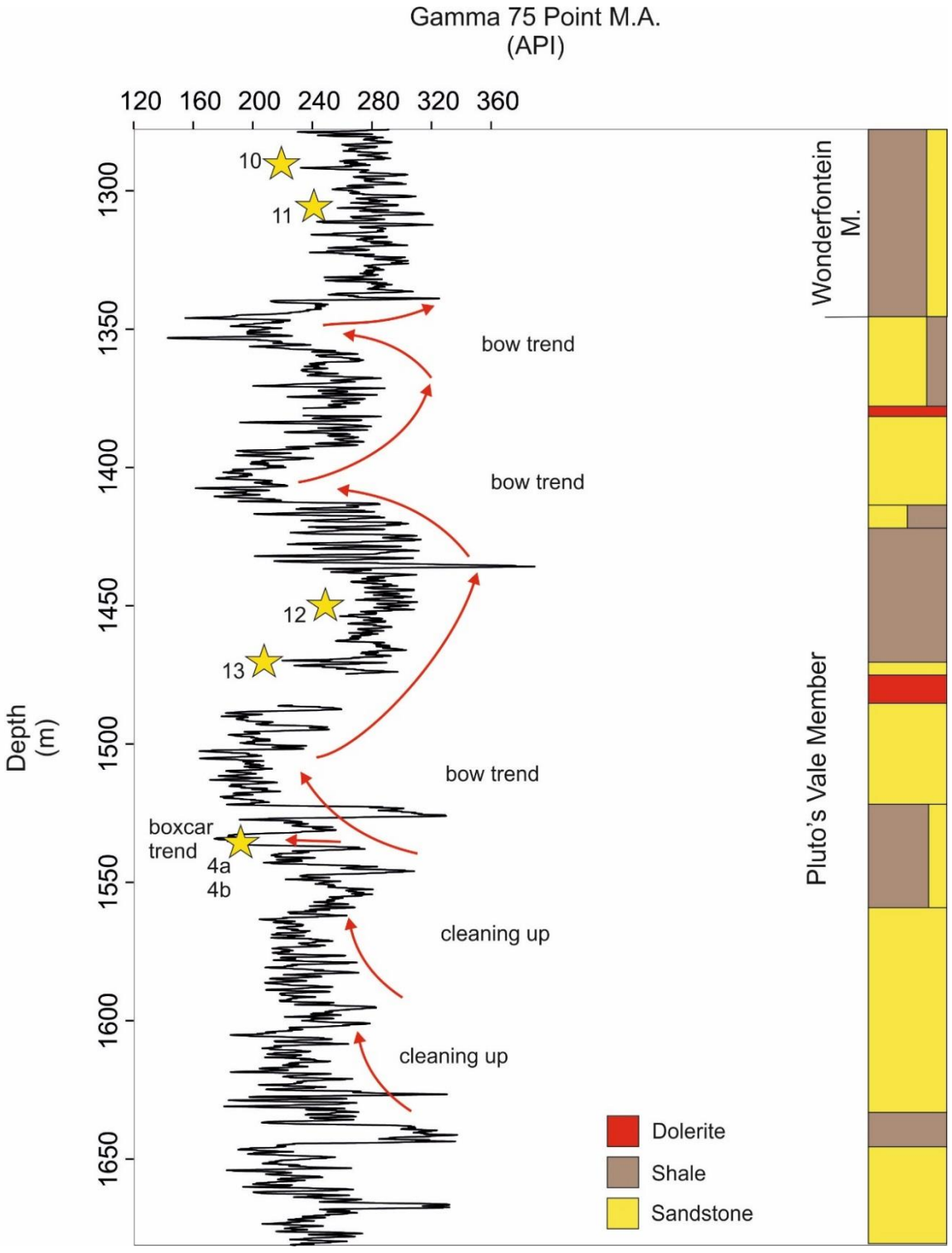

Figure 5.5: Ripon Fm. over view gamma log 2 with pronounced large-scale (50 m – 100 m) bow trends and basal cleaning up trends correlating with sandstone horizons. Stars indicate geothermal samples with corresponding sample number. Data from intervals containing dolerite has been removed. 75-point moving average applied.

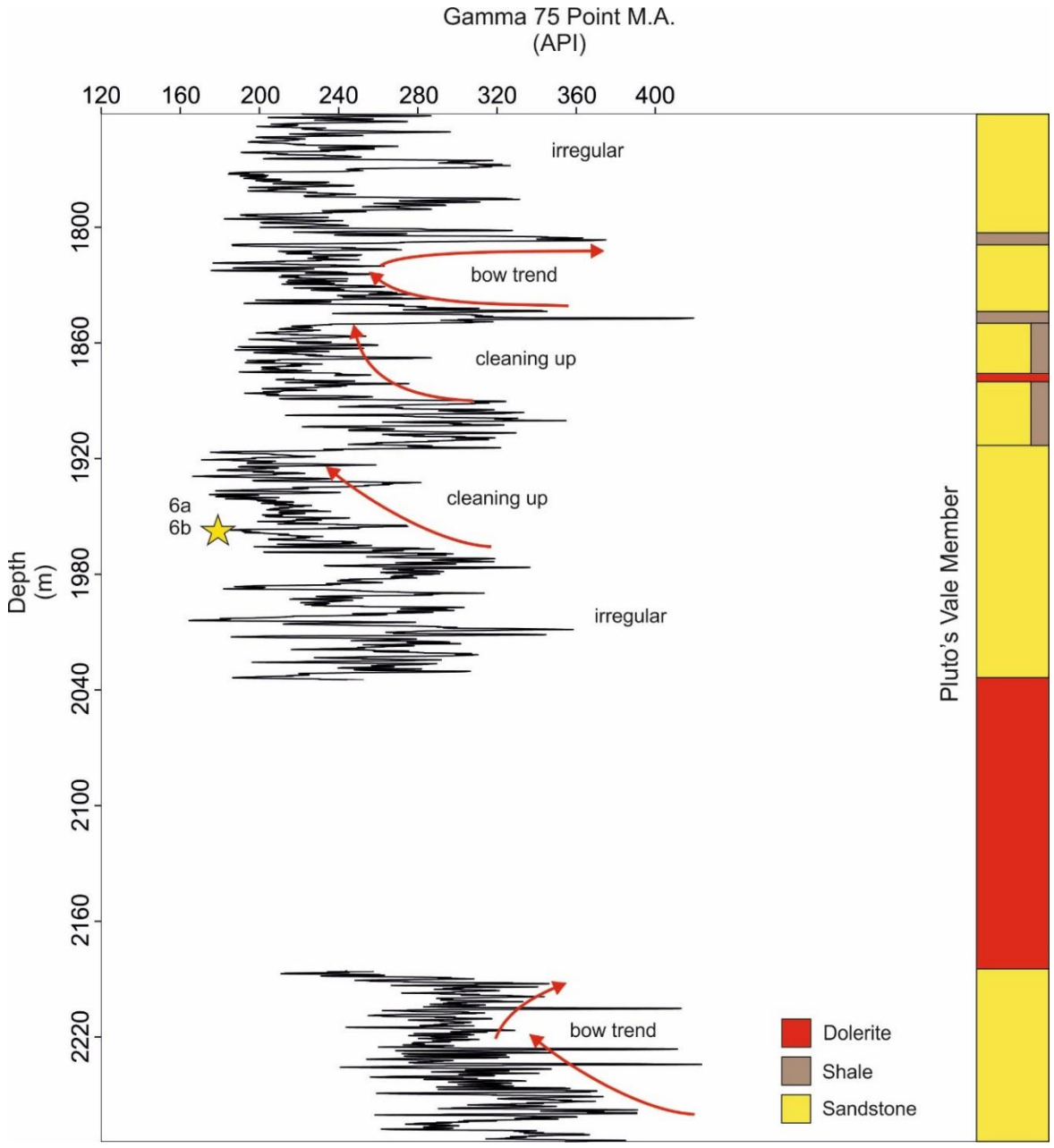

Figure 5.6: Ripon Fm. over view gamma log 3 with stacked cleaning up and bow trends (<20 m) visible with smaller scale (< 1 m) large gamma deviations (20 – 80 API) hindering clear cycle identification. Stars indicate geothermal samples with corresponding sample number. Data from intervals containing dolerite has been removed. 75-point moving average applied.

I. Trumpeters Member

The Trumpeters Member between the depths of 919.20 m – 946.16 m (Figure 5.4) consists of fine-grained laminated sandstone interbedded with laminated shale with occasional load casting and shale fragments. The gamma log shows a series of cleaning up and dirtying up trends (10 m – 20 m thick) with an overall cleaning up signal. Between 946.16 m – 1000.15 m the member is predominantly composed of dark laminated shale with minor sandstone lenses. A 10 m thick dolerite sill occurs at 955.48 m. The gamma log of the shale above the dolerite shows a cleaning up trend, transitioning into shale. Below the dolerite, a cleaning up and a dirtying up trend are visible within the shale. The lower segment of the Trumpeters Member, from 1000.15 m – 1048.40 m, is composed of dark fine-grained sandstone interbedded with laminated shale. The sandstone contains some disseminated and fault bound mineralisation (pyrite and calcite). The gamma log has a higher overall mean than the previous two intervals and exhibits clear bow-trends with a slight increase in mean gamma with depth. Smaller scale cyclical variations are clearly visible within larger order cycles.

Figure 5.7 shows a gamma log of the interval (928.77 m – 943.64 m) containing geothermal samples 1a and 1b (935.09 m – 935.15 m). The interval is predominantly composed of fine-grained laminated sandstone with minor shale interbeds. Load casting was observed at a depth of 932.00 and 933.10 m. The gamma log exhibits stacked dirtying up trends 2 m – 3 m thick, interspersed by single cleaning up trends of variable size (1 m – 4 m). Smaller scale trends (<1 m) are visible within larger cycles. Bow trends occur where there is an intersection of cleaning up and dirtying up trends (930 m, 936 m). Geothermal samples 1a and 1b occur midway up a dirtying up trend and are composed of very fine-grained sandstone with a mean thermal conductivity of 3.26 (W/(m.k)), mean thermal diffusivity of 1.31 ($m^2/s.10^{-6}$) and mean specific heat capacity of 0.939 (kJ/(kg.K)).

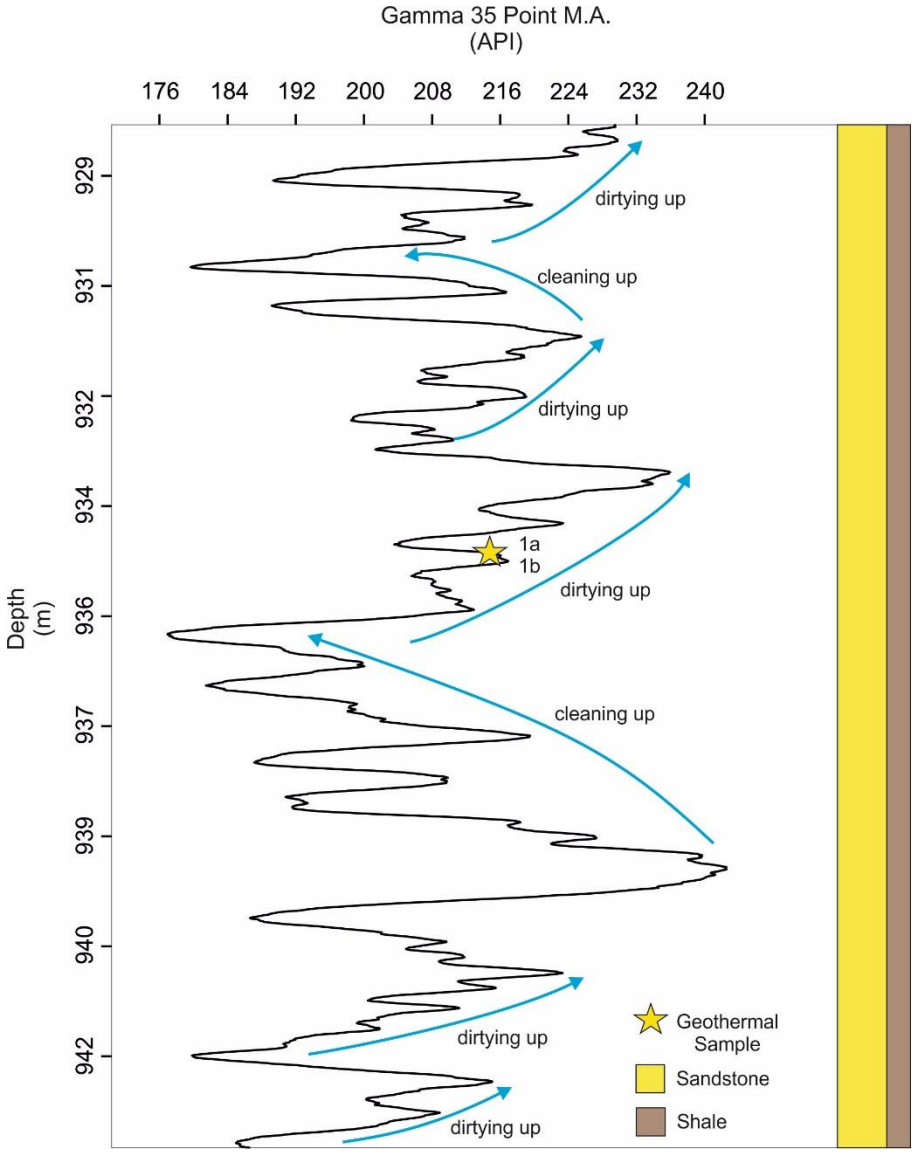

Figure 5.7: Gamma log (928.77 m – 943.64 m) showing trends from immediately above and below sample location 1a/1b. Stacked dirtying up trends 2 – 3 m thick are interspersed by single cleaning up trends of variable size (1 – 4 m). Smaller scale trends (<1 m) are visible within larger cycles. Geothermal sample 1a/1b is located within a dirtying up trend. 35-point moving average applied.

II. Wonderfontein Member

The Wonderfontein Member (Figure 5.4, 5.5) (1048.40 m – 1346.13 m) is composed of massive carbonaceous black shale and siltstone, intercalated with thin (2 mm – 5 mm) rhythmically bedded siltstone and shale layers. Minor sandstone layers (5 mm – 20 mm) thick occur at a depth of 1077 m. A fault at 45° to the core axis was observed at a depth of 1121.95 m, filled with quartz and containing pyrite on slickenside surfaces. Between the depths of 1249.79 m – 1259.43 m the core is characterised by massive shale and siltstone, with minor fine grained sandstone, followed by light grey very-fine grained sandstone (1259.43 m – 1270.56 m) grading to medium-grained with 5 – 8% black heavy mineral content. The base of the sandstone unit contains successive stacked horizons of black shale conglomerate with rounded shale clasts in sandstone. Massive and rhythmically bedded shale and siltstone underlie the sandstone unit (1270.56 m – 1346.13 m) with minor fine to very fine-grained sandstone layers up to 1 m thick. Numerous tuff layers up to 1 cm thick occur throughout the Wonderfontein Member.

Several large scale (20 m – 30 m) cleaning up cycles and bow trends are visible on the gamma log. Smaller scale fluctuations (<3 m) occur within larger cycles. No geothermal samples were selected from the upper portions of the Wonderfontein Member due to the large proportions of shale. The Wonderfontein Member between the depths of 1249.79 m – 1346.13 m contains more sandstone than the overlying section. The 10 m thick sandstone layer is characterised by a well-defined boxcar trend. The remaining shale/siltstone with interbedded sandstone does not exhibit trends on a large scale. Four geothermal samples were selected from the lower section of the Wonderfontein Member: samples 2a/2b (Figure 5.8), sample 10 (Figure 5.9), and sample 11 (Figure 5.10).

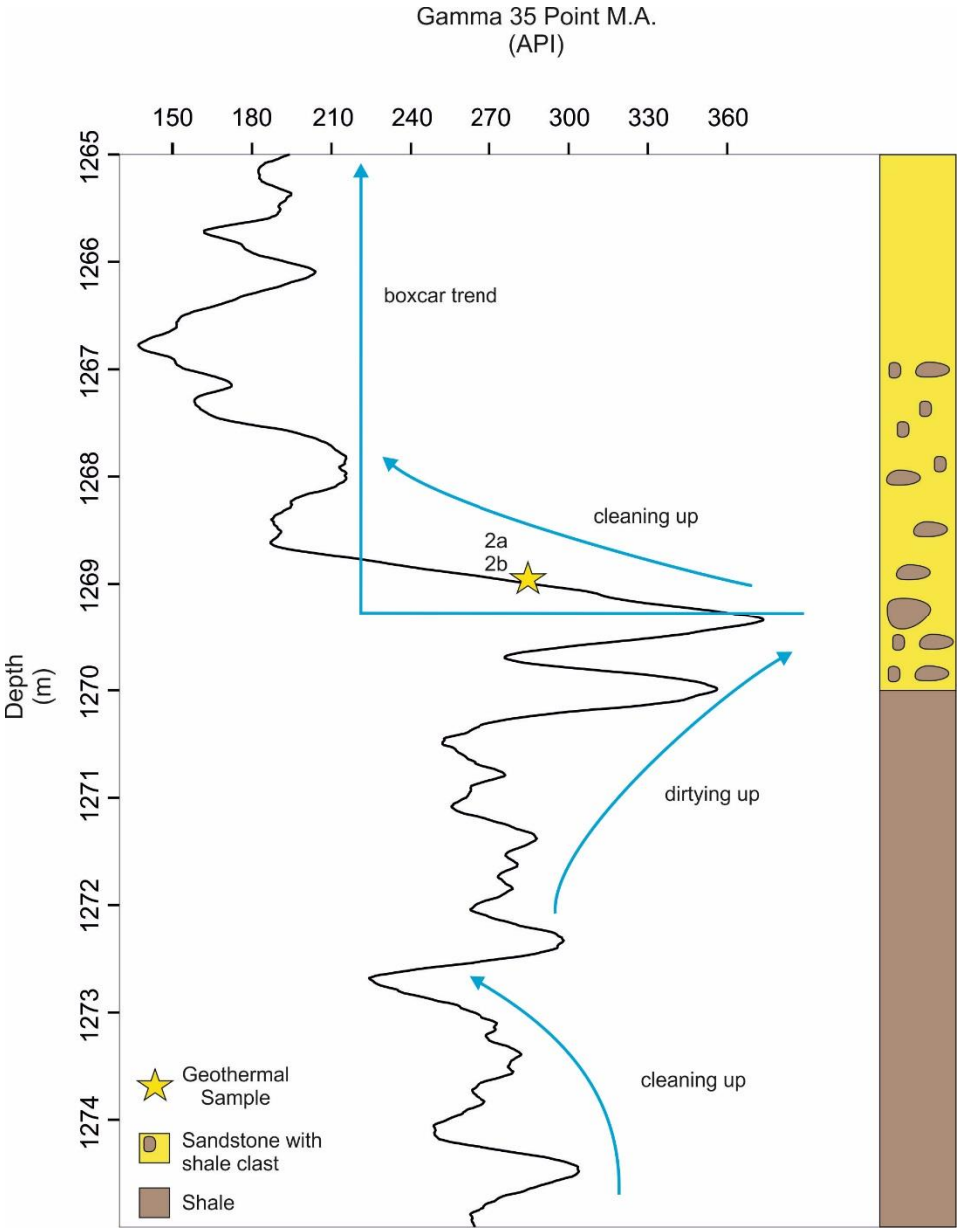

Figure 5.8: Gamma log (1265 m – 1275 m) showing trends from immediately above and below sample location 2a/2b. The sample is located on a rapidly cleaning up arm of a boxcar trend at the transition from shale to medium-grained sandstone. Cleaning up and dirtying up trends, 3 – 4 m thick, characterise the gamma log below the sample location. Smaller scale trends (<1 m) are visible within larger cycles. 35-point moving average applied.

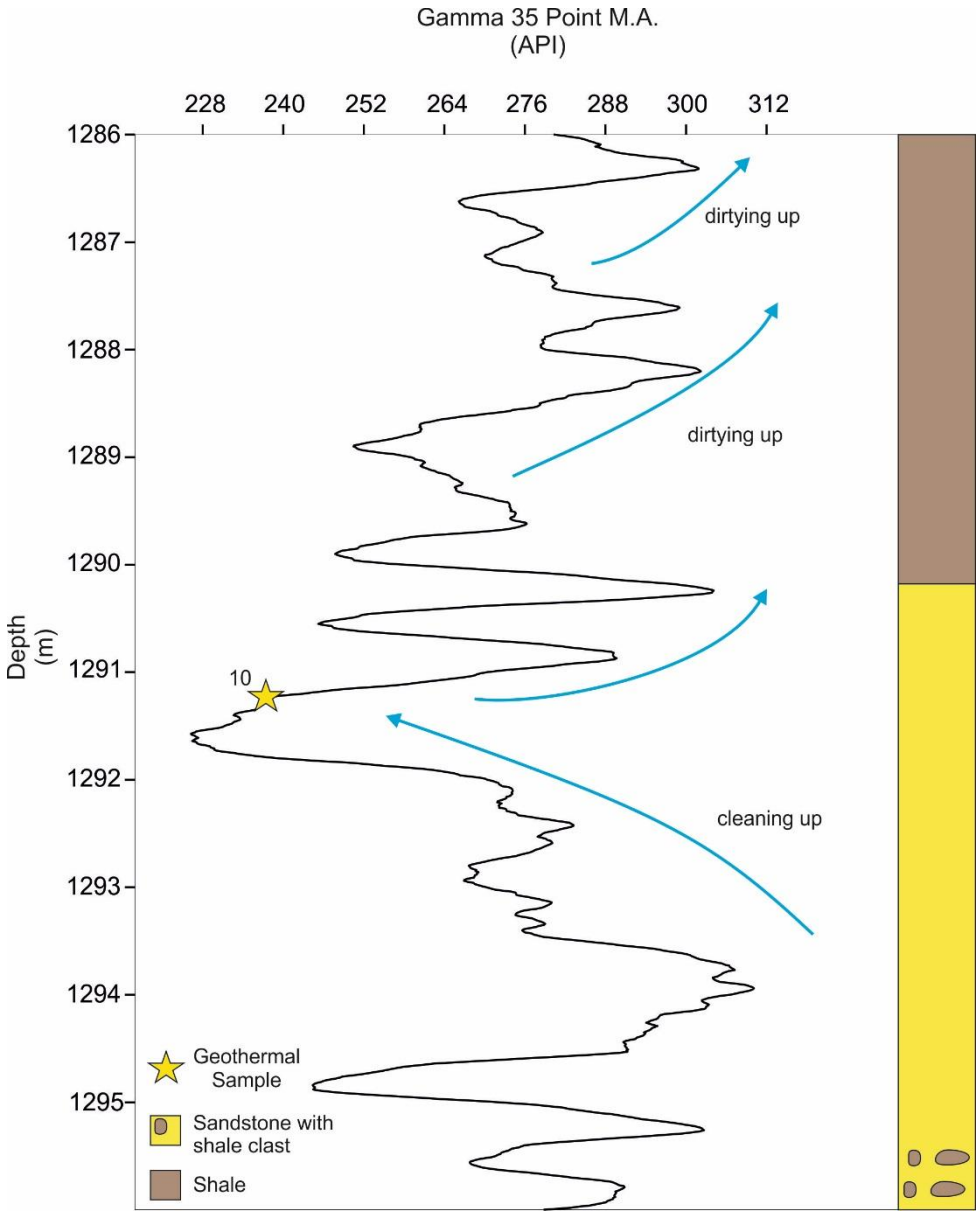

Figure 5.9: Gamma log (1286 m – 1296 m) showing trends from immediately above and below sample location 10. The sample is located at the apex of a cleaning upwards trend 3 m in thickness. Dirtying upwards trends (1 – 2 m thick) characterise the shale succession above the sample location. Smaller scale trends (<1 m) are visible within larger cycles. 35-point moving average applied.

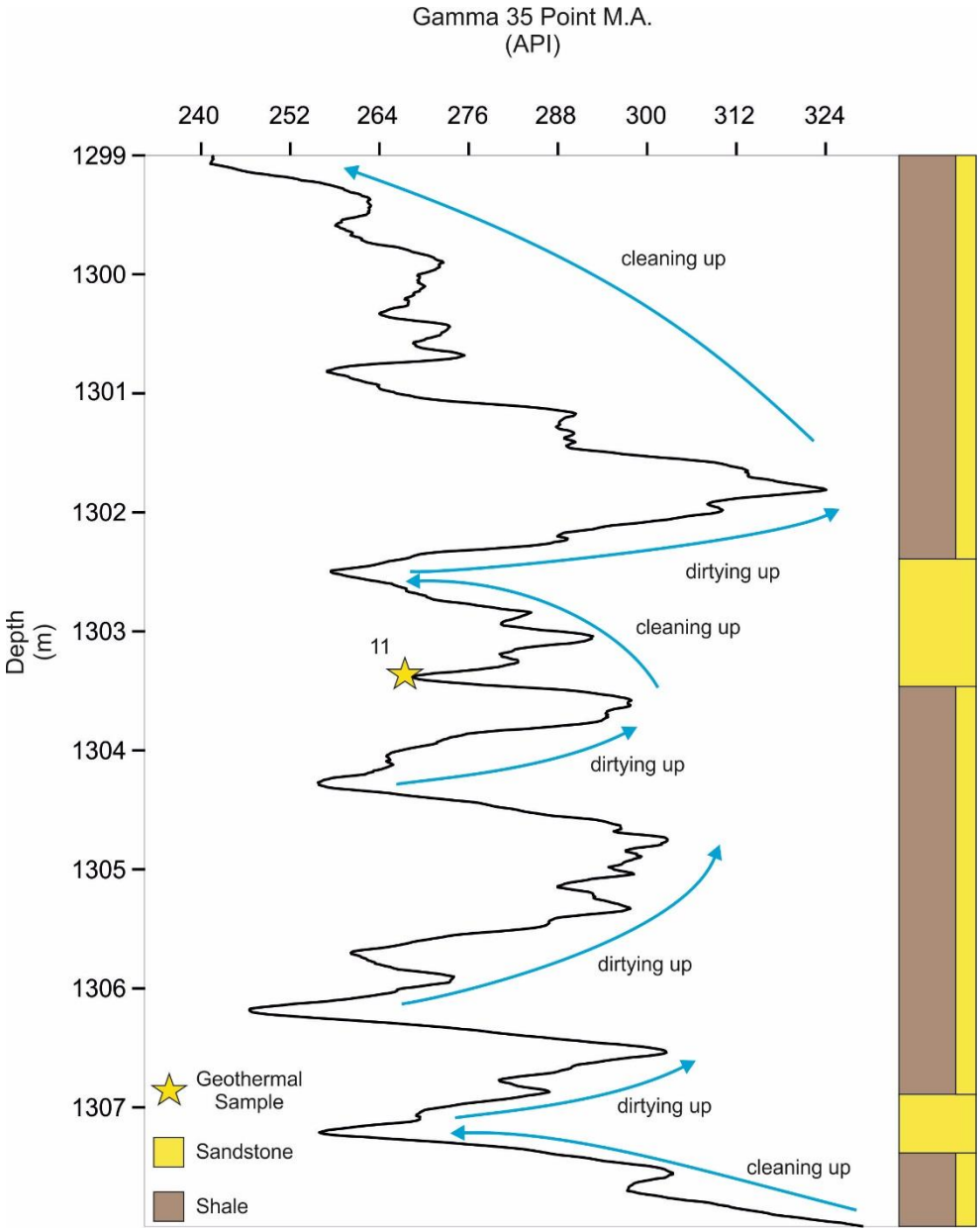

Figure 5.10: Gamma log (1299 – 1308 m) showing trends from immediately above and below sample location 11. The sample is located at the top of a small scale cleaning up trend (<50 cm) within a larger scale cleaning up trend (1 m). Stacked dirtying up trends 1 – 2 m thick, characterise the gamma log below the sample location. 35-point moving average applied.

Geothermal samples 2a and 2b (1269.41 m – 1269.50 m) comprise medium-grained sandstone located along the cleaning upwards limb of a boxcar trend (Figure 5.8) where the lithology becomes more sand-rich in comparison to the underlying shales. The samples have

a mean thermal conductivity of 3.19 (W/(m.k)), mean thermal diffusivity of 1.30 ($m^2/s.10^{-6}$) and mean specific heat capacity of 0.954 (kJ/(kg.K)). Relatively higher gamma cleaning up and dirtying up trends occur within the shale immediately below the geothermal sample. Geothermal sample 10 (1291.27 m) comprises a siltstone located at the base of a 2 m thick dirtying upwards trend (Figure 5.9). The siltstone has a thermal conductivity of 3.20 (W/(m.k)). Thermal diffusivity and specific heat capacity measurements were not possible on this sample due to the very fine-grained nature of the lithology. Calculated specific heat capacity is 0.8 (kJ/(kg.K)). Stacked dirtying up trends overlie the sample and a cleaning up trend underlies it. Geothermal sample 11 (1303.27 m) is a siltstone located within a cleaning up trend (Figure 5.10). The siltstone has a thermal conductivity of 3.29 (W/(m.k)). Again, thermal diffusivity and specific heat capacity measurements were not possible on this sample.

III. Pluto's Vale Member

The Pluto's Vale Member occurs between the depth of 1346.13 m – 2276.13 m and is 930 m thick (Figures 5.5 & 5.6). This member contains the largest proportion of sandstone in comparison with the overlying members. The Pluto's Vale member is characterised by stacked massive upwards fining successions of medium to fine-grained sandstone and interbedded fine to very-fine grained sandstone and shale. Several thick shale units (1413.60 m – 1470.63 m; 1627.00 m – 1646.80 m) comprising black carbonaceous shale, massive to finely bedded, with light-grey medium-grained sandstone layers (< 50 cm) and discrete tuff layers (< 2 cm) occur within the member along with dolerite intrusions up to 148 m thick.

The gamma log exhibits stacked bow trends up to 50 m thick between the depths of 1346 m – 1550 m corresponding to successive shale and sandstone units. Two clear cleaning up trends occur in a sandstone dominated interval of 1560 m – 1640 m that is underlain by an

irregular trend (closely spaced large API deviations) until a depth of approximately 1800 m within a, mainly, massive sandstone. A 50 m thick bow trend occurs at 1800 m underlain by stacked cleaning up cycles 60 m thick. Another section of gamma data with an irregular trend terminates at the intersection of a dolerite intrusion. Finally, a 50 m thick bow trend occurs in massive sandstone at the base of the Ripon Formation. Six samples were selected for geothermal analysis: samples 4a/4b (Figure 5.11), samples 6a/6b (Figure 5.12), sample 12 (Figure 5.13), and sample 13 (Figure 5.14).

Geothermal sample 12 (1450.27 m) is a siltstone sample from the apex of a cleaning up trend 1 m in thickness, within a larger scale (5 m) dirtying up trend (Figure 5.11). The sample is overlain by massive carbonaceous shale interbedded with thinly bedded (< 20 cm) medium-grained sandstone and discrete 2 mm – 3 mm thick tuff layers. Geothermal sample 12 has a thermal conductivity of 3.18 (W/(m.k)) and a calculated specific heat capacity of 0.81 (kJ/(kg.K)). Geothermal sample 13 (1465.27 m) is composed of siltstone and occurs at the apex of a 4 m thick dirtying up cycle (Figure 5.12). The sample is overlain and underlain by laminated carbonaceous shale. Numerous tuffs, up to 6 mm in thickness, occur within the shale above and below the sample.

Sample 13 has a thermal conductivity of 3.17 (W/(m.k)). Thermal conductivity or specific heat capacity measurements were not possible on this sample. Geothermal samples 4a and 4b (1530.84 m – 1530.92 m) are composed of fine-grained sandstone located at the apex of a small scale cleaning up trend, 50 cm in thickness, within a larger 3 m thick dirtying up trend (Figure 5.13). The sample location is overlain and underlain by medium to fine-grained sandstone with numerous horizons (2 cm – 20 cm thick) containing shale pebble conglomerates. Cleaning up and dirtying up trends are clearly visible above and below the sample location. Geothermal samples 4a and 4b have a mean thermal conductivity of 3.63

(W/(m.k)), mean thermal diffusivity of 1.53 of ($m^2/s.10^{-6}$), and mean specific heat capacity of 0.897 (kJ/(kg.K)).

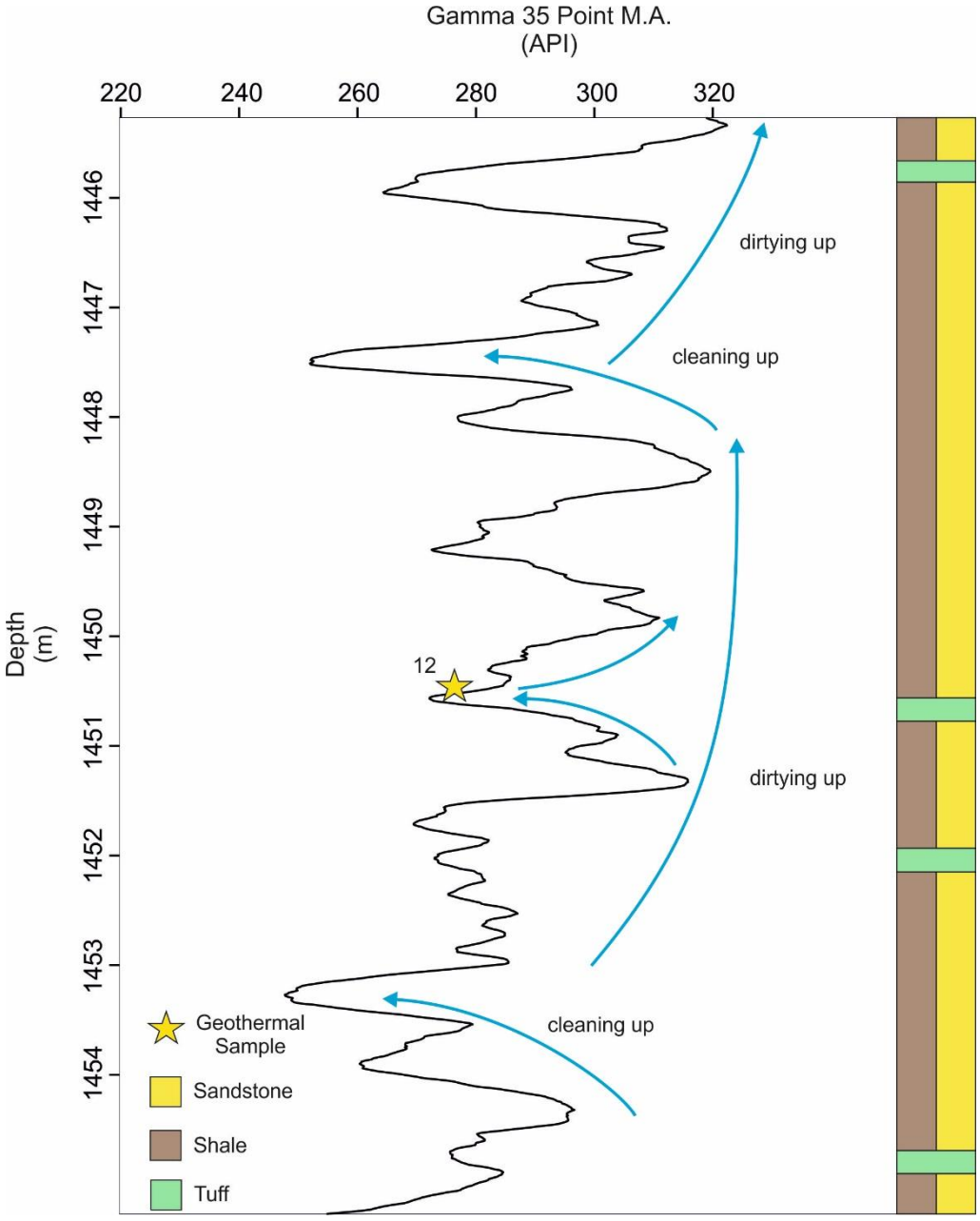

Figure 5.11: Gamma log (1445 m – 1455 m) showing trends from immediately above and below sample location 12. The sample is located at the apex of a small scale cleaning up cycle (1 m) within a larger dirtying up trend (5 m). 35-point moving average applied.

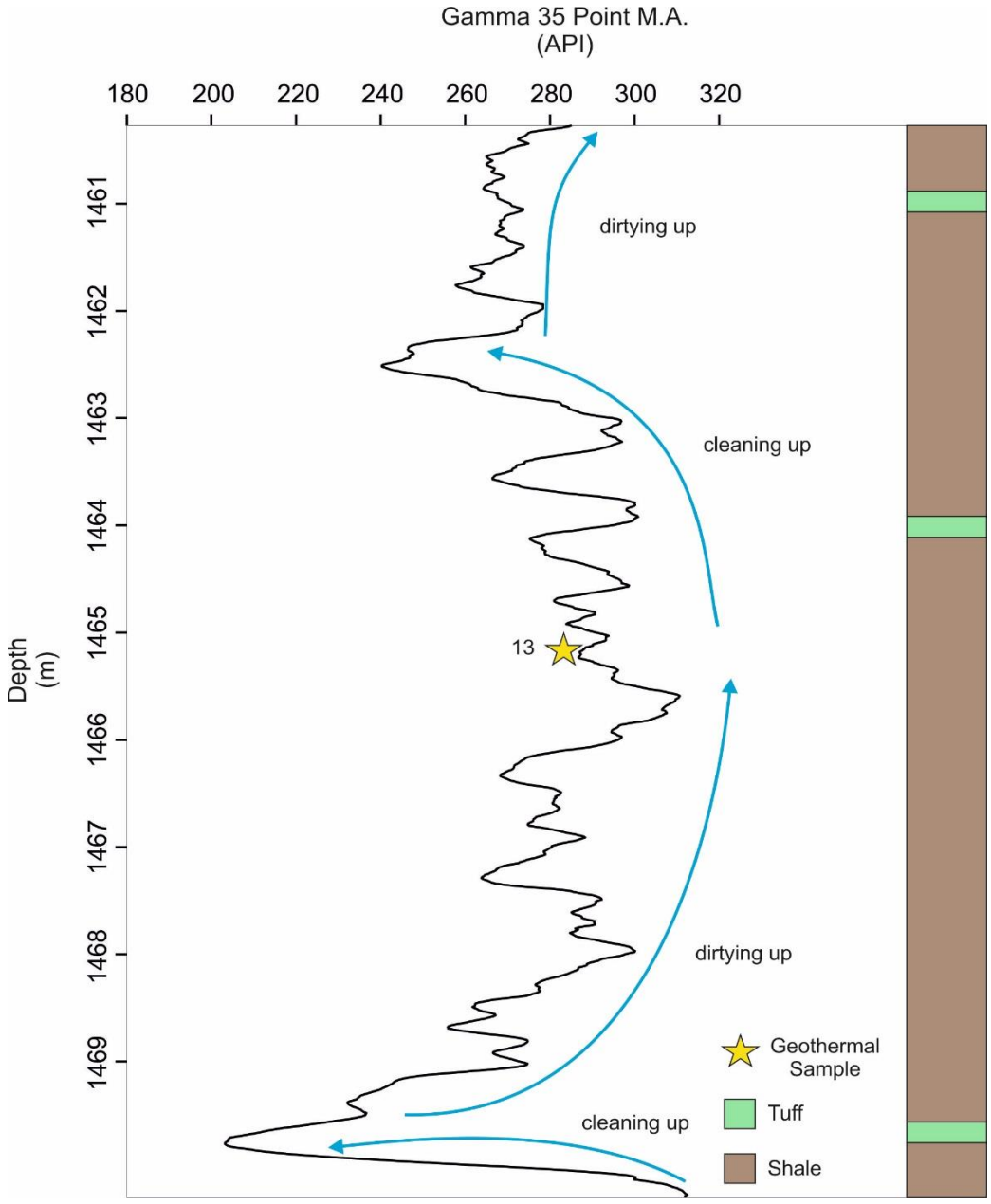

Figure 5.12: Gamma log (1460 m – 1470 m) showing trends from immediately above and below sample location 13. The sample is located at the apex of a dirtying up cycle 4 m in thickness. Cleaning up cycles characterise the trends adjacent to the sample location. 35-point moving average applied.

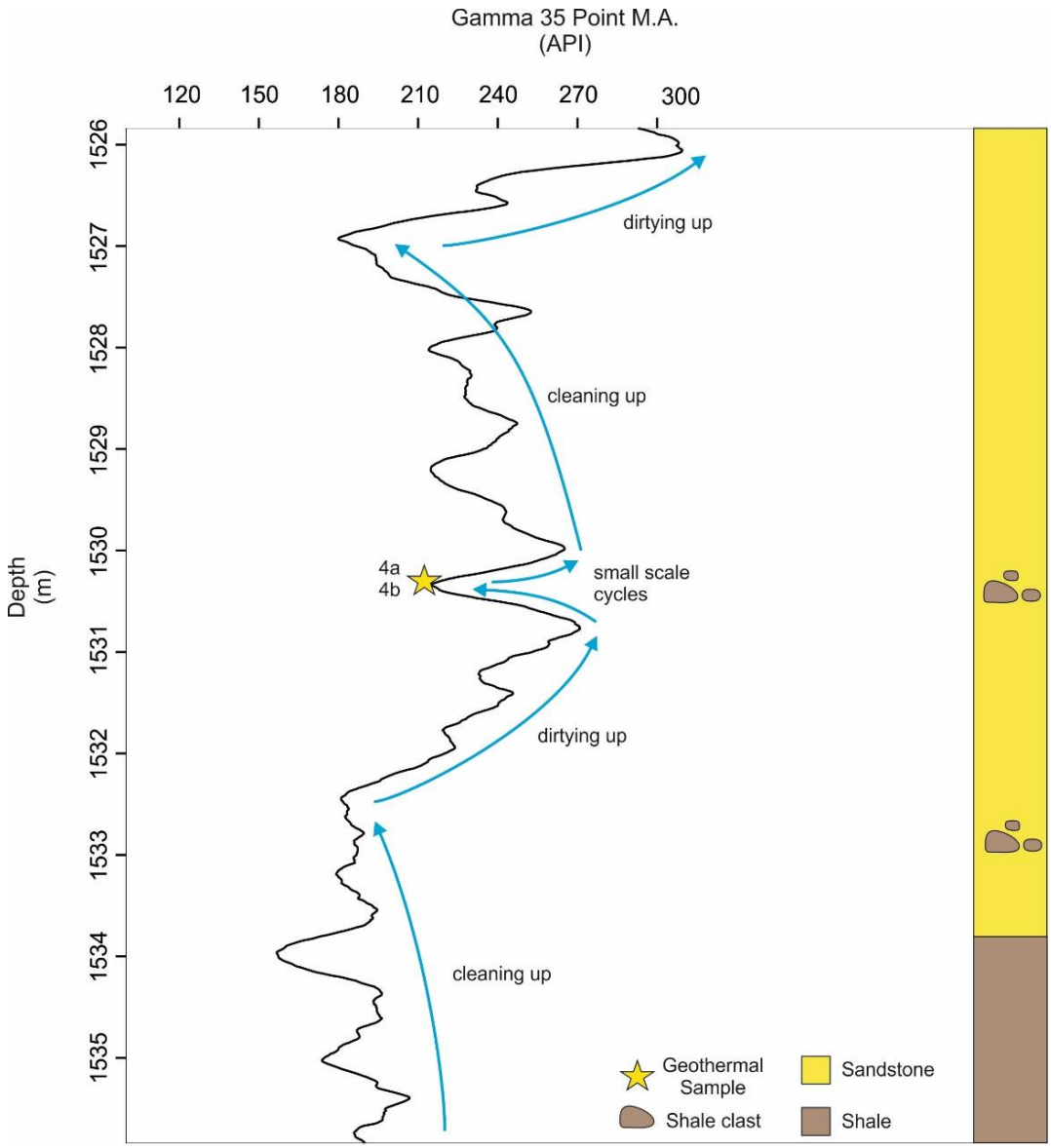

Figure 5.13: Gamma log (1526 m – 1536 m) showing trends from immediately above and below sample location 4a/4b. The sample is located at the apex of a small scale cleaning up cycle (50 cm) within a larger dirtying up trend (3 m). Successive cleaning up and dirtying up trends characterise the gamma log below the sample location. 35-point moving average applied.

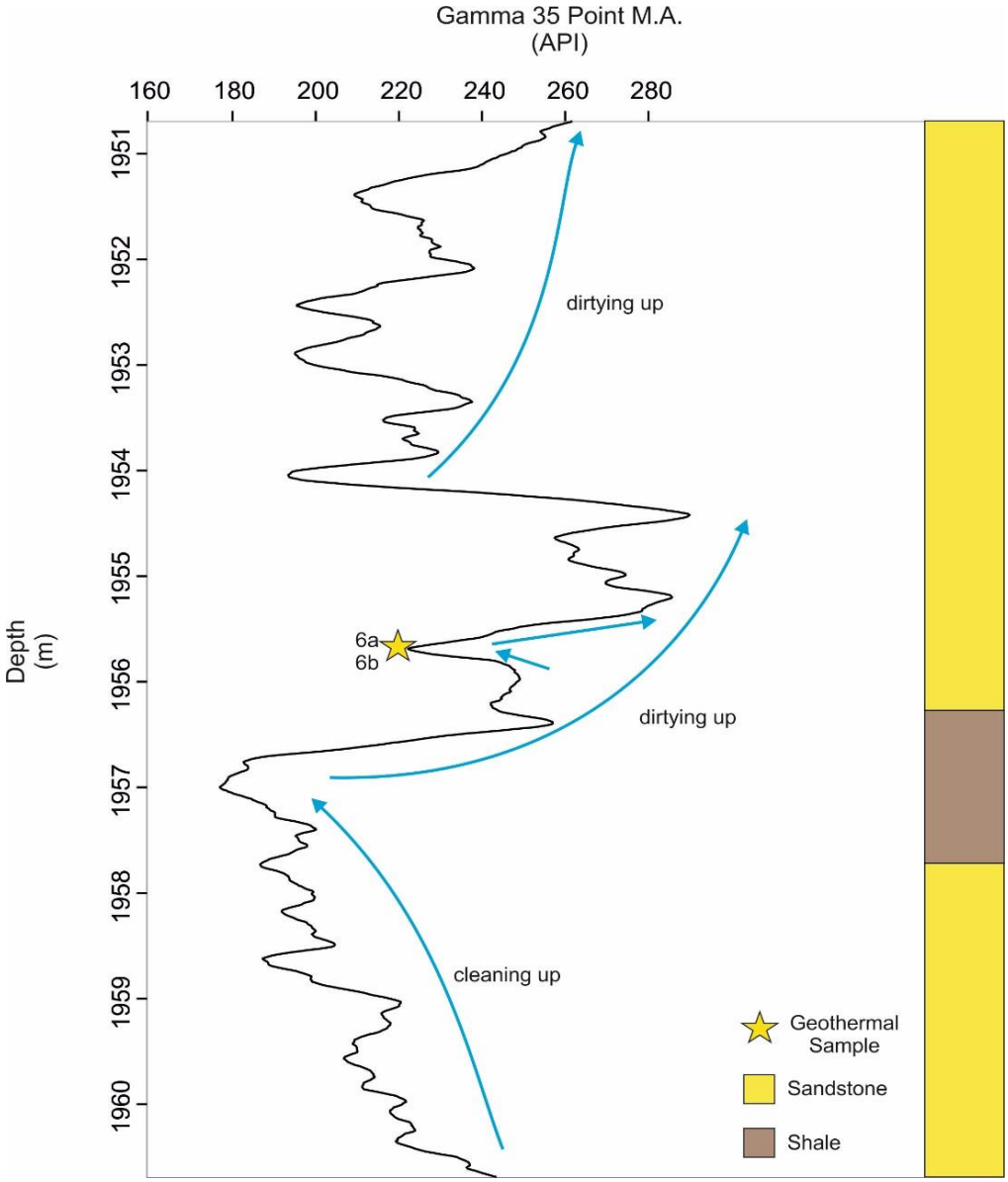

Figure 5.14: Gamma log (1950 m – 1960 m) showing trends from immediately above and below sample location 6a/6b. The sample is located at the base of a small scale dirtying up trend (1.5 m) within a larger dirtying up trend, 3 m thick. A large dirtying up trend occurs above and a large cleaning up trend occurs below the sample location. 35-point moving average applied.

Geothermal samples 6a and 6b (1955.69 m – 1955.73 m) (Figure 5.14) comprise fine-grained sandstone. The core at this depth is characterised by interbedded upwards fining sequences of fine-grained sandstone and laminated shale. Load cast structures were observed where sandstone overlies shale. Occasional shale clast conglomerates were also observed. Geothermal samples 6a and 6b have a mean thermal conductivity of 3.71 (W/(m.k)), mean thermal diffusivity of 1.41 of ($m^2/s.10^{-6}$), and mean specific heat capacity of 0.974 (kJ/(kg.K)).

5.4.4. Gamma versus Geothermal Potential

Table 5.2: Thermal conductivity, thermal diffusivity, specific heat capacity and gamma values of sandstone and siltstone samples from the Ripon Formation of borehole KWV-1.

Sample no.	Lithology	Depth (m)	Thermal Conductivity (W/(m K))	Thermal Diffusivity ($m^2/s.10^{-6}$)	Specific Heat Capacity (kJ/(kg·K))	Density (Kg/m^3)	Gamma Mean (API)
1a	VFG Sandstone	935.095-935.155	3.26	1.31	0.94	2680	234.4
1b	VFG Sandstone	935.095-935.155	3.26	1.31	0.939	2680	234.4
2a	MG Sandstone	1269.41-1269.50	3.19	1.30	0.951	2620	381.5
2b	MG Sandstone	1269.41-1269.50	3.19	1.30	0.957	2620	381.5
4a	FG Sandstone	1530.84-1530.92	3.63	1.53	0.898	2660	269
4b	FG Sandstone	1530.84-1530.92	3.63	1.53	0.895	2660	269

Sample no.	Lithology	Depth (m)	Thermal Conductivity (W/(m K))	Thermal Diffusivity ($m^2/s.10^{-6}$)	Specific Heat Capacity (kJ/(kg·K))	Density (Kg/m^3)	Gamma Mean (API)
6a	FG Sandstone	1955.69-1955.73	3.71	1.41	0.971	2730	239.3
6b	FG Sandstone	1955.69-1955.73	3.71	1.41	0.976	2730	239.3
10	Siltstone	1291.27	3.20	-	*0.80*	2730	227.4
11	Siltstone	1303.27	3.29	-	*0.80*	2740	247.8
12	Siltstone	1450.27	3.18	-	*0.81*	2770	298
13	Siltstone	1465.27	3.17	-	*0.80*	2750	298.7

Table 5.2 continued. Note: Specific Heat Capacity values in italics for samples 10 – 13 are calculated, as opposed to measured values for the remaining samples. Direct measurements were not possible so values were calculated at 25°C.

Table 5.2 displays thermal conductivity, thermal diffusivity, specific heat capacity and gamma values of sandstone and siltstone samples from the Ripon Formation of borehole KWV-1. Figures 5.15 – 5.17 are X-Y plots of geothermal measurements versus gamma. Figure 5.15 illustrates the fact that fine-grained sandstone has the highest thermal conductivity with a mean of 3.67 (W/(m.K)) compared to a range of 3.17 – 3.29 (W/(m.K)) for the very-fine grained sandstone, medium-grained sandstone and siltstone. In Figure 5.16, fine-grained sandstone has the highest thermal diffusivity with a mean of 1.47 (1E-6 mm^2/s). Very fine grained and medium-grained sandstone have similar values around 1.30 (1E-6 mm^2/s). In Figure 5.17, the various sandstone lithologies have a higher average specific heat capacity in comparison with siltstone. Fine-grained sandstone has a bi-modal distribution with a range of 0.895 – 0.971 (kJ/(kg·K)), followed by medium grained-sandstone with a mean 0.954 (kJ/(kg·K)), and very fine-grained sandstone with a mean of 0.94 (kJ/(kg·K)). Figure 5.18 displays density versus gamma data. Siltstone has the highest density with a mean of 2748 (Kg/m^3) compared to 2680 (Kg/m^3) for very-fine grained sandstone, and 2620 (Kg/m^3) for medium-grained sandstone. Fine-grained sandstone has a range of 2660 – 2730(Kg/m^3). Medium-grained sandstone has an anomalously high gamma reading of 381 API compared to 240 – 270 API for fine-grained sandstone, 234 API for very fine-grained sandstone and 227 – 299 API for siltstone.

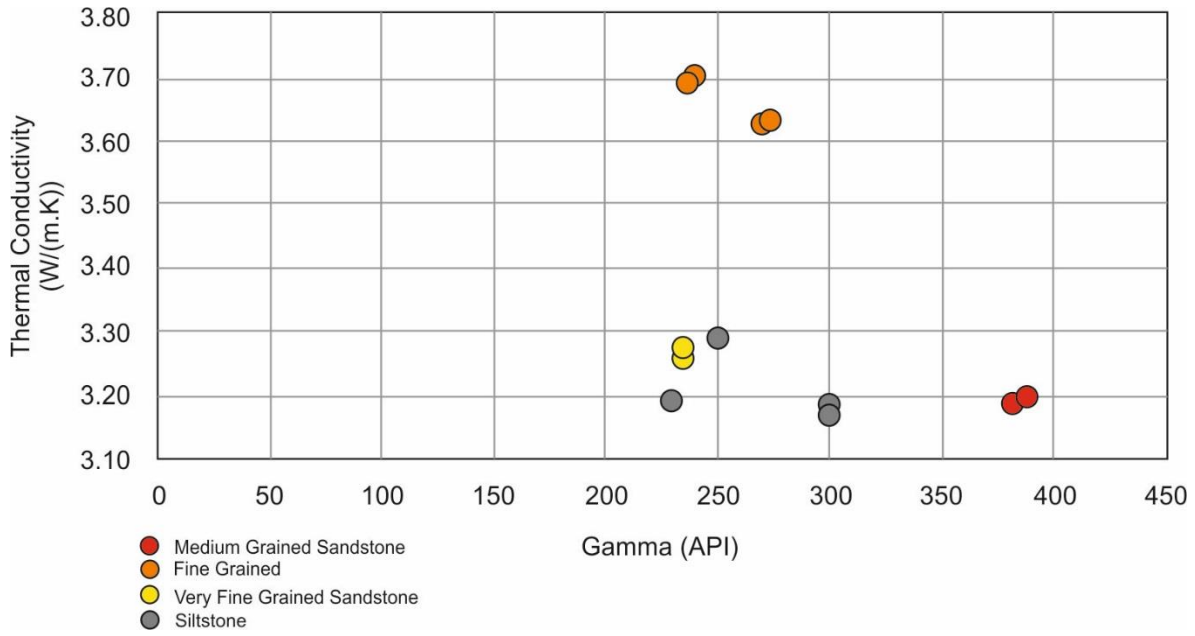

Figure 5.15: Thermal Conductivity versus Gamma for four lithologies from the Ripon Formation of borehole KWV-1. Fine-grained sandstones exhibit the highest thermal conductivity and shales the lowest with a similar gamma range for both lithologies (220 – 300 API).

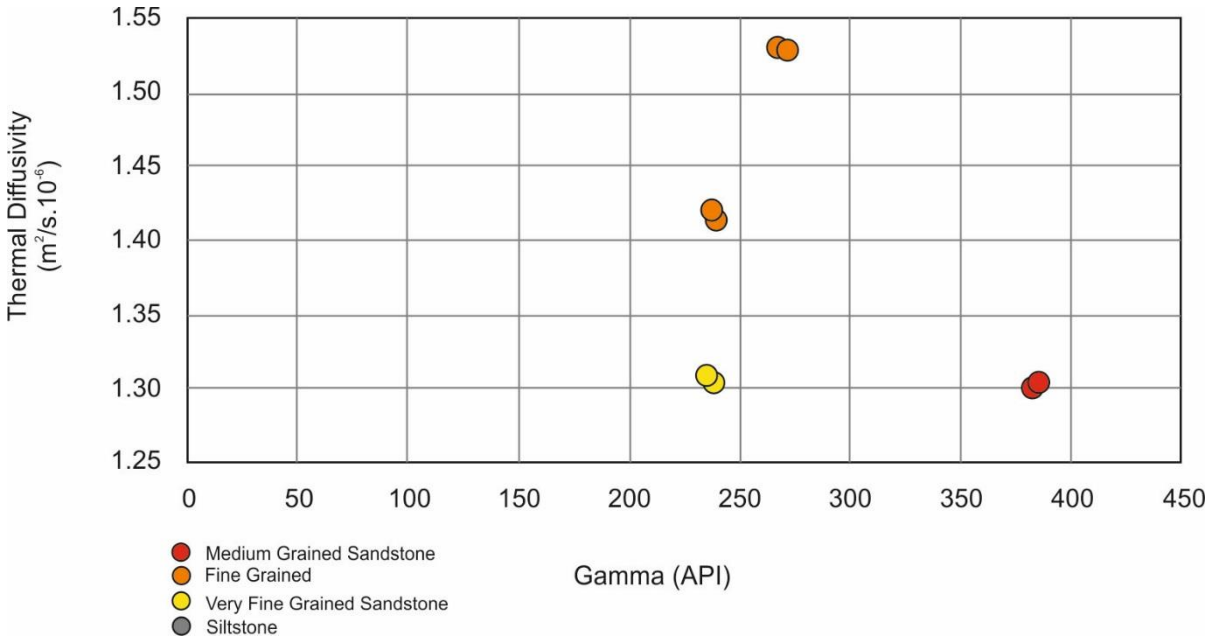

Figure 5.16: Thermal Diffusivity versus Gamma for four lithologies from the Ripon Formation of borehole KWV-1. Fine-grained sandstones exhibit the highest values for thermal diffusivity and medium-grained the lowest with a significant difference in gamma (150 API) between the two lithologies. Note: Siltstone measurements were not possible.

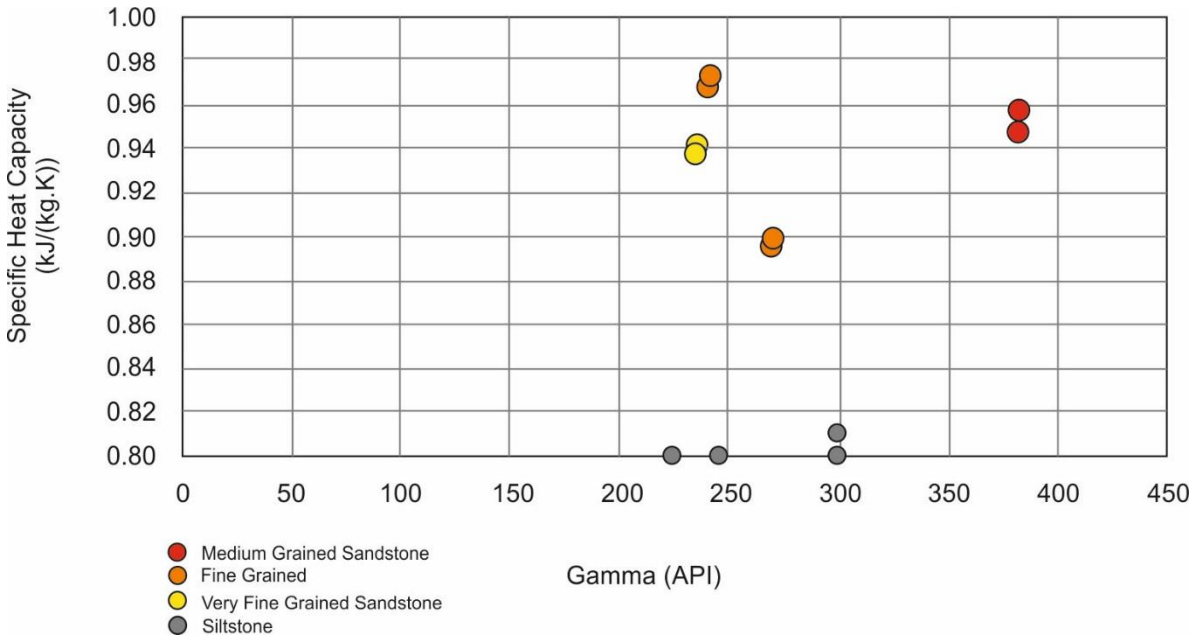

Figure 5.17: Specific Heat Capacity versus Gamma for four lithologies from the Ripon Formation of borehole KWV-1. Again, fine-grained sandstones exhibit the highest values for specific heat capacity however, a separate set of fine-grained samples had a 9 % lower value. Note: Siltstone values were calculated and not measured.

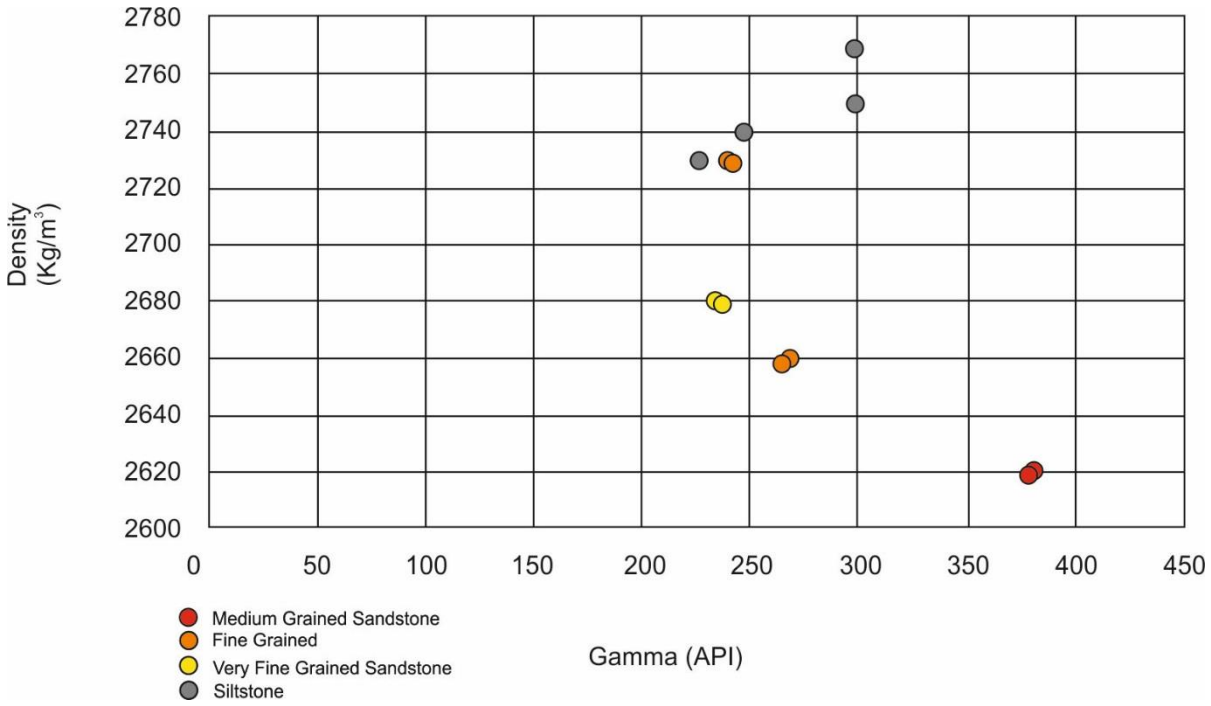

Figure 5.18: Density versus Gamma for four lithologies from the Ripon Formation of borehole KWV-1. Siltstone samples have the highest density, followed by fine-grained sandstone with a bimodal distribution. High gamma medium-grained sandstone has the lowest.

5.4.5. Depositional Facies

Facies	Texture	Structure
SDL	Fine-grained sandstone, dark grey	Planar laminated, occasional load casts and shale fragments. Rarely massive.
SLL	Fine-grained sandstone, light grey	Planar laminated to thinly bedded (2cm).
SLLV	Very fine-grained sandstone, light grey	Laminated. Darker and lighter layering.
SH	Dark grey to light black shale	Laminated with well-defined bedding by darker and lighter interbeds. Occasional slump structure. Fossil leaf found.
DOL	Dolerite	
BSH	Black shale	Well defined to poorly bedded with beds 1-5 mm.
STM	Grey Siltstone	Thinly bedded (<5mm) to massive.
SML	Medium-grained sandstone, light grey	Ripple marking, rare heavy mineral content. Occasional shards of shale parallel to bedding. Upwards fining to SLL. Load casting. Soft sediment deformation.
BSC	Black shale conglomerate in sandstone.	Angular to well-rounded clasts. Occasional upwards fining.
TU	Light grey, yellowish grey to brown-grey tuff	5 mm to 3 cm thick.
SLM	Very fine-grained sandstone, light grey, speckled/mottled.	Some reddish brown staining and bleached white alteration.
SMB	Browish-grey to dark grey medium-grained sandstone.	Thinly bedded.
FVD	Dark grey very fine-grained sandstone.	Bedded to massive.

Figure 5.19: Facies scheme for lithologies of the Ripon Formation from borehole KWV-1.

Figure 5.19 lists the different lithologies (sandstone, shale, siltstone, shale conglomerate, tuff, and dolerite) encountered within the Ripon Formation of borehole KWV-1 as well as their general texture and structure. Seven different sandstone varieties were observed ranging from medium-grained to fine-grained to very fine-grained with two general colour variations; light and dark. Sandstone bodies ranged in thickness from discrete millimetre to centimetre-sized beds to stacked massive bodies 10's of metres thick.

	Facies Codes	Process	Environment	Gamma Trend
1	BSH, STM, SH	Hemipelagic and pelagic sedimentation.	Inter lobe to basin plain.	Irregular saw-tooth, high gamma.
2	BSH, STM, SH, SLLV, FVD, SLL, SDL	Turbidity current and hemipelagic sedimentation.	Lower fan to basin plain.	Irregular. Shale high, sandstone low.
3	SDL, SLL, BSC, SH, SLM	Turbidity current and hemipelagic sedimentation.	Non-channelised lower fan.	Bow/boxcar.
4	SMB, SML, SLL, SDL, BSC	Turbidity current/debris flows	Channelised upper to mid-fan.	Bow/boxcar.

Figure 5.20: Facies associations (processes and environments) and general gamma trend of lithologies from the Ripon Formation of borehole KWV-1.

Two varieties of shale were documented, a dark grey variety and a black variety as well as a grey siltstone. The shale and siltstone ranges from laminated, with well-defined bedding, to massive. Thin tuff horizons and large-scale dolerite intrusions were also described.

Various lithologies were commonly observed together (Figure 5.20), which is indicative of palaeoenvironment and process with a corresponding gamma signature. Four submarine fan sub-environments were deduced from the facies associations: (1) An inter-lobe to basin plain setting characterised by laminated to thinly bedded siltstone and shale deposited by hemipelagic and pelagic sedimentation; (2) A lower fan to basin plain environment comprising laminated to thinly bedded siltstone and shale along with thinly bedded to massive very-fine-grained to fine-grained sandstone of varying colour, deposited by hemipelagic sedimentation and turbidity currents; (3) A non-channelised lower fan environment typified by thinly bedded very-fine to fine-grained sandstone interbedded with laminated shale and rip-up shale conglomerate deposited by hemipelagic sedimentation and turbidity currents; (4) A channelised upper to mid-fan setting characterised by thinly bedded

to massive fine-grained and medium-grained sandstone with shale rip-up clast conglomerates, deposited by turbidity currents and/or debris flows.

5.5. Discussion

5.5.1. Grainsize-Geothermal-Gamma Relationships

It would be not unreasonable to expect a quartz arenite or an arkosic arenite of varying grain sizes plotted against gamma to have a linear relationship. The mineralogy of the sandstone is a critical factor in its geothermal potential, due to the differing thermal conductivities minerals possess (e.g. quartz = 7.69 (W/(m.K), calcite = 3.59 (W/(m.K), K-feldspar = 2.31(W/(m.K)) (Clauser and Huenges, 1995; Horai, 1971 and Zimmerman, 1989 in: Maqsood and Kamran, 2005). Therefore, a medium-grained quartz arenite would have a high geothermal value (higher proportion of quartz) and a low gamma value (lower proportion of clay matrix) in comparison to a very fine-grained arenite/wacke with a low geothermal potential (lower proportion of quartz) and a high gamma value (greater proportion of clay matrix). The linear relationship would allow for a range of gamma values to be identified corresponding to high geothermal potential.

When attempting to develop a gamma-lithology framework it would seem logical to compartmentalise each lithology with its corresponding gamma value based on regional or even global standards. Therefore, a given gamma value would represent a clear-cut lithology of predetermined geothermal potential; for example, medium grained sandstone (high geothermal potential) – 100 API; fine-grained sandstone – 150 API; very fine-grained sandstone (low geothermal potential) – 180 API; siltstone – 200 API; and shale 250 – API.

This methodology would, however, not be a particularly accurate tool for geothermal exploration due to the scale and distribution of sediment within the submarine fan, and the fact that nearly all the lithologies are found together in varying proportions depending on location within the submarine fan. For example, wireline gamma data from a thick sandstone unit, with interbedded discreet shale/siltstone layers, would give widely differing gamma values depending on what millimetre scale lithological layer was selected (Figure 5.21a), even though the unit would be a potential reservoir. Additionally, a high-gamma arkosic sandstone (200 API) interbedded with an organic-rich black shale (300 API) would be misinterpreted and potentially over-looked as a potential reservoir (Figure 5.21b).

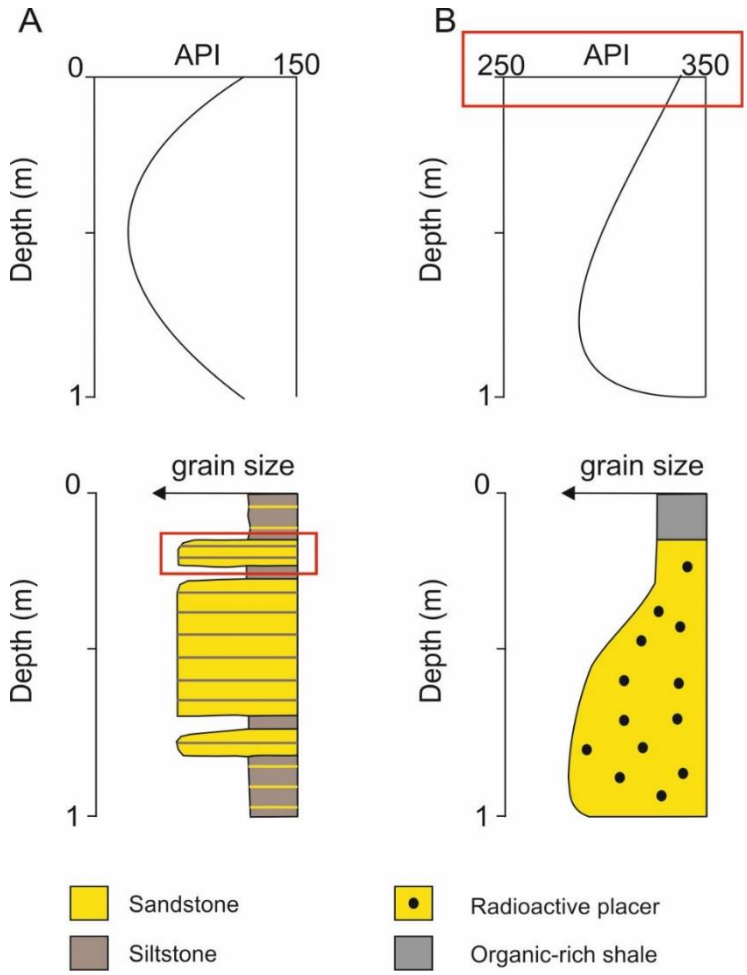

Figure 5.21: Gamma-ray curves and associated sedimentary packages. A: Interbedded sandstone and siltstone with interbeds on differing scales (red box) with an overall bow trend. Individual small-scale layers will have large gamma variations. B: A radioactive sandstone overlain by an organic-rich shale with API values higher (red box) than usually expected from sandstone, exhibiting an overall dirtying up trend.

5.5.2. KWV-1 Core Sample Analysis

A critical analysis of the potential geothermal reservoirs (PGR) characteristics from borehole KWV-1 samples (thermal diffusivity, thermal conductivity, specific heat capacity and density), modelled against corresponding wireline gamma-ray data, yields no discernible relationship. No relationship exists between grainsize or lithology and gamma. Thermal diffusivity, thermal conductivity and specific heat capacity modelled against gamma, all result in a coefficient of determination less than 0.3 (Figure 5.22, 5.23, 5.24) with specific heat capacity (Figure 5.24) having an R^2 value less than 0.05. Density versus gamma has the highest coefficient of determination (R^2 = 0.3021) (Figure 5.25). Fine-grained sandstone, very fine-grained sandstone and siltstone all have a similar gamma range (Figure 5.24), between 230 – 300 API, making differentiation of lithology/grainsize and therefore geothermal potential problematic.

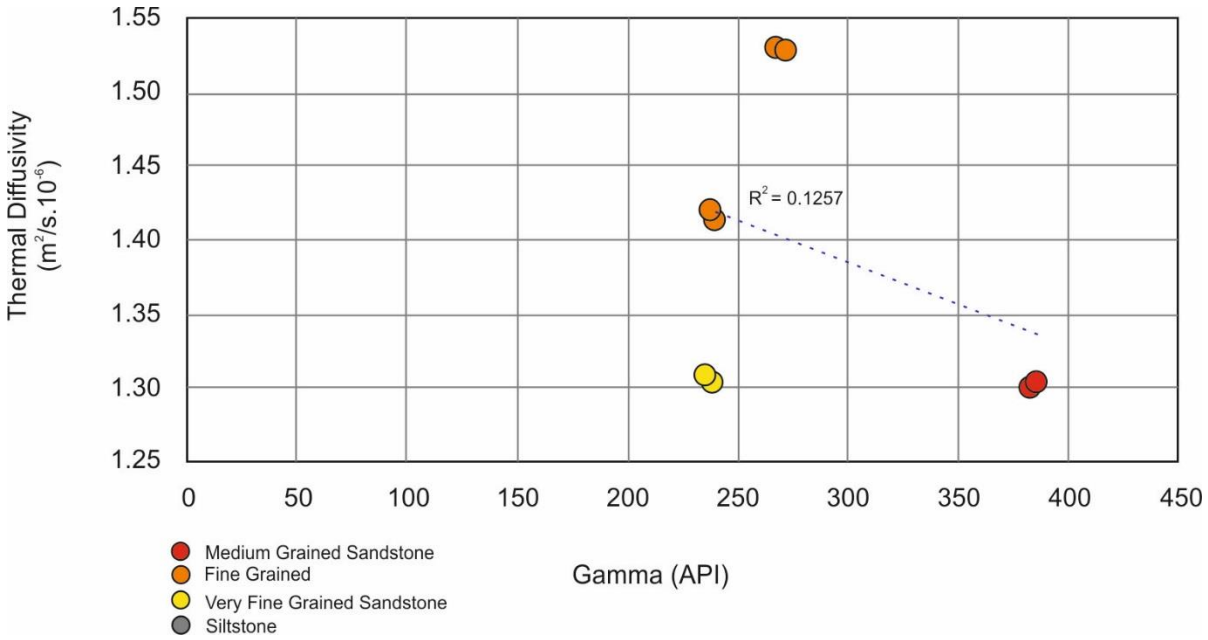

Figure 5.22: No statistically relevant linear relationship exists between thermal diffusivity and gamma data from the samples analysed for geothermal potential. R^2 = 0.1257. Note: Siltstone measurements were not possible.

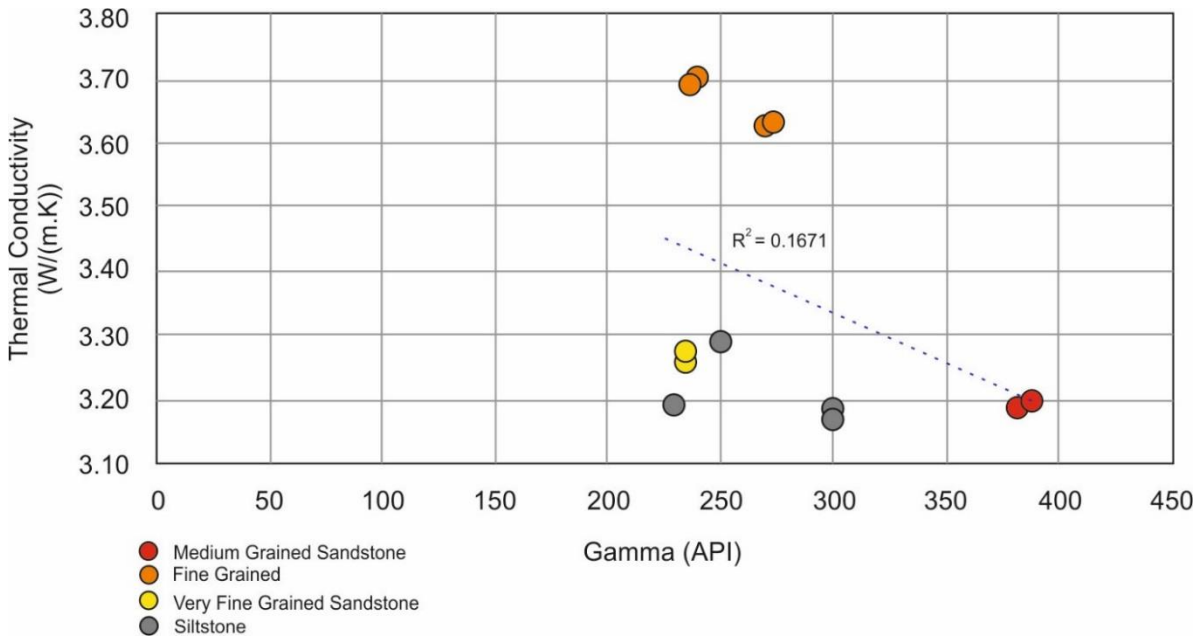

Figure 5.23: No statistically relevant linear relationship exists between thermal conductivity and gamma data from the samples analysed for geothermal potential. $R^2 = 0.1671$.

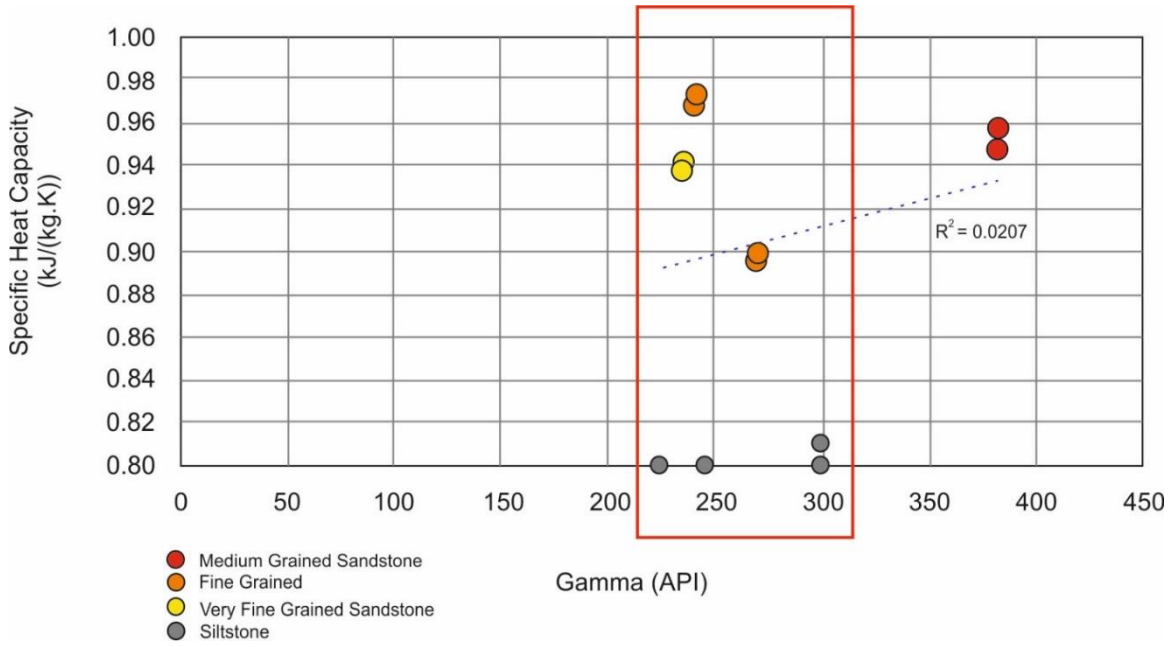

Figure 5.24: No statistically relevant linear relationship exists between specific heat capacity and gamma data from the samples analysed for geothermal potential. $R^2 = 0.0207$. Fine-grained sandstone, very fine-grained sandstone and siltstone have a similar gamma range (red box). Note: Siltstone values were calculated and not measured.

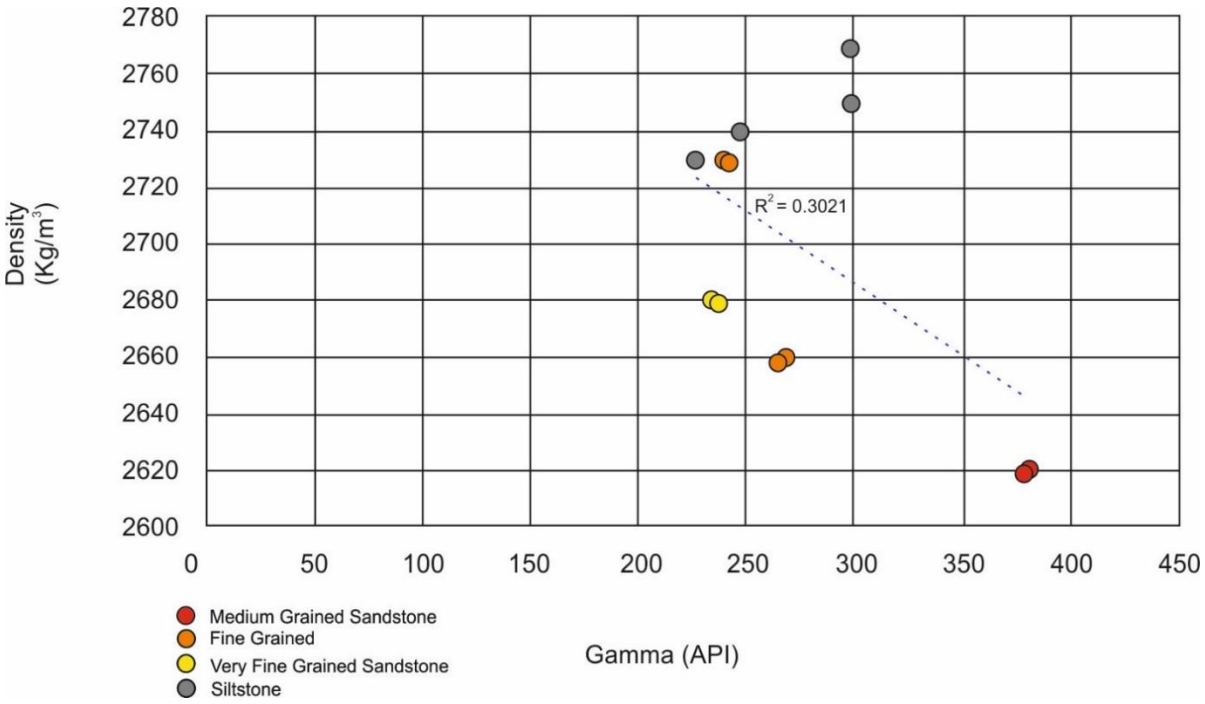

Figure 5.25: No statistically relevant linear relationship exists between density and gamma data from the samples analysed for geothermal potential. $R^2 = 0.3021$.

5.5.3. Medium-Grained Sandstone Gamma Anomaly

In borehole KWV-1, the medium-grained sandstone samples exhibit very high API values in comparison with fine and very fine-grained sandstone as well as siltstone and shale (Table 5.2). There may be several reasons for the anomaly:

1) The incorporation of high gamma rip-up shale clasts into the medium-grained sandstone. In borehole KWV-1, medium-grained sandstone commonly occurs in conjunction with conglomeritic horizons of sub-rounded to sub-angular shale/siltstone clasts within a sandstone matrix. Erosive turbidity currents occurring in the higher energy part of the submarine fan (i.e. channelised upper fan) scour the underlying high-gamma shale/siltstone and incorporate the clasts into the base of the turbidite as well as loose clayey sediment into the matrix (i.e. Bouma division T_a; Bouma et al., 1962). The resulting gamma-signal would be higher than 'clean' sandstone. Where stacked successions of high-energy turbidites

appear, the only remnants of the now completely eroded underlying shale layers may occur as repetitive conglomeritic layers, and manifest as high gamma spikes within thick low-gamma sandstone layers, corresponding to medium-grained sandstone in the core. However, according to Table 5.1, the medium-grained sandstone has a significantly higher API value than even the shale or siltstone which may have contributed to the overall higher value.

2) A higher abundance of potassium-rich feldspar components in the medium-grained sandstone. An arkosic arenite or feldspathic greywacke (Pettijohn, 1975) comprising K-rich feldspars (up to 16% K; Hurst, 1990) would have a gamma-ray signal considerably higher than a quartz arenite or quartz wacke respectively (Emery and Myers, 1996). If the high-gamma medium-grained sandstone observed in borehole KWV-1 has a higher proportion of feldspar in comparison to the remaining gauges of sandstone, siltstone and shale, then a gamma discrepancy would be visible. Thin section analysis of sandstone samples from borehole KWV-1 (Chapter 4, Figure 4.15) confirms the presence of feldspar within medium-grained sandstone (Figure 4.15c), however, feldspar is also present in very-fine and fine-grained sandstone samples. Additionally, it is highly unlikely that sandstone of varying gauges within the same formation would have a different provenance. The net effect of an arkosic sandstone is a rise in the gamma baseline of the sandstone as observed in borehole KWV-1. The presence of K-rich feldspar is unable to account for the anomalously high medium-grained sandstone API reading.

3) The presence of heavy mineral placer deposits. Unspecified black heavy minerals (up to 10%) were reported from two locations with the core of borehole KWV-1; at a depth of 1259.43 – 1270.56 m and 1346.13 – 1360.46 m. Zircon, apatite, tourmaline and sphene are common heavy minerals found in sandstone. Zircon $Zr(SiO_4)$ is strongly resistant to transport and may contain trace amounts of U and Th, however, it is commonly colourless (Nichols, 2009; mindat, 2018). Rutile (TiO_3) and Ilmenite ($Fe^{2+}TiO_3$) are brownish-red to

black minerals that make up 5 – 25% and 10 – 60% of typical total heavy mineral concentrates, with trace amounts of Th up to 37 and 9900 ppm and U of 37 and 1680 ppm (Deer et al., 1992).

Littoral and, less commonly, submarine slope environments, can host placer deposits (Lalomov, 2003). It may be possible that ilmenite or rutile, transported beyond the littoral environment by large rivers along with the coarsest sandstone fraction, were deposited by channelised high-energy turbidity currents. The anomalously high gamma medium-grained sandstone samples were selected from one larger sample that was collected at a depth of 1269.41 – 1269.50 m, where a light grey medium-grained sandstone was reported to contain unspecified black heavy minerals. Therefore, it would not be unreasonable to assume that medium-grained sandstone would have a mean gamma value within the region of the fine to very fine-grained sandstone (235 – 270 API), most-likely lower due to less silt/clay fraction, and that the anomalously high values were due to the rare occurrence of radioactive placers within the geothermal samples.

5.5.4. Revised Procedure for Geothermal Reservoir Identification

The above-mentioned approach (Section 5.5.1) had to be amended in order to circumvent the non-linear relationship between geothermal potential and gamma, as well as the problems of potentially non-accurate absolute gamma values. Instead, a stepwise procedure based on the analysis of smoothed gamma trends is used. Based on the limited number of analysed samples, and by utilising the gamma shape trends for identification of maximum sandstone deposition, it should be possible to detect zones of geothermal potential within the borehole:

1. Only trends favourable to maximum sandstone development (good geothermal reservoir potential) are utilised (bow, cleaning-up and boxcar trends). The gamma trend of a unit should be analysed, based on smoothed gamma-ray data (Figure 5.21a) in order to identify

relative grainsize variations i.e. sand to silt – high geothermal potential versus silt to clay – low geothermal potential.

2. A procedure for differentiating different dirtying up or cleaning up cycles (i.e. sand to silt – high geothermal potential; silt to clay – low geothermal potential) is based upon the gamma value of analysed samples. An upper limit of the gamma range for fine and very fine-grained sandstone samples is set at 270 API, therefore only suitably shaped gamma trends below the limiting value (270 API) are considered as potential geothermal reservoirs (Figure 5.26). Medium-grained sandstone samples had higher gamma values but are deemed unreliable (see section 5.5.3) and discounted. This procedure forms a further subdivision of trends, separating medium-grained to very fine-grained sandstone dirtying up trends, from siltstone to shale dirtying up trends. A lower limit of the subdivision is not necessary due to dolerite being the only lithology with a lower gamma

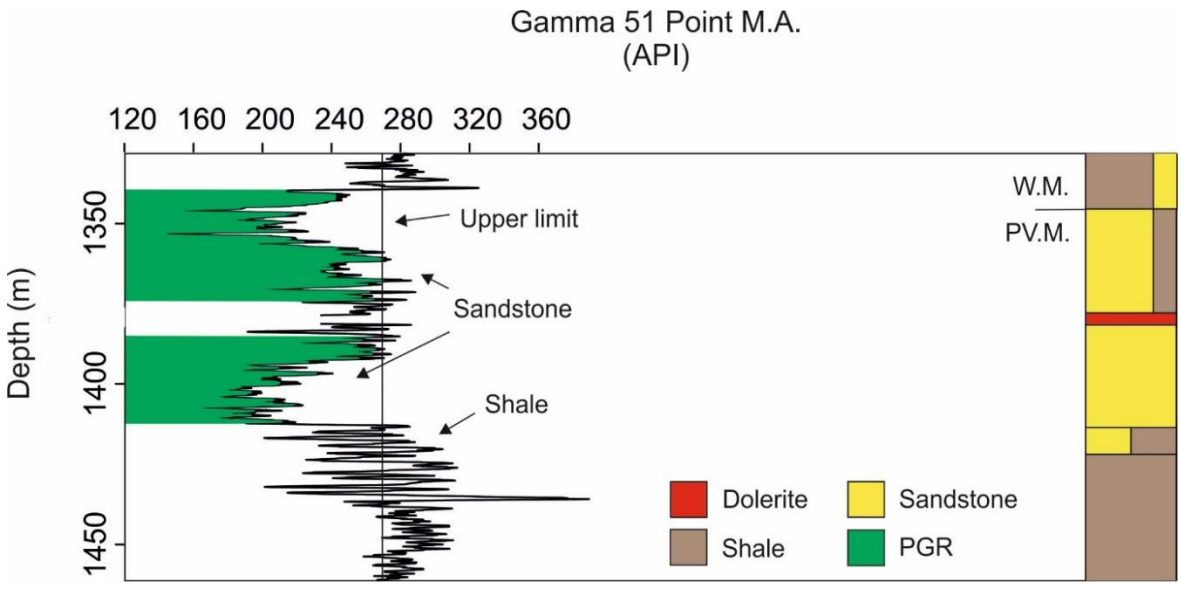

Figure 5.26: An example of PGR identification based on gamma shape trends and further refined by using an upper limit (270 API) based on analysed samples. Segregation of gamma trends based on the upper limit fits well with the lithological log and appears to differentiate between sandstone-rich gamma trends and shaley gamma trends. Abbreviations: W.M. = Wonderfontein Member, PV.M. = Pluto's Vale Member.

signal than sandstone in the borehole (<40 API) and dolerite gamma data was removed from the logs.

I. Potential Geothermal Reservoirs

The Pluto's Vale Member (Figure 5.23, 5.24) contains the highest number of potential geothermal reservoirs (PGR) with ten, compared with one from the Wonderfontein Member, and three from the Trumpeters Member (Figure 5.22). The distribution of sandstone-rich PGR across the Ripon Formation is in agreement with the descriptions of the members by Kingsley (1977, 1981), who observed rhythmic turbiditic units in the Pluto's Vale Member and greywackes and mudstones from the Wonderfontein and Trumpeters Members. The procedure of segregating the gamma trends into sandstone-rich cycles and siltstone/shale rich cycles by using a limiting gamma value that is based on analysed samples appears to be a valid methodology as is largely in agreement with the lithological logs in Figures 5.27, 5.28, 5.29. Only two instances of non-conformity occur. A clear bow trend is visible between the depths of 960 m – 1000 m (Figure 5.27) and is below the upper limit qualifying it as a PGR, however the bow trend corresponds with a shale interval in the lithological log, therefore it is discounted as a PGR. Additionally, a large bow trend occurs between the depths 1020 m – 1040 m (Figure 5.27), corresponding with a sandstone interval in the lithological log, however the majority of the trend occurs above the upper limit, again discounting it as a PGR.

Potential geothermal reservoirs also need to be subdivided based on thickness. Ideally, the thicker the reservoir, the greater the geothermal potential. However, the lower limit of acceptable reservoir thickness will depend on numerous techno-economic factors not within the scope of this study. For the purpose of thoroughness, reservoirs down to 12.5 m in thickness have been highlighted in the logs.

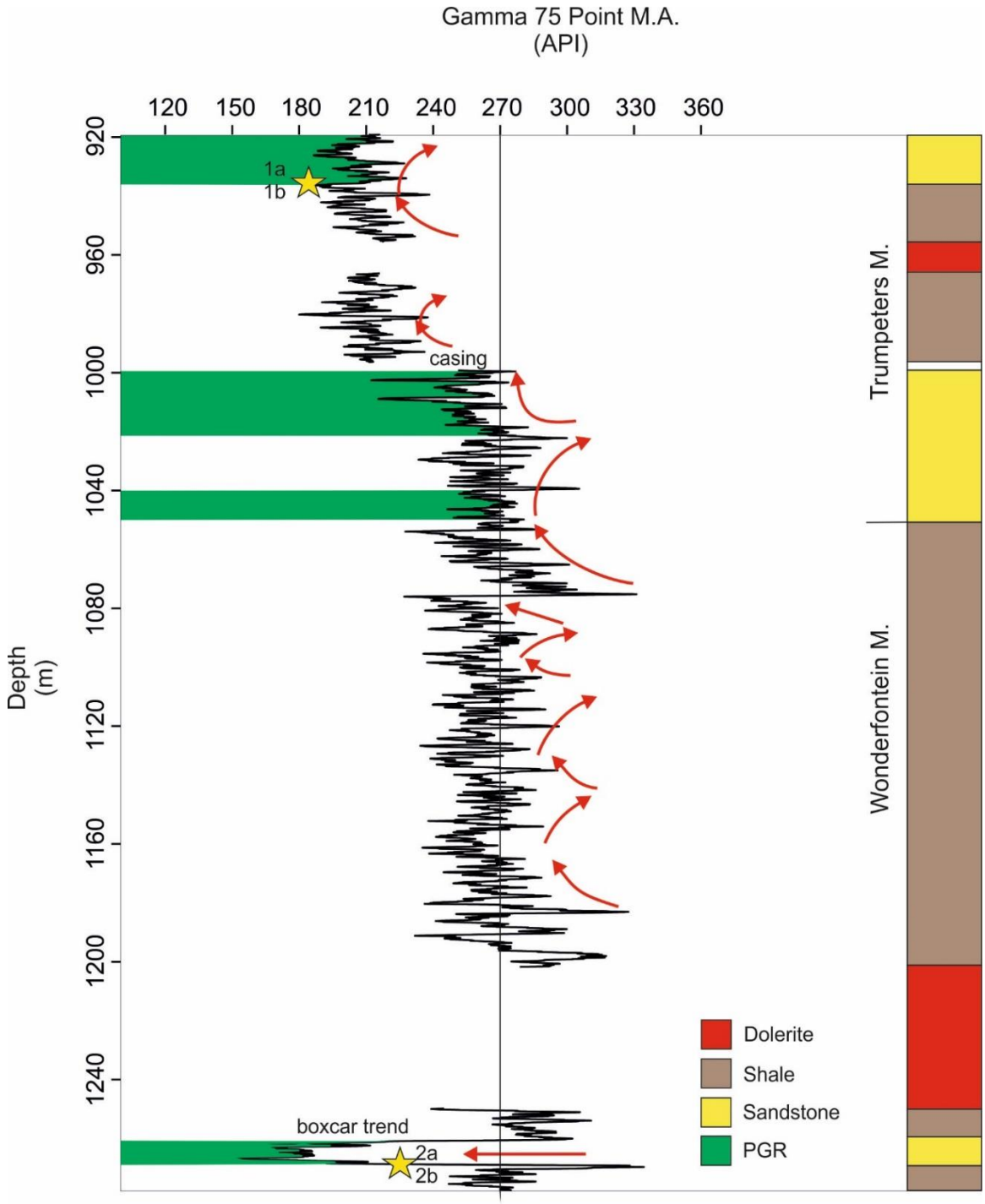

Figure 5.27: Ripon Formation gamma over view log 1 with potential geothermal reservoirs (PGR) between the depths of 919.20 m – 946.16 m, 1000.15 m – 1020.00 m, 1040.00 m – 1050.00 m (Trumpeters Member), and 1259.43 m – 1270.56 m (Wonderfontein Member).

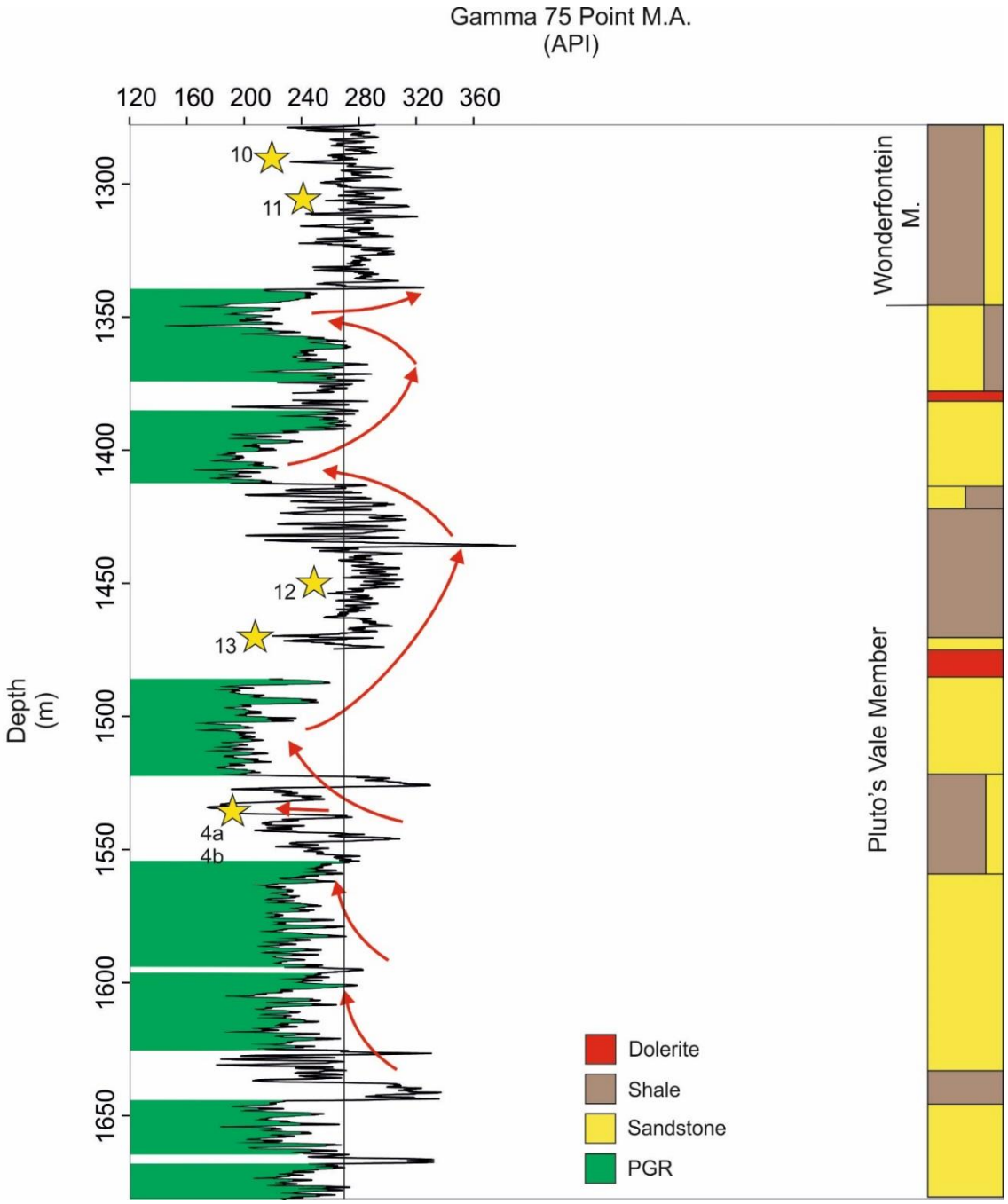

Figure 5.28: Ripon Formation gamma overview log 2 with potential geothermal reservoirs (PGR) between the depths of 1346.13 m – 1372.00 m (Wonderfontein Member), 1384.00 m – 1413.60 m, 1487.00 m – 1523.94 m, 1557.36 m – 1597.00 m, 1599.00 m – 1627.00 m, and 1646.48 m – 1670.00 m, 1675.00 m – 1687.00 m (Pluto's Vale member).

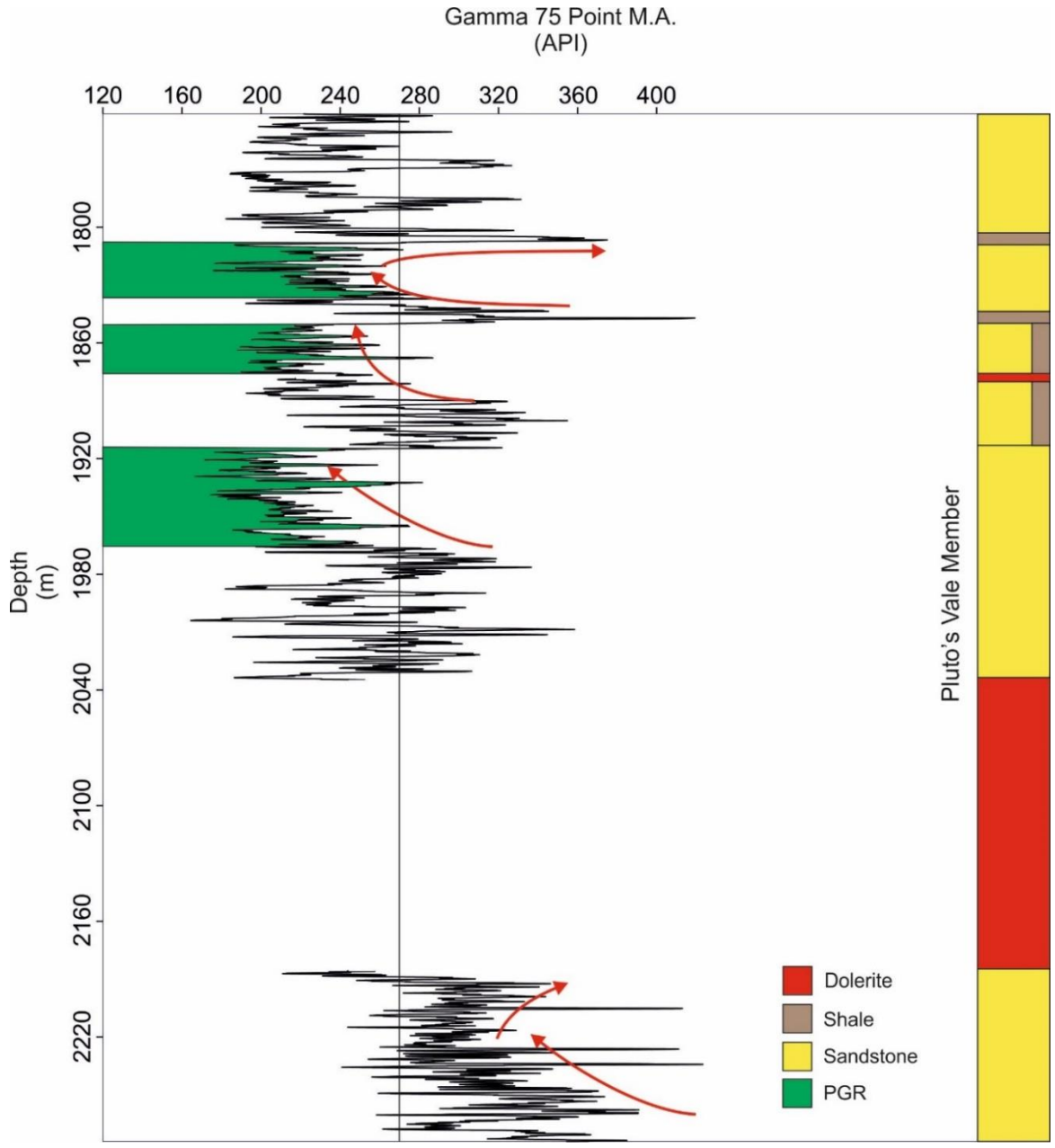

Figure 5.29: Ripon Formation gamma overview log 3 with potential geothermal reservoirs (PGR) between the depths of 1810.19 m – 1841.64 m, 1855.00 m – 1875.00 m, and 1918.00 m – 1978.00 m (Pluto's Vale member). Data corresponding to dolerite intrusions has been removed.

II. Geothermal Prone Facies and Palaeoenvironment

Strata identified as potential geothermal reservoirs range in thickness from 19.85 m – 59.00 m, with a cumulative thickness of 352.83 m within 1058 m of Ripon Formation rock. The predominant lithofacies identified from within the PGR (facies codes SDL, SLL, SH, BSC, SLLV, SML, STM, FVD, BSH; see Figure 5.19) approximately group into facies associations 3 and 4 with minor sandstone deposition from facies association 2 (Figure 5.30).

	Facies Codes	Process	Environment	Gamma Trend
1	BSH, STM, SH	Hemipelagic and pelagic sedimentation.	Inter lobe to basin plain.	Irregular saw-tooth, high gamma.
2	BSH, STM, SH, SLLV, FVD, SLL, SDL	Turbidity current and hemipelagic sedimentation.	Lower fan to basin plain.	Irregular. Shale high, sandstone low.
3	SDL, SLL, BSC, SH, SLM	Turbidity current and hemipelagic sedimentation.	Non-channelised lower fan.	Bow/boxcar.
4	SMB, SML, SLL, SDL, BSC	Turbidity current/debris flows	Channelised upper to mid-fan.	Bow/boxcar.

Figure 5.30: Strata identified as potential geothermal reservoirs based on gamma trends approximately group into facies associations 3 and 4, with deposition of geothermal-prone sediment occurring within the mid to lower submarine fan.

The environment and process on the submarine fan that supports deposition of potential reservoirs is demonstrated to be: (1) medium to fine-grained sandstone along with rip-up mud-clast conglomerate deposited as a result of turbidity currents and/or debris flows within the channelised portion of the upper to mid-fan and; (2) fine to very fine-grained sandstone deposited as a result of turbidity currents within the non-channelised lower fan.

Fine-grained sandstone has the highest geothermal potential with a mean thermal conductivity of 3.67 (W/(m.K)), a mean thermal diffusivity of 1.47 ($m^2/s.10^{-6}$) and a mean

specific heat capacity of 0.935 (kJ/Kg.K)). Fine grained sandstone is also widely distributed within the submarine fan. However, thick sandstone development is limited outside of depositional lobes, proximal to feeder channels (Figure 5.1) (Shanmugam et al., 1985). Large turbidity currents may deposit fine-grained sandstone on the basin plain but the intercalation with silt and mud will be detrimental to geothermal reservoir development.

Very fine-grained sandstone has a favourable specific heat capacity with a mean of 0.94 (kJ/Kg.K)), but limited reservoir potential due to the association of very fine-grained sand deposition with silt and clay deposition in the waning phase of a turbidity current (i.e. Bouma C, D and E (Bouma et al, 1962)).

Medium-grained sandstone also has favourable mean specific heat capacity, 0.954 (kJ/Kg.K)), but more limited distribution in comparison with fine-grained sandstone. Accumulations of thick units are restricted to feeder channels and the proximal overbank (Shanmugam et al, 1985). The incorporation of rip-up clasts of silt and shale (Bouma A; Bouma et al., 1962) are detrimental to geothermal development.

The lateral continuity of potential geothermal reservoirs is unknown and may depend on the geometry of the submarine fan, the sinuosity of the feeder channels as well as the propensity and frequency of lobe abandonment and channel avulsion. A detailed knowledge of the lithofacies and facies associations is only possible with detailed outcrop or core analysis. Knowing the approximate position of a geothermal reservoir on an ancient submarine fan may aid in exploration of new reservoirs. For example, a succession of shale overlain by thinly bedded fine-grained sandstone turbidites, cross-bedded medium-grained sandstone (geothermal reservoir) and slumped sandstone and siltstone, may indicate a prograding submarine fan. Therefore, additional geothermal reservoirs may be located in a more distal direction from the palaeo-hinterland, in the direction of the palaeo-current.

5.6. Conclusions

No relationship between geothermal characteristics (thermal conductivity, thermal diffusivity, and specific heat capacity) and gamma signature was apparent in analysed core samples, limiting the potential of a gamma-value based approach to reservoir exploration. R^2 values were less than 0.3 for a linear relationship between geothermal parameters and gamma. Instead, gamma shape trend analysis has proven to be a more successful methodology for identifying potential geothermal reservoirs. By utilising the gamma value of analysed core samples, a limit dividing similar gamma trend shapes of differing lithologies (sand-silt, silt-shale) can be used to further discriminate potential geothermal reservoirs. Although, as noted in Section 5.5.1 and 5.5.3, assigning gamma values to grainsize can be problematic due to anomalous radioactivity in minerals rich in U, Th and K. Outlier values should be discounted within reason and after careful investigation of the cause, thus refining the limit used for gamma trend subdivision.

Determination of facies and facies associations, in instances where core or outcrop data is available, may provide a useful tool for the prediction of additional favourable geothermal reservoirs, or for the establishment of lateral continuity of known reservoirs.

Eleven horizons have been identified, across the Ripon Formation, with high geothermal potential, ranging in thickness from 19.85 – 59.00 m, with a cumulative thickness of 340.83 m. The Pluto's Vale Member is the best target for geothermal exploration due to the numerous potential reservoirs. Areas of high geothermal potential are composed of medium to very fine-grained sandstone, deposited as a result of turbidity currents along the channelised mid-fan to non-channelised lower fan. Anomalously high gamma values from medium-grained sandstone samples are most likely due to the presence of radioactive placer deposits of a heavy mineral such as titanium dioxide (rutile or ilmenite). The overall high

gamma base line of the Ripon Formation in borehole KWV-1 is as a result of the feldspar content of the sandstones.

The small sample size of geothermal samples is a severely limiting factor in this study. Additional data would add to the robustness of the methodology and would greatly aid in increasing accuracy for using the methodology for geothermal exploration of nearby boreholes drilled in future. The addition of geothermal data from core samples from borehole KWV-1 would greatly aid in refining the upper ceiling of data segregation.

6. Risks, constraints, and the historical perspective

Chapter 6 analyses the geological constraints associated with the current stage of exploration for shale gas and geothermal in the Main Karoo Basin, as well as the risks associated with exploration and extraction related technologies with case studies from around the globe.

6.1. Introduction

Energy exploration within the Main Karoo Basin has to be viewed holistically, specifically concerning impediments and risks associated with exploration and development activities. The development of shale gas and geothermal resources within the basin share the same constraining geological factors, as well as similar potential risks, which have been historically proven and will be examined in this chapter.

6.2. Impact of Induced Seismicity from Hydraulic Stimulation

The National Research Council (NRC) (2013) defines induced seismicity, or induced earthquakes, as seismicity attributed to human activities. Historically, mining-related activities have been the cause of felt induced seismicity (Green et al., 2012). In recent times, activities surrounding energy production, more specifically the injection, and extraction of fluids from a geologic reservoir, has created public concern regarding seismic activity (NRC, 2013). Activities including geothermal energy development, carbon capture and storage (CCS), wastewater injection, and conventional and unconventional hydrocarbon extraction have been attributed to felt seismicity.

6.2.1. Mechanisms

Shallow earthquakes are caused by movement along a pre-existing fault. Movement or slip occurs when shear stress is larger than shear resistance (or shear strength) due to friction, i.e.

when the stress acting on the fault is larger than the resistance to sliding (Barton and Choubey, 1976).

The Coulomb Criterion defines the critical conditions relating to movement along a fault plane (Coulomb, 1776). Conditions for slip are given by equation (1):

$$\tau > \mu(\sigma - \rho) \quad (1)$$

Where,

τ = shear stress

μ = coefficient of friction

σ = normal stress

ρ = fluid pressure

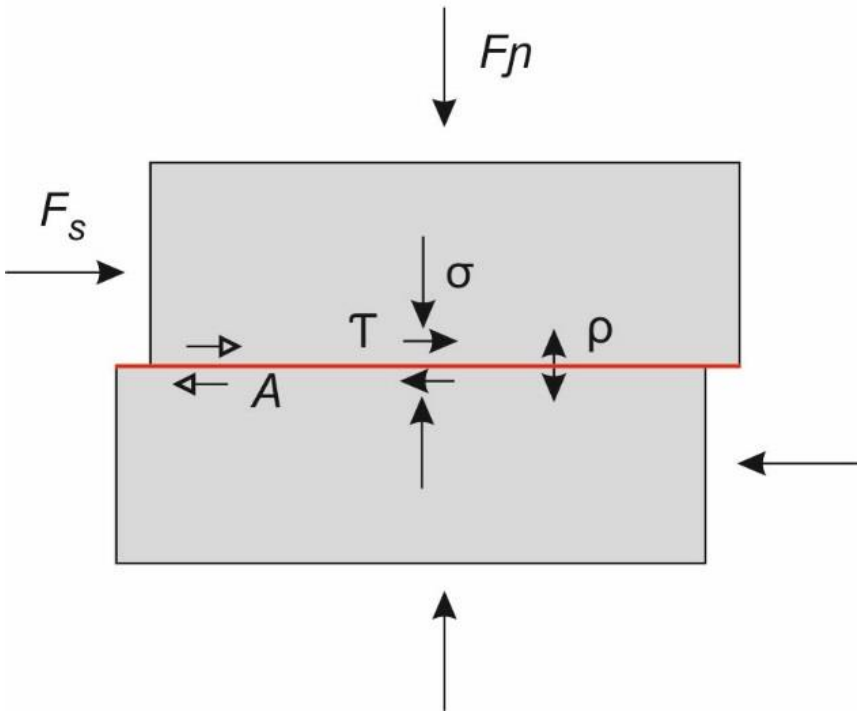

Figure 6.1: The Coloumb Criterion defines the critical conditions relating to movement along a plane. In order for movement to occur along a plane, *A*, shear stress (Fs), donated by τ, must be larger than frictional strength, $\mu(\sigma - \rho)$, where μ is the coefficient of friction, σ is normal stress (*F*n), and ρ is fluid pressure. Therefore, an increase in fluid pressure will lower frictional strength. Modified from NRC (2013).

There will be no movement along a plane as long as frictional strength ($\mu(\sigma - \rho)$) is greater than shear stress (τ). The term ($\sigma - \rho$) denotes effective stress and indicates that fluid pressure (ρ) counteracts the stabilising effect of normal stress (σ). Therefore, movement along a plane, *A*, can either be caused by a decrease in normal stress, an increase in fluid pressure, or an increase in shear stress (Figure 6.1).

Hydraulic stimulation of a reservoir may be performed in order to enhance permeability to aid in the extraction of hydrocarbons, in the case of shale gas, or heat, in the case of enhanced geothermal systems (EGS). In both instances, fluid pumped under pressure into a reservoir, changes the dynamic of the stress field in the reservoir as well as the surrounding rock.

The effect of a change in pore pressure can be demonstrated by regarding the injection of a limited volume of fluid into a porous elastic sphere surrounded by an impermeable elastic mass (Figure 6.2) (NRC, 2013):

An increase in fluid volume within the sphere leads to a change in pore pressure, ρ. The magnitude of the change in pore pressure, $\Delta\rho$, is proportional to the injected volume of fluid. When fluid is injected into a sphere that is confined by an impermeable elastic mass (Figure 6.2a), pore pressure will increase $\Delta\rho$ inside the sphere along with changes to stress $\Delta\sigma$ within the sphere and the surrounding impermeable mass, due to expansion of the sphere ΔV. If the sphere is removed from the surrounding impermeable mass (Figure 6.2b) then expansion will occur ΔV_* due to the increase in pore pressure $\Delta\rho$. An external confining stress $\Delta\sigma_*$ is needed to reduce the sphere to its original size (Figure 6.2c), which may result in non-isotropic, non-uniform stress perturbations, $\Delta\sigma$, outside of the sphere. An injection of fluid into the sphere causes compressive stress and withdrawal of fluid results in tensile stress.

The Hubbert-Rubey mechanism (Hubbert and Rubey, 1959) describes fluid injection induced seismicity using the Coloumb Criterion (equation 1). Induced seismicity will occur

when hydraulic pressures, due to stimulation, increase the ratio of shear stress to effective normal stress along existing fractures or plane of weakness, until the coefficient of friction is exceeded, and movement occurs.

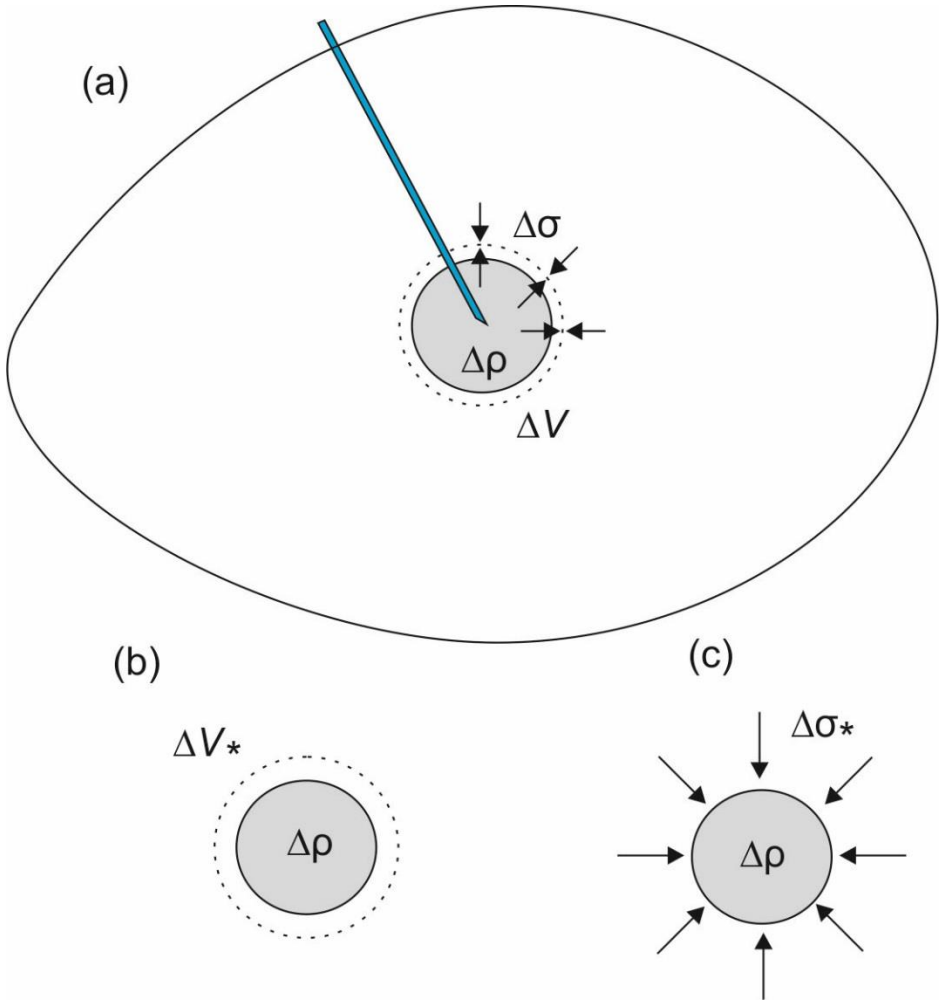

Figure 6.2: (a) Injection of fluid into a porous elastic sphere surrounded by an impermeable elastic mass results in a change of pore pressure $\Delta\rho$, a change of stress within and outside the sphere $\Delta\sigma$, and a change in volume of the sphere ΔV. (b) Removal of the surrounding mass results in expansion of the sphere ΔV_* due to the change in pore pressure. (c) A confining stress $\Delta\sigma_*$ is needed to return the sphere to its original size. Modified after NRC (2013).

According to de Pater and Baisch (2011), induced seismic activity will only occur when three prerequisites are met, based on equation 1:

1. An anisotropic stress field with stresses interacting on a shearing plane.
2. Sufficient rigidity of the shearing plane (mechanical strength) in order to support high shear stresses and therefore produce high seismic energy following a failure.
3. The shearing plane needs to permit fluid in order to build hydraulic pressure.

De Pater and Baisch (2011) also explain that the magnitude of an earthquake will, in part, be determined by the dimensions of the shear plane (fault or fracture plane), the shear modulus, and, the movement along the plane, given by equation 2 for the scalar seismic moment, M_0:

$$M_0 = GAd \quad (2)$$

Where,

G = shear modulus

A = area of the shear plane

d = movement occurring on the plane

The authors continue to state that the dominant parameter controlling seismic events within a reservoir is the area of the shear plane *A.* A common misconception is that fluids lubricate fault planes, causing slip, however fluids do not reduce the coefficient of friction.

6.2.2. Technologies

Numerous anthropogenic activities around the world have been associated with tremors (Figure 6.3), however, only activities related to hydraulic fracturing, i.e. shale gas fracking, waste water injection and, enhanced geothermal systems (EGS), will be discussed further.

Tight hydrocarbon reservoirs may have poor flow rates due to low permeability and can be enhanced to generate fracture networks to increase permeability (Figure 6.4) (Wuestefeld et al., 2011). Comparatively, Mukuhira et al. (2013) state that hydraulic stimulation is a critical element in the development of enhanced geothermal and hot dry rock systems, increasing well injectivity and reservoir productivity. The National Research Council (2013) defines hydraulic stimulation or enhancement as the process of injecting high pressure fluid and proppant under controlled conditions down a well and into a target formation. The fluid utilised by the stimulation process is usually a combination of water combined with chemical additives, to reduce pipe friction, and sand or ceramics to keep fractures open. After stimulation, the fluid used flows back into the well and is removed (ibid.).

I. Enhanced Geothermal Systems

Previously referred to as Hot Dry Rock (HDR), Enhanced Geothermal Systems (EGS) require some form of engineering to increase the permeability of hot impermeable rocks to allow for the circulation of fluids to sustain operations (Huenges, 2010). The primary method of permeability enhancement is hydraulic fracturing which requires the injection of pressurised liquid into a well (Moeck, 2014). The confining pressure of the rock needs to be overcome by the pressure of the injected fluids in order to force open natural fractures and planes of weakness. Micro seismic monitoring can be used to map fracture development (ibid.).

II. Unconventional Hydrocarbon Extraction

Unconventional hydrocarbons refer to hydrocarbons that have been generated and stored in the source rock. Gas is stored in the micro-pores of the shale and results in very low production rates prior to hydraulic stimulation (Law and Curtis, 2002). Stimulation of the reservoir by high-pressure fluids, in combination with horizontal drilling techniques, allows

for the extraction of hydrocarbons from usually impermeable lithologies (King and Morehouse, 1993; NRC, 1996).

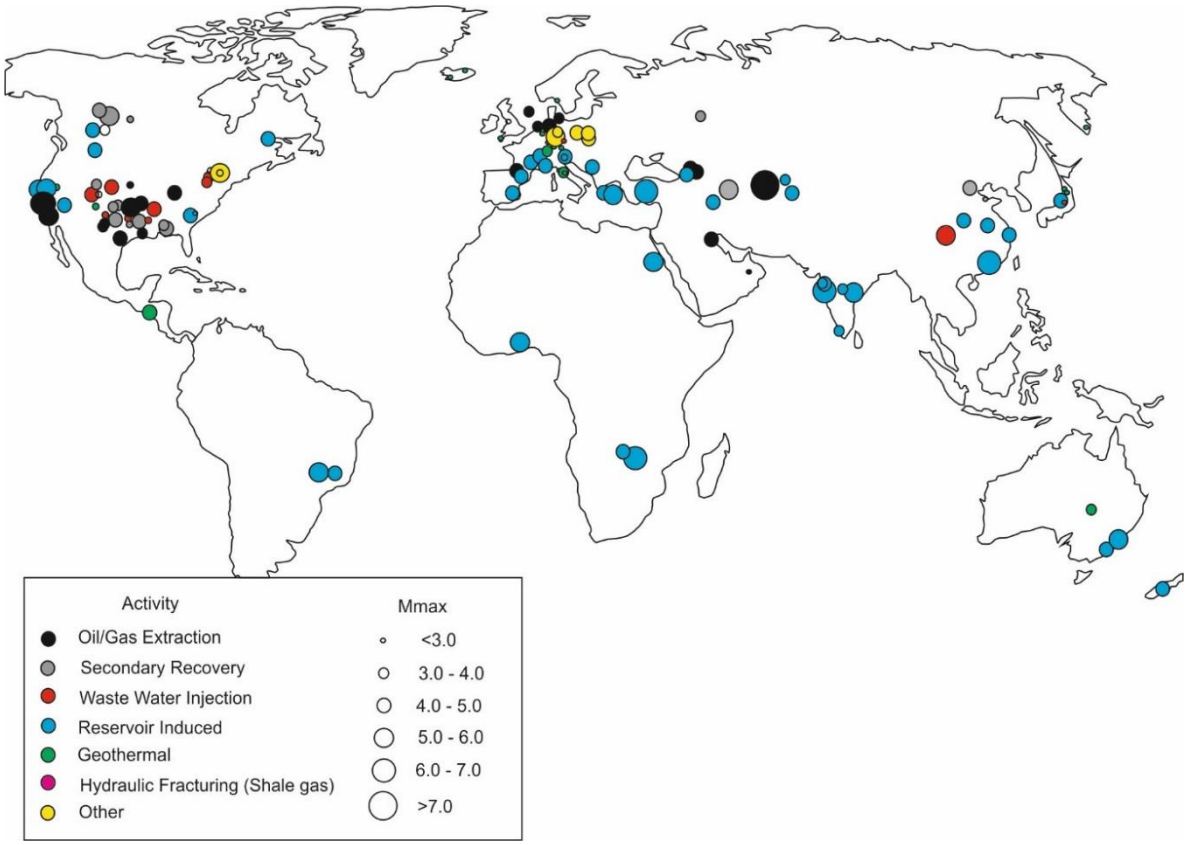

Figure 6.3: Global occurrences of anthropogenically induced seismic activity with associated causal activity and magnitude. Modified after NRC (2013). For a library of recent literature, concerning induced earthquakes with differing anthropogenic causes, see: www.inducedearthquake.com.

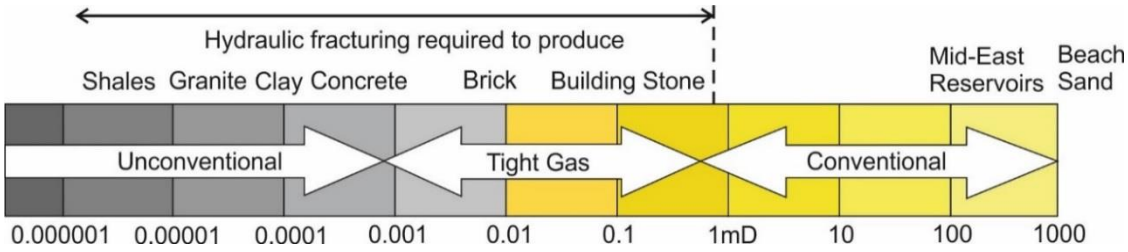

Figure 6.4: Permeability range of producing formations where fracturing is required. The higher the permeability the less resistance to flow from the reservoir into the production well. Hydraulic stimulation is required to produce from low-permeability reservoirs, such as tight sands and shales. Modified after NRC (2013).

III. Wastewater Injection

Wastewater injection or disposal is the process of injecting water that has been used in hydraulic stimulation, or generated by geothermal activities, down a well and into a target formation or lithology, in order to dispose of it (Warner, 1977; Karanen et al., 2013). It is estimated that in the United States alone, 20.9 billion barrels of wastewater is generated per annum with around 95% injected back down wells into the substrate (NRC, 2013).

6.2.3. Occurrences

Case studies are useful for identifying the parameters that lead to a seismic event and the resulting effects on the reservoir and proximal infrastructure, as well as public sentiment towards the causal technology (Section 6.2.4).

I. Blackpool, United Kingdom

Recent assessments of the shale gas potential of Carboniferous marine shales within northern England have been performed with promising results. A British Geological Survey resource assessment by Green (2012) estimates a range of gas in place (GIP) of 822 – 2281 tcf for the combined upper and lower Bowland-Hodder shale unit. The marine shales were deposited in tectonically complex basins and attain a maximum thickness of 5000 m with a TOC content between 1% – 3% and a vitrinite reflectance of >1.1% (Green, 2012).

In 2011, Cuadrilla Resources Ltd drilled the first dedicated shale gas exploration well located at Preese Hall 1 near Blackpool (Eisner et al., 2011; Clarke et al., 2014). During a multistage hydraulic fracture operation, the British Geological Survey reported two earthquakes. The first earthquake (01/04/2011; 02:34 A.M.) had a magnitude of 2.3ML and was reported 1.8 km from the well, at a depth of 3.6 km. It occurred 10 hours after the termination of hydraulic stimulation following the injection and lock-in of 2245 m^3 of fluid and 117 t of proppant.

The second, magnitude 1.5ML (27/05/2011; 00:48 A.M.), was reported from 1 km away, again, 10 hours after the termination of operations (Eisner et al., 2011; Clarke et al., 2014). 48 much weaker events were detected in addition to the two large events (de Pater and Baisch, 2011).

The seismic events at Preese Hall 1 are considered quite exceptional based on mapping of US shale gas plays, with maximum magnitude events of only 0.8ML (de Pater and Baisch, 2011). Subsequent studies have revealed several critical parameters that induced seismicity (de Pater and Baisch, 2011; Clarke et al., 2014):

- The Bowland shale consists of rigid impermeable shale.
- The dominant stress regime is strike slip with a stress difference of 4000 psi (US shales are generally only a few hundred psi).
- A fault with optimum geometric orientation (NE-SW) is located approximately 300 m from the injection interval.

According to Clarke et al. (2014), the gradual build-up of pore fluid pressure over several hours, along the already critically stressed fault (high horizontal anisotropy), led to a reduction in the effective normal stresses and subsequent series of slips along the fault. Fractures caused by the hydraulic stimulation are the most likely conduits for fluid flow from the well into the fault, although bedding planes may also have been opened during operations.

II. Central and Eastern United States

McNamara et al. (2015) state that the number of earthquakes with a magnitude >3ML has increased by 300% since 2009 in north central Oklahoma. Large numbers of these events have been felt at the surface (474 felt earthquakes), and have caused damage (ibid.).

In November 2011, a series of seismic events occurred near the town of Prague, Oklahoma, culminating in a ML 4.8, 5.7 and 4.8 earthquake series that caused damage to houses (McNamara et al., 2015). The events were most likely caused by wastewater injection, with a doubling of wastewater disposal volumes in the area between 2004 and 2008 (Karanen et al., 2014).

Studies have shown that the increase in seismicity does not correlate well with the statistical distribution of naturally occurring earthquakes (e.g. Llenos and Michael, 2013). Seismically actives zones do, however, correlate well with regions of active unconventional hydrocarbon exploitation (Keranen et al., 2014).

Enhanced oil recovery (EOR), the process of injecting fluid into depleted oil wells to bolster production, also occurs in the central and eastern United States (Weingarten et al., 2015), however, the authors note that wastewater disposal wells are 1.5 times more likely to be associated with an earthquake compared to EOR. EOR (injection and extraction), operates by diligently managing reservoir pressure, whereas wastewater disposal results in an increase in reservoir pressure (ibid.).

The wells experiencing seismicity in Oklahoma are located proximally to near vertical, optimally orientated (NE-SW, NW-SE), strike slip faults within crystalline basement (McNamara et al., 2015). The fault systems (Nemaha and Wilzetta) bound an uplifted region formed by the Ancestral Rocky Mountains Orogeny (Pennsylvanian) (ibid.).

The exact trigger mechanism for the events is not fully understood, however, the large volumes of injected fluids are either increasing pore pressure levels along critical fault planes, or changing the dynamics of the regional stress field (Ellsworth, 2013). Noticeable differences with regards to hydraulic stimulation induced seismicity, and wastewater

injection, is the time delay between injection and recorded seismicity, which can range from months to years for the latter (ibid.).

Karenen et al. (2014) explain that optimally oriented and critically stressed faults may rupture first, however the sheer volume of fluids injected with wastewater disposal increases the probability that faults further afield and less-stressed may be ruptured.

III. Basel, Switzerland

Between May and October 2006 the well, Basel-1, was drilled by Geothermal Explorers Ltd as part of the Deep Heat Mining Project, with the aim of developing an EGS plant in the city of Basel. The well was drilled to a depth of 5000 m and intersected 2400 m of sedimentary rocks followed by 2600 m of granitic basement (Häring et al., 2008).

Initiation of hydraulic stimulation commenced on 02/12/2006 and culminated in the injection of 10,000 m^3 of water, with a flow rate of 4000L/min reaching a wellhead pressure of 30MPa six days later (Mukuhira et al., 2013). A section between the depths of 4603 m – 5000 m, containing pre-existing permeable fractures, was targeted for stimulation (ibid.). The section had a fracture density of 0.2 – 0.3 per metre with dips exceeding 60°. Two major cataclastic fracture zones were detected at 4700 m and 4835 m (Häring et al., 2008).

Häring et al. (2008) continues to state that due to increasing seismic activity over 1ML, and in accordance with a micro seismic response procedure, flow rates were reduced on the 8/10/2006 and the well was shut in. This procedure was ineffective at mitigating the frequency of events > 1ML so a decision was made to bleed the well. Before bleed-off could commence a 3.4ML event was recorded. Three aftershocks > 3ML were recorded on the 06/01/07, 16/01/07, and the 2/02/07. The well pressure returned to hydrostatic within four days following pressure reductions.

Critical parameters relating to the induced seismicity are outlined below (Mukuhira et al., 2013; Häring et al., 2008):

- Critically pre-stressed fracture zones in close proximity.
- Rigidity of the igneous lithology.
- A history of large natural earthquakes in the area.

The driving mechanism is thought to be a change in stress state or coefficient of friction rather than pore pressure increases. Fluid flow rates started to increase above 80 bar, indicating a hydro-mechanical response of the rock mass. Pressure variations stabilised above 235 bar, indicating active permeability enhancement at increasing distances from the wellbore. Waveform signatures indicate a stepwise rupture process that may indicate the superposition of radiated seismic energy from numerous successive events with millisecond time differences along the pre-stressed optimally aligned fracture zones.

6.2.4. Public Sentiment

Government initiated studies have been undertaken as a result of public concern surrounding the increased development of unconventional energy exploration and production. Results indicate that hydraulic fracturing for shale gas production poses a low risk, while wastewater injection poses some risk (NRC, 2013).

The Blackpool event was widely reported both nationally and internationally. The British Government implemented an 18-month suspension of operations and commissioned risk studies into the technology (Clarke et al., 2015). The result of the events, in conjunction with widely publicised United States anti-fracking propaganda, is a large negative connotation associated with fracking and continued protest action in the UK as recently as mid 2017 by anti-fracking associations.

The Basel geothermal project was suspended for three years, before being permanently shut down, following the seismic events (Häring et al., 2008). However, public sentiment towards the technology is still perceived as more environmentally friendly, in comparison with shale gas and nuclear, and has largely remained positive with several new ventures underway in the UK.

6.2.5. Energy Extraction Associated Seismic Risk within the Main Karoo Basin

Hydraulic stimulation is required in order to extract gas from tight shales (NRC, 2013) as well as to extract heat from tight sandstones (Huenges, 2010). Hydraulic stimulation has been associated with induced seismicity in exceptional circumstances where critically stressed faults and fracture zones, proximal to stimulation wells, have been reactivated. In both borehole KZF-1 and KWV-1 major faults and fracture zones have been encountered in potential reservoirs that would require stimulation in order to facilitate production. The kinematics and style of faulting and fracturing varies greatly between the boreholes in accordance with local geological conditions, therefore, a detailed assessment of each location is warranted regarding induced seismicity risk analysis and mitigation.

The current regional stress field within the southern Main Karoo Basin is not well studied, however large scale normal faults have been mapped. Some of these faults appear to be reactivated thrust faults formed during tectonic inversion caused by compressive stresses, from the development of the Cape Fold Belt, being replaced by tensional stress due to the break-up of Gondwana (Johnson et al., 2006). Hill (1988) has reported relatively recent movement along some of these normal faults resulting in minor seismicity in the southwestern Cape.

I. Borehole KZF-1 (Western Cape, South Africa)

Stimulation of borehole KZF-1 would most likely prove highly complicated due to the thrusts propagating through the most organically rich horizons. It is possible that some of the original thrust faults may have reactivated as normal faults during the break-up of Gondwana, with movement to the south (Johnson et al., 2006). Bedding within the Whitehill and Prince Albert Formations, within borehole KZF-1, is predominantly dipping towards the south (Chapter 3, Figure 3.9).

Hydraulic stimulation of the Whitehill Formation within borehole KZF-1, performed within any section, would be proximal to fault planes and bedding planes, in line with the regional stress field. The abundance of quartz veins, proximal to fault planes (Chapter 3, Figure 3.10c, d, e), may serve to increase the overall rigidity of the lithology (in comparison to black shale) facilitating the build-up of strain. Caving of the borehole during drilling was experienced between the depths of 468.74 – 500.36 m, which may indicate some form of in-situ strain.

It is important to note that no mechanical stress tests have been performed on the Whitehill Formation shale, in order to constrain shear strength, and it is possible for strain to build up in black shales, as was the case in Blackpool (Clarke et al., 2014). It is likely that the underlying, more rigid, Dwyka Group could contain critically stressed normal faults. Figure 2.5 (Chapter 2) depicts large-scale faults cutting through the Ecca Group and into the underlying Cape Supergroup and Namaqua-Natal Mobile Belt.

Fracking fluids may migrate down through fracture zones, as was the case in Basel and Blackpool, towards an unseen stressed fault (possibly within the underlying Dwyka Group or basement). An increase in pore-pressure along the plane of weakness could lead to movement along the plane, and subsequent seismicity. The magnitude of the seismicity will depend on the surface area of the plane of weakness. The Preese Hall 1 well, Blackpool

(Clarke et al., 2014), contained numerous fractures that were favourable for the propagation of fracking fluids, however the fluids reached an unseen critically stressed fault which was activated by an increase in pore pressure, leading to felt seismicity and the shutdown of the entire project. The numerous polished slickensides along planes of weakness in borehole

Figure 6.5: A section of core displaying a polished slickenside surface from the Whitehill Formation in borehole KZF-1 at a depth of 443.3 m

Figure 6.6: Polished slickenside bedding surfaces from the well Preese Hall 1 in the United Kingdom. From de Pater and Baisch (2011).

KZF-1 (Figure 6.5) are similar to samples from within the Preese Hall 1 well (Figure 6.6), possibly indicating the prevalence of similar tectonic conditions. Additionally, the numerous fault planes may divert fracking fluids away from the target horizon towards the surface.

The potential shale gas reservoir in borehole KZF-1 is located close to the surface thus increasing the risk of shallow level aquifer contamination in the event of hydrocarbon or fracking fluid leakage.

It is highly likely that stimulation of borehole KZF-1 would result in unaccounted for fracking fluid and likely that fluids may reach a larger stressed fault in the basement with tensile strain acting towards to the south. It is therefore recommended that exploration activities be focused north of the southern basin margin, but south of the dolerite line (Figure 2.7). In the search for shale gas from the Whitehill Formation it is unlikely that the region proximal to the Cape Fold Belt will be stimulated due to the abovementioned reasons as well as reservoir dilution due to the compartmentalisation effects of thrust faulting.

However, even north of the Cape Fold Belt, high angle faults trending NNW to SSE have been identified from a seismic reflection profile, within the Ecca Group (Figure 2.5). Hydraulic stimulation away from the basin margin may still intercept these high angle faults that reach down into the basement (Table 6.1), but determination of the risk is premature as exploration licence areas have not yet been fully approved, inhibiting site selection for drilling. In addition, no detailed seismic reflection surveying has been performed in prospective areas, therefore the level of uncertainty is very high due to the lack of information.

II. Borehole KWV-1 (Eastern Cape, South Africa)

The extraction of heat from thick sandstone successions in the southern Main Karoo Basin is dependent on increases in porosity and permeability from natural and induced fractures. Several high angle fracture zones and fault zones were encountered within borehole KWV-1 (Figure 4.14d). Information on the state of the regional stress field around the drill site is limited. Tensile strain acting towards the south is assumed (Johnson et al., 2006).

The lower most sandstone successions identified as potential geothermal reservoirs would, most likely, respond well to hydraulic stimulation due to the rigidity of the sandstone (promoting fracture development) as well as the presence of natural fracture zones promoting fluid transfer. The potential reservoir is sufficiently deep >3000 m with sequences of impermeable shale and dolerite (Figure 4.18) located at shallower levels to prohibit the vertical migration of escaped fracking fluid towards sub-surface aquifers. No historically active fault zones are present, however the presence of stressed faults within the basement related to the Cape Fold Belt, is likely (Figure 2.5). It is unlikely that fracking fluid will migrate down into the basement during the hydraulic stimulation of the tight sandstones due to the thick successions of impermeable shale found within the Collingham, Whitehill and Prince Albert Formations.

III. Wastewater Injection

If the basin is successfully explored for shale gas and geothermal energy then it is likely that well development and production activities will generate large amounts of wastewater as is the case in the central and eastern United States (Weingarten et al., 2015). The disposal of large volumes of wastewater poses the largest risk with regards to induced seismicity in comparison to hydraulic stimulation of tight shales and sandstones. An isolated but permeable reservoir is needed to effectively store wastewater.

The large dolerite dykes and sills found throughout the basin, above the dolerite line (Figure 2.7) may provide a solution. Within borehole KWV-1, large sandstone bodies, up 400 m thick, were intersected that are bounded above and below by large impermeable dolerite sills. If these sills are proven to be laterally extensive, and the sandstone has sufficient porosity, then large volumes of wastewater could potentially be stored within these tabular bodies. Problems may arise where the vertical intrusion of a dyke has sufficiently fractured the

country rock to allow water to migrate either towards the surface, or down into the basement. The extremely long timespans and huge fluid volumes associated with wastewater make it highly likely that fluids will eventually intersect a stressed fault and induce large-scale seismicity (Table 6.1), as was the case in Oklahoma USA (McNamara et al., 2015). Again, analysis of this risk is grossly premature, however all eventualities should be considered when calculating the prospectivity of a basin.

IV. Potential Effect of a Seismic Event

The effects of seismicity need to be considered regardless of the level of risk of an event occurring. People and infrastructure are the primary affected parties. Figure 6.7 is a satellite

Figure 6.7: The area within a 25 km radius of borehole KZF-1 is largely uninhabited semi-arid land (see insert). The two roads proximal to the borehole are gravel roads. Seismicity recorded at the surface would have close to zero impact on infrastructure or people. Modified from Google Earth Pro 7.3.1. (2/19/16). Breede River DC. 32°53'44.40"S, 19°53'10.99"E. Eye Alt. 59.57 km. 2018 AfriGIS (Pty) Ltd. [14/08/17].

image of the area surrounding borehole KZF-1. The region is largely uninhabited, semi-arid land, used for livestock grazing. Small hills and fluvial deposits are cut by two regional roads, which are gravel surfaced.

A seismic event in the area, related to shale gas extraction, would have little to no effect on the surface, other than the chance of loose rocks tumbling downhill in the raised areas to the east and west of the borehole.

The proposed future geothermal exploration area (Area 123, Figure 6.8) is large, and the result of a seismic event is more difficult to constrain. Numerous low-income small villages and towns are located within the area (Figure 6.8), with a network of highways and smaller

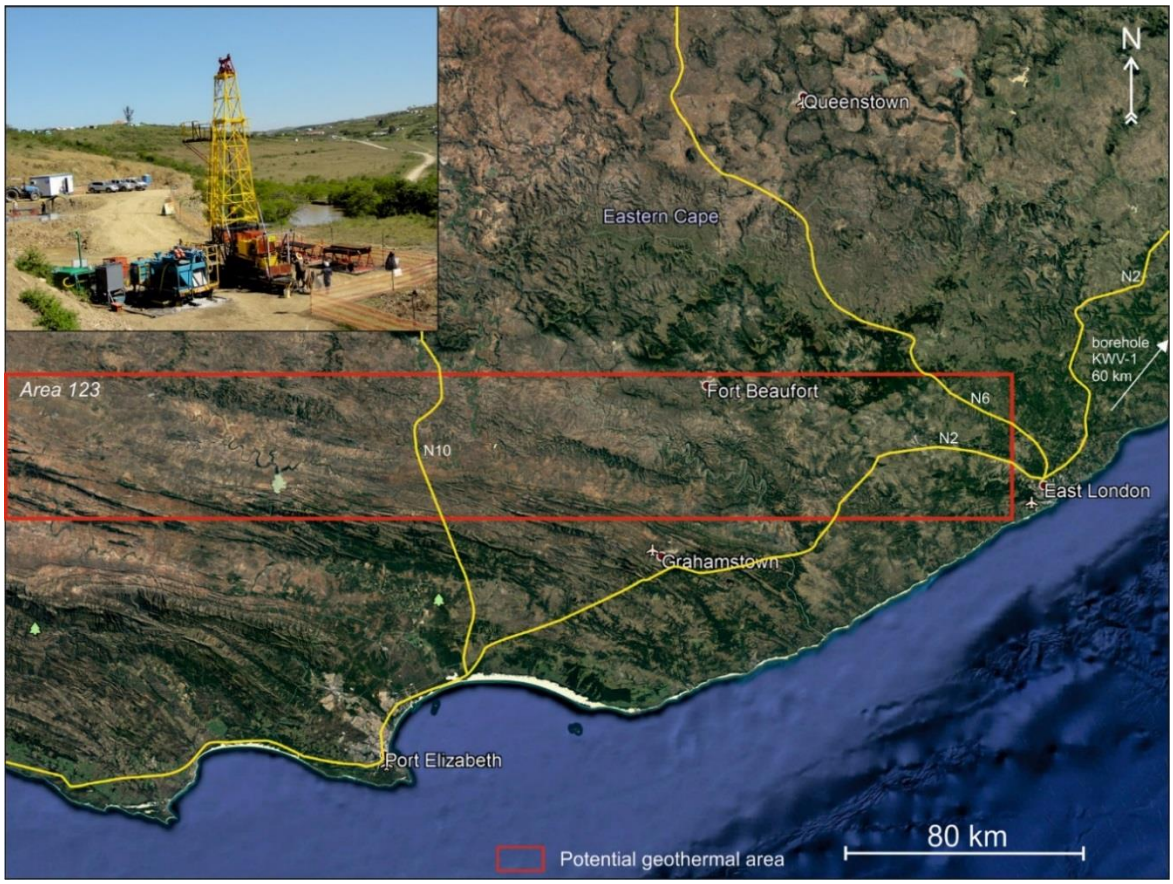

Figure 6.8: Geothermal exploration area 123 consists of several large towns connected by major highways, and rural farmland (insert). A seismic event near any large town could have a significant impact on people and infrastructure. Modified from Google Earth Pro 7.3.1. (12/14/15). Port Elizabeth. 33°02'42.46"S, 26°08'15.18"E. Eye Alt. 365.45 km. 2018 AfriGIS (Pty) Ltd. [08/02/18].

tarmacked roads connecting them. Seismicity would have the potential to damage poorly built infrastructure and roads with associated socio-economic impacts.

If any seismic event were to occur, due to either shale gas or geothermal exploration, then the knock-on effect with regards to public sentiment would be considerable. Currently, there is opposition to the exploration and development of unconventional hydrocarbons in South Africa by anti-fracking associations. Seismicity would be seen as a reason to abandon the project and would have negative consequences for future proposed developments globally.

Location	Geology	Activity	Risks	Effect
KZF-1	Thrust faults and fractures in black shale.	Hydraulic stimulation	Fault reactivation	Seismicity
			Fluid migration into near surface aquifer	Contamination
Area 123	Likely faults in basement. Fractured vertical igneous intrusions.	Wastewater injection	Basement fault reactivation	Seismicity.
			Fluid migration into near surface aquifer	Contamination.

Table 6.1: Energy extraction associated hazards from the Main Karoo Basin.

6.3. Unconventional Energy Potential of the Southern Main Karoo Basin

Conventional hydrocarbon exploration of the southern Main Karoo Basin in the 1960's and 70's revealed poor oil potential mainly due to the high thermal maturity of the reservoir rocks (Rowsell, 1976). Over maturity of the source rocks in the south was due to the thermal effects of the Cape Orogeny (low Greenschist metamorphism, Frimmel et al., 2001) in

combination with excessive burial depth (Rowsell, 1976). Source rocks in the north of the basin were downgraded due to the effect of the numerous dolerite intrusions (ibid.).

The formations originally targeted as potential conventional source rocks (lower Ecca shales: Collingham, Whitehill and Prince Albert Formations) are now the subject of intense study as potential unconventional hydrocarbon reservoirs.

6.3.1. Lower Ecca Shale Hydrocarbon Potential Summary

The lower Ecca shales (Collingham, Whitehill and Prince Albert Formations) demonstrate substantially higher TOC and thermal maturity compared to the upper Ecca shales (Fort Brown and Waterford Formations) (Kuuskraa et al., 2013).

The Whitehill Formation is the main target for shale gas exploration (Table 6.2). The Formation has TOC ranging from 0.5 to 17% with an average of 6% (Oelofsen, 1987; Cole and McLachlan, 1991, Kuuskraa et al., 2013). The Whitehill Formation is composed of up to 50% quartz in some areas (Decker, 2013) making it suitable for hydraulic stimulation. Vitrinite reflectance values range from 1 – 4% (ibid.). The Prince Albert Formation contains TOC ranging from 1.5% – 5.5% with an average of 2.5% and has a high thermal maturity of 2% – 4% Ro, well within the dry gas interval (Kuuskraa et al., 2013). The Collingham Formation has a lower TOC than the Whitehill Formation, ranging from 2 %– 8%, having a high thermal maturity of 3% Ro (Kuuskraa et al., 2013). The Collingham Formation is a less suitable potential reservoir due abundant volcanic ash layers (TOC 0.1%; Black et al., 2016) that may have diluted the overall organic content of the formation.

6.3.2. Barriers to Hydrocarbon Potential

Evaluations of potential shale gas reserves in the Main Karoo Basin are estimated between 32-485 trillion cubic feet (Decker and Marot, 2012). The vast range of the estimate is due to the uncertainty surrounding factors detrimental to shale gas potential.

Table 6.2: Shale gas reservoir properties of the Whitehill Formation, the main target for exploration. Modified after (Kuuskraa et al., 2013). Red box indicates highest potential.

Basic Data	Basin/Gross Area		Karoo (612,273 km^2)		
	Shale Formation		Prince Albert	Whitehill	Collingham
	Geologic Age		L. Permian	L. Permian	L. Permian
	Depositional Environment		Marine	Marine	Marine
Physical Extent	Prospective Area (km^2)		155,865	155,865	155,865
	Thickness (m)	Organically Rich	122	61	61
		Net	37	30	24
	Depth (m)	Interval	1,800 - 3,200	1,600 - 3,000	1,600 - 3,000
		Average	2,600	2,400	2,400
Reservoir Properties	Reservoir Pressure		Mod. Overpress.	Mod. Overpress.	Mod. Overpress.
	Average TOC (wt. %)		2.5%	6.0%	4.0%
	Thermal Maturity (% Ro)		3.00%	3.00%	3.00%
	Clay Content		Low	Low	Low
Resource	Gas Phase		Dry Gas	Dry Gas	Dry Gas
	GIP Concentration (Bcf/mi^2)		42.7	58.5	36.3
	Risked GIP (Tcf)		385.3	845.4	327.9
	Risked Recoverable (Tcf)		96.3	211.3	82.0

Previous studies have drawn attention to the over-maturity of the lower Ecca shales due to burial depth and contact with the metamorphosed Cape Fold Belt along the southern margin of the basin (Figure 6.9) (Geel, 2013; EIA, 2015). The lower Ecca shales outcrop along the northern margin of the CFB (Johnson et al., 2006) before dropping down to a depth in excess of 4000 m (Decker, 2013). The basin floor along the of the CFB ranges in depth between 4000 – 5000 m below sea level (EIA, 2015). The basin shallows to the north, with the Whitehill Formation wedging out northwards, outcropping adjacent to the northern basin

margin (Johnson et al., 2006). The Whitehill Formation thickness ranges from over 90 m in the south, to 6 m in the north (Decker, 2013). The deepest portion of the southern basin is deemed over-mature, however, maturity decreases northwards (Geel, 2013).

Large areas of the Main Karoo Basin contain igneous intrusions (dykes and sills) (Figure 6.9) contributing to the high thermal maturity of the Ecca shales (Kuuskra et al., 2013). The Whitehill Formation in the southern Main Karoo Basin, which is proximal to dolerite intrusions, has experienced low-grade metamorphism (250 - 300°C) (Smithard et al., 2015). According to Svensen et al. (2007), TOC content and vitrinite reflectance data from contact aureoles indicate an organic carbon depletion from the lower Ecca Shales. Thousands of breccia pipes (approximately 150 m in diameter) containing brecciated and metamorphosed black shale, formed by gas pressure accumulation due to metamorphism have been documented (ibid.). The western Main Karoo Basin may have lost up to 27,400 Gt of CO_2 due to dolerite intrusions (ibid.). The igneous sill intrusions may be detrimental to the quality of the organic-rich shale and will limit the use of seismic imaging, increasing the risk of shale exploration (EIA, 2015).

A smaller area has been identified, within the dry gas prospective zone, where the Whitehill Formation occurs at a depth in excess of 1500 m and still maintains a thickness and pay of over 30 m (Figure 6.9). Pay had been calculated by Decker (2013) as: Pay = Thickness – (0.6 x dolerite thickness). This area is further reduced by discounting a vitrinte reflectance

(R_o) above 3.5%. The resulting prospective area (Figure 6.9) is greatly reduced, accounting for the lower end of the gas reserve estimation.

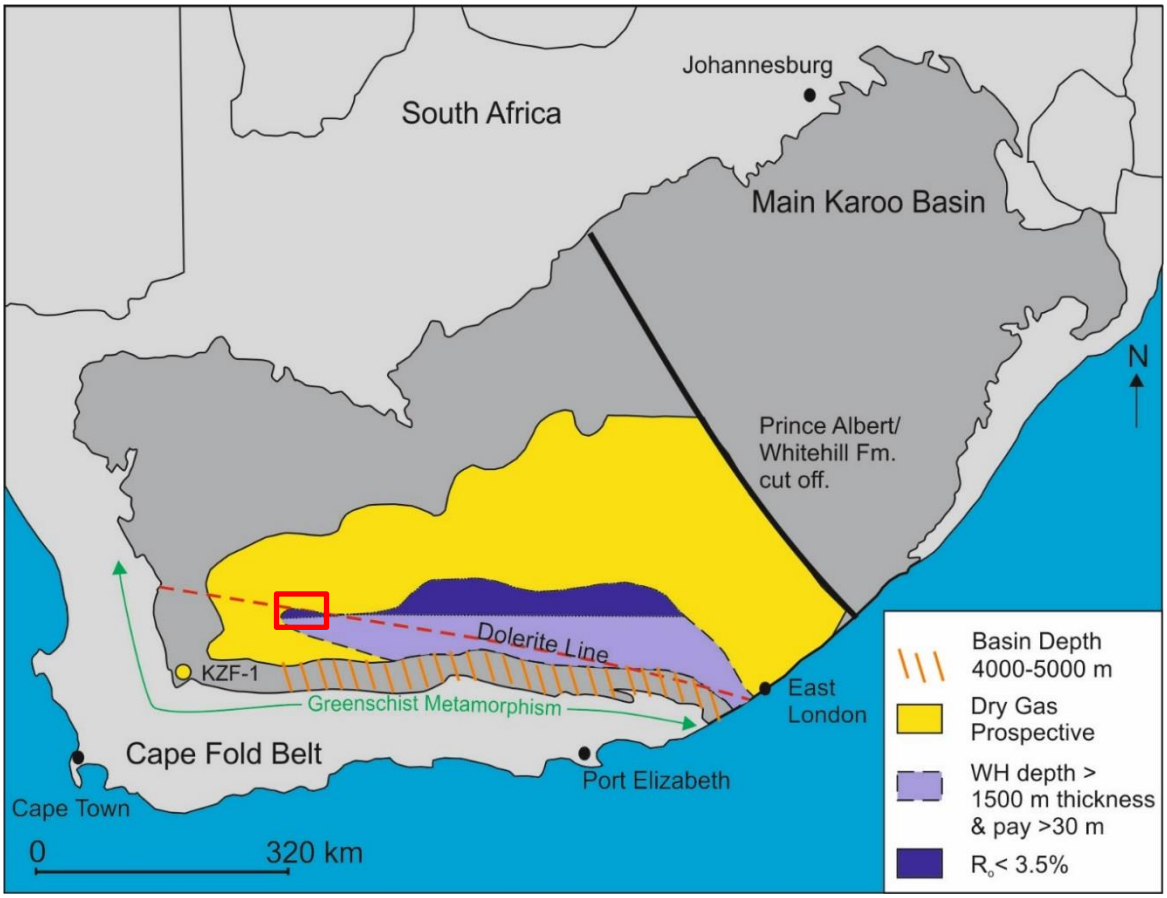

Figure 6.9: Map of the Main Karoo Basin. Factors negatively effecting shale gas prospectivity include excessive burial depth and metamorphism in the south, and dolerite intrusions in the north and east. The structural effects of the CFB on the prospective gas zone proximal to borehole KZF-1 are poorly constrained. Modified after EIA (2015) and Decker (2013). Red box indicates optimal area.

6.3.3. New Insights into Tectonics and Reservoir Potential

The limit of the prospective area along the southern margin is based on thermal properties. Conflicting information exists with regards to the tectonic effects of the Cape Fold Belt along the southern margin. Figure 6.10 is a schematic cross-section across the basin by McLachlan and Davis (2006) that illustrates the thrusts of the Cape Fold Belt that have deformed the

Cape Supergroup (Table Mountain, Bokkeveld and Witteberg Groups) but had no effect on the Karoo Supergroup.

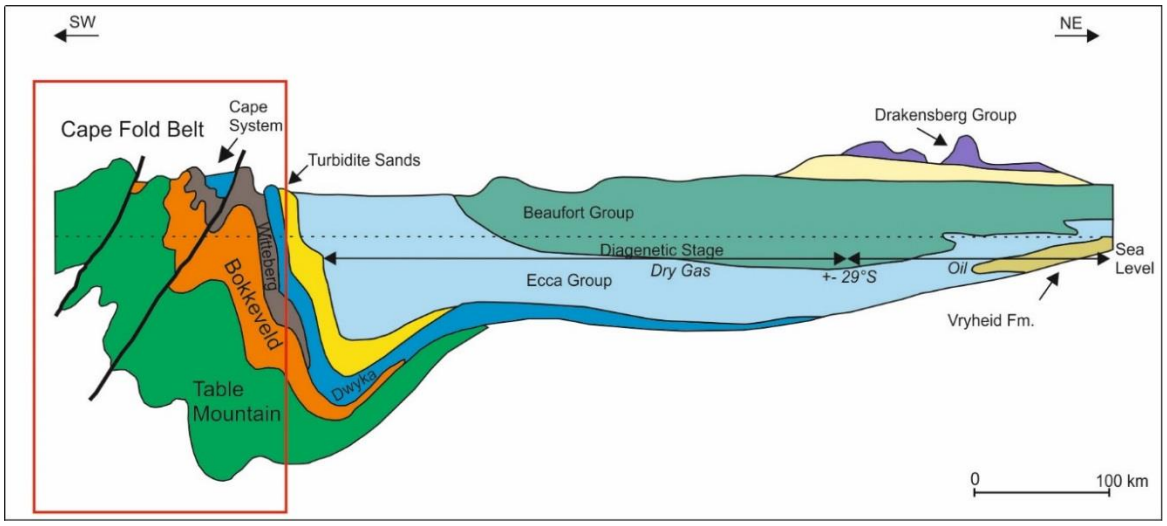

Figure 6.10: Schematic cross-section of the southern Main Karoo Basin after EIA, (2015). Red box insert highlights the Cape Fold Belt thrust faults not effecting the Ecca Group along the southern margin.

Confusion may exist with regards to the timing of the Cape Orogeny; $^{40}Ar/^{39}Ar$ dates from muscovites and biotites give a broad range of dates from circa 600 – 200 Ma, however, most researchers have identified relatively well constrained tectonic events from the Early Permian (Cisuralian) to Upper Triassic (e.g. Gentle et al., 1978; Hälbich et al., 1983; Gresse et al., 1992; Hansma et al., 2016; Blewett and Phillips, 2016). The onset of Karoo sedimentation occurred during the Late Carboniferous and continued until the Middle Jurassic (Johnson et al., 2006). It is however generally accepted that deposition of the Ecca shales predates the Cape Orogeny, therefore the uncertainty surrounding the extent of thrust propagation into the Karoo Supergroup must be rooted in doubt as to the magnitude of deformation by Cape Orogeny stress.

Lindeque et al. (2011) modelled the crust across the southern Main Karoo Basin based on a seismic reflection profile (Figure 6.11). Numerous south dipping faults are visible along the entire length of the profile. The Whitehill and Prince Albert Formations along the southern

margin of the profile have been disrupted by thrust faults, however, the effect on the Whitehill and Prince Albert Formations, further to the north, is less certain based upon the seismic reflection.

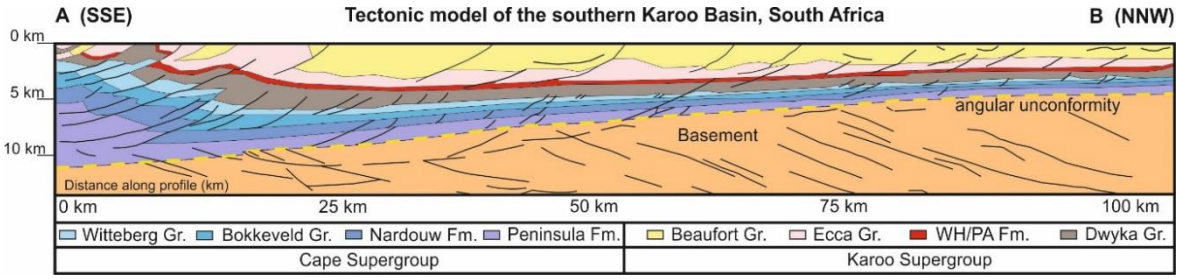

Figure 6.11: Tectonic model of the crust in the southern Main Karoo Basin based on a seismic reflection profile. Numerous south dipping faults cut through the Whitehill and Prince Albert Formations (red) along the entire length of the profile. Modified from Lindeque et al., 2011.

Chapter 3 draws attention to the effects of the CFB, and how tectonic stress propagated through the weak organic-rich shale of the lower Ecca Group. The effects of tectonic deformation on the shale gas potential are numerous. Compartmentalisation of the shale gas reservoir, stratigraphic and mixed-mode (combined stratigraphic and structural) compartmentalisation, segregate the reservoir by introducing low TOC lithologies (e.g. Prince Albert Formation) into the prospective shale gas reservoir (e.g. Whitehill Formation). Shales with high thermal exposure to the low-Greenschist metamorphism of the Cape Fold Belt (Frimmel et al., 2001), from further south in the basin, could also have been thrust into the reservoir, thus ‘diluting’ the shale gas potential by compartmentalising the organic-rich shale.

Fracture systems associated with fault planes may also be detrimental to reservoir potential. Open or mineral-filled faults and fractures have contrasting porosity and permeability with respect to the host rock layers, and will potentially dilate, slip, and propagate, and may compartmentalise fluid pressure increase during induced hydraulic fracturing. Pre-existing

structures can influence localisation of damage in response to fluid injection (Smart et al., 2014; Ferrill et al., 2014). In borehole KZF-1 fractures proximal to faults planes have been filled-in, reducing the effectiveness of the fracture systems with regards to porosity increases. Precipitation of minerals along fault planes might also limit the potential of the fault to act as a fluid pathway and the cementation of the fault breccia is evidence for this.

The lateral continuity of the decollement towards the north is uncertain. The location of borehole KZF-1 is proximal to the syntaxis (Figure 2.7) of the CFB, and accounts for the deformation observed in the core of the lower Ecca shales. Figure 6.11 documents faults cutting through as much as 100 km of the lower Ecca shales towards the north of the CFB, at the termination of the seismic reflection profile (Figure 6.11) at the northern margin of the

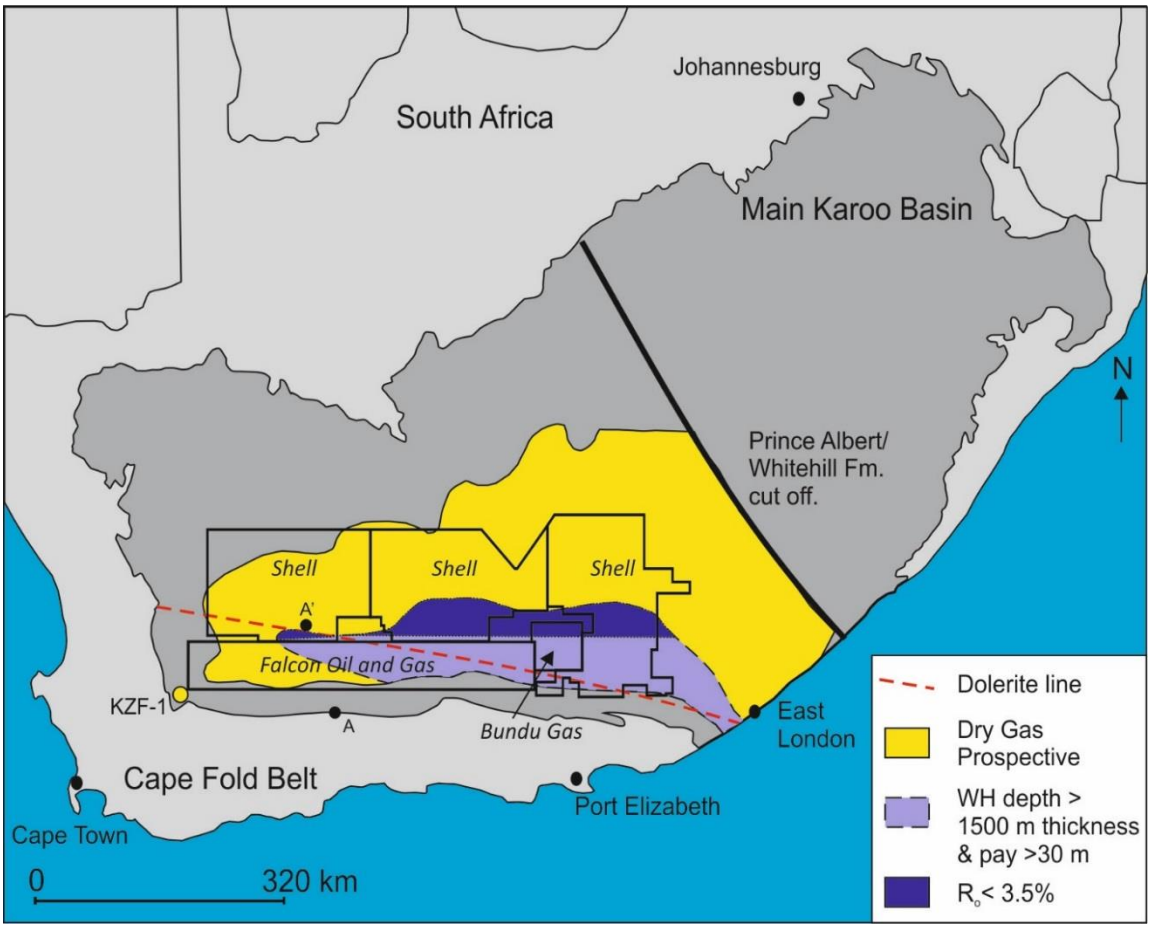

Figure 6.12: Map of the Main Karoo Basin with shale gas prospectivity zonation based on limiting parameters. Shale gas licence areas in the Karoo Basin as of 10/2017. For seismic transect A-A' see Figure 6.11. Modified after EIA (2015), Decker (2013) and PetroSa (2017).

reduced prospective area (Figure 6.12). The seismic profile incorporates both Falcon Oil and Gas and Shell's licence areas.

Exploration activities within the prospective zones will have to take into account the possibility that the Whitehill Formation, and possibly the Prince Albert Formation, were still acting as a decollement for northward-directed shortening during the Cape Orogeny. Further seismic imaging would help to identify blind faults, however, above the dolerite line seismic reflection will be hindered by the density and extent of the sills and dykes.

6.4. Geothermal Potential of the Southern Main Karoo Basin

6.4.1. Novel Geothermal Investigations in a Frontier Basin

Chapter 4 investigates and discusses the potential of deeply buried tight sandstones in the southern Main Karoo Basin to be used as geothermal reservoirs for small-scale heating/energy needs. Investigations are in their infancy with only estimates of heat in place and identification of potential exploration zones published by Campbell et al. (2016a, b). These studies are the only published research on the potential for geothermal energy from the Main Karoo Basin at a time when deep sedimentary basins around the globe are being assessed for geothermal energy (e.g., Eggeling et al. 2011; Zafar and Cutright, 2014; Horváth et al., 2015; Lenhardt and Götz, 2015; Zhu et al., 2015).

The southern Karoo Basin is a promising future target for geothermal energy exploration in South Africa. The Ripon Formation sandstones occur at depths in excess of 3000 m and, based on data from borehole KWV-1, a high thermal conductivity and high specific heat capacity can be assumed. In the region west of East London with deep thermal springs (Steyl et al. 2012), the highly fractured sandstones south of the dolerite line might act as transitional systems (Sass and Götz, 2012). These can be further enhanced by hydraulic fracturing.

Numerous factors will affect the geothermal potential of the basin including distribution of facies and thickness of prospective sandstone reservoir formations, sandstone provenance changes from east to west, localised changes in ground water geochemistry affecting sandstone cement, variations in diagenetic history, and the distribution of fault and fracture networks. Due to the large number of variables, extrapolating results from a single borehole across the basin remains difficult.

6.4.2. Methodology Development for Future Geothermal Exploration

Chapter 5 explores the viability of using existing boreholes, proximal to borehole KWV-1, for reservoir exploration by utilising downhole wireline gamma-ray logging. By analysing trends in the shape of gamma-ray logs, it is possible to identify thick geothermal-prone sandstone packages. Log trend analysis in conjunction with samples analysed from borehole KWV-1 may be applicable to nearby boreholes where subsurface conditions such as sandstone provenance, cement mineralogy and diagenetic history are similar. For the analysis of boreholes further afield, new samples will need to be analysed for geothermal potential in order to calibrate the cut-off point between similar shaped cycles of differing gamma-values (i.e. sandstone to siltstone dirtying up versus siltstone to shale dirtying up). Logging existing boreholes may be a cheaper alternative to drilling new holes, however, in the long term new deep boreholes will have to be drilled in areas of high potential in order to better model unknown variables.

6.5. Scope for Future Research

The advancement of research into energy from the Main Karoo Basin will depend heavily on the acquisition of new data. The aim of the KARIN project was to investigate the hydrocarbon potential of the Whitehill Formation and secured industry funding for the drilling of two boreholes. The information acquired from the boreholes KZF-1 and KWV-1,

uncovered numerous additional research questions and exposed novel fields of research for the Karoo such as deep geothermal.

Future research topics may include:

- Mapping of faults within shale-gas licence areas in order to ascertain the extent of Cape Orogeny deformation of the lower Ecca shales.
- A study to detail the amount of organic carbon lost from black shales with progressive distance from different sized Karoo dolerite dykes and sills, which could also investigate the potential for dolerite intrusions to naturally-fracture shales containing tight gas, and the associated hydrocarbon loss.
- The ground water geochemistry of deep aquifers from the Ripon Formation should be investigated to determine its effect on reservoir porosity, as well as to constrain any detrimental impact of mineralised water on geothermal production activities. Geothermometry studies should be untaken on existing boreholes to better constrain and understand heat flow at depth in comparison to the surface (see Figure 4.19).
- Heat flow modelling such as the research conducted by Brown (2018: pers. comm.) would be valuable in order to further constrain regions of high geothermal potential and reduce the exploration area.
- Magnetotellurics (MT) studies would provide valuable information on resistivity anomalies at depth, including changes in lithology, faults and cap rocks.
- Rock mechanic studies, on both the potential hydrocarbon-bearing shales as well as the geothermal sandstones, should be conducted as a matter of pertinence to mitigate the potential for induced seismicity during hydraulic stimulation activities.
- From a stratigraphic perspective the disappearance of the Collingham Formation needs to be investigated.

The analysis of additional core-samples from boreholes KZF-1 and KWV-1 would add statistical robustness to the present studies, which are limited by a small core-sample size. The wealth of geophysical data would be better understood with the addition of lithological data. The size and associated complexity of the Main Karoo Basin makes correlations and assumptions over any large distance problematic with data from widely spaced boreholes and outcrops.

Conducting further research will rely on industry funding, and securing such funding will involve making industry players aware of the potential benefits to production and exploration activities from academic led research, in a frontier basin such as the Main Karoo Basin.

7. Reference List

ABDULAGATOVA, Z., ABDULAGATOV, I. and EMIROV, V., 2009. Effect of temperature and pressure on the thermal conductivity of sandstone. International Journal of Rock Mechanics and Mining Sciences, 46(6), pp. 1055-1071.

ADAMS, J.A. and WEAVER, C.E., 1958. Thorium-to-uranium ratios as indicators of sedimentary processes: example of concept of geochemical facies. AAPG Bulletin, 42(2), pp. 387-430.

AGEMAR, T., ALTEN, J., GANZ, B., KUDER, J., KÜHNE, K., SCHUMACHER, S. and SCHULZ, R., 2014. The Geothermal Information System for Germany–GeotIS. Zeitschrift der deutschen Gesellschaft für Geowissenschaften, 165(2), pp. 129-144.

AGIC, H., 2016. Fossil Focus: Acritarchs. Palaeontology Online, 6(11), pp. 1-13.

AHRENS, T.J., 1995. Rock physics & phase relations: A handbook of physical constants. American Geophysical Union.

AINSWORTH, R., 2010. Prediction of stratigraphic compartmentalization in marginal marine reservoirs. Geological Society, London, Special Publications, 347(1), pp. 199-218.

AKKUS, I., AYDOGDU, O., AKILLI, H., GOKMENOGLU, O. and SARP, S., 2005. Geothermal energy and its economic dimension in Turkey, Proceedings World Geothermal Congress 2005 2005, pp. 24-29.

ALLABY, M. and PARK, C., 2013. A dictionary of environment and conservation. OUP Oxford.

ANDERSSON, P., WORDEN, R., HODGSON, D. and FLINT, S., 2004. Provenance evolution and chemostratigraphy of a Palaeozoic submarine fan-complex: Tanqua Karoo Basin, South Africa. Marine and Petroleum Geology, 21(5), pp. 555-577.

AOUDIA, K., MISKIMINS, J.L., HARRIS, N.B. and MNICH, C.A., 2010. Statistical analysis of the effects of mineralogy on rock mechanical properties of the Woodford shale and the associated impacts for hydraulic fracture treatment design, 44th US Rock Mechanics Symposium and 5th US-Canada Rock Mechanics Symposium 2010, American Rock Mechanics Association.

ARETZ, A., BÄR, K., GÖTZ, A.E. and SASS, I., 2016. Outcrop analogue study of Permocarboniferous geothermal sandstone reservoir formations (northern Upper Rhine Graben, Germany): impact of mineral content, depositional environment and diagenesis on petrophysical properties. International Journal of Earth Sciences, 105(5), pp. 1431-1452.

ARTHUR, M.A. and SAGEMAN, B.B., 1994. Marine black shales: depositional mechanisms and environments of ancient deposits. Annual Review of Earth and Planetary Sciences, 22(1), pp. 499-551.

BACHU, S. and BURWASH, R., 1994. Geothermal regime in the Western Canada sedimentary basin. Geological Atlas of the Western Canada Sedimentary Basin.Edited by G.Mossop and I.Shetsen.Canadian Society of Petroleum Geologists and Alberta Research Council, Special Report, 4, pp. 447-454.

BAKSI, A.K., 1994. Geochronological studies on whole-rock basalts, Deccan Traps, India: evaluation of the timing of volcanism relative to the KT boundary. Earth and Planetary Science Letters, 121(1-2), pp. 43-56.

BANGERT, B., STOLLHOFEN, H., LORENZ, V. and ARMSTRONG, R., 1999. The geochronology and significance of ash-fall tuffs in the glaciogenic Carboniferous-Permian Dwyka Group of Namibia and South Africa. Journal of African Earth Sciences, 29(1), pp. 33-49.

BÄR, K.M., 2012. Untersuchung der tiefengeothermischen Potenziale von Hessen.

BARTON, N. and CHOUBEY, V., 1977. The shear strength of rock joints in theory and practice. Rock mechanics, 10(1-2), pp. 1-54.

BEAUBOUEF, R., ABREU, V., VAN WAGONER, J., ROBERTS, H., ROSEN, N., FILLON, R. and ANDERSON, J., 2003. Basin 4 of the Brazos–Trinity slope system, western Gulf of Mexico: the terminal portion of a late Pleistocene lowstand systems tract, Shelf margin deltas and linked down slope petroleum systems: Global significance and future exploration potential: Proceedings of the 23rd Annual Research Conference, Gulf Coast Section SEPM Foundation 2003, pp. 45-66.

BINE, 2011. Tracking deep geothermal energy – Leibniz Institute for Applied Geophysics offers Internet access to basic data for deep geothermal energy. Projektinfo 09/2011. Leibniz Institute for Information Infrastructure: FIZ Karlsruhe.

BIRD, P., BEN-AVRAHAM, Z., SCHUBERT, G., ANDREOLI, M. and VIOLA, G., 2006. Patterns of stress and strain rate in southern Africa. Journal of Geophysical Research: Solid Earth, 111(B8),.

BLACK, D., BOOTH, P. and DE WIT, M., 2016. Petrographic, geochemical and petro-physical analysis of the Collingham Formation near Jansenville, Eastern Cape, South Africa–potential cap rocks to shale gas in the Karoo. South African Journal of Geology, 119(1), pp. 171-186.

BLACKWELL, D. and RICHARDS, M., 2004. Geothermal Map of North America.American Association of Petroleum Geologist (AAPG), 1 sheet, scale 1: 6,500,000.

BLEWETT, S.C. and PHILLIPS, D., 2016. An Overview of Cape Fold Belt Geochronology: Implications for Sediment Provenance and the Timing of Orogenesis. Origin and Evolution of the Cape Mountains and Karoo Basin. Springer, pp. 45-55.

BOCANGEL, W., SONDERGELD, C. and RAI, C., 2013. Acoustic mapping and characterization of organic matter in shales, SPE Annual Technical Conference and Exhibition 2013, Society of Petroleum Engineers.

BOGGS, S., 2009. Petrology of sedimentary rocks. Cambridge University Press.

BOHACS, K. and MISKELL-GERHARDT, K., 1998. Well-log expression of lake strata; controls of lake-basin type and provenance, contrasts with marine strata, AAPG Annual Meeting Expanded Abstracts, Tulsa, Oklahoma A 1998.

BOHACS, K., 1998. Contrasting expressions of depositional sequences in mudrocks from marine to non marine environs.

BOOTH, P. and SHONE, R., 2002. A review of thrust faulting in the Eastern Cape Fold Belt, South Africa, and the implications for current lithostratigraphic interpretation of the Cape Supergroup. Journal of African Earth Sciences, 34(3-4), pp. 179-190.

BOOTH, P., 2011. Stratigraphic, structural and tectonic enigmas associated with the Cape Fold Belt: challenges for future research. South African Journal of Geology, 114(3-4), pp. 235-248.

BORDY, E.M., HANCOX, P.J. and RUBIDGE, B.S., 2004. Basin development during the deposition of the Elliot Formation (Late Triassic-Early Jurassic), Karoo Supergroup, South Africa. South African Journal of Geology, 107(3), pp. 397-412.

BOSWORTH, W., 1984. Foreland deformation in the Appalachian Plateau, central New York: the role of small-scale detachment structures in regional overthrusting. Journal of Structural Geology, 6(1-2), pp. 73-81.

BOTHA, J. and CLOOT, A., 2004. Deformations and the Karoo aquifers of South Africa. Advances in Water Resources, 27(4), pp. 383-398.

BOTHA, J. and CLOOT, A., 2004. Karoo aquifers: deformations, hydraulic and mechanical properties. Water Research Commission.

BOTHA, J., VERWEY, J., VAN DER VOORT, I., VIVIER, J., BUYS, J., COLLISTON, W. and LOOCK, J., 1998. Karoo aquifers: Their geology, geometry and physical properties. Water Research Commission Report, 487(1), pp. 98.

BOTHA, J., WOODFORD, A. and CHEVALLIER, L.P., 2002. Hydrogeology of the Main Karoo Basin: Current knowledge and future research needs. Water Research Commission.

BOUMA, A.H. and WICKENS, H.D.V., 1994. Tanqua Karoo, ancient analog for fine-grained submarine fans, Submarine fans and turbidite systems. GCSSEPM Foundation 15th Annual Research Conference 1994, pp. 23-34.

BOUMA, A.H., KUENEN, P.H. and SHEPARD, F.P., 1962. Sedimentology of some flysch deposits: a graphic approach to facies interpretation. Elsevier Amsterdam.

BRANCH, T., RITTER, O., WECKMANN, U., SACHSENHOFER, R.F. and SCHILLING, F., 2007. The Whitehill Formation–a high conductivity marker horizon in the Karoo Basin. South African Journal of Geology, 110(2-3), pp. 465-476.

BRITISH PETROLEUM, 2015. Statistical Review of World Energy. London: BP.

BROOM, R., 1903. On the classification of the theriodonts and their allies. Report of the South African Association for the Advancement of Science, 1, pp. 286-294.

CALVERT, S. and FONTUGNE, M., 2001. On the late Pleistocene-Holocene sapropel record of climatic and oceanographic variability in the eastern Mediterranean. Paleoceanography, 16(1), pp. 78-94.

CALVET, E. and PRAT, H., 1963. Microcalorimetry [Russian translation]. Izd.Inostr.Lit., Moscow, .

CALVET, E. and PRAT, H., 2016. Recent progress in microcalorimetry. Elsevier.

CAMPBELL, S.A., 2014. The Ecca type section (Permian, South Africa): an outcrop analogue study of conventional and unconventional hydrocarbon reservoirs. MSc edn. Rhodes University.

CAMPBELL, S.A., GÖTZ, A.E. and MONTENARI, M., 2016. New insights on the Karoo shale gas potential from borehole KZF-1 (Western Cape, South Africa). Abstracts of the Contributions of the EGU General Assembly; Vienna., 18.

CAMPBELL, S.A., LENHARDT, N., DIPPENAAR, M.A. and GÖTZ, A.E., 2016. Geothermal energy from the Main Karoo Basin (South Africa): an outcrop analogue study of Permian sandstone reservoir formations. Energy Procedia, 97, pp. 186-193.

CAMPBELL, S.A., MIELKE, P. and GÖTZ, A.E., 2016. Geothermal energy from the Main Karoo Basin? New insights from borehole KWV-1 (Eastern Cape, South Africa). Geothermal Energy, 4(1), pp. 9.

CASTELLANO, A., KENDALL, A., NIKOMAROV, M. and SWEMMER, T., 2015. Brighter Africa: The growth potential of the sub-Saharan electricity sector. McKinsey Report.http://www.mckinsey.com/insights/energy_resources_materials/powering_africa, .

CATUNEANU, O. and BOWKER, D., 2001. Sequence stratigraphy of the Koonap and Middleton fluvial formations in the Karoo foredeep South Africa. Journal of African Earth Sciences, 33(3), pp. 579-595.

CATUNEANU, O. and ELANGO, H.N., 2001. Tectonic control on fluvial styles: the Balfour Formation of the Karoo Basin, South Africa. Sedimentary Geology, 140(3), pp. 291-313.

CATUNEANU, O., 2004. Retroarc foreland systems—evolution through time. Journal of African Earth Sciences, 38(3), pp. 225-242.

CATUNEANU, O., HANCOX, P. and RUBIDGE, B., 1998. Reciprocal flexural behaviour and contrasting stratigraphies: a new basin development model for the Karoo retroarc foreland system, South Africa. Basin Research, 10(4), pp. 417-439.

CATUNEANU, O., HANCOX, P., CAIRNCROSS, B. and RUBIDGE, B., 2002. Foredeep submarine fans and forebulge deltas: orogenic off-loading in the underfilled Karoo Basin. Journal of African Earth Sciences, 35(4), pp. 489-502.

CATUNEANU, O., WOPFNER, H., ERIKSSON, P., CAIRNCROSS, B., RUBIDGE, B., SMITH, R. and HANCOX, P., 2005. The Karoo basins of south-central Africa. Journal of African Earth Sciences, 43(1), pp. 211-253.

CERVENY, K., DAVIES, R., DUDLEY, G., KAUFMAN, P., KNIPE, R. and KRANTZ, B., 2004. Reducing uncertainty with fault-seal analysis. Oilfield Review, 16(4),.

CHAMBEFORT, I. and BIGNALL, G., 2016. SPECIAL ISSUE: Taupo Volcanic Zone Geothermal Systems, New Zealand: Exploration, Science and Development Preface. Geothermics, 59, pp. 147-147.

CHANDRASEKHARAM, D. and BUNDSCHUH, J., 2008. Low-enthalpy geothermal resources for power generation. CRC Press Leiden.

CHEN, W., CHEN, J., YUN, Q., XU, S., HUANG, J. and YAO, Z., 1977. Chen W, Chen J, Yun Q, Xu S, Huang J, Yao Z. 1977. Geological results report of petroleum general investigation of Fin-Wei Basin. The Third General Investigation Exploration Team, Xianyang. China: .

CHEVALLIER, L., MUSEKIWA, C. and DHANSAY, T., 2014. Geothermal energy potential in South Africa (Geological and socio-economical investigation). Progress report of the annual technical programme, , pp. 2014-0128.

CHEVALLIER, L.P., GOEDHART, M.L. and WOODFORD, A.C., 2001. Influence of Dolerite Sill and Ring Complexes on the Occurrence of Groundwater in Karoo Fractured Aquifers: A Morpho-tectonic Approach: Report to the Water Research Commission. Water Research Commission.

CHOROWICZ, J., 2005. The east African rift system. Journal of African Earth Sciences, 43(1), pp. 379-410.

CHUKWUMA, K. and BORDY, E.M., 2016. Spatiotemporal Sedimentary Facies Variations in the Lower Permian Whitehill Formation, Ecca Group, Karoo Basin. Origin and Evolution of the Cape Mountains and Karoo Basin. Springer, pp. 101-110.

CLARKE, C.E., HART, P.S., SCHULDT, J.P., EVENSEN, D.T., BOUDET, H.S., JACQUET, J.B. and STEDMAN, R.C., 2015. Public opinion on energy development: The interplay of issue framing, top-of-mind associations, and political ideology. Energy Policy, 81, pp. 131-140.

CLARKE, H., EISNER, L., STYLES, P. and TURNER, P., 2014. Felt seismicity associated with shale gas hydraulic fracturing: The first documented example in Europe. Geophysical Research Letters, 41(23), pp. 8308-8314.

CLAUSER, C. and HUENGES, E., 1995. Thermal conductivity of rocks and minerals. Rock physics & phase relations: a handbook of physical constants, pp. 105-126.

CLOETE, M., 2010. Atlas on geological storage of carbon dioxide in South Africa. Pretoria: Council for Geoscience.

COCHRAN, J.K., CAREY, A.E., SHOLKOVITZ, E.R. and SURPRENANT, L.D., 1986. The geochemistry of uranium and thorium in coastal marine sediments and sediment pore waters. Geochimica et Cosmochimica Acta, 50(5), pp.663-680.

COHEN, K., FINNEY, S., GIBBARD, P. and FAN, J., 2013. The ICS international chronostratigraphic chart. Episodes, 36(3), pp. 199-204.

COHUT, I. and BENDEA, C., 1997. Geothermal development opportunities in central and east European countries.

COLE, D. and BASSON, W., 1991. Whitehill Formation. Catalogue of South African Lithostratigraphic Units, 3, pp. 51-52.

COLE, D. and MCLACHLAN, I., 1991. Oil potential of the permian whitehill shale formation in the main Karoo Basin, South Africa. Proceedings, Gondwana Seven: Sao Paulo, Instituto de Geociencias, Universidade de Sao Paulo, pp. 379-390.

COLE, D., 1992. Evolution and development of the Karoo Basin. Inversion tectonics of the Cape Fold Belt, Karoo and cretaceous basins of Southern Africa, pp. 87-99.

COLE, D., DE WIT, M. and RANSOME, I., 1992. Evolution and development of the Karoo Basin. Inversion tectonics of the Cape Fold Belt, Karoo and cretaceous basins of Southern Africa, , pp. 87-99.

COLEMAN, J.M. and GARRISON, L.E., 1977. Geological aspects of marine slope stability, northwestern Gulf of Mexico. Marine Georesources & Geotechnology, 2(1-4), pp. 9-44.

COLEMAN, J.M., PRIOR, D.B. and GARRISON, L.E., 1980. Subaqueous sediment instabilities in the offshore Mississippi River delta. Bureau of Land Management, New Orleans OCS Office.

COLEMAN, J.M., ROBERTS, H.H. and STONE, G.W., 1998. Mississippi River delta: an overview. Journal of Coastal Research, pp. 699-716.

CONEY, L., REIMOLD, W.U., HANCOX, P.J., MADER, D., KOEBERL, C., MCDONALD, I., STRUCK, U., VAJDA, V. and KAMO, S.L., 2007. Geochemical and mineralogical investigation of the Permian–Triassic boundary in the continental realm of the southern Karoo Basin, South Africa. Palaeoworld, 16(1), pp. 67-104.

CORNFORD, C., 2005. The Petroleum System. In: SELLEY, R.C., COCKS, L.R.M., PLIMER, I.R, ed, Encyclopedia of Geology. 1 edn. Elsevier Ltd., pp. 268.

COSSU, R., WELLS, M. and PEAKALL, J., 2015. Latitudinal variations in submarine channel sedimentation patterns: the role of Coriolis forces. Journal of the Geological Society, 172(2), pp. 161-174.

COULOMB, C., 1776. An attempt to apply the rules of maxima and minima to several problems of stability related to architecture. Mémoires de l'Académie Royale des Sciences, 7, pp. 343-382.

COX, R. and LOWE, D.R., 1995. A conceptual review of regional-scale controls on the composition of clastic sediment and the co-evolution of continental blocks and their sedimentary cover. Journal of Sedimentary Research, 65(1),.

CROWELL, A.M. and GOSNOLD, W.D., 2011. Re-evaluating geothermal potential with GIS methods and new data: Williston Basin, North Dakota, AGU Fall Meeting Abstracts 2011, pp. 1480.

DASGUPTA, P., 2008. Experimental decipherment of the soft-sediment deformation observed in the upper part of the Talchir Formation (Lower Permian), Jharia Basin, India. Sedimentary Geology, 205(3-4), pp. 100-110.

DAVIES, R.K. and HANDSCHY, J.W., 2003. Introduction to AAPG Bulletin thematic issue on fault seals. AAPG Bulletin, 87(3), pp. 377-380.

DE BEER, C., 1992. Structural evolution of the Cape Fold Belt syntaxis and its influence on syntectonic sedimentation in the SW Karoo Basin. Inversion Tectonics of the Cape Fold Belt, Karoo and Cretaceous Basins of Southern Africa.Balkema, Rotterdam, Netherlands, pp. 197-206.

DE KOCK, M., BEUKES, N., GÖTZ, A., COLE, D., ROBEY, K., BIRCH, A., WITHERS, A. and VAN NIEKERK, H., 2016. Open file progress report on exploration of the Southern

Karoo Basin through CIMERAKARIN borehole KZF-1 in the Tankwa Karoo, Witzenberg (Ceres) district. DST-NRF Centre of Excellence for Integrated Mineral and Energy Resources Analysis (CIMERA), University of Johannesburg, South Africa.

DE KOCK, M., BEUKES, N., VAN NIEKERK, H., COLE, D., ROBEY, K., BIRCH, A. and GÖTZ, A., OPEN FILE PROGRESS REPORT ON INVESTIGATION OF THE SOUTHEASTERN MAIN KAROO BASIN THROUGH CIMERA-KARIN BOREHOLE KWV-1 NEAR WILLOWVALE IN THE EASTERN CAPE PROVINCE.

DE PATER, C. and BAISCH, S., 2011. Geomechanical study of Bowland Shale seismicity. Synthesis report, 57.

DE WIT, M.J. and RANSOME, I.G., 1992. Inversion Tectonics of the Cape Fold Belt, Karoo and Cretaceous Basins of Southern Africa: Proceedings of the Conference on Inversion Tectonics of the Cape Fold Belt, Cape Town, South Africa, 2-6 December 1991. Taylor & Francis.

DE WIT, M.J., 1977. The evolution of the Scotia Arc as a key to the reconstruction of southwestern Gondwanaland. Tectonophysics, 37(1-3), pp. 53-81.

DECKER, J. and MAROT, J., 2012-last update, Investigation of Hydaulic Fracturing in the Karoo of South Africa. Annexure A, Resource Assessment, Pertoluem Agency SA. [Homepage of Petroleum Agency SA], [Online]. Available: http://www.dmr.gov.za/publications/viewdownload/182/854.html2015].

DECKER, J., 2013. The Karoo Basin's Shale Gas Potential. Johannesburg: GeoForum.

DEER, W.A., HOWIE, R.A. and ZUSSMAN, J., 1992. An introduction to the rock-forming minerals. Longman Scientific & Technical Hong Kong.

DEGENS, E.T., 1965. Geochemistry of Sediments. Soil Science, 100(3), pp. 225.

DEKKER, J., NTHONTHO, M., CHOWDHURY, S. and CHOWDHURY, S., 2012. Economic analysis of PV/diesel hybrid power systems in different climatic zones of South Africa. International Journal of Electrical Power & Energy Systems, 40(1), pp. 104-112.

DEMAISON, G. and MOORE, G.T., 1980. Anoxic environments and oil source bed genesis. Organic Geochemistry, 2(1), pp. 9-31.

DEPARTMENT OF ENERGY, REPUBLIC OF SOUTH AFRICA, 2015-last update, Nuclear Energy [Homepage of Department of Energy], [Online]. Available: http://www.energy.gov.za/files/nuclear_frame.html2015].

DHANSAY, T., DE WIT, M. and PATT, A., 2014. An evaluation for harnessing low-enthalpy geothermal energy in the Limpopo Province, South Africa. South African Journal of Science, 110(3-4), pp. 01-10.

DOHER, L.I., 1980. Palynomorph preparation procedures currently used in the paleontology and stratigraphy laboratories, US Geological Survey.

DÖVÉNYI, P., HORVÁTH, F. and DRAHOS, D., 2003. Hungary. Atlas of Geothermal Resources in Europe. Publication No. 17811 of the European Commission.

DU TOIT, A.L. and REED, F.R.C., 1927. A geological comparison of South America with South Africa.

DU TOIT, A.L., 1926. The Geology of South Africa. 1 edn. Edinburgh: Oliver and Boyd, Ltd.

DU, T.A.L., 1937. Our Wandering Continents An Hypothesis Of Continental Drifting. Oliver And Boyd, London.

DUNCAN, A. and MARSH, J., 2006. The Karoo igneous province. The geology of South Africa, pp. 501-520.

DUNCAN, R. and PYLE, D., 1988. Rapid eruption of the Deccan flood basalts at the Cretaceous/Tertiary boundary. Nature, 333, pp. 841-843.

DUNCAN, R.A., HOOPER, P., REHACEK, J., MARSH, J. and DUNCAN, A., 1997. The timing and duration of the Karoo igneous event, southern Gondwana.

DUNCAN, R.A., HOOPER, P., REHACEK, J., MARSH, J. and DUNCAN, A., 1997. The timing and duration of the Karoo igneous event, southern Gondwana.

DYPVIK, H. and ERIKSENF, D., 1983. Natural radioactivity of clastic sediments and the contribution of U, Th and K. Journal of Petroleum Geology, 5(4), pp. 409-416.

EARLE, S., 2015. Physical Geology. CC-BY 4.0 International license.

EGGELING, L., KÖLBEL, T., SCHLAGERMANN, P. and MÜNCH, W., 2011. Geothermische stromerzeugung in Deutschland. Chemie Ingenieur Technik, 83(11), pp. 1834-1844.

EGHBAL, M., 2015. Geothermal Power Generation. Handbook of Clean Energy Systems.

EHRENBERG, S. and NADEAU, P., 2005. Sandstone vs. carbonate petroleum reservoirs: A global perspective on porosity-depth and porosity-permeability relationships. AAPG Bulletin, 89(4), pp. 435-445.

EINSELE, G., 1992. Sedimentary Basins

Evolution, Facies, and Sedimentary Budget. 1 edn. Springer-Verlag.

EISNER, L., HALLO, M., MATOUSEK, P., OPRSAL, I. and JANSKA, E., 2011. Seismic analysis of the events in the vicinity of the Preese Hall well. Report from Seismik to Cuadrilla Resources Ltd. [Available at www.cuadrillaresources.com/wpcontent/uploads/2011/12/Seismik_SeismicReport_final30 09111.pdf]

ELLSWORTH, W.L., 2013. Injection-induced earthquakes. Science (New York, N.Y.), 341(6142), pp. 1225942.

EMERY, D. and MYERS, K., 1996. Sequence Stratigraphy. Black Well Science Ltd.

ENERGY INFORMATION ADMINISTRATION, 2013-last update, Technically Recoverable Shale Oil and Shale Gas Resources. Available: www.eia.gov/analysis/studies/worldshalegas/. [September 2016, 10].

ERKAN, K., HOLDMANN, G., BENOIT, W. and BLACKWELL, D., 2008. Understanding the Chena Hot Springs, Alaska, geothermal system using temperature and pressure data from exploration boreholes. Geothermics, 37(6), pp. 565-585.

ESPOSITO, A. and AUGUSTINE, C., 2011. Geopressured Geothermal Resource and Recoverable Energy Estimate for the Wilcox and Frio Formations, Texas (Presentation).

EVANS, M.A., 1994. Joints and decollement zones in Middle Devonian shales: Evidence for multiple deformation events in the central Appalachian Plateau. Geological Society of America Bulletin, 106(4), pp. 447-460.

FAGERENG, Å. and BYRNES, G., 2015. A range of fault slip styles on progressively misoriented planes during flexural-slip folding, Cape Fold Belt, South Africa. Journal of Structural Geology, 70, pp. 156-169.

FAGERENG, Å., 2012. A note on folding mechanisms in the Cape Fold Belt, South Africa. South African Journal of Geology, 115(2), pp. 137-144.

FALCON, R., 1975. APPLICATION OF PALYNOLOGY IN SUB-DIVIDING COAL-BEARING FORMATIONS OF KARROO SEQUENCE IN SOUTHERN AFRICA. South African Journal of Science, 71(11), pp. 336-344.

FAURE, K. and COLE, D., 1999. Geochemical evidence for lacustrine microbial blooms in the vast Permian Main Karoo, Paraná, Falkland Islands and Huab basins of southwestern Gondwana. Palaeogeography, Palaeoclimatology, Palaeoecology, 152(3), pp. 189-213.

FERRILL, D.A., MCGINNIS, R.N., MORRIS, A.P., SMART, K.J., SICKMANN, Z.T., BENTZ, M., LEHRMANN, D. and EVANS, M.A., 2014. Control of mechanical stratigraphy on bed-restricted jointing and normal faulting: Eagle Ford Formation, south-central Texas. AAPG Bulletin, 98(11), pp. 2477-2506.

FERTL, W.H. and CHILINGAR, G.V., 1988. Total organic carbon content determined from well logs. SPE Formation Evaluation, 3(02), pp. 407-419.

FILDANI, A., DRINKWATER, N.J., WEISLOGEL, A., MCHARGUE, T., HODGSON, D.M. and FLINT, S.S., 2007. Age controls on the Tanqua and Laingsburg deep-water systems: new insights on the evolution and sedimentary fill of the Karoo basin, South Africa. Journal of Sedimentary Research, 77(11), pp. 901-908.

FILDANI, A., WEISLOGEL, A., DRINKWATER, N.J., MCHARGUE, T., TANKARD, A., WOODEN, J., HODGSON, D. and FLINT, S., 2009. U-Pb zircon ages from the southwestern Karoo Basin, South Africa—Implications for the Permian-Triassic boundary. Geology, 37(8), pp. 719-722.

FILOMENA, C., HORNUNG, J. and STOLLHOFEN, H., 2014. Assessing accuracy of gas-driven permeability measurements: a comparative study of diverse Hassler-cell and probe permeameter devices. Solid Earth, 5(1), pp. 1.

FISHER, Q. and WIGNALL, P., 2001. Palaeoenvironmental controls on the uranium distribution in an Upper Carboniferous black shale (Gastrioceras listeri Marine Band) and associated strata; England. Chemical Geology, 175(3-4), pp. 605-621.

FLINT, S., AND, HODGSON, D., SPRAGUE, A., BRUNT, R., VAN DER MERWE, W., FIGUEIREDO, J., PRÉLAT, A., BOX, D., DI CELMA, C. and KAVANAGH, J., 2011. Depositional architecture and sequence stratigraphy of the Karoo basin floor to shelf edge succession, Laingsburg depocentre, South Africa. Marine and Petroleum Geology, 28(3), pp. 658-674.

FÖLLMI, K.B. and GRIMM, K.A., 1990. Doomed pioneers: Gravity-flow deposition and bioturbation in marine oxygen-deficient environments. Geology, 18(11), pp. 1069-1072.

FRAKES, L., FRANCIES, J. and SYKTUS, J., 1992. Climate Modes of the Phanerozoic.− Cambridge Univ. Press, Cambridge.

FREY MARTINEZ, J., CARTWRIGHT, J. and HALL, B., 2005. 3D seismic interpretation of slump complexes: examples from the continental margin of Israel. Basin Research, 17(1), pp. 83-108.

FRIMMEL, H., FÖLLING, P. and DIAMOND, R., 2001. Metamorphism of the Permo-Triassic Cape Fold Belt and its basement, South Africa. Mineralogy and Petrology, 73(4), pp. 325-346.

FUCHS, S., SCHÜTZ, F., FÖRSTER, H. and FÖRSTER, A., 2013. Evaluation of common mixing models for calculating bulk thermal conductivity of sedimentary rocks: correction charts and new conversion equations. Geothermics, 47, pp. 40-52.

GALE, J.F., REED, R.M. and HOLDER, J., 2007. Natural fractures in the Barnett Shale and their importance for hydraulic fracture treatments. AAPG Bulletin, 91(4), pp. 603-622.

GALE, J.F., REED, R.M. and HOLDER, J., 2007. Natural fractures in the Barnett Shale and their importance for hydraulic fracture treatments. AAPG Bulletin, 91(4), pp. 603-622.

GARG, S.K. and COMBS, J., 2010. Appropriate use of USGS volumetric “heat in place” method and Monte Carlo calculations, Proceedings 34th Workshop on Geothermal Reservoir Engineering, Stanford university, Stanford, California, USA 2010.

GASTALDO, R.A., ADENDORFF, R., BAMFORD, M., LABANDEIRA, C.C., NEVELING, J. and SIMS, H., 2005. Taphonomic trends of macrofloral assemblages across the Permian–Triassic boundary, Karoo Basin, South Africa. Palaios, 20(5), pp. 479-497.

GEE, M., GAWTHORPE, R. and FRIEDMANN, S., 2006. Triggering and evolution of a giant submarine landslide, offshore Angola, revealed by 3D seismic stratigraphy and geomorphology. Journal of Sedimentary Research, 76(1), pp. 9-19.

GEE, M., MASSON, D., WATTS, A. and ALLEN, P., 1999. The Saharan debris flow: an insight into the mechanics of long runout submarine debris flows. Sedimentology, 46, pp. 317-335.

GEE, M.J., MASSON, D.G., WATTS, A.B. and MITCHELL, N.C., 2001. Passage of debris flows and turbidity currents through a topographic constriction: seafloor erosion and deflection of flow pathways. Sedimentology, 48(6), pp. 1389-1409.

GEEL, C., SCHULZ, H., BOOTH, P. and HORSFIELD, B., 2013. Shale gas characteristics of Permian black shales in South Africa: results from recent drilling in the Ecca Group (Eastern Cape). Energy Procedia, 40, pp. 256-265.

GENTLE, R., HOOKER, P., MILLER, J. and FITCH, F., 1978. Evidence for Cape Fold Belt overprinting of the Groot Haelkraal granite during the Upper Permian. Transactions of the Geological Society of South Africa, 81(1), pp. 105-107.

GLOBAL ENERGY NETWORK INSTITUTE, 06/30/2016, Renewable Energy Resources in Africa. Available: http://www.geni.org/globalenergy/library/renewable-energy-resources/world/africa/index.shtml2015].

GÖTZ, A.E. and RUCKWIED, K., 2014. Palynological records of the Early Permian postglacial climate amelioration (Karoo Basin, South Africa). Palaeobiodiversity and Palaeoenvironments, 94(2), pp. 229-235.

GÖTZ, A.E., TÖRÖK, Á. and SASS, I., 2014. Geothermal reservoir characteristics of Meso- and Cenozoic sedimentary rocks of Budapest (Hungary). Zeitschrift der Deutschen Gesellschaft für Geowissenschaften, 165(3), pp. 487-493.

GRADSTEIN, F. and OGG, J., 2004. Geologic time scale 2004–why, how, and where next! Lethaia, 37(2), pp. 175-181.

GREEN, C.A., STYLES, P. and BAPTIE, B.J., 2012. Preese Hall shale gas fracturing review and recommendations for induced seismic mitigation. London, UK: Department of Energy and Climate Change.

GRESSE, P., THERON, J., FITCH, F. and MILLER, J., 1992. Tectonic inversion and radiometric resetting of the basement in the Cape Fold Belt. Inversion Tectonics of the Cape

Fold Belt, Karoo and Cretaceous Basins of Southern Africa: Rotterdam, Balkema, pp. 217-228.

GROENEWALD, G. and KITCHING, J., 1995. Biostratigraphy of the Lystrosaurus assemblage zone. Biostratigraphy of the Beaufort Group (Karoo Supergroup), pp. 35-39.

HALBICH, I. and CORNELL, D., 1983. Metamorphic history of the Cape Fold belt. Geodynamics of the Cape Fold Belt.Special Publication of the Geological Society of South Africa, 12, pp. 131-148.

HÄLBICH, I., 1983. A tectogenesis of the Cape Fold Belt (CFB). Geodynamics of the Cape Fold Belt, 12, pp. 165-175.

HÄLBICH, I., 1992. Inversion Tectonics of the Cape Fold Belt, Karoo and Cretaceous Basins of Southern Africa.

HAMMER, Ø., HARPER, D. and RYAN, P., 2001. PAST-Palaeontological statistics. www.uv.es/~ pardomv/pe/2001_1/past/pastprog/past.pdf, acessado em, 25(07), pp. 2009.

HAMMONS, T., 2004. Geothermal power generation worldwide: Global perspective, technology, field experience, and research and development. Electric Power Components and Systems, 32(5), pp. 529-553.

HAMPTON, M.A. and BOUMA, A.H., 1977. Slope instability near the shelf break, western Gulf of Alaska. Marine Georesources & Geotechnology, 2(1-4), pp. 309-331.

HANCOX, P.J. and GÖTZ, A.E., 2014. South Africa's coalfields—A 2014 perspective. International Journal of Coal Geology, 132, pp. 170-254.

HANSMA, J., TOHVER, E., SCHRANK, C., JOURDAN, F. and ADAMS, D., 2016. The timing of the Cape Orogeny: New 40 Ar/39 Ar age constraints on deformation and cooling of the Cape Fold Belt, South Africa. Gondwana Research, 32, pp. 122-137.

HAQ, B.U. and AL-QAHTANI, A.M., 2005. Phanerozoic cycles of sea-level change on the Arabian Platform. GeoArabia, 10(2), pp. 127-160.

HAQ, B.U., HARDENBOL, J. and VAIL, P.R., 1987. Chronology of fluctuating sea levels since the triassic. Science (New York, N.Y.), 235(4793), pp. 1156-1167.

HÄRING, M.O., SCHANZ, U., LADNER, F. and DYER, B.C., 2008. Characterisation of the Basel 1 enhanced geothermal system. Geothermics, 37(5), pp. 469-495.

HARRIS, N.B., 2005. The deposition of organic-carbon-rich sediments: models, mechanisms, and consequences. SEPM.

HARRISON, T.M., CÉLÉRIER, J., AIKMAN, A.B., HERMANN, J. and HEIZLER, M.T., 2009. Diffusion of 40 Ar in muscovite. Geochimica et Cosmochimica Acta, 73(4), pp. 1039-1051.

HART, G., 1964. Where was the Lower Karroo sea. Scientific South Africa, 1(8), pp. 289-290.

HAUGHTON, S., 1925. Exhibit: tracks of animals preserved in the Ecca Shales of Cape Province. Transactions of the Royal Society of South Africa, 13, pp. 28-29.

HAUGHTON, S., 1928. The palaeontology of the Namaqualand costal deposits. South African Journal of Geology, 31(1), pp. 1-41.

HEDGES, J.I. and KEIL, R.G., 1999. Organic geochemical perspectives on estuarine processes: sorption reactions and consequences. Marine Chemistry, 65(1), pp. 55-65.

HERBERT, C. and COMPTON, J., 2007. Depositional environments of the lower Permian Dwyka diamictite and Prince Albert shale inferred from the geochemistry of early diagenetic concretions, southwest Karoo Basin, South Africa. Sedimentary Geology, 194(3), pp. 263-277.

HG READING, 1996. Sedimentary environments: Processes, facies and stratigraphy. Blackwell Publishing.

HILL, R., 1988. Quaternary faulting in the south-eastern Cape Province. South African Journal of Geology, 91(3), pp. 399-403.

HIRST, C.M., GLUYAS, J.G., ADAMS, C.A., MATHIAS, S.A., BAINS, S. and STYLES, P., 2015. UK Low Enthalpy Geothermal Resources: the Cheshire Basin. Proceedings World Geothermal Congress Melbourne, Australia.

HODGSON, D., DI CELMA, C., BRUNT, R. and FLINT, S., 2011. Submarine slope degradation and aggradation and the stratigraphic evolution of channel–levee systems. Journal of the Geological Society, 168(3), pp. 625-628.

HOFMANN, H., BLÖCHER, G., BÖRSING, N., MARONDE, N., PASTRIK, N. and ZIMMERMANN, G., 2014. Potential for enhanced geothermal systems in low permeability limestones–stimulation strategies for the Western Malm karst (Bavaria). Geothermics, 51, pp. 351-367.

HOLT, RINEHART and WINSTON, 2001. Holt Science and Technology:

Earth Science. USA: Holt, Rinehart and Winston.

HOMUTH, S., GÖTZ, A. and SASS, I., 2015. Reservoir characterization of the Upper Jurassic geothermal target formations (Molasse Basin, Germany): role of thermofacies as exploration tool. Geothermal Energy Science, 3(1), pp. 41-49.

HOMUTH, S., GÖTZ, A.E. and SASS, I., 2014. Lithofacies and depth dependency of thermo-and petrophysical rock parameters of the Upper Jurassic geothermal carbonate reservoirs of the Molasse Basin. Zeitschrift der Deutschen Gesellschaft für Geowissenschaften, 165(3), pp. 469-486.

HONDIUS, J., 1652. Klare besgryving van Cabo de Bona Esperanca [A clear description of the Cape of Good Hope]. Amsterdam.

HORAI, K., 1971. Thermal conductivity of rock-forming minerals. Journal of Geophysical Research, 76(5), pp. 1278-1308.

HORVÁTH, F., MUSITZ, B., BALÁZS, A., VÉGH, A., UHRIN, A., NÁDOR, A., KOROKNAI, B., PAP, N., TÓTH, T. and WÓRUM, G., 2015. Evolution of the Pannonian basin and its geothermal resources. Geothermics, 53, pp. 328-352.

HUBBERT, M.K. and RUBEY, W.W., 1959. Role of fluid pressure in mechanics of overthrust faulting I. Mechanics of fluid-filled porous solids and its application to overthrust faulting. Geological Society of America Bulletin, 70(2), pp. 115-166.

HUENGES, E., 2010. Geothermal energy systems. Exploration Development and Utilzation, Willey-VCH.

HURST, A., 1990. Natural gamma-ray spectrometry in hydrocarbon-bearing sandstones from the Norwegian Continental Shelf. Geological Society, London, Special Publications, 48(1), pp. 211-222.

HURTER, S., HAENEL, R., ROLLIN, K., KIRBY, G., ROWLEY, W. and BUCKLEY, D., 2002. Atlas of geothermal resources in Europe.

INESON, J., BOJESEN-KOEFOD, J., DYBKJ, K. and NIELSEN, L., 2001. Volgian-Ryazanian" hot shales" of the Farsund Formation in the Danish Central Graben, North Sea: stratigraphy, facies and geochemistry. The Jurassic of Denmark and Greenland.

INTERNATIONAL ENERGY AGENCY, 2014. World Energy Outlook. Paris, France: International Energy Agency.

JELSMA, H.A., DE WIT, M.J., THIART, C., DIRKS, P.H., VIOLA, G., BASSON, I.J. and ANCKAR, E., 2004. Preferential distribution along transcontinental corridors of kimberlites and related rocks of Southern Africa. South African Journal of Geology, 107(1-2), pp. 301-324.

JOHNSON, M., 1991. Sandstone petrography, provenance and plate tectonic setting in Gondwana context of the southeastern Cape-Karoo Basin. South African Journal of Geology, 94(2-3), pp. 137-154.

JOHNSON, M., 1991. Sandstone petrography, provenance and plate tectonic setting in Gondwana context of the southeastern Cape-Karoo Basin. South African Journal of Geology, 94(2-3), pp. 137-154.

JOHNSON, M., VAN VUUREN, C., HEGENBERGER, W., KEY, R. and SHOW, U., 1996. Stratigraphy of the Karoo Supergroup in southern Africa: an overview. Journal of African Earth Sciences, 23(1), pp. 3-15.

JOHNSON, M., VAN VUUREN, C., VISSER, J., COLE, D. and WICKENS, H., 2006. DE V., CHRISTIE, ADM, ROBERTS, DL & BRANDL, G. 2006. Sedimentary rocks of the Karoo Supergroup. The geology of South Africa, pp. 463-501.

JOHNSON, M.R., 1966. The stratigraphy of the Cape and Karroo systems in the Eastern Cape Province.

JOHNSON, M.R., 1976. Stratigraphy and sedimentology of the Cape and Karoo sequences in the Eastern Cape Province.

JOHNSON, S.D., FLINT, S., HINDS, D. and DE VILLE WICKENS, H., 2001. Anatomy, geometry and sequence stratigraphy of basin floor to slope turbidite systems, Tanqua Karoo, South Africa. Sedimentology, 48(5), pp. 987-1023.

JOHNSTON, S., 2000. The Cape Fold Belt and Syntaxis and the rotated Falkland Islands: dextral transpressional tectonics along the southwest margin of Gondwana. Journal of African Earth Sciences, 31(1), pp. 51-63.

JOLLEY, S., FISHER, Q. and AINSWORTH, R., 2010. Reservoir compartmentalization: an introduction. Geological Society, London, Special Publications, 347(1), pp. 1-8.

JONES, M., 1992. Heat flow in South Africa. Dept. of Mineral and Energy Affairs, Geological Survey.

JONES, M., 2001. Heat flow in Southern Africa and thermal structure of the Kaapvaal lithosphere, Slave-Kaapvaal workshop, Merrickville, Ontario, Canada 2001.

JOURDAN, F., FÉRAUD, G., BERTRAND, H., KAMPUNZU, A.B., TSHOSO, G., WATKEYS, M.K. and LE GALL, B., 2005. Karoo large igneous province: Brevity, origin, and relation to mass extinction questioned by new 40Ar/39Ar age data. Geology, 33(9), pp. 745-748.

JOURDAN, F., FÉRAUD, G., BERTRAND, H., WATKEYS, M. and RENNE, P., 2007. Distinct brief major events in the Karoo large igneous province clarified by new 40 Ar/39 Ar ages on the Lesotho basalts. Lithos, 98(1), pp. 195-209.

KANG, F., 2010. Sustainable development of geothermal resources in China, Proceedings of the 2010 World Geothermal Congress, Bali, Indonesia, April 2010, pp. 25-29.

KATZ, B.J., 2005. Controlling factors on source rock development—a review of productivity, preservation, and sedimentation rate.

KERANEN, K.M., WEINGARTEN, M., ABERS, G.A., BEKINS, B.A. and GE, S., 2014. Induced earthquakes. Sharp increase in central Oklahoma seismicity since 2008 induced by massive wastewater injection. Science (New York, N.Y.), 345(6195), pp. 448-451.

KETRIS, M. and YUDOVICH, Y.E., 2009. Estimations of Clarkes for Carbonaceous biolithes: World averages for trace element contents in black shales and coals. International Journal of Coal Geology, 78(2), pp. 135-148.

KING, R.C., 2005. The structural evolution of the Cape Fold Belt and SW Karoo Basin: implications on sediment storage and routeing to the SW Karoo Basin, South Africa.

KING, R.F. and MOREHOUSE, D., 1993. Drilling sideways—a review of horizontal well technology and its domestic application. Energy Information Administration Technical Report.

KINGSLEY, C., 1979. A composite turbidite-delta-fluvial model for Permian sedimentation in the Ecca and lower Beaufort of the eastern Cape Province.

KINGSLEY, C., 1981. A composite submarine fan-delta-fluvial model for the Ecca and lower Beaufort Groups of Permian age in the Eastern Cape Province, South Africa. Transactions of the Geological Society of South Africa, 84(1), pp. 27-40.

KINGSLEY, C.S., 1977. Stratigraphy and sedimentology of the Ecca Group in the Eastern Cape province, South Africa.

KITCHING, J., 1978. The stratigraphic distribution and occurrence of South African fossil Amphibia in the Beaufort Beds.

KLEMME, H. and ULMISHEK, G.F., 1991. Effective petroleum source rocks of the world: stratigraphic distribution and controlling depositional factors (1). AAPG Bulletin, 75(12), pp. 1809-1851.

Knight, R., Klassen, R. and Hunt, P., 2002. Mineralogy of fine-grained sediment by energy-dispersive spectrometry (EDS) image analysis–a methodology. Environmental Geology, 42(1), pp.32-40.

KORKMAZ, E., SERPEN, U. and SATMAN, A., 2014. Geothermal boom in Turkey: Growth in identified capacities and potentials. Renewable Energy, 68, pp. 314-325.

KOTZE, C., 2012-last update, Uranium-rich South Africa good environment for nuclear plants. [Homepage of Mining Weekly], [Online]. Available: http://www.miningweekly.com/article/uranium-rich-south-africa-good-environment-for-nuclear-plants-2012-04-062015].

KRISTENSEN, M.B., CHILDS, C.J. and KORSTGÅRD, J.A., 2008. The 3D geometry of small-scale relay zones between normal faults in soft sediments. Journal of Structural Geology, 30(2), pp. 257-272.

KUMAR, V., SONDERGELD, C.H. and RAI, C.S., 2012. Nano to macro mechanical characterization of shale, SPE Annual Technical Conference and Exhibition 2012, Society of Petroleum Engineers.

KUUSKRAA, V., STEVENS, S.H. and MOODHE, K.D., 2013. Technically recoverable shale oil and shale gas resources: an assessment of 137 shale formations in 41 countries outside the United States.

LALOMOV, A., 2003. Differentiation of heavy minerals in the alongshore debris flow and modeling of processes of coastal-marine placer formation. Lithology and Mineral Resources, 38(4), pp. 306-313.

LAW, B. and CURTIS, J., 2002. Introduction to unconventional petroleum systems. AAPG Bulletin, 86(11), pp. 1851-1852.

LENHARDT, N. and GÖTZ, A.E., 2015. Geothermal reservoir potential of volcaniclastic settings: The Valley of Mexico, Central Mexico. Renewable Energy, 77, pp. 423-429.

LI, K., BIAN, H., LIU, C., ZHANG, D. and YANG, Y., 2015. Comparison of geothermal with solar and wind power generation systems. Renewable and Sustainable Energy Reviews, 42, pp. 1464-1474.

LIGTENBERG, J., 2005. Detection of fluid migration pathways in seismic data: implications for fault seal analysis. Basin Research, 17(1), pp. 141-153.

LINDEQUE, A., DE WIT, M.J., RYBERG, T., WEBER, M. and CHEVALLIER, L., 2011. Deep crustal profile across the southern Karoo Basin and Beattie Magnetic Anomaly, South Africa: an integrated interpretation with tectonic implications. South African Journal of Geology, 114(3-4), pp. 265-292.

LINOL, B. and DE WIT, M.J., 2016. Origin and Evolution of the Cape Mountains and Karoo Basin.

LINOL, B., CHERE, N., MUEDI, T., NENGOVHELA, V. and DE WIT, M.J., 2016. Deep Borehole Lithostratigraphy and Basin Structure of the Southern Karoo Basin Re-Visited. Origin and Evolution of the Cape Mountains and Karoo Basin. Springer, pp. 3-16.

LIU, S., LEI, X., FENG, C. and HAO, C., 2015. Estimate of subsurface formation temperature in the Tarim basin, northwest China, EGU General Assembly Conference Abstracts 2015, pp. 2348.

LLENOS, A.L. and MICHAEL, A.J., 2013. Modeling earthquake rate changes in Oklahoma and Arkansas: Possible signatures of induced seismicity. Bulletin of the Seismological Society of America, 103(5), pp. 2850-2861.

LÓPEZ-GAMUNDÍ, O., 2006. Permian plate margin volcanism and tuffs in adjacent basins of west Gondwana: Age constraints and common characteristics. Journal of South American Earth Sciences, 22(3), pp. 227-238.

LOYDELL, D., BUTCHER, A., FRÝDA, J., LÜNING, S. and FOWLER, M., 2009. Lower Silurian "hot shales" in Jordan: a new depositional model. Journal of Petroleum Geology, 32(3), pp. 261-270.

LUND, J.W. and BOYD, T.L., 2015. Direct utilization of geothermal energy 2015 worldwide review. Geothermics, 60, pp. 66-93.

LÜNING, S., ARCHER, R., CRAIG, J. and LOYDELL, D.K., 2003. The Lower Silurian 'hot shales' and 'double hot shales' in north Africa and Arabia. The geology of northwest Libya (Ghadamis, Jifarah, Tarabulus and Sabratah basins): Tripoli, Earth Science Society of Libya, 3, pp. 91-105.

LÜNING, S., CRAIG, J., LOYDELL, D., ŠTORCH, P. and FITCHES, B., 2000. Lower Silurianhot shales' in North Africa and Arabia: regional distribution and depositional model. Earth-Science Reviews, 49(1), pp. 121-200.

LUNING, S., KOLONIC, S., LOYDELL, D.K. and CRAIG, J., 2003. Reconstruction of the original organic richness in weathered Silurian shale outcrops (Murzuq and Kufra basins, southern Libya). GEOARABIA-MANAMA-, 8, pp. 299-308.

LUNING, S., SHAHIN, Y., LOYDELL, D., AL-RABI, H., MASRI, A., TARAWNEH, B. and KOLONIC, S., 2005. Anatomy of a world-class source rock: Distribution and depositional model of Silurian organic-rich shales in Jordan and implications for hydrocarbon potential. AAPG Bulletin, 89(10), pp. 1397-1427.

MAJOROWICZ, J. and MOORE, M., 2014. The feasibility and potential of geothermal heat in the deep Alberta foreland basin-Canada for CO2 savings. Renewable Energy, 66, pp.541-549.

MANNING, C. and INGEBRITSEN, S., 1999. Permeability of the continental crust: Implications of geothermal data and metamorphic systems. Reviews of Geophysics, 37(1), pp. 127-150.

MAQSOOD, A. and KAMRAN, K., 2005. Thermophysical properties of porous sandstones: measurements and comparative study of some representative thermal conductivity models. International Journal of Thermophysics, 26(5), pp. 1617-1632.

MARSH, J. and EALES, H., 1984. The chemistry and petrogenesis of igneous rocks of the Karoo central area, southern Africa. Special Publication of the Geological Society of South Africa, 13, pp. 27-68.

MARSH, J. and MNDAWENI, M., 1998. Geochemical variations in a long Karoo dyke, Eastern Cape. South African Journal of Geology, 101(2), pp. 119-122.

MASSON, D., CANALS, M., ALONSO, B., URGELES, R. and HUHNERBACH, V., 1998. The Canary Debris Flow: source area morphology and failure mechanisms. Sedimentology, 45(2), pp. 411-432.

MCCARTHY, T. and RUBIDGE, B., 2005. Earth and Life. Kumba Resources.Struik, Pretoria.

MCDOUGALL, I. and HARRISON, T.M., 1999. Geochronology and Thermochronology by the 40Ar/39Ar Method. Oxford University Press on Demand.

MCGILVERY, T. and COOK, D.L., 2003. The influence of local gradients on accommodation space and linked depositional elements across a stepped slope profile, offshore Brunei, Shelf margin deltas and linked down slope petroleum systems: Global significance and future exploration potential: Gulf Coast Section SEPM 23rd Annual Research Conference 2003, pp. 387-419.

MCKAY, M.P., WEISLOGEL, A.L., FILDANI, A., BRUNT, R.L., HODGSON, D.M. and FLINT, S.S., 2015. U-PB zircon tuff geochronology from the Karoo Basin, South Africa: implications of zircon recycling on stratigraphic age controls. International Geology Review, 57(4), pp. 393-410.

MCKIE, T., JOLLEY, S. and KRISTENSEN, M., 2010. Stratigraphic and structural compartmentalization of dryland fluvial reservoirs: Triassic Heron Cluster, Central North Sea. Geological Society, London, Special Publications, 347(1), pp. 165-198.

MCLACHLAN, I. and ANDERSON, A., 1973. A review of the evidence for marine conditions in southern Africa during Dwyka times.

MCNAMARA, D.E., BENZ, H.M., HERRMANN, R.B., BERGMAN, E.A., EARLE, P., HOLLAND, A., BALDWIN, R. and GASSNER, A., 2015. Earthquake hypocenters and focal mechanisms in central Oklahoma reveal a complex system of reactivated subsurface strike-slip faulting. Geophysical Research Letters, 42(8), pp. 2742-2749.

MILDREN, S., HILLIS, R. and KALDI, J., 2002. Calibrating predictions of fault seal reactivation in the Timor Sea. APPEA journal, 42(1), pp. 187-202.

MILLER, K.G., KOMINZ, M.A., BROWNING, J.V., WRIGHT, J.D., MOUNTAIN, G.S., KATZ, M.E., SUGARMAN, P.J., CRAMER, B.S., CHRISTIE-BLICK, N. and PEKAR, S.F., 2005. The Phanerozoic record of global sea-level change. Science (New York, N.Y.), 310(5752), pp. 1293-1298.

MILLER, W., DE WIT, M.J., LINOL, B. and ARMSTRONG, R., 2016. New Structural Data and U/Pb Dates from the Gamtoos Complex and Lowermost Cape Supergroup of the Eastern Cape Fold Belt, in Support of a Southward Paleo-Subduction Polarity. Origin and Evolution of the Cape Mountains and Karoo Basin. Springer, pp. 35-44.

Mindat: Zircon.22/01/2018, 2018-last update [Homepage of Hudson Institute of Mineralogy], [Online]. Available: https://www.mindat.org/min-4421.html [01/15, 2018].

MINISINI, D., TRINCARDI, F., ASIOLI, A., CANU, M. and FOGLINI, F., 2007. Morphologic variability of exposed mass-transport deposits on the eastern slope of Gela Basin (Sicily channel). Basin Research, 19(2), pp. 217-240.

MOECK, I.S., 2014. Catalog of geothermal play types based on geologic controls. Renewable and Sustainable Energy Reviews, 37, pp. 867-882.

MONTAGUE, T., 2016. World Energy Resources. Geothermal. World Energy Council. [Online]. Available: https://www.worldenergy.org/wp-content/uploads/2017/03/WEResources_Geothermal_2016.pdf

MOSCARDELLI, L. and WOOD, L., 2008. New classification system for mass transport complexes in offshore Trinidad. Basin research, 20(1), pp. 73-98.

MOSCARDELLI, L., WOOD, L. and MANN, P., 2006. Mass-transport complexes and associated processes in the offshore area of Trinidad and Venezuela. AAPG Bulletin, 90(7), pp. 1059-1088.

MUFFLER, P. and CATALDI, R., 1978. Methods for regional assessment of geothermal resources. Geothermics, 7(2-4), pp. 53-89.

MUKUHIRA, Y., ASANUMA, H., NIITSUMA, H. and HÄRING, M.O., 2013. Characteristics of large-magnitude microseismic events recorded during and after stimulation of a geothermal reservoir at Basel, Switzerland. Geothermics, 45, pp. 1-17.

MURRAY, R., COBBING, J., WOODFORD, A., RAVENSCROFT, L. and CHEVALLIER, L., 2006. Groundwater research needs in the Eastern Karoo basin of South Africa. Pretoria: Water Research Commission.

MUTTI, E. and GHIBAUDO, G., 1972. Un esempio di torbiditi di conoide sottomarina esterna: le Arenarie di San Salvatore (Formazione di Bobbio, Miocene) nell'Appennino di Piacenza. Accademia delle scienze.

MUTTI, E. and NORMARK, W.R., 1991. An integrated approach to the study of turbidite systems. Seismic facies and sedimentary processes of submarine fans and turbidite systems. Springer, pp. 75-106.

MUTTI, E., 1979. Turbidites et cones sous-marins profonds. Sédimentation détritique (fluviatile, littorale et marine), 1, pp. 353-419.

NÁDOR, A., 2014. Danube Region Geothermal Report. Danube region strategy, energy. [Online] available at: http://www.danube-region.eu

NATIONAL RESEARCH COUNCIL, 1996. Rock fractures and fluid flow: contemporary understanding and applications. National Academies Press.

NATIONAL RESEARCH COUNCIL, 2013. Induced seismicity potential in energy technologies. National Academies Press.

NEUMANN, E., SVENSEN, H., GALERNE, C.Y. and PLANKE, S., 2011. Multistage evolution of dolerites in the Karoo large igneous province, Central South Africa. Journal of Petrology, 52(5), pp. 959-984.

NEWTON, A., SHONE, R. and BOOTH, P., 2006. The Cape fold belt. The Geology of South Africa, Johannesburg/Council of Geoscience, Pretoria, pp. 521-528.

NEWTON, C., SHIPP, R., MOSHER, D. and WACH, G., 2004. Importance of mass transport complexes in the Quaternary development of the Nile Fan, Egypt, Offshore Technology Conference 2004, Offshore Technology Conference.

NICHOLS, G., 2009. Sedimentology and stratigraphy. John Wiley & Sons.

NOREM, H., LOCAT, J. and SCHIELDROP, B., 1990. An approach to the physics and the modeling of submarine flowslides. Marine Georesources & Geotechnology, 9(2), pp. 93-111.

NORMARK, W.R., 1970. Growth patterns of deep-sea fans. AAPG Bulletin, 54(11), pp. 2170-2195.

OELOFSEN, B., 1987. The biostratigraphy and fossils of the Whitehill and Iratí Shale Formations of the Karoo and Paraná Basins. Gondwana Six: Stratigraphy, Sedimentology, and Paleontology, , pp. 131-138.

OLIVEIRA, C.M., HODGSON, D.M. and FLINT, S.S., 2011. Distribution of soft-sediment deformation structures in clinoform successions of the Permian Ecca Group, Karoo Basin, South Africa. Sedimentary Geology, 235(3), pp. 314-330.

PÁNGARO, F. and RAMOS, V.A., 2012. Paleozoic crustal blocks of onshore and offshore central Argentina: new pieces of the southwestern Gondwana collage and their role in the accretion of Patagonia and the evolution of Mesozoic south Atlantic sedimentary basins. Marine and Petroleum Geology, 37(1), pp. 162-183.

PANKHURST, R.J., RAPELA, C.W., FANNING, C. and MÁRQUEZ, M., 2006. Gondwanide continental collision and the origin of Patagonia. Earth-Science Reviews, 76(3), pp. 235-257.

PARKINSON, D., 1996. Gamma-ray spectrometry as a tool for stratigraphical interpretation: examples from the western European Lower Jurassic. Geological Society, London, Special Publications, 103(1), pp. 231-255.

PASSEY, Q., CREANEY, S., KULLA, J., MORETTI, F. and STROUD, J., 1990. A practical model for organic richness from porosity and resistivity logs. AAPG Bulletin, 74(12), pp. 1777-1794.

PASSEY, Q.R., BOHACS, K., ESCH, W.L., KLIMENTIDIS, R. and SINHA, S., 2010. From oil-prone source rock to gas-producing shale reservoir-geologic and petrophysical characterization of unconventional shale gas reservoirs, International oil and gas conference and exhibition in China 2010, Society of Petroleum Engineers.

PATON, D.A., MACDONALD, D.I. and UNDERHILL, J.R., 2006. Applicability of thin or thick skinned structural models in a region of multiple inversion episodes; southern South Africa. Journal of Structural Geology, 28(11), pp. 1933-1947.

PEDERSEN, T. and CALVERT, S., 1990. Anoxia vs. productivity: what controls the formation of organic-carbon-rich sediments and sedimentary Rocks?(1). AAPG Bulletin, 74(4), pp. 454-466.

PETROLEUM AGENCY SOUTH AFRICA, 2015-last update, History of Exploration and Production [Homepage of Petroleum Agency SA], [Online]. Available: http://www.petroleumagencysa.com/index.php/petroleum-geology-resources/exploration-history2015].

PETROLEUM AGENCY SOUTH AFRICA, 2017-last update, Exploration Activites Map [Homepage of PetroSA], [Online]. Available: http://petroleumagencysa.com/index.php/maps2018].

PETTIJOHN, F.J., 1975. Sedimentary Rocks. 3rd edn. New York: Harper and Row.

PI, D., LIU, C., SHIELDS-ZHOU, G.A. and JIANG, S., 2013. Trace and rare earth element geochemistry of black shale and kerogen in the early Cambrian Niutitang Formation in Guizhou province, South China: Constraints for redox environments and origin of metal enrichments. Precambrian Research, 225, pp. 218-229.

PIPER, D. and CALVERT, S., 2009. A marine biogeochemical perspective on black shale deposition. Earth-Science Reviews, 95(1), pp. 63-96.

POLLACK, H.N., HURTER, S.J. and JOHNSON, J.R., 1993. Heat flow from the Earth's interior: analysis of the global data set. Reviews of Geophysics, 31(3), pp. 267-280.

POPOV, Y.A., PRIBNOW, D.F., SASS, J.H., WILLIAMS, C.F. and BURKHARDT, H., 1999. Characterization of rock thermal conductivity by high-resolution optical scanning. Geothermics, 28(2), pp. 253-276.

POTTER, P.E., MAYNARD, J.B. and DEPETRIS, P.J., 2005. Mud and mudstones: Introduction and overview. Springer Science & Business Media.

RAFFERTY, K., 2000. Geothermal Power Generation. Geo-Heat Center.

RAMOS, V.A., 2008. Patagonia: A paleozoic continent adrift? Journal of South American Earth Sciences, 26(3), pp. 235-251.

RAUP, D.M. and SEPKOSKI, J.J.,JR, 1986. Periodic extinction of families and genera. Science (New York, N.Y.), 231, pp. 833-836.

RAWCLIFFE, H.J., HODGSON, D.M., BRUNTI, R.L. and WEISLOGEL, A., 2012. Late-Permian Volcanism of Southern Gondwana as recorded by tuffs of the Tierberg Formation, South Africa. , VMSG Annual Meeting, Durham. 2012.

RENNE, P.R., ERNESTO, M., PACCA, I.G., COE, R.S., GLEN, J.M., PREVOT, M. and PERRIN, M., 1992. The age of Paraná fl ood volcanism, rifting of Gondwanaland, and the Jurassic-Cretaceous boundary. Science, , pp. 975-979.

RICHARDS, M., BOWMAN, M. and READING, H., 1998. Submarine-fan systems I: characterization and stratigraphic prediction. Marine and Petroleum Geology, 15(7), pp. 689-717.

RIDER, M. and KENNEDY, M., 2011. The Geological Interpretation of Well Logs. 3rd edn. Rogart: Rider French Consulting Limited.

RIDER, M., 1990. Gamma-ray log shape used as a facies indicator: critical analysis of an oversimplified methodology. Geological Society, London, Special Publications, 48(1), pp. 27-37.

RIDGWELL, A., 2005. A Mid Mesozoic Revolution in the regulation of ocean chemistry. Marine Geology, 217(3), pp. 339-357.

RIMMER, S.M., 2004. Geochemical paleoredox indicators in Devonian–Mississippian black shales, central Appalachian Basin (USA). Chemical Geology, 206(3), pp. 373-391.

ROCHA-CAMPOS, A.C., BASEI, M., NUTMAN, A.P., KLEIMAN, L.E., VARELA, R., LLAMBIAS, E., CANILE, F. and DA ROSA, O DE CR, 2011. 30million years of Permian volcanism recorded in the Choiyoi igneous province (W Argentina) and their source for younger ash fall deposits in the Paraná Basin: SHRIMP U–Pb zircon geochronology evidence. Gondwana Research, 19(2), pp. 509-523.

ROURE, F. and SASSI, W., 1995. Kinematics of deformation and petroleum system appraisal in Neogene foreland fold-and-thrust belts. Petroleum Geoscience, 1(3), pp. 253-269.

ROWSELL, A., 1976. Diagenesis in Cape and Karroo sediments, South Africa, and its bearing on their hydrocarbon potential. South African Journal of Geology, 79(1), pp. 81-145.

ROWSELL, D.M. and DE SWARDT, A.M.J., 1976. Daigenesis in Cape and Karoo Sediments, South Africa, and its bearing on thier hydrocarbon potential. Transactions of the Geological Society of South Africa, 79, pp. 81-145.

RUBIDGE, B.S., 2005. Re-uniting lost continents--Fossil reptiles from the ancient Karoo and their wanderlust. South African Journal of Geology, 108(1).

RUBIO-MAYA, C., DIAZ, V.A., MARTINEZ, E.P. and BELMAN-FLOREZ, J.M., 2015. Cascade utilization of low and medium enthalpy geothermal resources− A review. Renewable and Sustainable Energy Reviews, 52, pp.689-716.

RUCKWIED, K., GÖTZ, A.E. and JONES, P., 2014. Palynological records of the Permian Ecca Group (South Africa): Utilizing climatic icehouse–greenhouse signals for cross basin correlations. Palaeogeography, Palaeoclimatology, Palaeoecology, 413, pp. 167-172.

RÜHAAK, W., GUADAGNINI, A., GEIGER, S., BÄR, K., GU, Y., ARETZ, A., HOMUTH, S. and SASS, I., 2015. Upscaling thermal conductivities of sedimentary formations for geothermal exploration. Geothermics, 58, pp. 49-61.

SANTOS, R.V., SOUZA, P.A., DE ALVARENGA, CARLOS JOSÉ SOUZA, DANTAS, E.L., PIMENTEL, M.M., DE OLIVEIRA, C.G. and DE ARAÚJO, L.M., 2006. Shrimp U–Pb zircon dating and palynology of bentonitic layers from the Permian Irati Formation, Paraná Basin, Brazil. Gondwana Research, 9(4), pp. 456-463.

SASS, I. and GÖTZ, A.E., 2012. Geothermal reservoir characterization: a thermofacies concept. Terra Nova, 24(2), pp. 142-147.

SCHELLSCHMIDT, R., 1999. Vergleichsmessungen der spezifischen Wärmekapazität an Proben aus dem Schweizer Molassebecken mit einem Dynamischen Wärmestrom-Differenz-Kalorimeter. Hannover: Institut für Geowissenschaftliche Gemeinschaftsaufgaben (GGA); 1999. Institut für Geowissenschaftliche Gemeinschaftsaufgaben (GGA), Hannover.

SCHELLSCHMIDT, R., SANNER, B., PESTER, S., and SCHULZ, R., 2010. Geothermal Energy Use in Germany. Proceedings World Geothermal Congress 2010 Bali, Indonesia, 25-29 April 2010

SCHIEBER, J., 1998. Possible indicators of microbial mat deposits in shales and sandstones: examples from the Mid-Proterozoic Belt Supergroup, Montana, USA. Sedimentary Geology, 120(1), pp. 105-124.

SCHIEBER, J., 1999. Microbial mats in terrigenous clastics; the challenge of identification in the rock record. Palaios, 14(1), pp. 3-12.

SCHIEBER, J., 2003. Simple gifts and buried treasures—implications of finding bioturbation and erosion surfaces in black shales. The Sedimentary Record, 1(2), pp. 4-8.

SCHNELLMANN, M., ANSELMETTI, F.S., GIARDINI, D. and MCKENZIE, J.A., 2005. Mass movement-induced fold-and-thrust belt structures in unconsolidated sediments in Lake Lucerne (Switzerland). Sedimentology, 52(2), pp. 271-289.

SCHULZ, H., CHERE, N., GEEL, C., BOOTH, P. and DE WIT, M.J., 2016. Is the Postglacial History of the Baltic Sea an Appropriate Analogue for the Formation of Black Shales in the Lower Ecca Group (Early Permian) of the Karoo Basin, South Africa? Origin and Evolution of the Cape Mountains and Karoo Basin. Springer, pp. 111-117.

SENGER, K., BUCKLEY, S.J., CHEVALLIER, L., FAGERENG, Å., GALLAND, O., KURZ, T.H., OGATA, K., PLANKE, S. and TVERANGER, J., 2015. Fracturing of doleritic intrusions and associated contact zones: implications for fluid flow in volcanic basins. Journal of African Earth Sciences, 102, pp. 70-85.

SERRA, O., 1984. Natural Gamma-Ray Spectrometry. Developments in Petroleum Science, 15, 113-134, Elsevier.

SETHI, P.S. and SCHIEBER, J., 1998. Economic aspects of shales and clays: an overview. Shales and mudstones II, E.Schweizerbart'sche Verlagsbuchhandlung, Stuttgart, pp. 237-253.

SHANMUGAM, G., 2016. Submarine fans: a critical retrospective (1950–2015). Journal of Palaeogeography, 5(2), pp. 110-184.

SHANMUGAM, G., DAMUTH, J. and MOIOLA, R., 1985. Is the turbidite facies association scheme valid for interpreting ancient submarine fan environments? Geology, 13(4), pp. 234-237.

SHIPTON, Z., EVANS, J. and THOMPSON, L., 2005. The geometry and thickness of deformation-band fault core and its influence on sealing characteristics of deformation-band fault zones.

SHONE, R. and BOOTH, P., 2005. The Cape Basin, South Africa: A review. Journal of African Earth Sciences, 43(1), pp. 196-210.

SMART, K.J., OFOEGBU, G.I., MORRIS, A.P., MCGINNIS, R.N. and FERRILL, D.A., 2014. Geomechanical modeling of hydraulic fracturing: Why mechanical stratigraphy, stress state, and pre-existing structure matter. AAPG Bulletin, 98(11), pp. 2237-2261.

SMITH, R., 1990. A review of stratigraphy and sedimentary environments of the Karoo Basin of South Africa. Journal of African Earth Sciences (and the Middle East), 10(1-2), pp. 117-137.

SMITH, R., ERIKSSON, P. and BOTHA, W., 1993. A review of the stratigraphy and sedimentary environments of the Karoo-aged basins of Southern Africa. Journal of African Earth Sciences (and the Middle East), 16(1), pp. 143-169.

SMITH, R.M., 1995. Changing fluvial environments across the Permian-Triassic boundary in the Karoo Basin, South Africa and possible causes of tetrapod extinctions. Palaeogeography, Palaeoclimatology, Palaeoecology, 117(1-2), pp. 81-104.

SMITHARD, T., BORDY, E. and REID, D., 2015. The effect of dolerite intrusions on the hydrocarbon potential of the Lower Permian Whitehill Formation (Karoo Supergroup) in South africa and Southern Namibia: A preliminary study. South African Journal of Geology, 118(4), pp. 489-510.

SÖHNGE, A., 1983. The Cape Fold Belt-Perspective. Geodynamics of the Cape Fold Belt, 12, pp. 1-6.

SOMERTON, W.H., 1992. Thermal properties and temperature-related behavior of rock/fluid systems. Elsevier.

SPALLETTI, L.A., FANNING, C. and RAPELA, C.W., 2008. Dating the Triassic continental rift in the southern Andes: the Potrerillos Formation, Cuyo basin, Argentina. Geologica Acta: an international earth science journal, 6(3).

STEVENS, C.H. and STONE, P., 2005. Interpretation of the Last Chance thrust, Death Valley region, California, as an Early Permian décollement in a previously undeformed shale basin. Earth-Science Reviews, 73(1-4), pp. 79-101.

STEYL, G., VAN TONDER, G.J. and CHEVALLIER, L.P., 2012. State of the Art: Fracking for Shale Gas Exploration in South Africa and the Impact on Water Resources: Report to the Water Research Commission. Water Research Commission.

STOLLHOFEN, H., STANISTREET, I.G., BANGERT, B. and GRILL, H., 2000. Tuffs, tectonism and glacially related sea-level changes, Carboniferous–Permian, southern Namibia. Palaeogeography, Palaeoclimatology, Palaeoecology, 161(1), pp. 127-150.

STOW, D., HUC, A. and BERTRAND, P., 2001. Depositional processes of black shales in deep water. Marine and Petroleum Geology, 18(4), pp. 491-498.

SULTAN, N., COCHONAT, P., CANALS, M., CATTANEO, A., DENNIELOU, B., HAFLIDASON, H., LABERG, J., LONG, D., MIENERT, J. and TRINCARDI, F., 2004. Triggering mechanisms of slope instability processes and sediment failures on continental margins: a geotechnical approach. Marine Geology, 213(1-4), pp. 291-321.

SULTAN, N., VOISSET, M., MARSSET, B., MARSSET, T., CAUQUIL, E. and COLLIAT, J., 2007. Potential role of compressional structures in generating submarine slope failures in the Niger Delta. Marine Geology, 237(3-4), pp. 169-190.

SVENSEN, H., CORFU, F., POLTEAU, S., HAMMER, Ø. and PLANKE, S., 2012. Rapid magma emplacement in the Karoo large igneous province. Earth and Planetary Science Letters, 325, pp. 1-9.

SVENSEN, H., PLANKE, S., CHEVALLIER, L., MALTHE-SØRENSSEN, A., CORFU, F. and JAMTVEIT, B., 2007. Hydrothermal venting of greenhouse gases triggering Early Jurassic global warming. Earth and Planetary Science Letters, 256(3), pp. 554-566.

SVENSEN, H., PLANKE, S., CHEVALLIER, L., MALTHE-SØRENSSEN, A., CORFU, F. and JAMTVEIT, B., 2007. Hydrothermal venting of greenhouse gases triggering Early Jurassic global warming. Earth and Planetary Science Letters, 256(3-4), pp. 554-566.

SZANYI, J. and KOVÁCS, B., 2010. Utilization of geothermal systems in South-East Hungary. Geothermics, 39(4), pp. 357-364.

TANKARD, A., WELSINK, H., AUKES, P., NEWTON, R. and STETTLER, E., 2012. Geodynamic interpretation of the Cape and the Karoo basins, South Africa. Phanerozoic Passive Margins, Cratonic Basins and Global Tectonics Maps, 869.

TANKARD, A., WELSINK, H., AUKES, P., NEWTON, R. and STETTLER, E., 2009. Tectonic evolution of the Cape and Karoo basins of South Africa. Marine and Petroleum Geology, 26(8), pp. 1379-1412.

TESTER, J.W., DRAKE, E.M., DRISCOLL, M.J., GOLAY, M.W. and PETERS, W.A., 2012. Sustainable energy: choosing among options. MIT press.

THOMAS, C.G., 2001. Sedimentology and stratigraphy of the Falkland Islands Permian with comparisons to Gondwanan stratigraphy of South Africa and South America.

TIKHOMIROV, V., 1968. The thermal conductivity of rocks and its relationship to density, moisture content, and temperature. Neftianoe Khoziaistvo, 46, pp. 36-40.

TOURTELOT, H.A., 1979. Black shale; its deposition and diagenesis. Clays and Clay Minerals, 27(5), pp. 313-321.

TRABUCHO-ALEXANDRE, J., HAY, W.W. and DE BOER, P.L., 2012. Phanerozoic environments of black shale deposition and the Wilson Cycle. Solid Earth, 3(1), pp. 29-42.

TREWIN, N., MACDONALD, D. and THOMAS, C., 2002. Stratigraphy and sedimentology of the Permian of the Falkland Islands: lithostratigraphic and palaeoenvironmental links with South Africa. Journal of the Geological Society, 159(1), pp. 5-19.

TRIBOVILLARD, N., ALGEO, T.J., LYONS, T. and RIBOULLEAU, A., 2006. Trace metals as paleoredox and paleoproductivity proxies: an update. Chemical Geology, 232(1-2), pp. 12-32.

TROUW, R.A. and DE WIT, M.J., 1999. Relation between the Gondwanide Orogen and contemporaneous intracratonic deformation. Journal of African Earth Sciences, 28(1), pp. 203-213.

TURNER, B., STANISTREET, I. and WHATELEY, M., 1981. Trace fossils and palaeoenvironments in the Ecca Group of the Nongoma Graben, northern Zululand, South Africa. Palaeogeography, Palaeoclimatology, Palaeoecology, 36(1-2), pp. 113-123.

TURNER, B.R., 1999. Tectonostratigraphical development of the Upper Karooforeland basin: Orogenic unloading versus thermally-induced Gondwana rifting. Journal of African Earth Sciences, 28(1), pp. 215-238.

TYSON, R., 1987. The genesis and palynofacies characteristics of marine petroleum source rocks. Geological Society, London, Special Publications, 26(1), pp. 47-67.

TYSON, R., 2001. Sedimentation rate, dilution, preservation and total organic carbon: some results of a modelling study. Organic Geochemistry, 32(2), pp. 333-339.

TYSON, R., 2005. The" productivity versus preservation" controversy: cause, flaws, and resolution. SPECIAL PUBLICATION-SEPM, 82, pp. 17.

TYSON, R.V., 1995. Abundance of organic matter in sediments: TOC, hydrodynamic equivalence, dilution and flux effects. Sedimentary organic matter. Springer, pp. 81-118.

UNITED STATES ENERGY INFORMATION ADMINISTRATION, 2015. Technically recoverable shale oil and shale gas resources: South Africa. US Energy Information Administration.

VAN DER MERWE, W., HODGSON, D. and FLINT, S., 2009. Widespread syn-sedimentary deformation on a muddy deep-water basin-floor: the Vischkuil Formation (Permian), Karoo Basin, South Africa. Basin Research, 21(4), pp. 389-406.

VAN DIJK, D., CHANNING, A. and VAN DEN HEEVER, J., 2002. Permian trace fossils attributed to tetrapods (Tierberg formation, Karoo basin, South Africa).

VAN DONGEN, B.E., SCHOUTEN, S., BAAS, M., GEENEVASEN, J.A. and DAMSTÉ, J.S.S., 2003. An experimental study of the low-temperature sulfurization of carbohydrates. Organic Geochemistry, 34(8), pp. 1129-1144.

VAN LENTE, B., 2004. Chemostratigraphic trends and provenance of the Permian Tanqua and Laingsburg depocentres, southwestern Karoo basin, South Africa.

VAN TONDER, G. and KIRCHNER, J., 1990. Estimation of natural groundwater recharge in the Karoo aquifers of South Africa. Journal of Hydrology, 121(1-4), pp. 395-419.

VAN WEES, J., KRONIMUS, A., VAN PUTTEN, M., PLUYMAEKERS, M., MIJNLIEFF, H., VAN HOOFF, P., OBDAM, A. and KRAMERS, L., 2012. Geothermal aquifer performance assessment for direct heat production–Methodology and application to Rotliegend aquifers. Netherlands Journal of Geosciences, 91(4), pp. 651-665.

VEDOVA, B., LUCAZEAU, F., PASQUALE, V., PELLIS, G. and VERDOYA, M., 1991. Heat flow in the tectonic provinces of the European Geotraverse. Tectonophysics, 244(57), pp. e74.

VEEVERS, J., 2004. Gondwanaland from 650–500 Ma assembly through 320 Ma merger in Pangea to 185–100 Ma breakup: supercontinental tectonics via stratigraphy and radiometric dating. Earth-Science Reviews, 68(1-2), pp. 1-132.

VEEVERS, J., COLE, D. and COWAN, E., 1994. Southern Africa: Karoo basin and Cape fold belt. Geological Society of America Memoirs, 184, pp. 223-280.

VELBEL, M., 1983. A dissolution-reprecipitation mechanism for the pseudomorphous replacement of plagioclase feldspar by clay minerals during weathering. Pétrologie des Altérations et des Sols, 1, pp. 139-147.

VELICIU, S. and ŠAFANDA, J., 1998. Ground temperature history in Romania inferred from borehole temperature data. Tectonophysics, 291(1-4), pp. 277-286.

VILJOEN, J.H.A., 1992. Lithostratigraphy of the Collingham Formation (Ecca Group), including the Zoute Kloof, Buffels River and Wilgehoute Members and the Matjiesfontein Chert Bed. Lithostratigraphy Service South African Commission of Stratigraphy, 22, pp. 10.

VILJOEN, J.H.A., 2004. Piroklastiese afsettings van Perm-ouderdom in die hoof-Karookom met spesiale verwysing na die Collingham Formasie, Ecca Groep. Memoir- Council for Geoscience.

VILLIERS, D., J. 1944. A review of the Cape orogeny. Annals of the University of Stellenbosch 42 (A), (10), pp. 183-208.

VISSER, J., 1978. Water depth in the main Karoo basin, South Africa, during Ecca (Permian) sedimentation. South African Journal of Geology, 81(2), pp. 185-191.

VISSER, J., 1992. Deposition of the Early to Late Permian Whitehill Formation during a sea-level highstand in a juvenile foreland basin. South African Journal of Geology, 95(5-6), pp. 181-193.

VISSER, J., 1994. A Permian argillaceous syn-to post-glacial foreland sequence in the Karoo Basin, South Africa. Earth's Glacial Record.International Geological Correlation Project, 260, pp. 193-203.

VISSER, J.N., 1996. Controls on Early Permian shelf deglaciation in the Karoo Basin of South Africa. Palaeogeography, Palaeoclimatology, Palaeoecology, 125(1-4), pp. 129-139.

VON HUENE, F. and POMPECKJ, J.F., 1931. Beitrag zur Kenntnis der Fauna der südafrikanischen Karrooformation:[Joseph Felix Pompeckj 10. 5. 1867-8. 7. 1930]. G. Fischer.

VON HUENE, FRIEDRICH R FREIHERR, 1925. Die südafrikanische Karroo-Formation als geologisches und faunistisches Lebensbild. Gebrüder Borntraeger.

VOSTEEN, H. and SCHELLSCHMIDT, R., 2003. Influence of temperature on thermal conductivity, thermal capacity and thermal diffusivity for different types of rock. Physics and Chemistry of the Earth, Parts A/B/C, 28(9), pp. 499-509.

WALKER, R.G., 1978. Deep-water sandstone facies and ancient submarine fans: models for exploration for stratigraphic traps. AAPG Bulletin, 62(6), pp. 932-966.

WANG, G., LI, K., WEN, D., LIN, W., LIN, L., LIU, Z., ZHANG, W., MA, F. and WANG, W., 2013. Assessment of geothermal resources in China, Proceedings of the 38th workshop on geothermal reservoir engineering, Stanford, California, 11-13 February 2013.

WANG, K., 2010. General Characteristics of Geothermal Areas in China, Proceedings of World Geothermal Congress 2010 Bali, Indonesia, 25-29 April 2010.

WARNER, D.L., 1977. An introduction to the technology of subsurface wastewater injection. Municipal Environmental Research Laboratory, Office of Research and Development, US Environmental Protection Agency.

WATKEYS, M.K., 2006. Gondwana break-up: A South African perspective. In: M.R. JOHNSON, C.R. ANHAEUSSER and R.J. THOMAS, eds, The Geology of South Africa. Pretoria: Geological Society of South Africa, pp. 691.

WEATHERFORD INTERNATIONAL LTD, 2011. GEOSERVE SA-UJ Log Report: Tools Used and Tool Description. UJ_001. South Africa: Weatherford.

WEI, G., LIU, Y., LI, X., SHAO, L. and LIANG, X., 2003. Climatic impact on Al, K, Sc and Ti in marine sediments: evidence from ODP Site 1144, South China Sea. Geochemical Journal, 37(5), pp. 593-602.

WEI, H., CHEN, D., WANG, J., YU, H. and TUCKER, M.E., 2012. Organic accumulation in the lower Chihsia Formation (Middle Permian) of South China: constraints from pyrite morphology and multiple geochemical proxies. Palaeogeography, Palaeoclimatology, Palaeoecology, 353, pp. 73-86.

WEINGARTEN, M., GE, S., GODT, J.W., BEKINS, B.A. and RUBINSTEIN, J.L., 2015. INDUCED SEISMICITY. High-rate injection is associated with the increase in U.S. mid-continent seismicity. Science (New York, N.Y.), 348(6241), pp. 1336-1340.

WERNE, J.P., SAGEMAN, B.B., LYONS, T.W. and HOLLANDER, D.J., 2002. An integrated assessment of a “type euxinic” deposit: evidence for multiple controls on black shale deposition in the Middle Devonian Oatka Creek Formation. American Journal of Science, 302(2), pp. 110-143.

WIGNALL, P. and NEWTON, R., 2001. Black shales on the basin margin: a model based on examples from the Upper Jurassic of the Boulonnais, northern France. Sedimentary Geology, 144(3), pp. 335-356.

WIGNALL, P.B., 1994. Black shales. Clarendon Press Oxford.

WILLIAMS, C.F., REED, M. and MARINER, R.H., 2008. A Review of Methods Applied by the US Geological Survey in the Assessment If Identified Geothermal Resources. US Department of Interior, US Geological Survey.

WINTER, H DE LA R, VENTER, J. and HAUGHTON, S., 1970. Lithostratigraphic correlation of recent deep boreholes in the Karroo-Cape sequence. Soekor.

WUESTEFELD, A., VERDON, J.P., KENDALL, J., RUTLEDGE, J., CLARKE, H. and WOOKEY, J., 2011. Inferring rock fracture evolution during reservoir stimulation from seismic anisotropy. Geophysics.

ZAFAR, S.D. and CUTRIGHT, B.L., 2014. Texas' geothermal resource base: a raster-integration method for estimating in-place geothermal-energy resources using ArcGIS. Geothermics, 50, pp. 148-154.

ZHANG, X., HE, M. and ZHANG, Y., 2012. A review of research on the Kalina cycle. Renewable and sustainable energy reviews, 16(7), pp.5309-5318.

ZHU, J., HU, K., LU, X., HUANG, X., LIU, K. and WU, X., 2015. A review of geothermal energy resources, development, and applications in China: Current status and prospects. Energy, 93, pp. 466-483.

ZIMMERMAN, R.W., 1989. Thermal conductivity of fluid-saturated rocks. Journal of Petroleum Science and Engineering, 3(3), pp. 219-227.

Appendices

Appendix A

-Borehole KZF-1 Wireline Logs

-Borehole KZF-1 Descriptive Logs

-Borehole KZF-1 Lithological Log key

-Borehole KZF-1 Lithological Log

Appendix B

-Ecca Pass Descriptive Log

-Ecca Pass Lithological Log Key

-Ecca Pass Lithological Key

Appendix C

-Borehole KWV-1 Wireline Logs

-Borehole KWV-1 Descriptive Logs

-Borehole KWV-1 Lithological Log Key

-Borehole KWV-1 Lithological Log

See attached CD for Appendices